Dissertation

submitted to the

Combined Faculties for the Natural Sciences and for Mathematics

of the Ruperto-Carola University of Heidelberg, Germany

for the degree of

Doctor of Natural Sciences

Put forward by

DIPL.-PHYS. WOLFGANG MISCHLER

born in Ludwigshafen

Date of Oral Examination: 12.11.2014

Systematic Measurements of Bubble Induced Gas Exchange for Trace Gases with Low Solubilities

Referees:

Prof. Dr. BERND JÄHNE

Prof. Dr. WERNER AESCHBACH-HERTIG

Abstract: This thesis reports on a systematic experimental study on bubble-mediated gas transfer. Trace gas concentrations were measured using a quadrupole mass spectrometer with two silicone membrane inlets in the gas and water phase of the gas tight bubble tank. Fourteen trace gases with a wide range of solubilities and diffusivities – SF_6, Neon, N_2, HD, D_2, O_2, Krypton, Pentafluoroethane, Xenon, N_2O, C_2H_2, CH_3Cl, Benzene and DMS – were used to investigate the dependency on these two physico-chemical parameters. Bubbles were generated by a water jet with adjustable kinetic energy, which entrained a controllable gas volume flux into the water tank. Bubble size distributions in a radius range from $10\,\mu m$ to $5000\,\mu m$ and velocity distributions in a range from $70\,\mu m$ to $3000\,\mu m$ were measured at 60 positions by a telecentric optical setup. Invasion and evasion experiments with a variety of conditions were conducted including salt water ($1.75\,\%$ NaCl), the addition of the soluble surfactant Triton X-100, n-butanol and glycerol. All used additives tend to increase the fraction of small bubbles generated and therefore increase the transfer velocity at constant gas volume flux and energy input. The addition of salt had the strongest effect, leading to an enhancement of the transfer velocity up to a factor of ~ 4. The increase of the transfer velocity adding Triton X-100 was found to be lower than $5\,\%$. The transition between diffusivity controlled and solubility controlled transfer occurs at solubilities ranging from 0.05 to 0.44. The transition is shifted to lower solubilities by a factor of ~ 3 by the addition of salt. Existing models for bubble mediated gas transfer are tested. Simple power law dependencies turn out to be incapable to describe the transfer for the whole range of solubilities and diffusivities. An extension of the parametrization proposed by Woolf [71] requiring 4 parameters fits the data best. A simple model using only 2 parameters is proposed. Its performance is almost as good as the extended Woolf model.

Zusammenfassung: In dieser Arbeit wurde ein Experiment zur Untersuchung von blasen-induzierten Gasaustausch entwickelt und durchgeführt. Spurengase wurden mithilfe von einem Quadrupol Massenspektrometer mit zwei Silikonmembran-Einlässen auf der Luft- und auf der Wasserseite eines gasdichten Glastanks gemessen. Vierzehn Gase – SF_6, Neon, N_2, HD, D_2, O_2, Krypton, Pentafluoroethane, Xenon, N_2O, C_2H_2, CH_3Cl, Benzol und DMS – wurden gemessen, um eine große Spanne an Löslichkeiten und Diffusionskonstanten abzudecken. Die Luftblasen wurden mittels eines Wasserstrahls mit einstellbarer kinetischer Energie erzeugt, welcher einen einstellbaren Luftvolumenstrom in das Wasser des Tanks trägt. Die Blasengrößen- und Geschwindigkeitsverteilungen wurden in einem Radiusbereich von 10 - $5000\,\mu m$ bzw. von 70 - $3000\,\mu m$ an 60 Positionen mit einem telezentrischen optischen Aufbau vermessen. Invasions und Evasions Messungen wurden an einer Vielzahl von Bedingungen durchgeführt, zu denen Salzwasser ($1.75\,\%$ NaCl), die Zugabe von dem Oberflächenfilm Triton X-100, n-Butanol und Glycerin gehören. Alle Zusätze erhöhen tendenziell den Anteil an kleinen Blasen, was zu einer Beschleunigung des Gastransfers, bei gleichebleibendem Gasfluss und Energieeintrag, führt. Die Zugabe von Salz zeigte den größten Effekt, der die Transfergeschwindigkeit um einen Faktor ~ 4 erhöhte. Der Einfluss von Triton X-100 blieb unter $5\,\%$. Der Wert der Löslichkeit für den Übergang von dem diffusionskontrollierten Regime zu dem löslichkeitskontrollierten Regime lag im Bereich von 0.05-0.44. Dieser Übergang verschob sich um einen Faktor ~ 3 zu niedrigeren Löslichkeiten für Salzwasserbedingungen. Existiernede Modelle zur Beschreibung des blasen-induzierten Gasaustauschs wurden überprüft. Mit einfachen Potenzgesetzen ist es nicht möglich den Gastransfer über alle Löslichkeiten und Diffusionskonstanten zu beschreiben. Eine Erweiterung des Modells von Woolf [71] beschreibt die gemessenen Daten am besten. Ein neues Modell mit nur zwei Parametern liefert fast so gute Ergebnisse wie das erweiterte Modell von Woolf.

Contents

1. Introduction

Gas exchange between gas and liquid phases is important in many contexts in nature and engineering. The most prevailing topic at these days is probably the climate change. The impact of different species of greenhouse gases on the global energy budget now and in the future is subject to a lively discussion [30]. Exchange processes between the atmosphere and the ocean play a large role in determining the global distribution of these gases. Particularly the fate of anthropogenic atmospheric emissions is depending strongly on processes at the large atmosphere-ocean interface, which covers the majority of the Earth's surface. Latest state of the art claims that e.g. about 20% of the anthropogenic CO_2 ends up in the oceans. Understanding this partitioning is important for reliable predictions of the future climate. Although models for air-sea gas transfer today have limited impact on global climate modeling, this is expected to change when climate models evolve to higher resolutions and accuracies [24]. Wind-generated waves on the water surface enhance gas exchange rates, since they increase the surface area and, more importantly, generate near surface turbulence through wave breaking [64]. As an additional effect they can produce bubbles, which increase the gas exchange further due to the additional surface area and turbulence induced by rising bubbles.

Bubble mediated gas transfer has several unique characteristics compared to gas transfer at free surfaces. At first sight bubbles increase the surface, which is available for gas exchange and therefore enhance gas exchange. While it is generally true that bubbles enhance gas exchange through the enlargement of the total air-water interface surface, bubbles surfaces do not need to be "active" for the whole bubble lifetime. Especially smaller bubbles can equilibrate with the surrounding liquid phase and stop exchanging gases. The extent of this bubble equilibration depends on the radius of the bubble, the surface conditions as well as the solubility of the exchanged trace gas. The higher the solubility, the faster the bubble equilibrates. Thus, bubble mediated gas transfer has a strong dependence on trace gas solubility. Due to the hydrostatic pressure and bubble surface tension, the gas in the bubbles is compressed, leading to higher apparent gas concentrations (super saturation). Also, bubbles may dissolve completely on their way through the liquid. These bubbles contribute to the invasion of trace gases from air to water, but not to the evasion from water to air, as they never reach the surface. This causes an invasion/evasion asymmetry. As both effects depend on the bubble size, knowledge of the distribution of radii is required to properly model bubble induced gas exchange.

Several experiments have been conducted in the past to investigate bubble mediated gas exchange. Even simple experiments with individual bubbles show that a wide range of transfer velocities can be observed depending on the boundary conditions at the interface. This is mainly dependent on the boundary conditions at the interface. In clean water, the transfer rates are usually

higher than when surface active substances (surfactants) are present, which attach to the bubble surface [48, 57]. Surfactants slow down transfer across the bubble surface, but also decrease the rise velocity, since they act as a resistance for the rising bubbles [2]. The surface condition of a bubble can change dynamically, as soluble surfactants accumulate over time during the rising of the bubble.

Laboratory experiments in wind wave tunnels, which simulate water surface conditions as found in the field, done in the past, were mostly not focused on bubble mediated transfer, but on wave parameters. Although analysis included bubble effects for higher wind speeds, which produced breaking waves and hence bubbles. Merlivat and Memery [51] measured two trace gases - Argon and N_2O - for different wind conditions and for sea and fresh water in a closed wind wave tunnel. The general effects and tendencies for super saturation and transfer enhancement could be verified and were in good agreement with field measurements. Because only two tracers were used it was not possible to verify the functional dependence from the solubility. Wanninkhof et al. [69] measured four gases - CO_2, N_2O, SF_6 and Helium - during the WABEX-93 experiment, which was conducted in a fresh water surf pool, which was equipped with mechanical wave generators. This experiment compared the data to parametrizations proposed by Keeling [37] and Woolf et al. [72]. It was found that the latter fits the data much better, though it was derived using sea water measurements. The problem with the comparison was the white capping W_c, a parameter describing the percentage of the surface covered by whitecaps [71], used as parameter for field measurements, since the white capping changes significantly for fresh and sea water. During the LUMINY experiment [17] conducted in the linear wave tank in Marseille, one set of experiments was performed to investigate the effect of bubbles on gas exchange. Bubble size distributions were measured during these experiments by Leifer and De Leeuw [44]. Four gases were measured - SF_6, N_2O, CH_3Br and Helium - at different wave conditions and additional artificial aeration to produce a significant bubble effect. To test for super saturation effects, the aeration was switched between invasion and evasion mode. The proposed functional form of the model of Woolf et al. [72] could be confirmed satisfactory, while the actual parametrization only applies to special conditions, and it is argued that it could be possible to calculate transfer velocity from accurate bubble distribution measurements.

Asher et al. [3] designed a dedicated bubble gas transfer experiment. Bubbles were produced in a closed tank by tipping a bucket of water into the tank to simulate a breaking wave. Five gases have been measured - O_2, CO_2, SF_6, DMS and Helium - to correlate the bubble induced gas transfer to the whitecap coverage. In the experimental conditions this was possible with a proposed parametrization [4]. This model is an extension of the model of [37], but has the same limitations. Namely the asymptotic behavior for the solubility, which is enforced by physical constraints are not met for both models. This hints at the limited usability of these models. In contrast the model of Woolf et al. [72] has the correct limits and also was found to be the best describing model in the latest experiments [69, 72].

Zhang [73] uses the mentioned models to derive a global estimate of the fraction of bubble mediated gas transfer of total gas exchange. He states that the fraction of the asymmetric bubble induced CO_2 uptake of the ocean up to 20%. This shows, that understanding the underlying effects

is crucial to make reliable estimates on global climate.

1.1. Goal of this Work

Although there has been progress in the modeling of bubble-mediated gas transfer, systematic experimental verification of these models is still missing. Therefore, the aim of this thesis is to verify and/or to reveal the limits of the existing models for bubble mediated gas exchange. To accomplish this, experiments using many gases with a solubility and diffusivity range that is much wider than in previous experiments are conducted. Bubble size distributions and residence times of the bubbles are measured in-situ with an optical setup developed by the author in his diploma thesis [53]. This enables the direct calculation of the bubble mediated gas transfer. The test of which assumptions in this direct calculation apply, will help to understand the processes in a bubble plume and its gas transfer. This promises deeper insights in the fundamental mechanisms of bubble mediated gas transfer, such as what are the important parameters, which determine the gas exchange of bubbles. Since many conditions are measured the experimental process was automated to a large extent.

2. Models

In this chapter, the fundamentals of gas exchange at interfaces are introduced, followed by the special features of bubble mediated gas transfer and an overview of existing models and parametrizations of bubble mediated gas transfer. The chapter is closed by the modeling of the gas transfer for the bubble tank used in the experiments conducted in this thesis.

2.1. Gas Exchange at Water Surfaces

The transport of substances, called tracer hereafter, between gaseous and liquid media is governed by diffusion. This diffusion has its origin in statistical thermal movement of the molecules and is described for immobile carrier substances by Fick's first law:

$$\vec{j} = -D\vec{\nabla}c \,, \tag{2.1}$$

with j being the net flux of the tracer regarded, D its diffusion coefficient and c the local concentration of the tracer. Here one can see that the flux is proportional to the concentration gradient present. In particular no net flux exists for a constant spatial concentration distribution.

More generally the transport is enhanced by currents and turbulence in the fluids, which can be modeled in a simple form by an additional turbulent diffusion coefficient $K(x)$ [33]. This term is added to the molecular diffusion coefficient and depends on the distance to the boundary layer x:

$$\vec{j} = -(D + K(x))\vec{\nabla}c \tag{2.2}$$

Under the assumption of statistical homogeneity it is enough to consider just one dimension and integration of eq. (2.2) yields:

$$c(x_2) - c(x_1) = -j \int_{x_1}^{x_2} \frac{1}{(D + K(x))} dx \tag{2.3}$$

Analogous to an electrical circuit the integral, denoted as R, corresponds to an electrical resistance, if one understands c as the electrical potential and j as a current density. This is a common concept to understand the transfer at the water surface. Thus the transfer at the surface can be split up into different channels to identify the dominant transport effect. An example is shown in fig. 2.1, which illustrates the effects of air sided, water sided and bubble induced resistance. Here the bubble induced effect can be viewed as an additional resistance parallel to the one associated to (turbulent) diffusion.

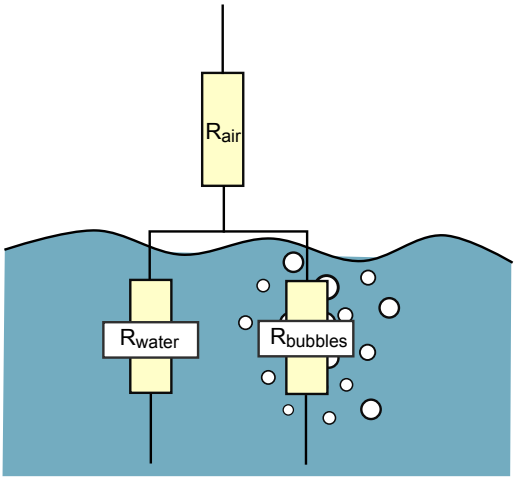

Figure 2.1.: Model of bubble induced gas exchange in the concept of transfer resistances. The total resistance is modeled as the sum of an air sided resistance R_{air} and two parallel resistances R_{water} and R_{bubbles}. If enough bubbles are present, R_{bubbles} gets small compared to R_{water} and acts as an short cut to the mass transport.

A more common way to treat gas transfer is the inverse of the transfer resistance R, the transfer velocity k, which is analogous to the electrical conductivity. The transfer velocity k is therefore given by:

$$k = \frac{1}{\int_{x_1}^{x_2} \frac{1}{(D+K(x))} dx} \tag{2.4}$$

The transfer velocity is often called piston velocity, since it can be imagined as the velocity of a piston pressing a given volume of trace gas through the boundary layer. The unknown in this equation embodies the term $K(x)$. For this term several models exist, whereby none can satisfactory explain the empirical findings of gas exchange field studies under all common conditions.

Usually the term of interest is the transfer velocity k, which can be determined through the equation:

$$j = k(c(x_2) - c(x_1)) \tag{2.5}$$

This form is only valid if no phase boundaries are present in the transport path along x. If this is the case the solubility α of the fluids has to be accounted for. This is defined as the fraction of the equilibrium concentration in the water phase c_w and the air or gaseous phase c_a:

$$\alpha = \frac{c_w}{c_a} \tag{2.6}$$

To correct eq. (2.5) for the existence of a phase boundary and remove this discontinuity, α is included:

$$j = k(c_w - \alpha c_a) \tag{2.7}$$

This equation can be derived by partitioning the resistance into an air sided and an water sided part. Here, α was used to correct the air sided concentration, so water sided values are used all

over the equation. This means k is to be understood as the *water sided* transfer velocity. It is also possible to use *air sided* transfer velocities, which is explicitly marked, when used in this thesis.

Since the transfer velocity is heavily dependent on the diffusion coefficient D of a given tracer in a fluid with kinematic viscosity ν the Schmidt-number is introduced as a dimensionless parameter:

$$\mathrm{Sc} = \frac{\nu}{D} \tag{2.8}$$

With this parameter, the transfer velocity for simple boundary conditions can be calculated [41]:

$$k = \begin{cases} Sc^{-\frac{2}{3}} & \text{rigid wall or surfaces with surfactants} \\ Sc^{-\frac{1}{2}} & \text{free surface or clean surfaces} \end{cases} \tag{2.9}$$

These relations exclude the effects of turbulence or waves, which cannot be solved analytically. However, one common parametrization for wind driven free water surfaces is [41]:

$$k = \frac{1}{\beta} u_* Sc^{-n} \,, \tag{2.10}$$

with β being an empiric parameter describing the strength of the near-surface trubluence, u_* the friction velocity, which describes the vertical transfer of the horizontal momentum, and n a condition dependent exponent between the limiting cases $\frac{1}{2}$ and $\frac{2}{3}$. Sc and α generally depend on temperature T and pressure p.

Two-Box Model Here the simplest model incorporating two media [31], the air compartment with volume V_a and concentration c_a and the water compartment with volume V_w and concentration c_w, is discussed. These two boxes are connected by an interface A, through which the gas transport occurs. For this model the two boxes are considered well-mixed, so that the concentration inside each box is uniform. The temporal evolution of the concentrations is then given by:

$$\begin{aligned} c_a(t) &= \frac{1}{V_a + \alpha V_w} \left(\left(c_{a_0} V_a + c_{w_0} V_w\right) - V_w \left(c_{w_0} - \alpha c_{a_0}\right) \exp\left(-\frac{t}{\tau}\right) \right) \\ c_w(t) &= \frac{1}{V_a + \alpha V_w} \left(\alpha \left(c_{a_0} V_a + c_{w_0} V_w\right) + V_a \left(c_{w_0} - \alpha c_{a_0}\right) \exp\left(-\frac{t}{\tau}\right) \right) \end{aligned} \tag{2.11}$$

Laboratory experiments with the given prerequisites are used to determine the transfer velocity k in this setup by measuring the time series of one or both of the concentrations in the compartments and determining the characteristic time τ. The transfer velocity is then given by:

$$k = \frac{V_a V_w}{V_a + \alpha V_w} \frac{1}{A} \frac{1}{\tau} \tag{2.12}$$

For an open configuration, i.e. assuming an infinitely large volume for the air side V_a, the

solution is:

$$c_a(t) = c_{a_0}$$
$$c_w(t) = \alpha c_{a_0} + (c_{w_0} - \alpha c_{a_0}) \exp\left(-\frac{t}{\tau}\right) , \tag{2.13}$$

and

$$k = \frac{V_w}{A}\frac{1}{\tau} . \tag{2.14}$$

2.2. Bubble-Mediated Gas Exchange

Compared to the previously discussed gas exchange bubbles introduce special features to the gas transfer. As indicated in the previous section and shown in fig. 2.1 the gas exchange in presence of bubbles is described as two parallel transfer resistances, what corresponds to two additive transfer velocities:

$$k_{\text{tot}} = k_{\text{A}} + k_{\text{bub}} \tag{2.15}$$

Here, the air sided part of the transfer resistance was neglected, what is reasonable for the range of solubilities regarded in the following. For example Kräuter [42] shows that the air sided transfer resistance can be neglected for tracers with solubilities lower than 300. In the following models, we consider only the term k_{bub} to avoid confusion.

Bubbles in general enhance the gas transfer, since the inter-facial area is increased by the bubble surface. The difference in this surface is, that it can become inactive as the bubble comes into equilibrium with its surrounding water. Additionally the concentration inside of the bubble increases as the bubbles are compressed by hydrostatic pressure and Laplace pressure, generated by the surface tension. This pressure potentially leads to complete dissolution of the bubble, what increases the transport as well. Since this effect is unidirectional, bubble mediated gas transfer is asymmetric for invasion and evasion of gases.

2.2.1. Model of Jähne

The model of Jähne et al. [36] is based on a time constant analysis for the different effects addressed in the introduction. An overview of all time constants is shown in fig. 2.2. Hereafter each of those is discussed shortly.

Time constants

The Residence Time τ_{res} denotes the time a bubble is in contact with the water phase, i.e. submerged under water, until it rises to the surface again and releases its content to the atmosphere. This time is governed by two values - the initial depth x_0 and the rise velocity v_{rise}. In this view,

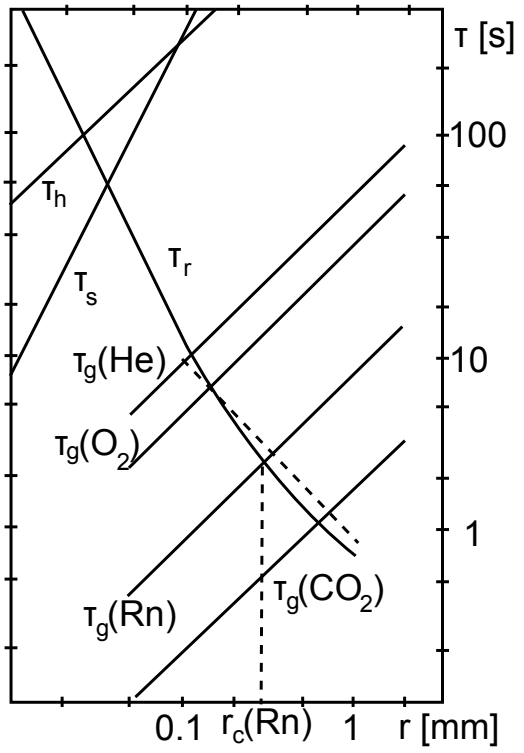

Figure 2.2.: Characteristic times for bubble mediated gas exchange. Shown are the radius dependent times for the dissolution due to hydrostatic pressure τ_h and surface tension τ_s. The time $\tau_r$denotes the average residence time of a bubble of radius r under water. The characteristic exchange time τ_g is shown for four different tracers. r_c denotes the critical radius, where the residence time equals the gas exchange time. Reproduced from Jähne et al. [36]

the process of submerging the bubbles is neglected over the process of rising back to the surface. The time τ_{res} is then given by:

$$\tau_{\text{res}} = \frac{x_0}{v_{\text{rise}}} \tag{2.16}$$

While the initial penetration x_0 depth strongly depends on the bubble generation process and the kinetic energy input, several parametrizations do exist for the rise velocity v_{rise} [13]. To discuss these, the Reynolds number Re for spherical objects with radius r in media with kinematic viscosity ν is introduced:

$$Re = \frac{2 r v_{\text{rise}}}{\nu} \ . \tag{2.17}$$

The two used equations for modeling the rise velocity are Stokes' classical expression for small clean bubbles and Clift et al. [13] for larger clean bubbles:

Stokes: $$v_{\text{rise}} = \sqrt{\frac{8}{3}\frac{rg}{c_{\text{D}}}} \tag{2.18}$$

Clift [13]: $$v_{\text{rise}} = \sqrt{4.28\frac{\rho r}{\sigma} + 1.01 g r} \tag{2.19}$$

Because of the drag coefficient c_{D} the relation depends on the flow conditions, i.e. the Reynolds

number, and on the presence of surface active substances. Here common cases are summarized:

$$\text{Keeling [37]:} \qquad c_{\mathrm{D}} = \frac{24}{Re}(1 + 0.566 Re^{\frac{1}{2}}) \qquad Re < 260 \tag{2.20}$$

$$\text{Clift [13]:} \qquad c_{\mathrm{D}} = \frac{24}{Re}(1 + 0.1935 Re^{0.6305}) \qquad 20 < Re < 260 \tag{2.21}$$

In this thesis, two cases are distinguished - the clean and the dirty case. Whereby dirty denotes the presence of surface active material. These cases and their parametrizations are selected from the review of Clift et al. [13] resp. Frössling [23], which were supported in the measurements of Alves et al. [2].

$$\text{Clean:} \qquad v_{\text{rise}} = \begin{cases} \frac{24}{Re} & Re < 20 \\ \sqrt{4.28\frac{\rho r}{\sigma} + 1.01 gr} & Re > 560 \end{cases} \tag{2.22}$$

$$\text{Dirty:} \qquad v_{\text{rise}} = \frac{24}{Re}(1 + 0.1935 Re^{0.6305}) \tag{2.23}$$

The Gas Exchange Time τ_{ex} denotes the characteristic time it takes for a bubble of radius r to reach equilibrium regarding the mass transport of a tracer. This time is to be understood as an exponential decay time, i.e. the time it takes to adapt the concentration up to a factor of e^{-1}. This time is derived by applying the two box model for an infinitely large water volume and the volume of a bubble as the air volume, see section 2.1. This yields a radius dependent exchange time τ_{ex}:

$$\tau_{\text{ex}} = \frac{r}{3\alpha k_b(r)} \tag{2.24}$$

with $k_b(r)$ being the transfer velocity for a single bubble. This velocity is radius dependent as well, since the radius influences the flow conditions and therefore the boundary layer around the bubble. Based on this equation it is clear that the total exchange time is dependent on the solubility α as well. To model this time a parametrization of k_b is necessary, which is again adopted from Clift et al. [13] using Higbie's equation and Frössling [23] for the clean and dirty bubble case respectively:

$$\text{Higbie:} \quad k_b = 1.13 \frac{D}{2r} Re^{\frac{1}{2}} Sc^{\frac{1}{2}} \tag{2.25}$$

$$\text{Frössling:} \quad k_b = 0.60 \frac{D}{2r} Re^{\frac{1}{2}} Sc^{\frac{1}{3}} \tag{2.26}$$

$$\tag{2.27}$$

The Dissolution Times τ_{h} and τ_{s} describe the mean time it takes for small bubbles to dissolve due to the hydrostatic pressure or the Laplace-pressure, generated by surface tension. These times are given by [35]:

$$\tau_{\mathrm{h}} = p_0 \frac{r}{\alpha_{\mathrm{gas}} k_b(r) \rho g x} \tag{2.28}$$

$$\tau_{\mathrm{s}} = p_0 \frac{r^2}{4\alpha_{\mathrm{gas}} k_b \sigma} \ , \tag{2.29}$$

where p_0 denotes the atmospheric pressure, ρ the specific density of the liquid media and σ the surface tension. Since this overpressure can result in a super saturation of the water phase compared to equilibrium conditions, the equation for the mass flux (2.7) is often extended [71]:

$$j = k(c_w - (1+\delta)\alpha c_a) \tag{2.30}$$

In this equation δ models the super saturation produced by overpressure and dissolution effects. From another point of view, this supersaturation could be attributed to an altered effective solubility $\alpha^* = \alpha(1+\delta)$, which can be seen in equation (2.30).

In fig. 2.2 the time constants are shown in an overview. In this diagram, the lowest time constant is the dominant one for gas exchange, which determines the amount of transfer gas. Since the time constants are dependent on α, the total bubble mediated gas transfer inherits this dependency. In the following, the radius for which the residence time equals the exchange time is denoted the critical radius r_{c}. For bubbles with larger radius the residence time dominates and for smaller bubbles the exchange time is the determining constant. On the basis of this rationale the gas transfer can be distinguished into two limiting cases for the solubility α or the critical radius r_{c}.

High Solubilities First the case of high solubilities, i.e. solubilities for which the residence time is much larger than the exchange time, is discussed:

$$\tau_{\mathrm{res}} \gg \tau_{\mathrm{ex}} \qquad \text{or} \qquad r \ll r_{\mathrm{c}} \tag{2.31}$$

In this case all bubbles submerged under water come into equilibrium with the water. This means that the net flux of tracer is described by the volume flux of all bubbles Q through the water bulk. If this flux is given, the total bubble mediated transfer velocity over a water surface area A is given by:

$$k_{\mathrm{bub}} = \frac{1}{\alpha} \frac{Q}{A} \tag{2.32}$$

Low Solubilities In contrast to the latter case, a low solubility implies a short residence time compared to the exchange time of the bubble:

$$\tau_{\text{res}} \ll \tau_{\text{ex}} \qquad \text{or} \qquad r \gg r_{\text{c}} \tag{2.33}$$

Consequently, the concentration inside the bubble hardly changes, so that it is regarded constant. This means that the flux or transfer velocity through the bubble surface is also constant. Therefore, the bubble surface acts simply as additional surface, across which gas transfer happens. The total bubble mediated transfer velocity is then given by the additional bubble surface multiplied by the transfer velocity of the bubble of given radius r:

$$k_{\text{bub}} = \int 4\pi r^2 \Psi_A(r) k_b(r) dr \tag{2.34}$$

where $\Psi_A(r)$ denotes the total number of bubbles in the radius interval $[r; r + dr]$ found below the water surface A in the bulk.

On the basis of these limiting cases and simulations below (see end of section 2.3) the terms high and low solubilites in this thesis can be understood as much bigger resp. much lower than $\alpha = 10$.

In fig. 2.3 a parametrization for bubble mediated gas transfer by Woolf et al. [72] is shown. By this example one can see both limiting cases discussed before. Picking one fixed diffusivity, the transfer velocity follows the relation given in eq. (2.32) for high solubilities and stays constant for low solubilities.

2.2.2. Parameters Affecting Bubble Generation

As showed in the previous section the bubble distribution in the form of area and volume distribution regarding the bubble radius is essential for the bubble mediated gas transfer. There are several parameters, which determine the bubble size distribution at a given volume flux of bubbles:

- The *Turbulent Kinetic Energy (TKE)* at the location the air is entrained, denoted as ϵ. Turbulence leads to bubble break up and determines to which radii the entrained gas volume flux

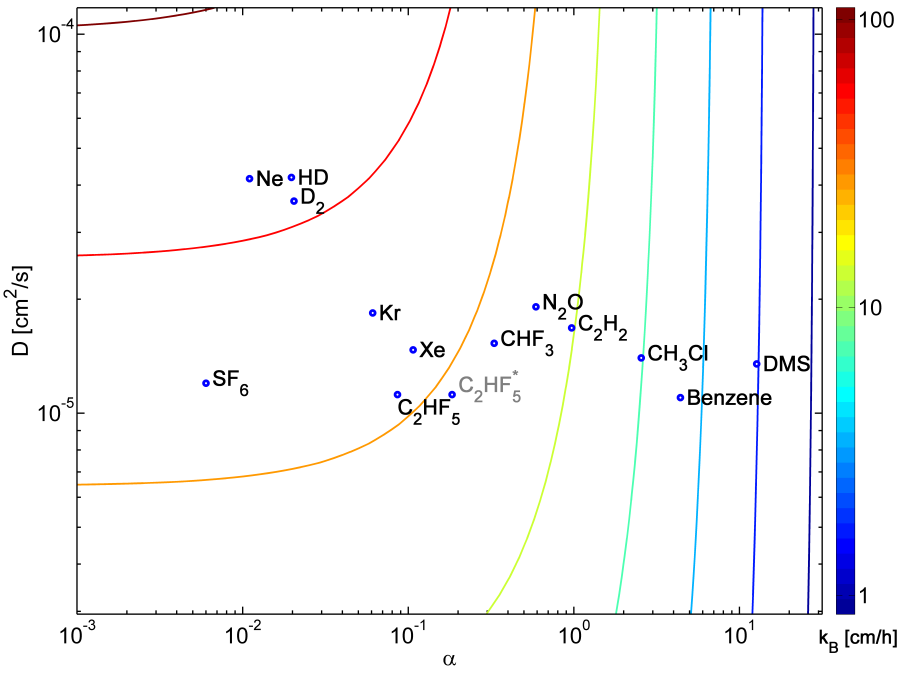

Figure 2.3.: Parametrization after Woolf et al. [72] of bubble mediated gas transfer velocities k_b. Shown are tracers used in this thesis (see section 5.2.1). This parametrization shows that bubble mediated gas transfer is dependent on solubility. *) solubility of 0.184 was state of knowledge when the experiments were performed.

is distributed. Hinze [28] introduced a radius - the Hinze scale r_{H}, which denotes the radius, such that 95% of the air volume is in smaller bubbles. The ϵ dependence of the Hinze scale is given by Garrett et al. [25] as $\propto \epsilon^{-\frac{2}{5}}$. Garrett et al. [25] argues that the size spectrum $\Psi(r)$ is proportional to $\epsilon^{-\frac{1}{3}}$. In investigations on air entrainment of plunging jets El Hammoumi et al. [19] relate the incoming jet velocity to the air entrainment rate. The initial velocity of the jet is a measure of the kinetic energy deposited in the water and therefore a measure for the TKE.

- The *Salinity S* of the water has a big impact on the bubble distribution. Salt or ionic compounds have a significant influence on the bubble coalescence and its suppression. Chanson et al. [12] prove that the air entrainment rates for salt and sea water are less than for fresh water. Although the size distribution is dominated by smaller bubbles in presence of certain salts. This effect is not well understood, but has its origin in bubble coalescence inhibition due to enrichment of ions on the bubble surfaces, which promote the repelling of two colliding bubbles. These effects are discussed e.g. by Craig [14]. McGillis et al. [49] investigate the influence of salts and sea water on gas transfer. It is found that at the same air volume flux the bubble mediated part of the transfer velocity is enhanced for sea water, which supports the findings that more small bubble are present in water with salt. Broecker and Hasse [10] quantifies this result, which shows that maximum enhancement occurs at $\sim 2\%$ NaCl

concentration.

- *Surfactants* in water can alter the size distribution of entrained bubbles. Surfactants are generally molecules with a hydrophilic and a hydrophobic part. This leads to an enrichment of the molecules at air-water phase boundaries, since at this boundary the hydrophilic part can reside in the water, while the hydrophobic part stays in the air. In this way the energy is minimized. The hydrophobic part consists usually of a hydrocarbonic chain, whereas there exist different kinds of the hydrophilic head. There are non-ionic, cationic, anionic and amphoteric, i.e. composed of cations and anions, types of hydrophilic structures. Two different kinds of surfactants can be distinguished - soluble and non-soluble surfactants. Soluble surfactants can physically dissolve in water, but enrich at air-water phase boundaries. On the contrary non-soluble surfactants cannot dissolve physically and enrich only on the surface of the water. In case of concentrations, that saturate the phase boundary, these surfactants form micelles. These are molecular structures of the surfactant, which shape closed objects, in which the hydrophobic tails point inwards, so that only the hydrophilic parts point outwards and have contact to the surrounding water. These structures are able to reside in the water bulk in contrast to a surfactant molecule alone. The differentiation between soluble and non-soluble films is important, because soluble films can attach to the bubble surface even after the entrainment process, whereas non-soluble films have to attach to the bubbles at the moment of entrainment. The described effects stabilize the film formed when two bubbles collide and therefore inhibit bubble coalescence [14]. This pronounces the small bubbles in the size distribution. Since surface films also decrease the rise velocity [2] and decrease the single bubble transfer velocity [68] they also have indirect influence on the bubble mediated gas transfer.

- The *Surface Tension* σ of the fluid determines the energy needed to form new surfaces. The static surface tension is the surface tension in equilibrium, whereas the dynamic surface tension denotes the instantaneous value and its temporal evolution, while the surfactant is attaching to the surface [40]. This directly affects the generated bubble cloud, because the amount of energy needed to form or split surfaces is altered. El Hammoumi et al. [19] describes the dependence of the air entrainment on the surface tension.

- The *Temperature* T changes all parameters described before, as well as solubility and diffusivity, so that it is obvious that temperature will change the value of the bubble mediated transfer velocity.

2.2.3. Model of Memery and Merlivat

Memery and Merlivat [50] give an in-depth discussion of the gas transfer of a bubble cloud based on single bubble transfer [51]. The model includes the effects of pressure increase due to hydrostatics and surface tension, the radius decrease due to gas transfer, dissolution effects and super saturation of the water due to bubbles. They state that the gas flux through bubbles can be written as the sum of the gas content of bubbles that dissolve completely, the flux of bubbles that come into equilibrium with the water bulk and bubbles that do not come into equilibrium during the residence time. A consequence of completely dissolving bubbles is that an asymmetry is introduced to the bubble mediated gas transfer. For invasion processes dissolving bubbles contribute to the transfer, whereas for evasion processes they are irrelevant. Memery and Merlivat [50] give a parametrization for the evasion process as follows:

$$k_{\text{bub},e} = a_1 \alpha^{-1} + b_1 f_1(\alpha, Sc) \tag{2.35}$$

Here the first term $\propto \alpha^{-1}$ considers the bubbles which reach equilibrium. This flux is equal to the bubble volume flux divided by α, compare to eq. (2.32). The second term describes the bubbles which do not reach equilibrium. Their contribution is dependent on the bubble size distribution and their dynamics. Assuming fixed conditions for these, the gas transfer still depends on the physio-chemical parameters of diffusivity D or Sc and solubility α, which is modeled through a general function f_1 of Sc and α.

For invasion processes the transfer velocity is given as:

$$k_{\text{bub},i} = a_1 \alpha^{-1} + b_1 f_1(\alpha, Sc) + a_2 \alpha^{-1} + b_2 f_2(\alpha, Sc) \tag{2.36}$$

As mentioned before, there are additional effects for invasion, which are irrelevant for evasion. So the additional a_2/α term in this parametrization reflects the dissolving bubbles and the term $b_2 f_2$ represents the fraction of non equilibrating bubbles, which can be accounted to overpressure effects (cmp. section 2.2.1) for invasion.

This model gives a general form of bubble mediated gas transfer, where the coefficients and functions depend on the specific conditions of the bubble distribution and flux. This parametrization illustrates the special features of bubble mediated gas exchange, which distinguishes it from gas transfer at a water surface. The explicit forms of these functions are not given and therefore have to be derived with given models for the bubble distributions and dynamics. Memery and

Merlivat [50] discuss this model for assumed bubble populations and dynamics, but do not give a functional parametrization of k_b.

2.2.4. Model of Keeling

This section presents the model of bubble mediated gas transfer of Keeling from 1993 [37]. Here the bubble populations and dynamics are modeled with the assumptions for a model of the rise velocity (eq. (2.20)), bubble size distribution $\propto r^{-4}\exp(-\frac{x}{x_0})$ and a constant equilibration distance of $25\,\mathrm{cm}$. This distance gives the distance traveled by a bubble until the concentration difference inside the bubble and the water has reduced by a factor of $1/e$. This assumption is an approximation, since this distance depends on the radius and hydrodynamic conditions. Keeling [37] proposes a parametrization of the form:

$$k_{\text{bub}} = c\,\alpha^m Sc^n \tag{2.37}$$

with c being a constant and m and n being parameters depending on the bubble population and dynamics. It is stated that the bubble mediated gas transfer should be a function of the parameter $\alpha D^{1/2}$ alone.

This parametrization was extended by Asher et al. [4] with a term for saturated bubbles:

$$k_{\text{bub}} = \frac{c_1}{\alpha} + c_2\alpha^m Sc^n \tag{2.38}$$

2.2.5. Model of Woolf

The model of Woolf et al. [72] extend the previous concepts by interstitial water. This water is assumed to exchange gas with the bubble cloud and mixes afterwards with the bulk water. This considers the effect, that the water inside the bubble cloud can come into or near equilibrium with the bubbles, while the bulk water keeps its concentration. So it is possible that less gas is exchanged than for direct exchange between the bubble cloud and the bulk water. A parameter $\dot{V}_z$ for this effect is introduced, which denotes the volume flow of the interstitial water around

the bubble cloud. In contrast to the previous parametrizations this model reproduces the correct asymptotes for the limiting cases of low and high solubility, as discussed in section 2.2.1. Also the total gas volume flux by bubbles Q is a direct parameter of this model. Woolf et al. [72] propose the following parametrization:

$$k_{\text{bub}} = X\frac{Q}{\alpha}(1+(X\chi)^{\frac{1}{f}})^{-f} \quad \text{with} \quad \chi = \frac{AQ}{\alpha\int j\mathrm{d}A_b} \quad \text{and} \quad X = \frac{\alpha\dot{V}_z}{\alpha\dot{V}_z+Q} \tag{2.39}$$

with f being an empirical parameter modeling the strength of the transition of both limiting cases. The only term, which directly depends on the bubble population and its dynamics is the integral of the flux over the bubble surface A_b. This integral incorporates all the problems with modeling the bubble population, transfer velocity of single bubbles and residence times.

2.3. Model of Gas Exchange in the Bubble Tank

The gas exchange in the bubble tank is modeled by three boxes, one representing the gas phase with volume V_a and tracer concentration c_a in the head space of the tank (I.), one representing the water phase with volume V_w and concentration c_w (II.), and one modeling the gas submerged into the water by bubbles with volume V_b, area A_b and concentration c_b (III.) (see 2.4). Gas and water phase are assumed to be well mixed, which is reasonable, since we have turbulent flow in the water and a enhanced mixing in the head space through bursting bubbles. Bubbles are injected with a volume flux of $Q_{\text{jet}} = Q$ into the water bulk with an initial concentration c_{b_0}. Gas is removed at the same rate $Q_{\text{flush}} = Q$ from the head space of the tank to fulfill mass conservation. Supersaturation effects are neglected in this model, since the effect is expected to be below the measured concentration resolution. For each compartment mass balances are set up and the complete system is solved in the following.

2.3.1. Mass Balance for a Bubble Stream

The central part of the modeling are the bubbles moving through the water phase and exchanging gas with the surrounding water. At first a mass balance for a single bubble is set up. This is later extended to a full bubble distribution. For a single bubble a mass balance of the form of eq. (2.7)

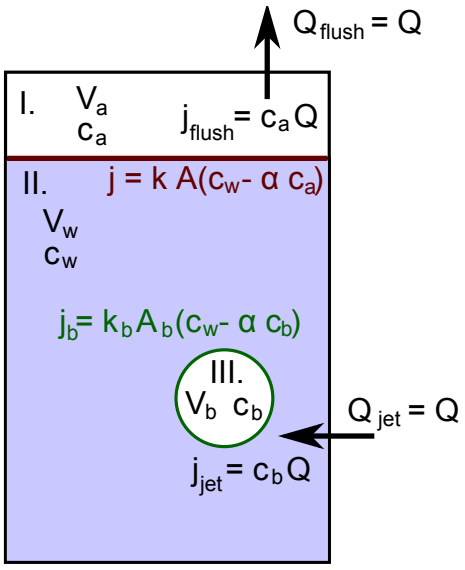

Figure 2.4.: Model for gas exchane in the bubble tank.

can be formed:

$$\dot{c}_b(t,t') = \frac{\partial}{\partial t'} c_b(t,t') = \frac{1}{V_b} A_b k_b (c_w(t) - \alpha c_b(t,t')) \tag{2.40}$$

Here t denotes the time in the experiment and t' the time the bubble is in contact with the water. The transfer velocity for a single bubble is denoted k_b and it should not be confused with the total transfer velocity mediated by bubbles k_{bub}. With the assumption of a constant c_w this is solved by[1]:

$$c_b(t,t') = C \exp\left(-k_b \frac{A_b}{V_b} \alpha t'\right) + \frac{c_w(t)}{\alpha} \tag{2.41}$$

As an initial condition the concentration of the bubble is set to $c_b(t=0) = c_{b_0}$, which yields:

$$c_b(t,t') = \left(c_{b_0} - \frac{c_w(t)}{\alpha}\right) \exp\left(-k_b \frac{A_b}{V_b} \alpha t'\right) + \frac{c_w(t)}{\alpha} \tag{2.42}$$

[1] This is reasonable, because residence times of the bubbles are smaller than the time constant for the gas exchange of the water bulk by several orders of magnitude.

To simplify and understand this equation a new parameter λ is introduced:

$$\lambda = \exp\left(-k_b \frac{A_b}{V_b} \alpha \, \tau_{\text{res}}\right) \tag{2.43}$$

with τ_{res} being the residence time of the bubble in the water, i.e. the time the bubble exchanges gas with the water. With this parameter the difference of initial concentration and concentration as the bubble leaves the water can be written as:

$$(c_{b_0} - c_b(t, \tau_{\text{res}})) = \left(c_{b_0} - \frac{c_w(t)}{\alpha}\right)(1 - \lambda(\tau_{\text{res}})) \tag{2.44}$$

The parameter λ is a measure of equilibration of the bubble. For $\lambda \to 0$ the bubble is in full equilibrium with the surrounding water. Whereas the bubble has not changed concentration significantly for $\lambda \to 1$.

This is valid for bubbles of the same kind, i.e. for bubbles of the same radius r and the same residence time τ_{res}. To generalize this model to bubbles with different radii and residence times k_b is replaced by $k_b(r)$ and τ_{res} is replaced by $\tau_{\text{res}}(x_0, r)$. Here x_0 denotes the initial depth the bubble is assumed to start its exchange process. The time the bubble takes to reach that depth is neglected because it is assumed to be small compared to the total residence time of the bubble. Thus:

$$\lambda(x_0, r) = \exp\left(-k_b(r) \frac{A_b}{V_b} \alpha \, \tau_{\text{res}}(x_0, r)\right) \tag{2.45}$$

$$c_b(t, x_0, r) = \left(c_{b_0} - \frac{c_w(t)}{\alpha}\right) \lambda(x_0, r) + \frac{c_w(t)}{\alpha} \tag{2.46}$$

For each bubble a mass of m_b^1 is transferred:

$$m_b^1(t, x_0, r) = V_b(r)\,(c_{b_0} - c_b(t, x_0, r)) = V_b(r)\left(c_{b_0} - \frac{c_w(t)}{\alpha}\right)(1 - \lambda(x_0, r)) \tag{2.47}$$

Since a number distribution of bubbles $\Psi(x_0, r) = \Psi(\vec{x}_0, r)dV_0$ starting to exchange gas at position $\vec{x}_0$ is assumed, the bubbles in the radius range $[r; r + dr]$ transport the following amount of tracer:

$$m_b(t, x_0, r) = \Psi(x_0, r)V_b(r) \left(c_{b_0} - \frac{c_w(t)}{\alpha} \right) (1 - \lambda(x_0, r))\, dr \tag{2.48}$$

The right hand side of this equation divided by $\tau_{\text{res}}(x_0, r)$, to get the time derivative of this equation because in this time the total volume is replaced once:

$$\dot{m}_b(t, x_0, r) = \frac{\Psi(x_0, r)V_b(r)}{\tau_{\text{res}}(x_0, r)} \left(c_{b_0} - \frac{c_w(t)}{\alpha} \right) (1 - \lambda(x_0, r))\, dr \tag{2.49}$$

To get the total exchanged amount of trace gas it is integrated over all radii and starting positions:

$$\dot{m}_b(t) = \left(c_{b_0} - \frac{c_w(t)}{\alpha} \right) \int_{V_0} \int_0^{r_{\text{max}}} \frac{\Psi(x_0, r)V_b(r)}{\tau_{\text{res}}(x_0, r)} (1 - \lambda(x_0, r))\, dr dV_0 \tag{2.50}$$

$$\dot{m}_b(t) = \left(c_{b_0} - \frac{c_w(t)}{\alpha} \right) Q_{\text{tot}}\ (1 - \lambda_{\text{tot}}) \tag{2.51}$$

with

$$Q_{\text{tot}} = \int_{V_0} \int_0^{r_{\text{max}}} \frac{\Psi(x_0, r)V_b(r)}{\tau_{\text{res}}(x_0, r)} dr dV_0 \tag{2.52}$$

$$\lambda_{\text{tot}} = \frac{1}{Q_{\text{tot}}} \int_{V_0} \int_0^{r_{\text{max}}} \frac{\Psi(x_0, r)V_b(r)}{\tau_{\text{res}}(x_0, r)} \lambda(x_0, r) dr dV_0 \tag{2.53}$$

2.3.2. Mass Balance for Head Space

In the head space of the tank there are three contributions for the mass balance. A mass of $\dot{m}_Q$ is removed from the gas volume per time by the flushing:

$$\dot{m}_Q(t) = -Qc_a(t)$$

The flux of gas by the bubbles balances the loss from the flushing and results in an increase in mass $\dot{m}_b$, which is the remaining tracer in the bubbles and is calculated with eq. (2.51) using $Q_{\text{tot}} = Q$:

$$\dot{m}_b(t) = Q\left(\frac{c_w(t)}{\alpha} + \left(c_{b_0} - \frac{c_w(t)}{\alpha}\right)\lambda_{\text{tot}}\right) \tag{2.54}$$

The last effect is the classic gas exchange at the water surface A:

$$\dot{m}_s(t) = k_A A(c_w(t) - \alpha c_a(t))$$

The total change in concentration is therefore given by:

$$\dot{c}_a(t) = \frac{1}{V_a}(\dot{m}_Q(t) + \dot{m}_s(t) + \dot{m}_b(t)) \tag{2.55}$$

$$\dot{c}_a(t) = \frac{1}{V_a}\left(-Qc_a(t) + k_A A\left(c_w(t) - \alpha c_a(t)\right) + Q\left(\frac{c_w(t)}{\alpha} + \left(c_{b_0} - \frac{c_w(t)}{\alpha}\right)\lambda_{\text{tot}}\right)\right) \tag{2.56}$$

2.3.3. Mass Balance for Water Phase

The mass balance of the water compartment is governed by two effects. First there is classical gas exchange at the water surface:

$$\dot{m}_s(t) = -k_A A(c_w(t) - \alpha c_a(t))$$

And secondly there is the amount of tracer transported by the bubbles according to eq. (2.51)

$$\dot{m}_b(t) = Q\left(c_{b_0} - \frac{c_w(t)}{\alpha}\right)(1 - \lambda_{\text{tot}})$$

This gives the total mass balance for the water side:

$$\dot{c}_w(t) = \frac{1}{V_w}\left(\dot{m}_s(t) + \dot{m}_b(t)\right) \tag{2.57}$$

$$\dot{c}_w(t) = \frac{1}{V_w}\left(-k_A A\left(c_w(t) - \alpha c_a(t)\right) + Q\left(c_{b_0} - \frac{c_w(t)}{\alpha}\right)(1 - \lambda_{\text{tot}})\right) \tag{2.58}$$

2.3.4. Complete Mass Balance

Rearranging and simplifying eq. (2.56) and (2.58) gives a system of differential equations:

$$\begin{pmatrix}\dot{c}_a \\ \dot{c}_w\end{pmatrix} = \begin{pmatrix}-\frac{Q}{V_a} - \frac{k_A A\alpha}{V_a} & \frac{k_A A}{V_a} + \frac{Q}{V_a\alpha}(1 - \lambda_{\text{tot}}) \\ \frac{k_A A\alpha}{V_w} & -\frac{k_A A}{V_w} - \frac{Q}{V_w\alpha}(1 - \lambda_{\text{tot}})\end{pmatrix}\begin{pmatrix}c_a \\ c_w\end{pmatrix} + \begin{pmatrix}\frac{Q}{V_a}c_{b_0}\lambda_{\text{tot}} \\ \frac{Q}{V_w}c_{b_0}(1 - \lambda_{\text{tot}})\end{pmatrix} \tag{2.59}$$

The full solution can be found in appendix A. Here, two special cases are discussed, which

are relevant for the following experiments. The gas transfer at the water surface is neglected for both cases because the characteristic time for the exchange at the surface is much longer than the exchange due to bubbles in the chosen geometry of the used bubble tank, compare to section 9.

Evasion

The first case assumes that the initial concentration of the bubbles fulfill $c_{b_0} = 0$. This corresponds to an evasion experiment as it was conducted in this thesis. This yields the following system neglecting k_A:

$$\begin{pmatrix} \dot{c}_a \\ \dot{c}_w \end{pmatrix} = Q \begin{pmatrix} -\frac{1}{V_a} & \frac{1}{V_a \alpha}(1 - \lambda_{\text{tot}}) \\ 0 & -\frac{1}{V_w \alpha}(1 - \lambda_{\text{tot}}) \end{pmatrix} \begin{pmatrix} c_a \\ c_w \end{pmatrix} \tag{2.60}$$

This system is solved by first solving for $c_w(t)$, which is straightforward because it is independent from $c_a(t)$. The solution is used in the equation for $c_a(t)$, which then is solved by the standard formula for partial differential equations of first order. The solution is:

$$c_a(t) = c_{w_0} \frac{1}{\alpha V_w - (1-\lambda)V_a} \Bigg((\alpha\lambda V_w - (1-\lambda)\, V_a) \exp\left(-\frac{t}{\tau_1}\right) + \alpha\,(1-\lambda)\, V_w \exp\left(-\frac{t}{\tau_2}\right) \Bigg) \tag{2.61}$$

$$c_w(t) = c_{w_0} \exp\left(-\frac{t}{\tau_2}\right) \tag{2.62}$$

with

$$\tau_1 = \frac{V_a}{Q} \tag{2.63}$$

$$\tau_2 = \frac{\alpha V_w}{Q(1-\lambda)} \tag{2.64}$$

and the initial conditions $c_w(0) = c_{w_0}$ and $c_a(0) = \frac{c_{w_0}}{\alpha}$.

Invasion

The second case assumes that the initial concentration of the bubbles c_{b_0} equals the head space concentration $c_a(t)$, i.e. that gas from the head space is used to feed the bubble generation. This corresponds to an invasion experiment as it was conducted in this thesis. This yields the following system:

$$\begin{pmatrix} \dot{c}_a \\ \dot{c}_w \end{pmatrix} = Q(1-\lambda_{\text{tot}}) \begin{pmatrix} -\frac{1}{V_a} & \frac{1}{V_a \alpha} \\ \frac{1}{V_w} & -\frac{1}{V_w \alpha} \end{pmatrix} \begin{pmatrix} c_a \\ c_w \end{pmatrix} \tag{2.65}$$

This system is solved by decoupling the equation by diagonalizing the matrix and solving the individual equations. The solution is:

$$c_a(t) = \frac{c_{a_0}}{V_a + \alpha V_w} \left(V_a + \alpha V_w \exp\left(-\frac{t}{\tau}\right)\right) \tag{2.66}$$

$$c_w(t) = \frac{c_{a_0} \alpha V_w}{V_a + \alpha V_w} \left(1 - \exp\left(-\frac{t}{\tau}\right)\right) \tag{2.67}$$

with

$$\tau = \frac{1}{Q(1-\lambda)} \frac{\alpha V_w V_a}{(V_a + \alpha V_w)} \tag{2.68}$$

and the initial conditions $c_w(0) = 0$ and $c_a(0) = c_{a_0}$.

Transfer Velocity

In order to get the transfer velocity per water surface area, we compare the characteristic times of the bubble tank model with the times of a simple two box model. The transfer velocity of a model for two connected boxes, with h being the height of the finite water volume, is given by:

$$k = \frac{h}{\tau_{\text{ex,tot}}} \tag{2.69}$$

as can be derived from eq. (2.14) and eq. (2.12). This gives the equations for the transfer velocity for the two discussed cases - evasion and invasion:

$$k = \frac{1}{\alpha}\frac{Q}{A}(1 - \lambda_{\text{tot}}) \tag{2.70}$$

$$k = \frac{1}{\alpha}\frac{Q}{A}(1 - \lambda_{\text{tot}})\frac{V_a + \alpha V_w}{V_a} \tag{2.71}$$

The right hand side is derived by comparison to eq. (2.64) and eq. (2.68). We discuss only the evasion case in the following, since asymetric mechanisms are neglected by this model anyhow.

$$k = \frac{1}{\alpha}\frac{Q}{A} - \frac{1}{\alpha}\frac{Q}{A}\lambda_{\text{tot}} \tag{2.72}$$

$$k = \frac{1}{\alpha}\frac{Q}{A} - \frac{1}{\alpha}\frac{Q}{A}\lambda_{\text{tot}}(\alpha) \tag{2.73}$$

$$\lambda_{\text{tot}}(\alpha) \xrightarrow{\alpha \to 0} \frac{1}{\alpha}\frac{Q}{A} - \frac{\alpha}{Q_{\text{tot}}} \int_{V_0} \int_{0}^{r_{\max}} \Psi(x_0, r) A_b(r) k_b(r) dr dV_0 \tag{2.74}$$

One can see this limiting behavior by expanding the exponential function in λ (eq. (2.45)) in the integral to the first order of t.

$$\lambda_{\text{tot}}(\alpha) \xrightarrow{\alpha \to \infty} 0 \tag{2.75}$$

These limiting cases reproduce the expected behaviors of the transfer rates for low and high solubilities as explained in section 2.2.

To illustrate the impact of the central parameters of this model, several synthetically generated bubble distributions are discussed. As simulation domain the data from the experimental tank was used, i.e. a water volume of $V_w = 130\,\text{l}$ with an surface area $A = 10.5\,\text{dm}^2$, a depth of 124 cm and a bubble flux of $Q = 0.7$ l/min. A uniform spatial distribution of bubbles was assumed. The rise velocity and the transfer velocity for single bubbles was modeled for two different cases. The case

for clean water was modeled after Higbies's equation [13] with eq. (2.22) for the rise velocity and eq. (2.25) for the transfer velocity for single bubbles. The case for dirty water was modeled after Frössling [23] with eq. (2.23) for the rise velocity and eq. (2.26) for the transfer velocity for single bubbles. In figure 2.5, the total equilibration parameter for the bubbles is shown for both cases. One can see the effect of solubility on the level of equilibration. In the clean case, the bubbles come into equilibrium slightly faster, while the transition occurs faster than in the dirty case.

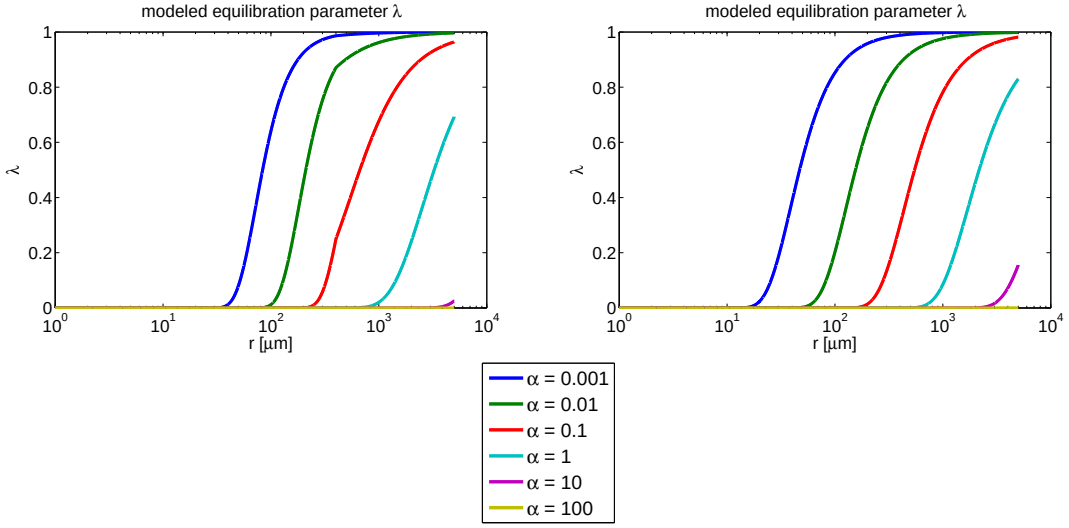

Figure 2.5.: Equilibration parameter λ vs. radius for several solubilities α. Residence time τ_r is modeled with the rise velocity after Clift et al. [13]. Bubble exchange time τ_b is modeled after eq. (2.24) with the transfer rate k_b taken from Alves et al. [2] for clean case (left) resp. from Frössling [23] for dirty case (right)

The result of the simulations is shown in figure 2.6. In this model the calculated transfer velocity has only a weak dependence on clean or dirty conditions. Except for the *UNIFORM* distribution, a radius distribution with a mean radius given in table 2.1 was used. The simulation shows the expected tendencies, for high solubilities, i.e. equilibrated bubbles, the transfer velocity equals the predefined bubble flux. For unequilibrated bubbles or low solubilities the transfer velocity is proportionol to the bubble surface area, which is larger for smaller bubbles at the same volume flux. If fig. 2.5 is compared to fig. 2.6 one can see for example that the onset of equilibration in dirty conditions is at $\sim 1800\,\mu m$ for a solubility of 1. This reflects the start of the transition in the transfer velocity for the *BIG* bubble case.

Table 2.1.: Mean radius for synthetic bubble distributions used for simulation.

Name	SMALL	MEDIUM	BIG	VERYBIG	UNIFORM
Radius [µm]	35	525	1500	3800	6 - 5000

This model reproduces the parametrization of Woolf [71] for $f = 1$ and $\alpha \dot{V}_z \gg Q$, see section 2.2.5.

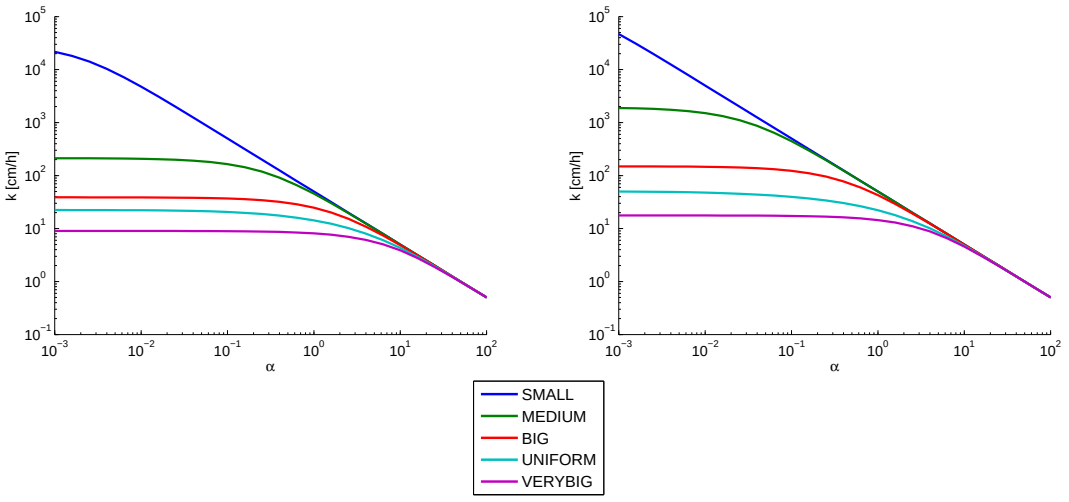

Figure 2.6.: Transfer rates for different model bubble distributions at constant volume flux. Residence time τ_r is modeled with the rise velocity after Clift et al. [13]. Bubble exchange time τ_b is modeled after eq. (2.24) with the transfer rate k_b taken from Alves et al. [2] (left) resp. Frössling [23] (right)

3. Experimental Methods

This chapter gives an overview of available techniques to measure the main properties of the conducted experiments, i.e. tracer concentrations and bubble size and velocity distributions. The used methods are explained in more detail to enable the reader to follow the experimental procedure, the discussion of the experimental pitfalls and errors and the discussion of the results. For in depth understanding of the experimental equipment the reader is referred to the given references in the following sections.

3.1. Gas Exchange Measurements

For detecting and measuring trace gases a lot of methods are available. There is a variety of devices dedicated for detecting a single gas by special physical or chemical effects only applicable to a single species. For example O_2 probes work by quenching a fluorescent dye or CO_2 probes are available as electro-chemical sensors. In the conducted experiments it is of importance to be able to measure a large number of different trace gases simultaneously. Thus the focus of this section is on methods, which are capable to adapt to and measure several tracers at the same time.

Approved methods used in gas exchange measurements are IR-spectrometry [41], UV-spectrometry [18] and Gas-chromatography [67]. These methods limit the choice of trace gases by their spectral properties. Noble gases can not be measured with IR-spectrometry, since the technique is only sensitive on molecular bonds. UV-spectrometry is mainly sensitive on aromatic structures or double bonds of hydro carbons. Gas chromatography needs a higher experimental effort to measure distinct samples, which leads to a low temporal resolution. Proton transfer mass spectrometry has also been used in gas exchange measurements [52]. Although it has orders of magnitude higher sensitivities than ordinary mass spectrometry, is not able to detect noble gases.

Since a special interest exists in noble gases, because they have reliable diffusivity and solubility data. Therefore quadrupole mass spectrometry was chosen as method to perform the concentration

measurements. This method has the advantage to be able to measure a wide variety of species including noble gases, in contrast to the methods mentioned before, which are limited to certain substances. A special membrane inlet allows for continuous measurements in gas and liquid phase. Alaee et al. [1] already used this method in gas exchange experiments, which did not investigated bubble induced effects though. Especially membrane inlet mass spectrometry (MIMS) is used in field experiments [7] and monitoring applications recently [55].

3.1.1. Quadrupole Mass Spectrometry with Membrane Inlet

This section gives an overview of the mass spectrometry used in this thesis. It explains the basics and principles needed to understand the effects discussed in the experiments (section 5.2.2). For more information it is referred to a pertinent textbook, e.g. Gross [27].

The device used in this thesis is a quadrupole mass spectrometer. Its defining component is, as the name suggests, an electric quadrupole, which acts as the mass discriminating element [1]. There is a variety of other types of mass spectrometers, which are based on different principles of mass analysis. The widely known types are the time of flight (ToF) and sector field mass spectrometers, which measure the mass-charge ratio by time dispersion of a pulsed ion beam resp. by the deviation in a magnetic field. In the last decades several other types have been established in the laboratories. Among these are Fourier-transform ion cyclotron resonance (FT-ICR) spectrometers. Here the quadrupole field mass spectrometer is introduced - for the other types, please refer to Gross [27].

Another unit which distinguishes mass spectrometers is the sample inlet. There are several possibilities to get the sample into the measurement chamber. In this experiment a membrane inlet (MI) system was used. It connects the sampling volume to the interior of the mass spectrometer through a thin silicone membrane, through which the sample molecules diffuse into the MS. This has the advantage of continuous measurements and being able to measure in gas and liquid media with the very same setup.

Electron-impact Ionization The first step in detecting particles is ionization. This allows for the usage of electromagnetic fields to deflect and accelerate the particles. In this case electron-impact ionization is used. Electrons are accelerated and shot at the sample molecules or atoms. If the kinetic energy of the electron is sufficient, it is possible that a hitting electron detaches another electron from the molecule. Since the energy needed to detach an electron from a molecule

[1] Actually not the mass, but the ratio of mass and charge is differentiated.

differs from species to species, it is important to control the kinetic energy of the electrons. This is realized by accelerating the electrons, generated by a hot cathode, with an electric field of controllable voltage. See the upper left part of fig. 3.1. In fig. 3.2 the ionization cross section for electron impact is shown for methane. The plateau at about 70 eV is the reason why most mass spectrometers are set by default to an electron energy at 70 eV. In the plateau the cross section is stable for variations in the kinetic energy, which compensates for deviations in acceleration voltage. It also balances differences among mass spectrometers. In this region the kinetic energy is enough to ionize most molecules. Besides detaching electrons from atoms or molecules it is also possible that molecules are fragmented. The remaining fragments can be ionized and therefore detected by the spectrometer. The generated fragments are dependent on the kinetic energy of the electrons as well and can act as a measure for specific species. [27]

The electrons ionize the molecules in the ionization volume, see fig. 3.1, where the generated ions are accelerated and focused into the next stage of the analysis - the quadrupole field for mass analysis.

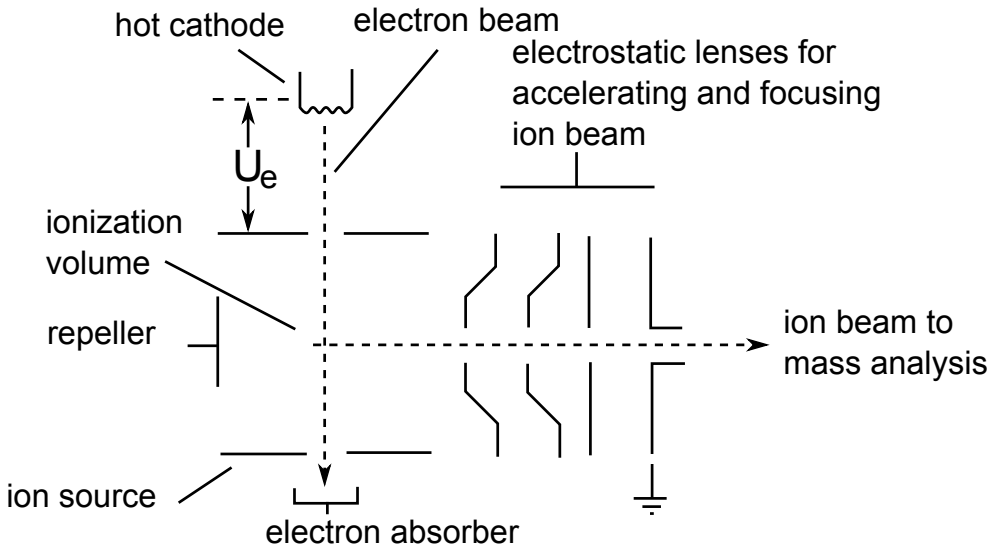

Figure 3.1.: Illustration of a typical ion source. It consists of an electron source for ionizing the sample molecules and an accelerating and focusing unit. The electrons are generated by a hot cathode and are accelerated to a defined kinetic energy by a voltage U_e. These electrons ionize the molecules in the ionization volume by electron impact. The ionized particles are then accelerated and focused by electrostatic lenses. The leaving ion beam is then fed to the mass discriminating element. Reproduced from Gross [27].

Mass Filtering by a Quadrupole Field A quadrupole mass spectrometer uses an electric quadrupole field as a mass filter. A sketch is shown in fig. 3.3. The ionized particles enter the quadrupole field and are deflected. Depending on the mass to charge ratio the trajectory is stable or unstable. So only the particles with suitable masses are able to pass that field. It is obvious that in the whole mass spectrometric system a vacuum has to be maintained to be sure that the mean

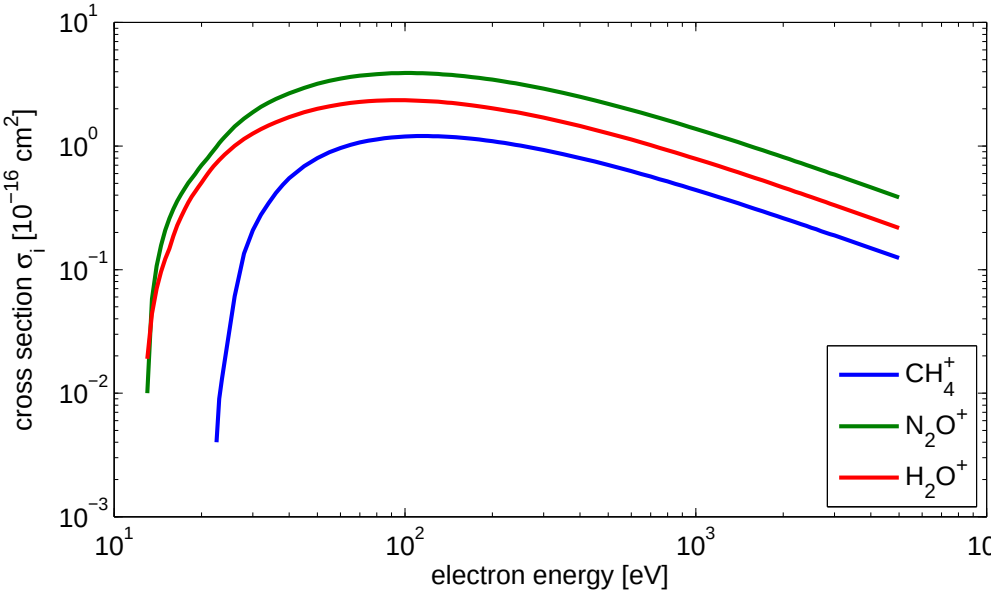

Figure 3.2.: The ionization cross section by electron impact for methane, N_2O and water are shown for different electron energies. Data from Kim et al. [38]

free path is long enough to ensure undisturbed movement of the ions in the spectrometer.

The potential Φ applied to the four electrodes is given by the following equation:

$$\Phi = U + V\cos(\omega t) \tag{3.1}$$

with the DC voltage U and the Radio frequency voltage V with frequency ω.

Thereby opposing electrodes have the same potential and neighboring electrodes have inverted potential. The derived equations of motions have the following form:

$$\frac{d^2x}{d\tau^2} + (a_x + 2q_x\cos 2\tau)x = 0 \tag{3.2}$$

$$\frac{d^2y}{d\tau^2} + (a_y + 2q_y\cos 2\tau)y = 0 \tag{3.3}$$

with,

$$a_x = -a_y = \frac{4eU}{mr^2\omega^2}, \qquad q_x = -q_y = \frac{2eV}{mr^2\omega^2}, \qquad \tau = \frac{\omega t}{2}. \tag{3.4}$$

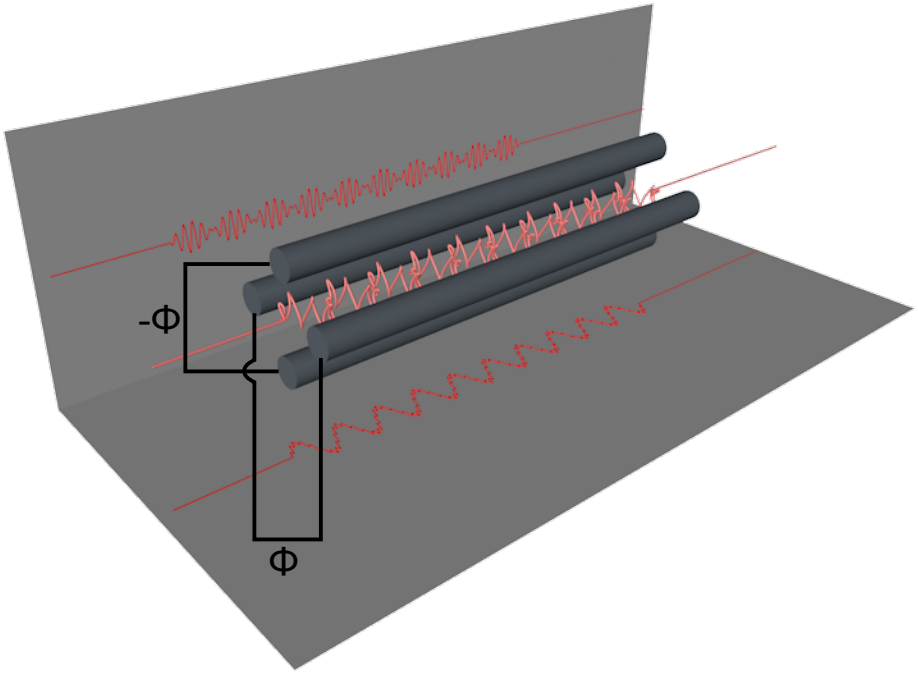

Figure 3.3.: Sketch for a stable ion trace passing through an electric quadrupole field. The projections in x and y direction are also shown. Adapted from Gross [27].

It can be shown that there is one region in (q, a) space, that results in a stable ion trajectory for a given mass to charge ratio. A diagram of this region is shown in fig. 3.4. The resolution of the filter is given by the ratio a/q, the higher the the ratio the better the resolution. By scanning the potentials U and V with constant ratio, the masses for stable trajectories can be scanned. The ions passing the filter enter the next stage of analysis - the detection itself.

Ion detection There exists a variety of ion detectors. Almost all detectors are measuring the ion currecnt directly or indirectly. The used mass spectrometer has two detectors - one direct and one indirect:

Faraday Cup is a cup shaped electrode, which catches the ion beam and collects the charges of the ions. This current is converted to a voltage, which is then converted to a digital signal.

Secondary Electron Multiplier (SEM) detectors use a cascade of dynodes to amplify the ion current. The ion current hits the first of the dynodes, which are usually made out of metal or a semiconductor, and releases electrons out of the dynode. These electrons are accelerated by

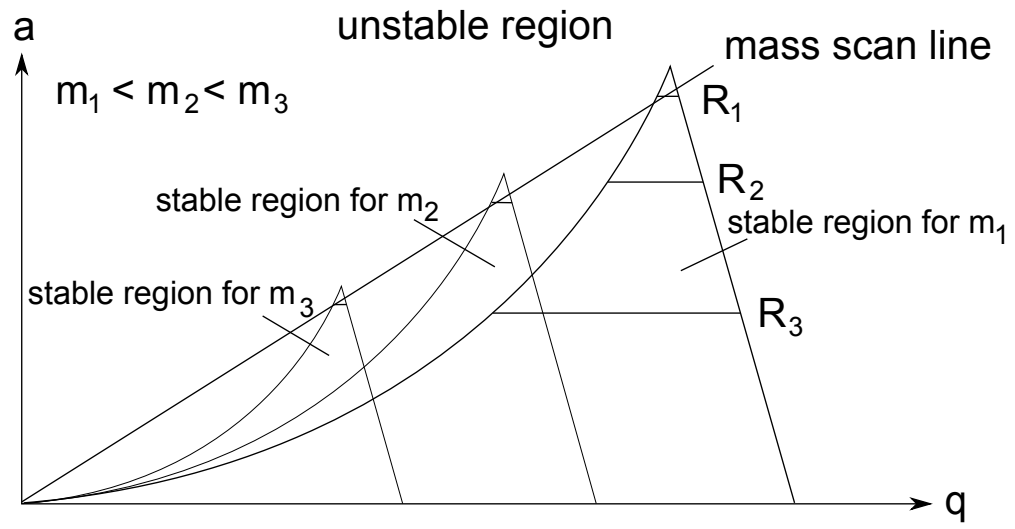

Figure 3.4.: Diagram showing regions of stable traces for different masses. The ratio a/q determines the resolution of the filter, the higher the the ratio the better the resolution. This is shown in the diagram by the horizontal lines $R_1 > R_2 > R_3$. Only ions being above these lines pass the quadrupole. Scanning the potentials U and V resp. a and q, while keeping the ratio constant, the masses for stable trajectories can be scanned. Reproduced from Gross [27].

a voltage applied between the first and the second dynode, where the electrons release further electrons again. These are accelerated towards the next dynode and so on. Typical SEMs have 12-18 dynodes to amplify the current. At the last stage the electrons are collected and converted by an pre-amplifier to get a usable signal.

Diffusion through Silicone Membranes

There are several ways to get the sample material into the ionization volume of the mass spectrometer. For solid or liquid materials it is necessary to get the atoms or molecules into gaseous phase to be able to measure them in the mass spectrometer. Since in this thesis only gases are measured, it is not necessary to change the phase of the measured species. To get the sample gas into the measurement chamber usually direct or indirect injection or a configuration as a second analysator behind a gas chromatic system is used.

In the used system a special method, the membrane inlet, for the gas injection is used,. It allows for continuous sampling in gas and liquid phases. It uses a silicone membrane to separate the mass spectrometer from the sample volume. Through this membrane gasses are able to diffuse into the mass spectrometer. The advantage is that this process happens continuously and the probes with the membranes can be directly placed into liquids. Additionally they reduce the gas load on the vacuum pumps attached to the mass spectrometric system, since no bursts of molecules are added

at once.

A short summary of the flow and concentration conditions at a membrane is given, following the description in Bell et al. [7]. Ficks's First Law, see eq. (2.1), gives the flux j_G through a membrane of area A for steady state conditions:

$$j_G(x) = -D_G \alpha_G A \left(\frac{dc_G(x)}{dx} \right) = -P_G A \left(\frac{dc_G(x)}{dx} \right), \tag{3.5}$$

where D_G denotes the diffusion constant of the substance in the membrane, α_G is a partition coefficient defined as the ratio of the concentrations at the membrane-sample interface analogous to a solubility and c_G denotes the concentration at position x in the membrane. The permeability P_G is defined as the product of α_G and D_G. Since on the mass spectrometer side of the membrane at $x = 0$ a vacuum is maintained it can be assumed that $c_G(0) = 0$. Hence for steady state conditions, which means a constant flux or a constant concentration gradient has established, the flux is proportional to the concentration $c_G(l)$ at the membrane-sample interface at $x = l$. The measured ion current in the spectrometer is proportional to the inward gas flux through the membrane. The characteristic properties are preserved for a cylindrical probe geometry, as it is used in this thesis.

For non steady state conditions, which are usually measured in time series, the solution for cylindrical geometries is well approximated by the solution for a sheet membrane [15]:

$$j_G(t) = j_G \left[1 + 2 \sum_{n=1}^{\infty} (-1)^n \exp - \frac{n^2 \pi^2 D_G t}{l^2} \right], \tag{3.6}$$

with j_G being the steady state flux, l being the membrane thickness. The characteristic time for the flux to follow changes in the concentration conditions is given by:

$$\tau_{\text{membrane}} = \frac{l^2}{\pi^2 D_G}. \tag{3.7}$$

This time is a lower limit for detecting changes in concentration. Faster changes will be distorted and delayed. To get a reliable signal, changes should not be faster than $5 \times \tau_{\text{membrane}}$, i.e. their change should be in the order of the concentration resolution during that time.

Other effects that should be considered are: The partition coefficient α_G changes with pressure, and the diffusion coefficient D_G with temperature. In general these effects have to be calibrated for to be able to deduce the concentration from the measured gas flux. These effects can be ignored if pressure and temperature conditions are kept constant. Usually the permeability P_G is measured to

estimate the flux through the membranes. Therefore most data available is on permeability and not on the diffusion coefficient, which is necessary to get an estimate for the membrane equilibration time τ_{membrane}.

It is important to keep the flow conditions around the probe constant and suppress tracer depletion in the sampled phase. Since the volume around the membrane is limited, tracer depletion may occur if the same volume element stays at the membrane for a longer time and a large fraction of the contained traces already diffused through the membrane. This lowers the concentration, hence the flux, which distorts the measurements. It has to be ensured that no sample volume element connects too long to the membrane to significantly change its concentration due to the diffusion through the membrane. This is realized by a high flow rate at the membrane, e.g. by restricting geometries and/or high pump rates. This also implies that the flow conditions have to be constant, since they influence the flux through the membrane.

3.2. Bubble Size Distribution and Velocity Measurements

Rodrigues and Rubio [59] give an overview of existing methods for bubble and void fraction measurements. Two major techniques have been approved in experiments, acoustical and optical methods. Acoustical methods use the resonant oscillations of bubbles to measure the bubbles and their sizes. The acoustical methods have been successfully applied in laboratory and field experiments for measuring bulk concentrations [11, 21, 47]. The acoustical methods are not capable of performing the velocity measurements and fail for non spherical bubbles. Fiber glass probes use changing reflective properties of a fiber glass tip when a bubble passes by to detect bubbles and their size. These probes work reliably, but are sampling the bubble distribution at a single spot and are intrusive, since the probe has to be put into the bubble cloud [5, 46, 60]. Imaging techniques, which can be divided into bright field and dark field setups, have the advantage to capture spherical and non spherical bubbles and are not necessarily intrusive. Dark field setups have been tested by e.g. Balschbach [6]. Bright field setups are more common and have been used in laboratory conditions [26, 35, 45] and field experiments [63, 65].

The mentioned imaging techniques are all capable of performing velocity measurements given their sampling rate, i.e. frame rate, is high enough to resolve the movement and allow for unique identification for the particles or at least regions in the images. A bright field method was chosen, since it is not intrusive, capable of velocity measurements and can handle non spherical bubbles.

3.2.1. Bright Field Depth from Focus Imaging

The used method is a special case of a bright field setup. It uses a telecentric illumination and a telecentric imaging lens. It was originally developed by Geißler [26] for bubble measurements. It was adapted and improved with up to date equipment by the author in his diploma thesis [53]. In this thesis processing was improved and the method was extended to be able to conduct velocity measurements. The description given here follows Mischler [53].

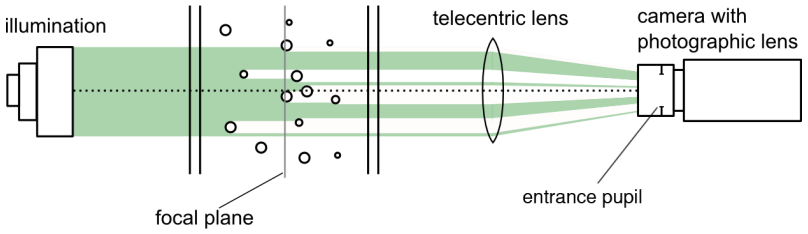

Figure 3.5.: Principle of a bright field setup for measuring bubbles. A camera is looking into a light source, so it sees a "bright field". Bubbles crossing the optical path block and reflect the light out of the imaging path, so that the bubbles appear as black disks or rings.

Light Scattering by Spherical Bubbles

Davis [16] described the light scattering of spherical bubbles by means of geometrical optics. Since the cameras limit the resolution to bubbles larger than the used wavelengths of the used illuminations, the geometric approximation is applicable. In fig. 3.6 the cross section of spherical bubbles for light scattering is shown. It is assumed that the incident light hits the bubble from a direction of $0°$. One can see that most of the light is scattered in angles larger than $\pm 5°$ out of the optical path. If bubbles are illuminated with light in a narrow angular distribution, most of the light will be reflected out of the optical path, as illustrated in fig. 3.5. If the lens of the camera is adjusted to capture light only in a narrow angular range too, the bubbles will appear as dark spots in the images. To ensure a narrow opening angle a small aperture of the lens is used. With telecentric setups it is possible to fix the opening angle of the captured or emitted light rays for the whole object space at a small value. These setups can be used for imaging resp. illumination.

Telecentric Setup

The defining property of telecentric setups is that the principle rays are parallel to the optical axis either in the object space, image space or both. In fig. 3.7 an example for a telecentric setup in

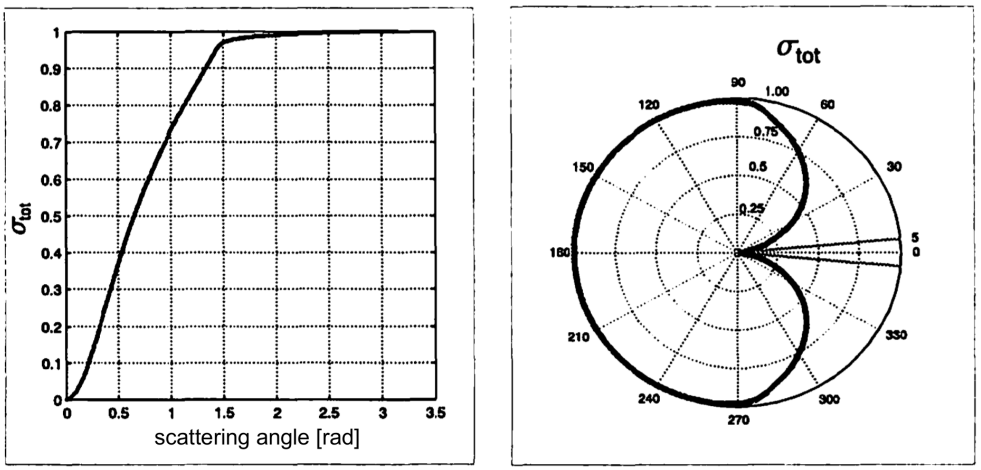

Figure 3.6.: Total cross section of spherical bubbles for light scattering. Taken from Geißler [26].

object space is shown. To yield parallel principal rays, the aperture is moved to the focal plane of the telecentric lens. For illuminations this can be achieved by putting a small light source in the focal plane of a lens. The consequence of telecentricity is that the magnification of the optical system does not change with the distance to the lens. The opening angle is still controlled by the aperture of the lens resp. the size of the light source.

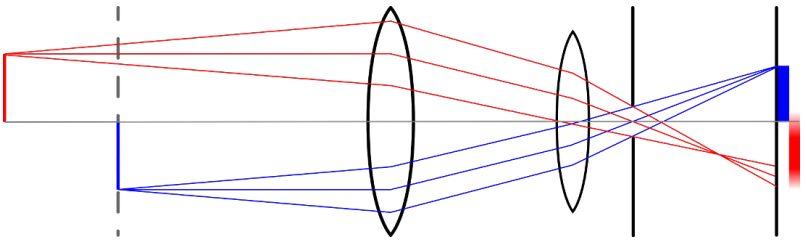

Figure 3.7.: Illustration of a telecentric setup. Two objects of the same size at different distances to the focal plane are shown. The object in the focal plane is images sharp, whereas the out of focus object is imaged blurred. The difference to normal optics is, that both objects are imaged with the same size, i.e. the principal rays of their edges have the same distance. Taken from Mischler [53].

Since in this thesis measurements in water are performed, the differences of the optical imaging in air and water are addressed. The phase transition at the air-water interface changes the opening angle of the imaged light rays according to Snell's Law for refraction. This is illustrated in fig. 3.8 comparing an imaged object in air and water. Since the opening angle determines the depth of field of the imaging, this will change in water too. This is important for deriving the measurement volume from calibrations done without water. According to Snell's Law, the change in depth of field will be a factor of

$$\gamma = \frac{z}{z'} = \frac{n_{\text{water}}}{n_{\text{air}}} = 1.33 \quad ,$$

with n being the refractive indices of air and water and z and z' being the distances from the focal plane in air resp. water.

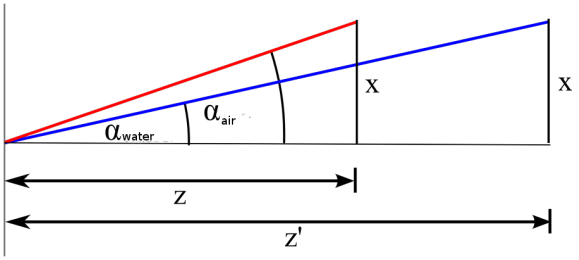

Figure 3.8.: Two objects of same size imaged in air and in water. Shown are the extremal rays for an imaging setup in the air phase resp. in the air phase outside the water. The phase transition leads to a change in the opening angle. Taken from Mischler [53].

4. Experimental Setup

In this chapter the experimental setup is described. First a short introduction to the used bubble tank is given. Afterward each of the individual parts is characterized in detail. Different modes of operation are explained and how the MIMS is integrated into the setup. The used cameras and the corresponding light sources are discussed and their mounting on the tank will be shown.

4.1. Bubble Tank

Figure 4.1.: Photograph of running bubble tank with illumination from below. Red circle marks a single camera for the bubble measurement setup.

The tank used in this thesis was constructed during the author's diploma thesis. For detailed considerations for the construction refer to this thesis [53]. Here only a short recap is given.

The tank has dimensions of 130 cm × 15 cm × 70 cm (H×D×W) and is built from *Borofloat* glass panes with a thickness of 18 mm. All walls are opaque to allow access for all sorts of opti-

cal measurement techniques. The height was chosen, aside from simulating realistic penetration depths, to capture the hydrostatic effects on bubbles and allow for sufficiently large residence times for the bubbles. To generate bubbles and simulate a breaking wave the idea is to use a water jet, which submerges air while impinging the water surface. If the composition of the atmosphere at the position, where the jet pierces the water surface, is controlled, the gas content of the submerged bubbles can be controlled as well.

To conduct gas exchange measurements the tank was designed to be gas tight, so that closed circuit measurements are possible. Open configurations for evasion measurements are also possible. To be able to use a wide variety of trace gases and liquids the material of all used parts was chosen to be as chemical inert as possible. In the closed configuration the total water volume including tubing is $V_w = 130\,l$ for a full filling of the tank. The air volume comes to $V_a = 15\,l$. The following sections describe the tubing for the water and the air compartment of the tank and their modes of operation.

4.1.1. Water-sided Circuit

The tubing of the water side is shown in fig. 4.2. The tubing itself is made out of polypropylene. It consists of a 300 W *Speck BADU 42* pump to circulate the water from the bottom of the tank through the nozzle of the bubble generator into the tank again. The pump is powered by a frequency converter *Siemens SINAMICS G110*, which is remotely controlled via an RS484 interface by the measurement PC.

The Bubble Generator works using the principle of a water-jet pump. A water jet is generated through a stainless steel nozzle with a diameter of 8.5 mm. This jet submerges surrounding gas into bubbles and pushes these bubbles under water. This technique was also used by Koga [39] and Maiß [48] to simulate conditions of a breaking wave. It can be argued the the production process is similar to a breaking wave, since the jet produces a convergence zone on the water surface, which also occurs during wave breaking. The air space surrounding the jet is contained in an extra chamber, which has an independent gas supply. That way it is possible to control the atmosphere, which is entrained into the water, as well as the gas flow rate which is pumped through the water bulk.

A Heat Exchanger driven by 40 peltier elements (*Quickcool* QC-127-2.0-15.0M, 5 W) on an eloxed aluminum body containing a water channel was integrated into the circulation line to be

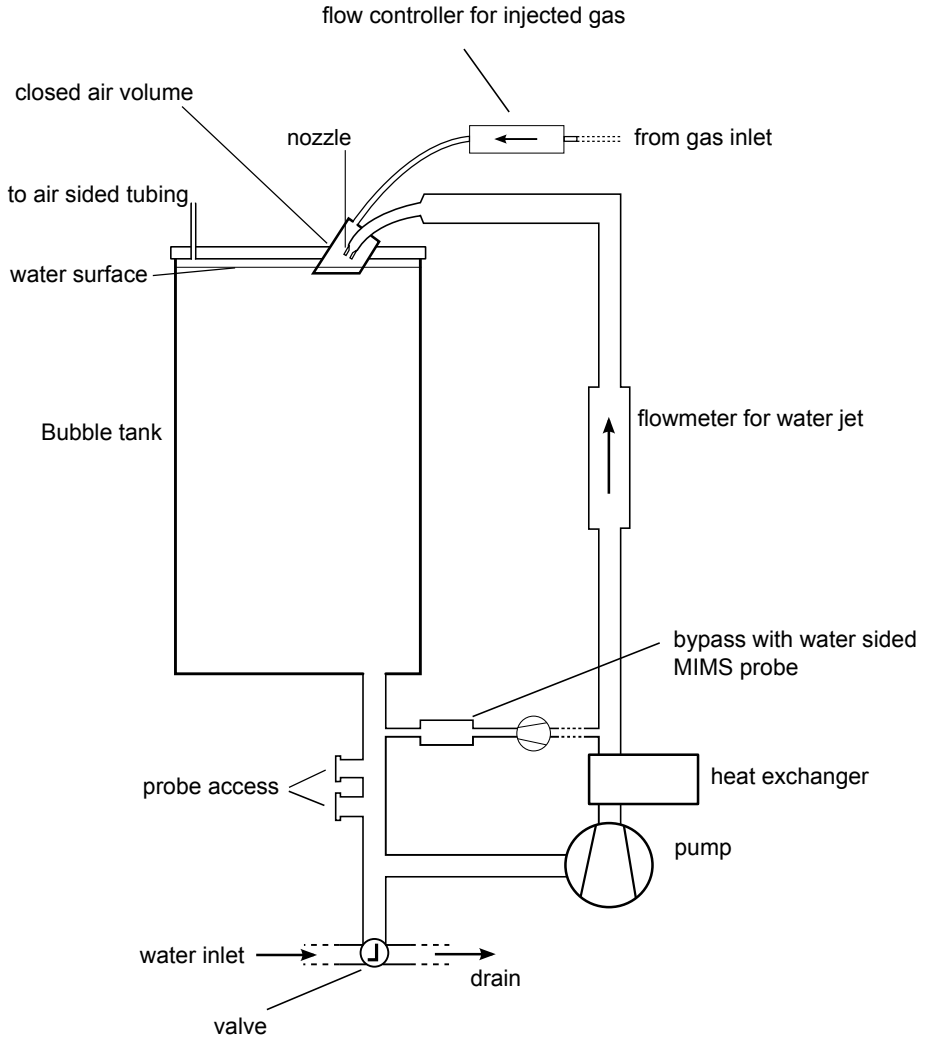

Figure 4.2.: Illustration for the bubble tank used in the experiments. Shown are the water sided tubing and devices. In the bypass for the MIMS probe a pump is integrated to ensure constant flow conditions at the MIMS-probe. The water is taken from the bottom of the tank and is pumped through the bubble generator forming a jet and submerging bubbles into the water. A heat exchanger for temperature control is integrated in the pumping line.

able to control the water temperature and balance the heating from the circulation pump[1]. With this device a heat flux of about 700 W at 25°C is possible. This corresponded to a temperature adjustable in a range of 20°C-30°C at usual conditions in the laboratory.

The MIMS Probe is placed in a bypass circuit. The integrated probe is shown in fig. 4.3, right. To provide stable flow conditions in the probe chamber an additional pump (*Totton HPR6/8*) is used in the bypass line. The chamber consists of stainless steel screwing for the probe feed-through and a glass tube for visual inspection of the MIMS-probe head. A temperature sensor is built into the chamber. An identically constructed chamber was used for the air sided probe with

[1] thermal output of ca. 180 W

an additional pressure sensor. For detailed description of the probe chambers see section 4.2.

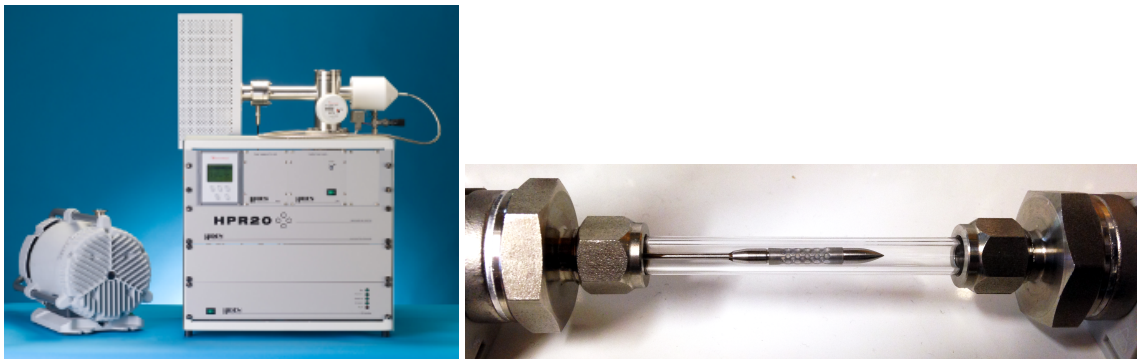

Figure 4.3.: left: *Hiden HPR* quadrupole mass spectrometer, which was used in this thesis. right: one of the membrane-inlet probes used. These probes can be used for gas and water phase. Here the probe is shown built into the gas circuit probe chamber.

4.1.2. Air-sided Circuit

Tubing

In fig. 4.4 a schematic of the air sided tubing of the bubble tank is shown. The individual devices shown as boxes in the figure are described in this section. With this setup several modes of operation are possible. To automatically switch between these modes four magnetic valves (*Bükert 6628*) and four mass flow controllers (one not shown, *Analyt-MTC*) are used. The flow controllers are operated directly by the measurement computer via an RS232 interface. The magnetic valves are switched by a relay-array (*Conrad, 197730*), which itself is operated by the same computer via RS232. To generate a gas flow in the circuit five parallel peristaltic pumps (*Watson Marlow 3X3 series*) are used. These pumps have a maximal flow rate of $1\,l/\mathrm{min}$ at given conditions. The modes of operation are:

- closed circuit

  Gas is taken from the head space of the bubble tank and is pumped with a controlled flow rate through the MIMS probe chamber into the water jet chamber. There new bubbles are generated and submerged into the tank. The bubbles release their content into the head space again, so no additional gas is added, nor gas gas taken[2] from the system.

- open circuit

[2] except for the small amount, which diffuses into the MIMS

A carrier gas - in this experiment solely Argon was used - is fed into the water jet chamber at a given flow rate. There bubbles are generated, which take up the trace gases, which are dissolved in the water before, and release the formed mixture into the head space of the tank. From the head space gas is pumped at the same flow rate as the Argon input through the MIMS probe chamber and then pumped into the laboratory's waste gas disposal system, which is referred to as ventilation system in the following.

- in-gassing

  This mode is used for seeding the head space of the bubble tank with trace gases. Gases are fed one after another through a flow controller into the head space of the tank. To avoid overpressure the head space is open to the ventilation system at the other end of the tank. The loss of gases to the ventilation system has to be accounted for.

- purge gas inlet

  To remove remaining trace gases, which are not wanted, it is possible to purge the input line with a gas of choice.

- reference

  For reference measurements, i.e. to measure a pure gas, it is possible to pump the gas fed into the tubing from the gas inlet directly into the MIMS and dump it in the ventilation afterward.

In-gassing Setup

The device used for seeding the tank with trace gases is shown in fig. 4.5. It consists of an array of 16 magnetic valves (*Bükert 6628*), which are connected to the individual trace gas supply. All of the valves are connected to a shared line, which is connected to the tank through a flow controller (see fig. 4.4). This enables the controlled injection, even though mutually exclusive, of each trace gas with only one flow controller.

Bottled gases were connected through a pressure regulator to the gas mixing device (see fig.

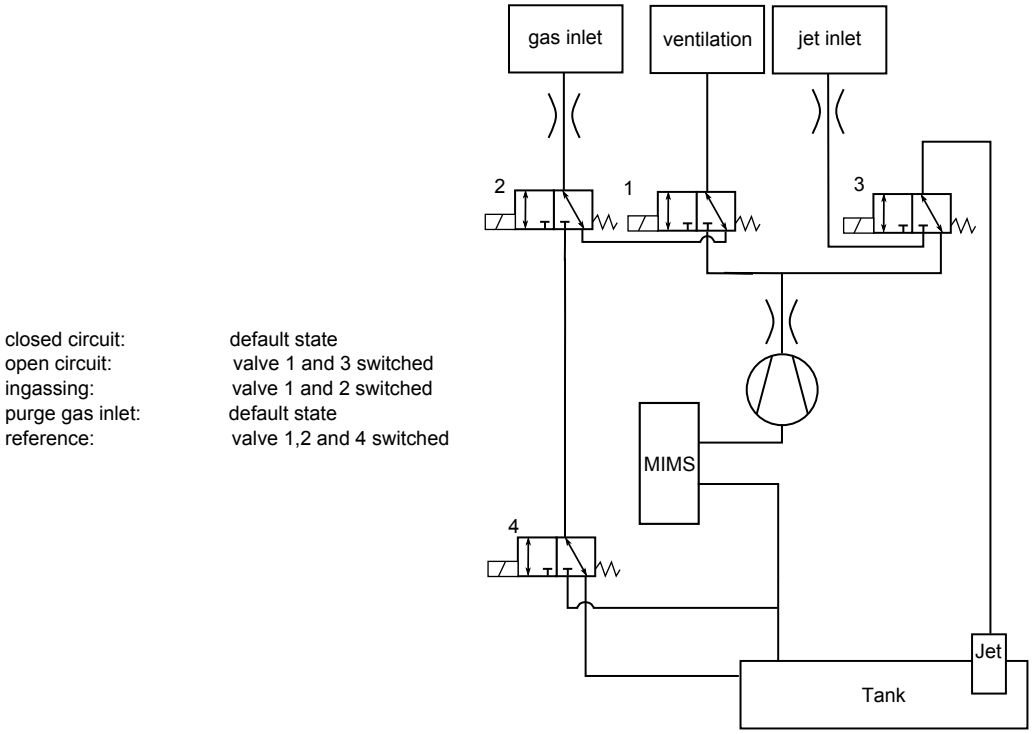

Figure 4.4.: Air side circuit with bubble tank. This setup enables five modes of operation, which can be switched automatically. This is accomplished by using computer controlled valves and flow controllers. For description of individual modes refer to text.

4.5). Three gases, which were not available in gas bottles, were used. Hydrogen resp. Deuterium was generated by electrolysis of heavy water. The heavy water (99.7% D_2O) was mixed with 10% 1-molar KOH to impose conductivity. Oxygen produced during this process was also used as a trace gas. Benzene and Dimethylsulfide (DMS), which are liquids at room temperature, were applied through washing bottles. Argon was flushed through the bottles with pure substances at a given flow rate. The loaded carrier gas was then fed into the tank through the valve array.

4.2. Membrane Inlet Mass Spectrometer (MIMS)

In this experiment a *Hiden HPR 40* quadrupole mass spectrometer was used (see fig. 4.3). Detailed technical data can be found in appendix B. Its measurement chamber is connected to two capillaries, which have inlets covered by a thin silicone membrane at their ends (see fig. 4.3). Gases are able to diffuse through that membrane and reach the interior of the capillaries, which can be sampled distinctively in the measurement chamber of the spectrometer. One of the probes was used in the gas phase, the other in the water phase. Next to the probe in the gas phase a temperature sensor (*Greisinger GMH 3710*) and an absolute pressure sensor (*Greisinger GMH 3111*) were mounted. In the waterphase only a temperature sensor was used, because the pressure hardly

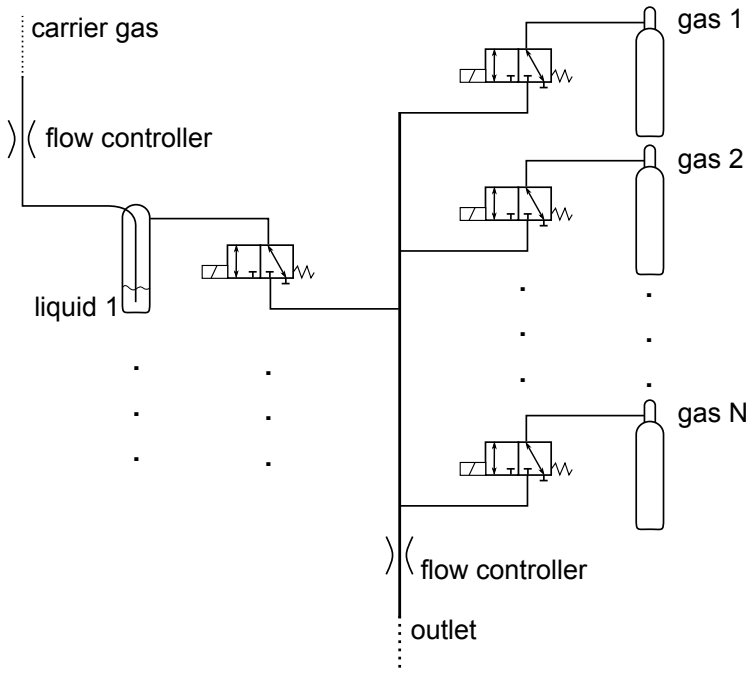

Figure 4.5.: Setup used for seeding the head space of the bubble tank with trace gases. All gases are connected to a shared line by an array of valves. The shared line is connected to the tank through a flow controller. It is possible to inject a given amount of each tracer into the bubble tank one after another. Substances, which were available in liquids only, were applied with washing bottles.

changes during one measurement run. These sensors were used to ensure constant conditions. Two different detectors are used in the spectrometer to measure ionized molecules and atoms. Ionization is accomplished by electron impact (refer to section 3.1.1). The electrons are produced by heating a filament with a current and accelerating the emitted electrons in an electrical field. The ionized particles are then filtered by a quadrupole field according to their mass to charge ratio. The ion detection is accomplished by a Faraday detector, which captures the ionized particle stream in a conducting cap and measures the generated current. The second, by five orders of magnitude more sensitive, detector is a secondary electron multiplier (SEM), compare to section 3.1.1. Here a current of secondary electrons is measured. Secondary electrons are produced when the particles to be measured hit the first of a cascade of dynodes, which then generate an electron avalanche. These electrons are captured and measured (refer to section 3.1.1).

4.3. Bubble Measurements

4.3.1. Optical Setup

For bubble sizing and velocimetry measurements two different cameras were used. Essential technical parameters are summarized in table 4.1. Main reason for using two cameras was the desired radius range, which could be resolved. For velocity measurements a *basler acA2000* camera was used in a telecentric setup, as described in section 3.2.1. Telecentricity was achieved by mounting an additional 135 mm *Minolta* lens in front of the camera with a 50 mm *Pentax* lens. The distance of the lenses had to be adjusted to yield telecentric imaging (see section 5.1.1). This camera was connected via *CameraLink* to a *Silicon Software mEIV-VD4* frame grabber card in the measurement computer. To be able to determine the motion of individual bubbles, image straddling was used. This means the camera was operated at maximum exposure time, whereby the actual exposure was done by pulsed LED light sources. That way it is possible to get two consecutive images with a smaller time difference than the camera itself would allow. To get short time periods the first light pulse is applied at the end of the first image and the second pulse at the beginning of the second image. This procedure is illustrated in fig. 4.6. The camera was triggered at 20 Hz with an exposure time of 49.9 ms. As light sources LEDs of type *Cree XE blue* were used. They were driven by custom electronics and controlled by a function generator *Tektronix AFG 3022B*, which also triggered both cameras. The LEDs were mounted in the focal plane of two *Schneider Kreuznach 0.95 mm* lenses to produce telecentric illumination. To remove structures in the illumination from circuits on the LED an additional holographic filter was placed in front of the illumination lens. This filter widens the bundle of beams by $\pm 1^\circ$. Due to the filter and size of the LED itself the illuminations have an effective f-number of $n_{\mathrm{f,LED}} = 16$. [53] The second camera used a *Olympus* 80 mm with extension tubing to get a high magnification. This camera was connected via *GigE* to the measurement computer. Both cameras were operated without any built in corrections and at minimum gain.

camera	basler acA2000 340-km (velocimetry)	basler acA2500 14-gm (high resolution)
Pixel pitch [μm] image space	5.5	2.2
Pixel pitch [μm] object space	21.9	1.9
Bit Depth [Bit]	12	12
Framerate [Hz]	20	10
Expsoure [ms]	49.9	98
Length of LED pulse [μs]	0.7	40.5
Used lens	135 mm/50 mm	80 mm[3]
Resolution [px]	1536×1080	2592×1944
Eff. f-number	22	36

Table 4.1.: Technical parameters of the used cameras

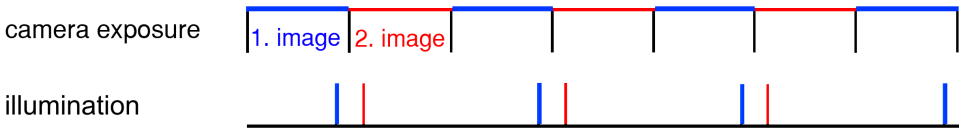

Figure 4.6.: Illustration of the concept of image straddling. This method is used to achieve a short time interval between two images for velocity estimation. The exposure of the camera is set to the maximum value, whereby the imaging light pulses are applied at the end resp. at the beginning of two subsequent images.

4.3.2. Mounting

The mounting of the cameras on the tank is illustrated in fig. 4.7. Both cameras and light sources are mounted on a semi-automatic translation stage in a vertical distance of 90 mm. The vertical translation stages (*igus Type SLW-1040*) are driven by stepping motors (*nanotec Type ST6018L3008*), which are controlled by the measurement pc via *nanotec SMCI-47-S-2* driver units. In that direction the deviation of the position is less than 20 μm after 24 full round trips. In horizontal direction manual adjustable translation stages were used (*igus DryLin-T*). The distance of the cameras to the tank was chosen in a way, that the focal plane was located in the middle (z-direction) of the water tank.

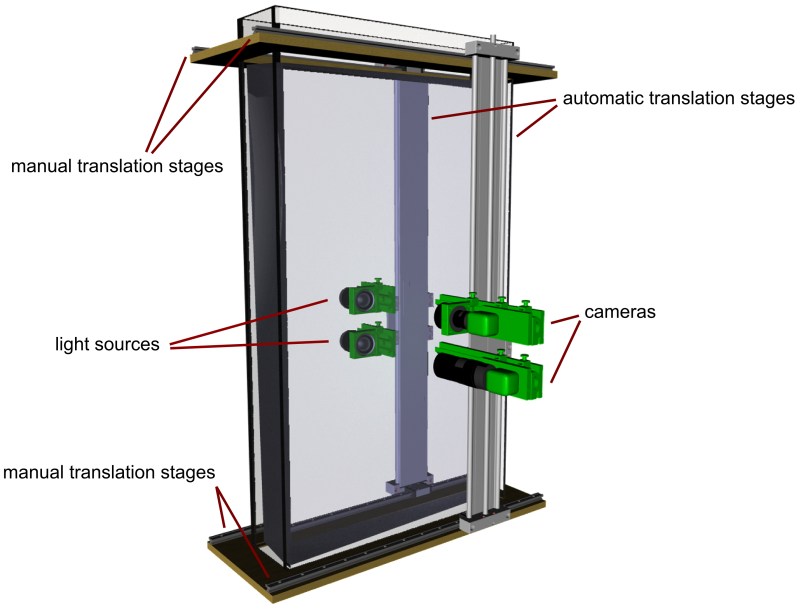

Figure 4.7.: illustration of the used dual camera setup. Automated translation stages were driven by stepper motors.

5. Preliminary Experiments

This chapter present the experiments, which were conducted in order to design the experiment or to characterize the measurement devices, like calibration or determination of response times. In the first section the bubble measurement setup is addressed and the focus of the second section is on the mass spectrometer usage and the design of the gas exchange experiment.

5.1. Calibration of Bubble Measurement

The procedure for adjustment and calibration for the cameras of the bubble measurement technique follows the steps described in Mischler [53]. Here the essential steps and equations are recalled.

5.1.1. Adjustment of Telecentricity

As discussed in section 3.2.1, an optical projection is telecentric if and only if the magnification factor is independent of the distance of the lens. This feature was used to adjust the distance of the telecentric lens to the lens of the camera. Images of a steel target with laser-ed holes in an defined grid were taken in front of and behind the plane of focus (fig. 5.2). Telecentricity demands that the distance of the holes stays the same for both images. The distance was calculated by determining the centers of gravity of the imaged holes and the distance between them. Object segmentation was done by using a simple threshold (compare to section 7.2). By taking two images it is easy to check whether the aperture of the camera lens is too close or too far away from the telecentric lens: If the aperture of the camera is too close to the lens the magnification factor will drop with increasing distance. Or vice versa, if the aperture is too far away the magnification will rise with increasing distance. This is illustrated in fig. 5.1. If the aperture is to close to the telecentric lens the principal ray will diverge. This means an object of same size will be imaged smaller, so that the magnification factor decreases. If the aperture is too far away, the principal ray will

converge and the magnification will rise. The distance was adjusted iteratively until the change in the magnification factor was minimized within the limits of the mounting. The minimum deviation of the magnification factor was lower than 1%.

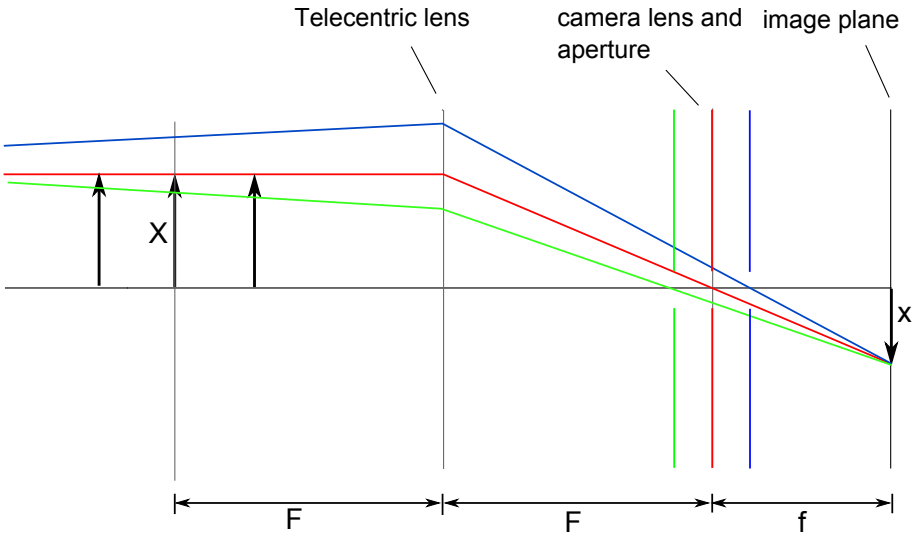

Figure 5.1.: Sketch to illustrate the telecentric adjustment. The principal rays for three cases are shown. The aperture is to close too the image plane (blue), in the focal plane (red) and too far away from the focal plane (green).

5.1.2. Calibration of Cameras

Linearity of the cameras was checked according to EMVA 1288 standard [20] by Aeon. Among other parameters, the deviation from linearity and the SNR of the cameras were tested with this standard. The values are included in table 4.1. The intensity range, i.e. the exposure time resp. LED pulse time was adjusted to operate the camera in the linear region. The maximum intensity was kept below 3700 DN.

Depth series and measurement volume To calibrate the cameras in terms of magnification factor and measurement volume, depth series of several targets were recorded. Five circular apertures made by *Owis* and two custom made steel sheets were used. The sizes, accuracies and measured depth ranges are summarized in table 5.1. Smaller targets need a smaller depth range, since they get out of focus and do not produce a measurable signal outside the given range. Each depth range was sampled at 20 equal spaced positions around the focal plane. An automatic translation stage manufactured by *Owis* was used to acquire these images in air. For the actual measurements the calculated values for the measurement depth were adjusted to water according to eq. (3.2.1).

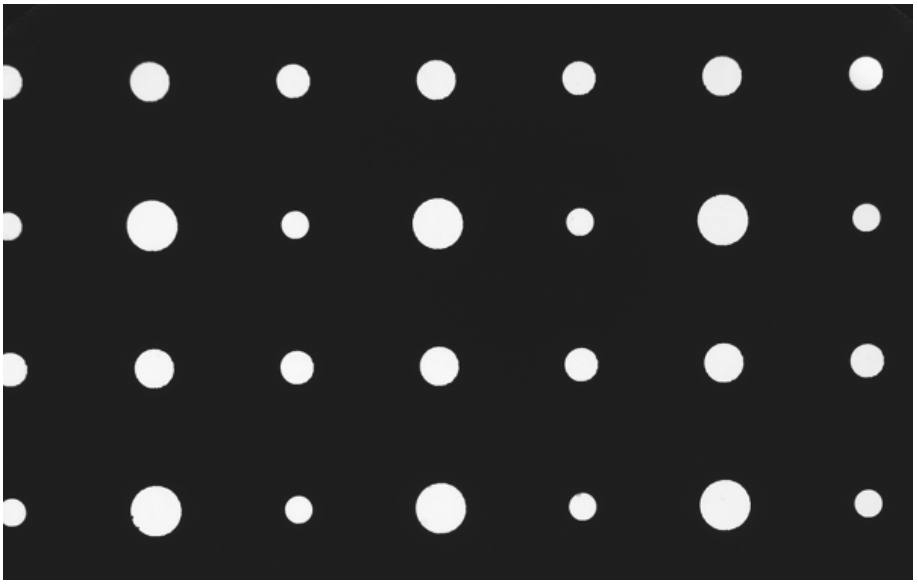

Figure 5.2.: Image of steel target with holes of defined diameter used for calibration.

Table 5.1.: Summary of used targets for size and depth calibration of the cameras.

Radius [μm]	Depth range [mm]	Type
5 ± 0.5	2	circular aperture
10 ± 1.0	2	circular aperture
15 ± 1.0	4	circular aperture
50 ± 2.5	20	circular aperture
150 ± 25	40	circular aperture
300 ± 50	50	steel sheet
350 ± 50	50	steel sheet
400 ± 50	50	steel sheet
500 ± 50	50	steel sheet

These depth series were analyzed with the same algorithm used for bubble detection, which is explained in the next chapter 8. The radii determined by the algorithm were fitted with a linear function against the known real radii to get the magnification factor for both cameras. For the non-telecentric high resolution camera a constant magnification factor was assumed, since its change was below 2.5% in the determined measurement volume. The effective measurement depth was determined by looking for the maximal distance to the focal plane for each target in the depth series and fitting a linear function of the radius to this distance. The results for the telecentric camera are shown in fig. 5.3 and given for both cameras in table 5.2.

Table 5.2.: Calibration parameters of the used cameras

camera	basler acA2000 (velocimetry)	basler acA2500 (high resolution)
Magnification m_x	22.9 ± 0.02	1.91 ± 0.01
Depth factor m_z	0.037 ± 0.006	0.025 ± 0.002

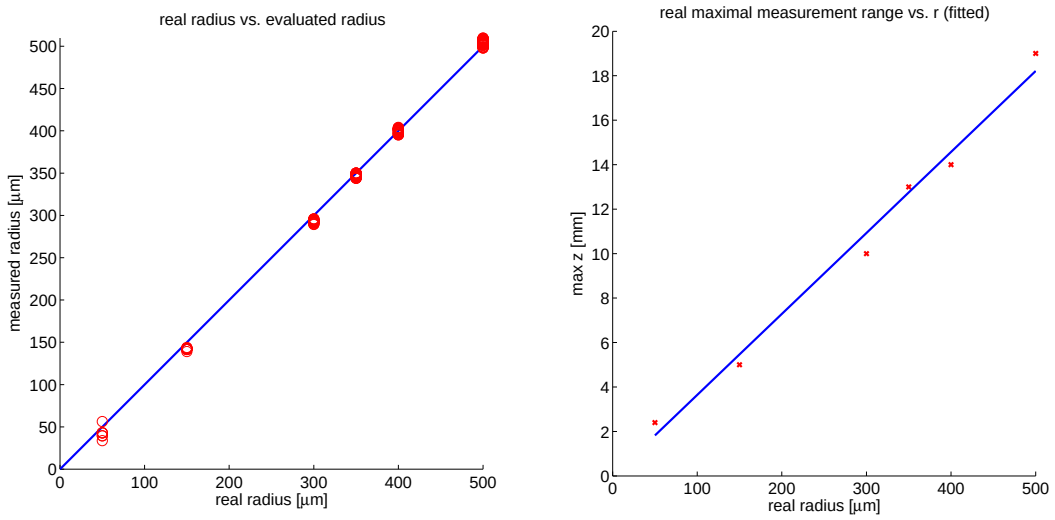

Figure 5.3.: Linear calibration curves for the telecentric basler acA2000 camera for the radius (left) and the maximal measurement depth (right). The calculated values are given in table 5.2.

5.2. Design of Gas Exchange Measurements

The gas exchange measurements are a central part of this thesis. This section gives the considerations taken into account for the design of the experiments and the individual steps.

5.2.1. Selection of Trace Gases

As discussed in section 2.2, gas transfer rates get dependent on tracer solubility in presence of bubbles. To capture the effects of bubbles in the best possible way it is crucial to choose tracers, which cover the interesting ranges of solubility and diffusivities. Here the criteria for the selection of trace gases is given and it is argued which gases were finally chosen due to experimental limitations.

Physico-chemical Parameters

The regions in $\alpha - \mathrm{D}$-space, which are relevant for bubble mediated gas exchange, are identified by a parametrization done by Woolf et al. [72]. An overview of this parametrization is shown in figure 5.4. A preselection of trace gases along with expected masses for the mass spectrometer is given in table 5.3. Besides solubility and diffusivity, the gases were chosen regarding availability,

cost and toxicity. Detailed information for these gases is given in the appendix B. As can be seen in figure 5.4 these gases cover a wide range of solubilities, where a change in gas transfer is to be expected. The reason for the diffusion constants being in a small range for high solubilities is that common gases with different diffusivities don't exist.

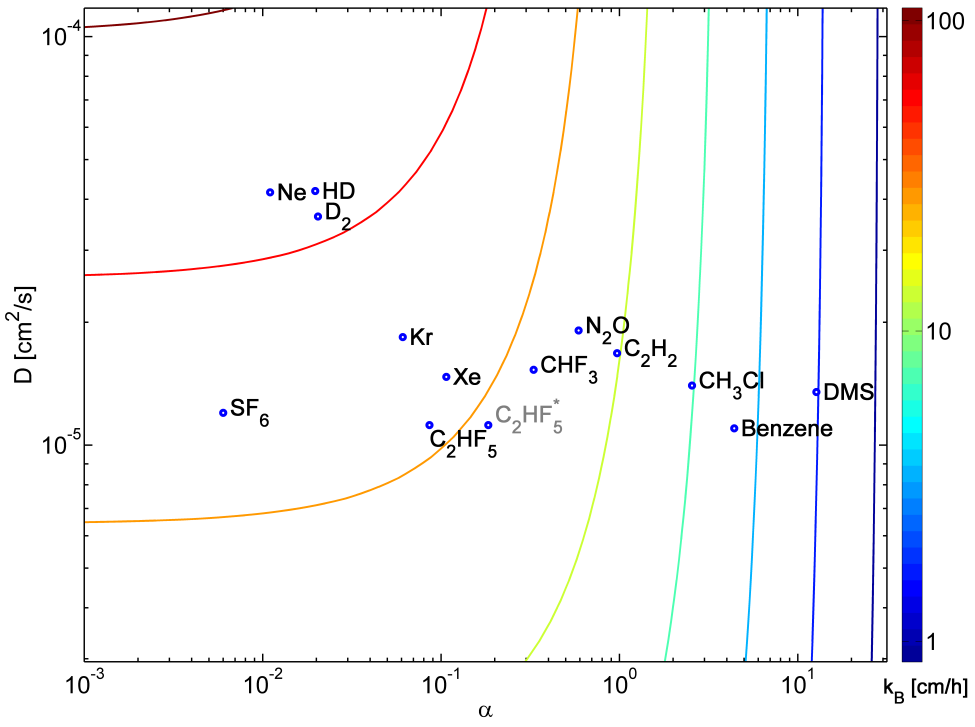

Figure 5.4.: Overview of the used tracers. The shown gas transfer velocity k_b is parametrized after Woolf et al. [72]. The spacing of the contour lines of constant transfer velocity is by a factor of two. *) solubility of 0.184 was state of knowledge when the experiments were performed.

Measurement Sensitivity

Each tracer was measured individually in an Argon atmosphere. In these experiments an Argon flow was pushed past one of the MIMS-probes, which was put into PVDF tubing. This gas flow was enriched with one percent of the measured tracer. Both gases were mixed with the same flow controller used in the bubble tank setup (*Analyt-MTC*). Figure 5.5 shows the measured values by the Faraday probe of the spectrometer. This result was used as a first guess for the initial concentration for the gas exchange measurements. A target start concentration $1 \cdot 10^{-8}$torr was chosen. This concentration is in the upper measurement range of the SEM sensor of the spectrometer, so that several orders of magnitude can be tracked, even if the start concentration is not reached.

Tracer	weight [u]	α	D [10^{-5}cm^2/s]	Sc	dominant masses [u]
H_2	2.02	0.0191	5.13	194	1, 2
HD	3.02	0.0197[a]	4.19	239	3
D_2	4.03	0.0202[a]	3.63	275	4
N_2	14.01	0.0161	1.88	532	14, 28
Neon	20.18	0.0110	4.16	240	20, 22
C_2H_2	26.01	0.97	1.68	595	25, 26
O_2	32.00	0.031	2.4	371	32
Argon	39.95	0.034	2.0	500	20, 40
N_2O	44.01	0.591	2.6	385	44, 30
CO_2	44.01	0.86	1.92	521	44
CH_3Cl	50.49	2.55	1.40	714	50
DMS	62.13	12.7	1.35	741	47, 62
CHF_3	70.01	0.33	1.53	654	-
Benzene	78.11	4.4	1.10	909	78
Krypton	83.79	0.061	1.84	543	84, 86
CF_4	88.01	0.0052	1.42	704	-
Pentafluoroethane (C_2HF_5)	120.02	0.086*	1.12	893	101, 119
Xenon	131.29	0.107	1.47	680	129, 131, 132
SF_6	146.06	0.006	1.2	833	89, 127

[a]) calculated from the value of H_2 by an assumed square root dependence of the diffusion constant to the molecular mass, see e.g. [66].
*) solubility of 0.184 was state of knowledge when the experiments were performed.

Table 5.3.: Summary of examined tracers and their important physio-chemical parameters.

5.2.2. Characterization of Membrane Inlet Mass Spectrometer

Settings for Individual Tracers

A central parameter for measuring the molecules in the mass spectrometer is the kinetic energy of the electrons used for ionizing the target molecules. This energy is provided for ionization, so that it is only possible to measure molecules with a lower ionization energy. This property of the tracer molecules can be used as an additional selection parameter for the spectrometer measurements. When the electron energy exceeds the ionization energy, ionization can happen and the molecule can be measured by the spectrometer. Increasing the electron energy further a bigger fraction of molecules is ionized, so that the signal increases. At the energy all molecules are ionized the signal reaches a plateau. In fig. 5.6 this is shown using the example of Xenon. When the energy is increased even further, the signal drops again. These are quantum mechanical effects, which determine the cross-section of the molecule ionization on electron impact. Since this effect does not affect these measurements, please refer for example to Wetzel et al. [70] or Rudge [61] for detailed explanation of these effects. For each tracer the onset of the plateau was determined to use this energy for further measurements. It is desirable to use an energy as low as possible,

Table 5.4.: Used settings for mass spectrometer for different measured masses.

mass [u]	Detector	Molecule	Tracer	Electron energy [eV]	τ_{mims} [min]
1	SEM	H^+	H_2	35.0	< 1
2	SEM	H_2^+	H_2	35.0	< 1
3	SEM	HD^+	HD	35.0	< 1
4	SEM	D_2^+	D_2	35.0	< 1
14	SEM	N^+	N	40.0	< 1
16	SEM	O^+	O	40.0	< 1
20	SEM	Ar^{2+}, Ne^+	Argon, Neon	40.0	< 1
20	SEM	Ar^{2+}, Ne^+	Argon, Neon	35.0	< 1
22	SEM	Ne^+	Neon	70.0	< 1
25	SEM	C_2H^+	C_2H_2	20.0	7
26	SEM	$C_2H_2^+$	C_2H_2	20.0	7
28	Faraday	N_2^+	N_2	40.0	< 1
32	Faraday	O_2^+	O_2	40.0	< 1
40	Faraday	Ar^+	Argon	40.0	-
44	SEM	N_2O^+	N_2O	20.0	2
47	SEM	CH_3S^+	DMS	15.5	8
50	SEM	CH_3Cl^+	CH_3Cl	22.0	< 1
62	SEM	$C_2H_6S^+$	DMS	15.5	8
78	SEM	C_6H_6	Benzene	19.5	80
84	SEM	Kr^+	Krypton	21.0	< 1
86	SEM	Kr^+	Krypton	21.0	< 1
89	SEM	SF_4^+	SF_6	40.0	< 1
101	SEM	$C_2HF_4^+$	C_2HF_5	40.0	< 1
119	SEM	$C_2F_5^+$	C_2HF_5	40.0	< 1
127	SEM	SF_5^+	SF_6	40.0	< 1
129	SEM	Xe^+	Xenon	19.0	< 1
131	SEM	Xe^+	Xenon	19.0	< 1
132	SEM	Xe^+	Xenon	19.0	< 1

because electrons with high energies are capable of splitting the molecules in the measurement chamber in many ways or ionize atoms or molecules twice. These charged molecule particles spoil other masses, which was avoided as good as possible. The advantage of comparability to other spectrometers was abandoned since no absolute measurements were conducted.

The default value of 200 μA for the electron current was reduced to 70 μA to allow for low electron energies. If a high current is used at low electron energies it is possible that the filament overheats and is destroyed. Changing the current during the measurement was not an option, because waiting for stable conditions for the electron current would increase the sampling time for each measured mass. For all other parameters default values have been used - a summary of those is given in table 5.5. A summary for default settle and dwell times for different concentration ranges is given in table .1. These times determine how much time the electronics is given to settle resp. how long ions a collected to measure the concentrations.

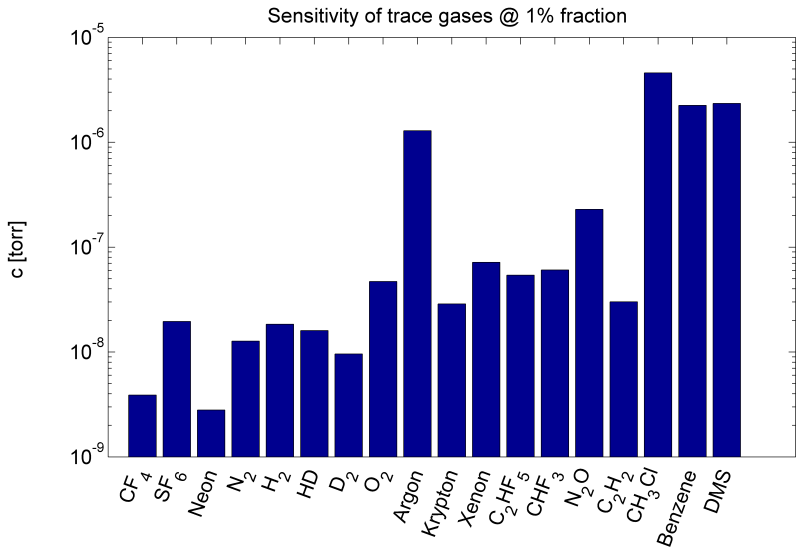

Figure 5.5.: Measured pressure values for the used tracers. Tracers were mixed into an argon flow with a volume fraction of 1 %. A ionization energy of 70 eV was used.

For each tracer the measurement as for Xenon shown in fig. 5.6 has been conducted. The concentration was measured against electron energies. With this measurement the onset values of the plateaus for the measured masses were determined. Therefore the electron energy was chosen, where the second measured concentration value reached the plateau value. The obtained values are included in table 5.4.

Table 5.5.: Global settings of the mass spectrometer

electron current	70 μA
cage voltage	3.0 V
multiplier voltage	850 V

Stability of Concentration Measurements

There are several parameters, besides the properties of the trace gas itself, which influence the response time of the membrane inlet. The effects of swelling and competitive sorption, which occur if a significant amount of tracer is stored in the membrane, are not expected, because the used concentrations are too low [22]. It has been shown that in these conditions, a calibration of the membrane permeability as a function of temperature, pressure and flow parameters is necessary under changing conditions [43]. Since in this experiment these parameters are controlled, it is possible to fix these to constant values. This saves the effort of systematic calibration measurements.

To verify that the accuracy of the temperature control-loop is sufficient for not affecting the

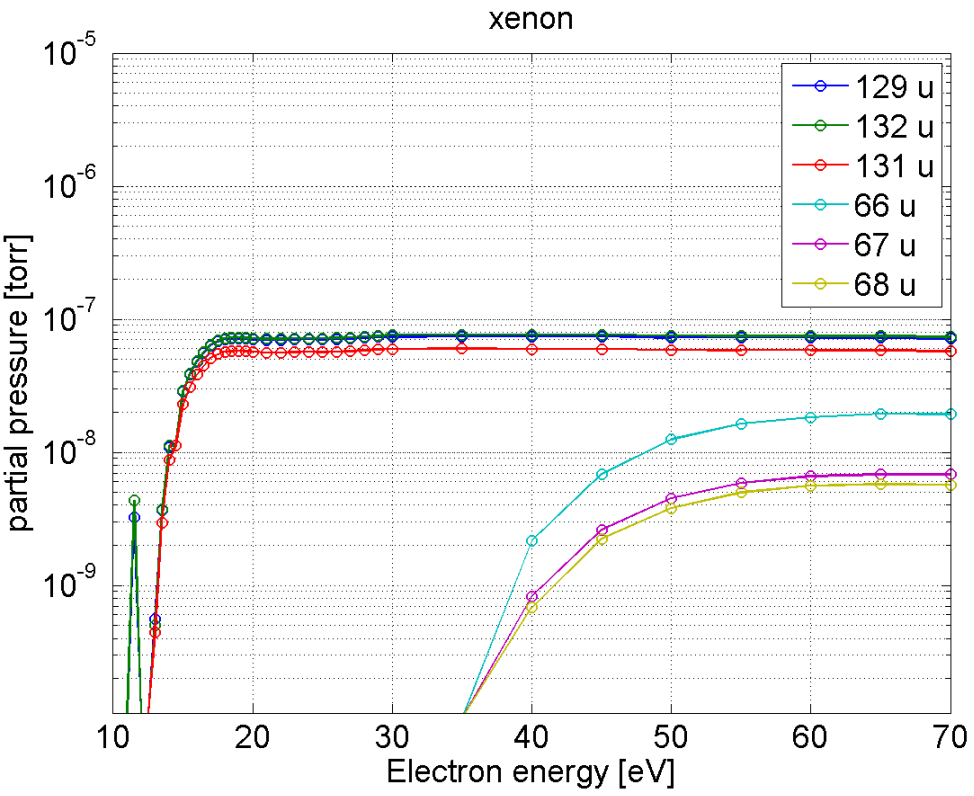

Figure 5.6.: Measured partial pressure vs. ionization energy using the example of Xenon. Several isotopes of Xenon are shown. At 35 eV the onset of Xenon atoms, which have been double ionized, can be seen.

membrane properties, a time series of a constant concentration have been acquired. In this series all expected conditions are represented. This covers a temperature change over a range of $0.5°C$ and all used flow settings. This measurement is shown in figure 5.7. As a result a maximal relative rms-deviation of smaller than 2.5% was found. This should be seen as upper boundary, because actual temperature variations during the measurements were not bigger than $0.2°C$.

Response Times

As explained in section 3.1.1 it is important to characterize the response of the permeating gas flux through the membrane to a change in ambient concentration. In addition there is some time needed to remove the sample gas from the measurement chamber of the spectrometer. These times depend heavily on the observed tracer. Here an upper bound for a response time τ_{mims} was measured. This time can be understood as the maximum time needed for the system (spectrometer and membrane) to adapt to a different sample concentration. Thereby the time to reduce the difference to the steady state flux of the new concentration to a fraction of $\frac{1}{e}$ is chosen as the characteristic response time. This choice allows an easy comparison to other relevant characteristic times, in particular the concentration equilibration times of the trace gases τ_{eq}.

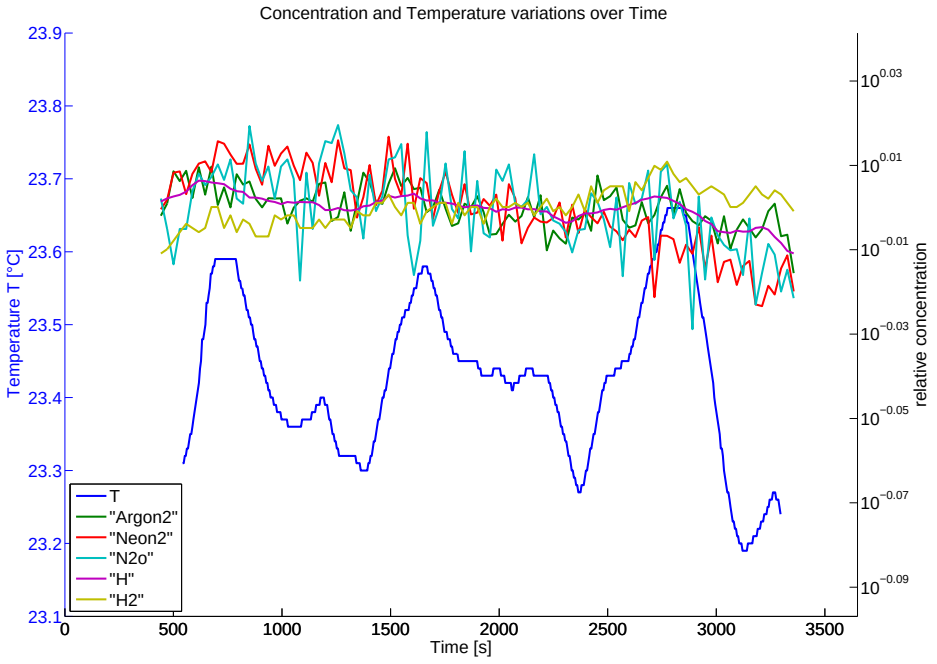

Figure 5.7.: Variations of measured concentration of various gases. The actual concentration was held constant to test the influence of temperature and pump power on the measured values. It was found that the variations were below 2.5%.

The time to flush the measurement chamber is particularly important, if the probe inlets are switched. Then it is possible that the sample at one probe produces a high background concentration, which covers a lower concentration at the other probe. In these cases one needs to wait at least τ_{mims} to get a valid signal.

For the time needed to remove the sample from the measurement chamber by the vacuum pump an exponential decay was assumed. This decay superposes with the time constant of the membrane as given in 3.6. As only an upper bound was estimated, it was sufficient to approximate the combined response with a simple exponential decay with τ_{mims} as time constant.

To measure τ_{mims} for each tracer, the same setup as for the sensitivity measurements was used (see section 5.2.1). An Argon gas flow was mixed with 1% trace gas and was exposed to the MIMS-probe. The probe was placed in PVDF tubing to assure sufficient throughput to avoid a depletion of the tracer in the flow, due to the sampling flux. After a constant value for the concentration was reached, the tracer supply was closed, so that pure Argon was measured from that moment on. The time difference to reach 99% of the background concentration, i.e. 1% remaining tracer concentration, again was determined. This time was then converted to an exponential time constant τ_{mims}.

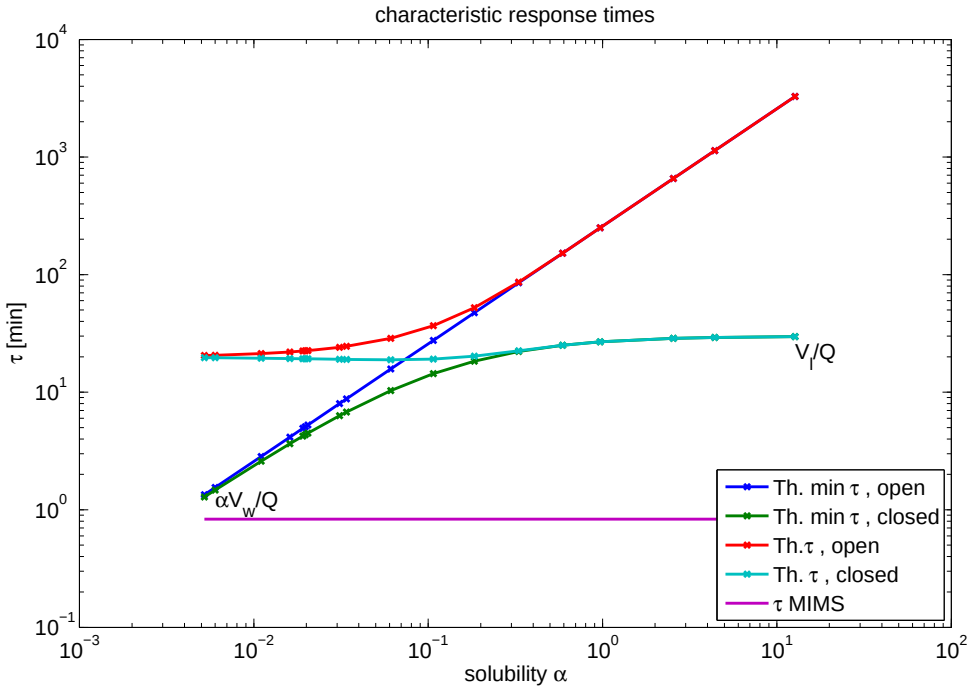

Figure 5.8.: Characteristic response times for gas exchange in the bubble tank and the mass spectrometer at a flush rate of 1 l/min. The minimal theoretical response time and a response time for a bubble cloud with 50% effectiveness ($\lambda = 0.5$) are presented. Each of both is shown for the open and the closed mode of measurement.

The measured response times τ_{mims} are summarized in table 5.4. Sampling period was about 1 min, so smaller values could not be resolved.

Tracer	D_G [10^{-5} cm^2/s]	α_G	P_G [Barrer]
O_2	1.6	0.31	600
N_2	1.5	0.15	280
C_2H_2	-	-	26400

Table 5.6.: Permeability data in PDMS for selected tracers from [58]

Selection of Trace Gases

In table 5.4 the measured masses and corresponding tracers for the systematic gas exchange measurements are given. All tracers of the preselected set could be used, with two exceptions: The three fluorinated hydrocarbons, CHF_3, CF_4 and C_2HF_5, all produce signals at the characteristic masses 31 (CF^+), 50 (CF_2^+), 51 (CHF_2^+) and 69 (CF_3^+). To avoid the superposition of the measurement signals, only one tracer was chosen. The physio chemical properties of C_2HF_5 are in the region of greatest change in the parametrization shown in figure 5.4, what made it the most interesting candidate as a tracer. CHF_3 and CF_4 were dropped. Unfortunately available literature values for C_2HF_5 proofed erroneous after conducting the experiments. The value is about half of

the previously assumed value, what creates a gap in the solubility coverage of measured transfer values.

5.2.3. Leak Rate of Bubble Tank

Due to technical difficulties in keeping the gas chamber around the water jet gas tight, a leakage rate has to be considered in several circumstances. For the central evasion measurements this effect can be easily corrected for, since Argon, which leaves the chamber through the leak, just decreases the gas flow through the tank. This happens in a constant manner, as could be verified by the exponential fits in section 8.1. Therefore the actual flow can be determined by the equilibration time of a high soluble gas through eq. (2.32). This procedure yields an actual flow rate around 0.7 l/min instead of 1 l/min as set at the flow controller, see the discussion in section 9.2. For invasion measurements this effect leads to an superposed exponential reduction of the concentrations. A lower bound for the characteristic time τ_{leak} can be estimated with the volume of the head space and the leakage rate from the evasion measurements. The actual time constant should be considerably bigger, since in the closed configuration for invasion much less overpressure is produced in the bubble generator. This estimate gives $\tau_{\text{leak}} > 47$ min. This value is about double of the expected equilibration times for gas exchange in the closed configuration (see fig. 5.8).

6. Experiments

In this thesis experiments under several conditions were conducted. Here the procedure of these experiments is described and explained. Overview and motivation for the choice of conditions is given.

6.1. Procedure of Experiments

The first step of each run is the preparation of the water. Starting point is always a cleaned tank with deionized water (conductivity $< 1\mu$S). The water is then deaerated by pumping pure Argon bubbles through the bulk until the O_2 concentration was constant. Usually Helium is used as gas in this application, but this would superpose the D_2 measurements in the experiment due to equal molecular masses. At this point minimum ambient air concentration in the water for this setup is reached - the outward air flux through the bubbles is balanced by an inward leakage flow through the jet. For the following special treatments of the water, like salt or alcohol additions, refer to section 6.2. For detailed description of setup, see section 4.1.

6.1.1. In-gassing

The first stage is filling the head space of the bubble tank with the trace gases. The tank was connected to the in-gassing unit on one side and was open to the ventilation at the other side to avoid overpressure, as described in section 4.1.2. The tracers were pushed into the tank one after another, so a small amount of tracers were lost through the over pressure ventilation. However this does not change anything on the used mass balances, since the reference concentrations were taken in the next stages. Since the used electrolysis cell was only capable of producing a flux of 15 ml/min, it took about 33 min to produce enough Deuterium and Oxygen. To prevent the other tracers from evading in this time, Deuterium was applied first. DMS and Benzene were mixed

in one washing bottle for technical reasons, so it is not possible to give the exact amount of each individual tracer. These gases contaminate the tubing, so that these gases were applied at last. In this way it is avoided that the other tracers take remaining DMS or Benzene with them. After each experiment, the in-gassing unit was flushed with Argon. In table 6.1 the initial amounts of tracers are given. These amounts were determined experimentally with the sensitivity measurements (see section 5.2.1) as a starting point. The tracers DMS and Benzene were applied only to a new water filling once, since the concentration never dropped considerably during the experiments due to their high solubility.

Tracer	initial gas [sccm]
D_2/HD/O_2	500/-/250
C_2H_2	150
Ne	500
SF_6	250
N_2O	12
C_2HF_5	500
Xe	100
CH_3Cl	6
Kr	200
DMS/Benzene*	2

Table 6.1.: Initial gas volumes of tracers used for closed invasion experiments. *) only applied the first time the water was used, because afterward the concentration never dropped considerably due to gas exchange measurements.

6.1.2. Invasion - Closed Configuration

After the purging of the head space with Argon is finished, the system is switched into closed configuration. This means that the tank is no longer connected to the atmosphere and gas used for the bubble generator is taken from the head space. To achieve the desired gas flow rate of 1 l/min, a peristaltic pump is used. Gas and water side concentrations are sampled with the two silicone membrane probes in the mass spectrometer, as described in section 4.2. The probes are switched every 10 min to allow for adaption of the measurement chamber to the changing sampling path. The sampling period depends on the measurement range of each measured mass, which was adjusted automatically by the spectrometer software during the measurements. A full scan of all measured masses usually took a time period of 40s-120s. The jet pump is set to the desired frequency and is turned on. The temperature control to balance the heat output of the pump is switched on. The system runs until the change in concentration of each tracer is negligible, so that the tracers are in equilibrium between water and gas phase. This typically takes about 130 min.

6.1.3. Evasion - Open Configuration

From equilibrium state the system is switched into open configuration. The bubble generator is supplied with 1 l/min pure Argon, while gas from the head space is pumped into ventilation to balance the pressure. Jet and temperature control are operated with the same settings as in the closed configuration. In this stage only water side concentrations are monitored with a single membrane probe. This experiment runs until most of the tracer concentrations are below detection limit. For highly soluble gases the expected equilibration times are that long, so that it is not feasible to wait until the concentration drops that much. So the experiment runs the maximum feasible time possible in one day, which was at least 8 hours.

During this measurement the bubble distribution and velocity measurements were conducted. Vertical profiles were recorded automatically at 11 positions at each horizontal position. Horizontal positions were changed manually after each vertical profile. Six horizontal positions were approximately reproduced using a simple ruler at the translation stage. These positions were approximatly equally spaced with one additional position at the jet submerging the bubbles. The positions are given in table 6.2. At each position 2000 images were taken with the velocimetry camera acA2000 and 500 with the high resolution camera acA2500. The time period between two LED pulses for the velocity measurement was chosen to be 2.3 ms.

y_i [mm]	40	190	290	390	54	670					
x_i [mm]	200	300	400	500	600	700	800	900	1000	1100	1200
y_i [mm]	40	190	290	390	54	670					
x_i [mm]	100	200	300	400	500	600	700	800	900	1000	1100

Table 6.2.: measured positions for bubble density and velocity measurements. upper: acA2000 lower: acA2500

Pulsed Bubble Generation

For one special condition pulsed bubble clouds were produced. This was a special variant of the open configuration. Here the bubble generator was provided periodically with pure Argon at a flow rate of 1 l/min. The flow controller was periodically switched open for 5 s and then closed for 5 s. Since the flow controller needs some adjustment time this yields a flow rate lower than 0.5 l/min. To capture periodic effects in the bubble distributions the image acquisition of the cameras was synchronized to the bubble production cycle. This synchronization was done via network based semaphores.

6.2. Experimental Conditions

In section 2.2.2 it is discussed, which parameters affect the bubble generation and the resulting bubble size distributions. To cover a wide variety of parameters, several experiments have been conducted. In table 6.4 an overview of all conducted systematic measurements is given. Each experiment is given a unique tag, so that it can be referred to easily hereafter. The first parameter which was changed was the jet frequency, which changes the kinetic energy deposited into the tank and put into bubble surface generation. With this parameter also the depth into which the bubbles are submerged is changed. This increases the residence time of the bubbles under water. In table 6.3 flow conditions for different jet frequencies are given. To compare the transfer rate of a steady state bubble distribution, with a distribution changing in over time - as in wave breaking - one measurement with a periodically changing distribution was made. Salt additives in water heavily change the bubble spectra, since coalescence is suppressed. Since gas transfer rates are interesting for salt water in particular, two experiments with salt water have been conducted. Since surfactants are the common case on water surfaces, two experiments with different Triton-X concentrations were conducted. Two additional experiments were conducted to test the influence of surface tension and viscosity.

In the following section the motivation of each experiment is given and the special features and problems are addressed.

Pump Frequency [Hz]	Water volume flow [l/h]	Kinetic jet energy [W]	Re
15.0	400 ± 50	$(0.2 \pm 0.1) \cdot \beta$	1660 ± 208
20.0	600 ± 50	$(0.7 \pm 0.2) \cdot \beta$	2500 ± 208
25.0	800 ± 50	$(1.7 \pm 0.3) \cdot \beta$	3330 ± 208
30.0	1000 ± 50	$(3.3 \pm 0.5) \cdot \beta$	4160 ± 208
35.0	1200 ± 50	$(5.8 \pm 0.7) \cdot \beta$	5000 ± 208
40.0	1400 ± 50	$(9.1 \pm 1.0) \cdot \beta$	5800 ± 208
45.0	1550 ± 50	$(12.6 \pm 1.2) \cdot \beta$	6650 ± 208
50.0	1750 ± 50	$(17.8 \pm 1.5) \cdot \beta$	7500 ± 208

Table 6.3.: Mapping of pump frequency to water flow rate and kinetic jet energy. Here β denotes the drag coefficient for tube flows, which is 1 for turbulent flows and 2 for laminar flow. The critical Reynolds number in this configuration is about 2000.

6.2.1. Special Features of Experimental Conditions

VE_20_open was a measurement condition with a jet setting of 20 Hz and completely deionized water (german "'voll entsalzt"' (VE)). This experiment was repeated with different jet settings, namely 30 Hz and 40 Hz.

Tag	Date	Type	Jet [Hz]	Q [ml/min]	T [°C]	Description
VE_20_closed	12.06.2014	closed	20	1000	23.9	deionized water
VE_20_open	12.06.2014	open	20	1000	23.9	deionized water
VE_30_closed	13.06.2014	closed	30	1000	23.9	deionized water
VE_30_open	13.06.2014	open	30	1000	23.9	deionized water
VE_40_closed	14.06.2014	closed	40	1000	23.9	deionized water
VE_40_open	14.06.2014	open	40	1000	23.9	deionized water
SALT_20_closed	24.06.2014	closed	20	1000	23.9	salt water (1.75%)
SALT_20_open	24.06.2014	open	20	1000	23.9	salt water (1.75%)
SALT_30_closed	25.06.2014	closed	30	1000	23.9	salt water (1.75%)
SALT_30_open	25.06.2014	open	30	1000	23.9	salt water (1.75%)
VE_30_pulsed_closed	27.06.2014	closed	30	1000	23.9	deionized water
VE_30_pulsed_open	27.06.2014	open	30	1000/0	23.9	deionized water, pulsed, 10s cycle
TRITON43_30_closed	28.06.2014	closed	30	1000	23.9	4.3 mg TritonX
TRITON43_40_open	28.06.2014	open	40	1000	23.9	4.3 mg TritonX
TRITON216_30_closed	28.06.2014	closed	30	1000	23.9	21.6 mg TritonX
TRITON216_40_open	28.06.2014	open	40	1000	23.9	21.6 mg TritonX
BUTANOL_30_closed	02.07.2014	closed	30	1000	23.9	3 ml Butanol
BUTANOL_30_open	02.07.2014	open	30	1000	23.9	3 ml Butanol
GLYCEROL_20_closed	03.07.2014	closed	20-30	1000	23.9	20.5% Glycerol
GLYCEROL_20_open	03.07.2014	open	20	1000	23.9	20.5% Glycerol

Table 6.4.: Summary of experimental conditions.

VE_30_open Same as above, but with jet setting of 30 Hz.

VE_40_open Same as above, but with jet setting of 30 Hz.

At time 00:20 the hoses of the peristaltic pump were readjusted, because the delivery rate of the pump dropped. About time 04:00, ambient air leaked into the bubble generator, leading to an injection of atmospheric gases into the water. This problem occurred at the measurement with a high jet frequncey, because the water jet produces a larger underpressure in the chamber around the jet at high water flow rates.

VE_30_pulsed_open was conducted to compare the transfer rates of a constant bubble distribution and a periodically changing distribution. This test if interstitial water between the bubbles in the cloud behaves any different than bulk water as Woolf et al. [72] hinted at. The bubble cloud was generated in a 10 s cycle, whereby 5 s Argon was provided to the jet chamber and 5 s the chamber was closed (see section 6.1.3). The jet was running non-stop.

About time 04:20 ambient air leaked into the bubble generator, leading to an injection of atmospheric gases into the water. This problem occurred at the pulsed measurement, because the water jet produces underpressure in the chamber around the jet while the gas supply is closed. During normal measurements this underpressure is constantly balanced by the Argon supply. The reason that this effect appeared after 4 hours measuring could be that the leak was closed in the beginning and opened up due to the constant load of the pressure difference. To counter this effect it was tried to adjust the gas flow rate out of the tank at time 06:38 to 400 ml/min, at 08:01 to 250 ml/min and to 0 ml/min for one minute at time 08:34. In addition the hoses of the peristaltic pump were readjusted at time 05:38. Both countermeasures were not successful.

SALT_20_open was an experiment simulating sea water with a jet setting of 20 Hz. 2.275 kg NaCl were added to the water to get a salt concentration of 1.75 %. This corresponds to half of the mean ocean salt concentration. According to Broecker [9, pg. 85] using full concentration does not increase the transfer velocities significantly.

SALT_30_open Jet setting 30 Hz. This experiment was conducted to improve comparability to the standard conditions, though it was doubtful if the bubble distributions can be measured reliably.

The problem was that the bubble density was that high that the bubble measurement technique was limited.

At times 00:09, 00:13, 00:58 and 04:44 the hoses of the peristaltic pump were readjusted, because the delivery rate of the pump dropped.

TRITON43_40_open was used to study the effects of surfactants on bubble mediated gas transfer. 4.3 mg of Triton X-100 were added to clean deionized water. The same concentrations were chosen as in laboratory experiments conducted by Krall [41] in the big circular wind wave facility "Aeolotron" in the same laboratory to allow for easy comparison of transfer velocities. Description of the soluble, non-ionic surfactant Triton X-100 can be found in the appendix B. A jet frequency of 40 Hz was used to maximize the residence time of the bubbles. This maximizes the effect of the surfactant, which is adsorbed on the bubbles surfaces over time. A soluble surfactant was chosen, since non-soluble films are removed from the water bulk very effectively by bubbles [62].

TRITON216_40_open was the second experiment with surfactants. Here a total of 21.6 mg of Triton X-100 were added to the water.

BUTANOL_30_open should test the influence of surface tension on bubble generation. To reduce the surface tension by 50 % about 61 of n-Butanol are necessary. As it turned out far less Butanol was necessary to yield a significant change in the bubble distribution. The amounts used eliminated an effect based on surface tension. Finally 3 ml of Butanol were used to measure gas exchange with one more altered bubble distribution. At this concentration influence on surface tension was not measurable.

GLYCEROL_20_open used a 20.5%-glycerol water mixture to increase the viscosity by a factor of two. This simulates low temperature effects, which could not be set in the used setup. The viscosity corresponds to a temperature below zero degree Celsius, so that this experiment is of academic nature.

To get an impression of how different the bubble distributions looked like, a set of sample images is shown in figure 6.1.

VE_20_open

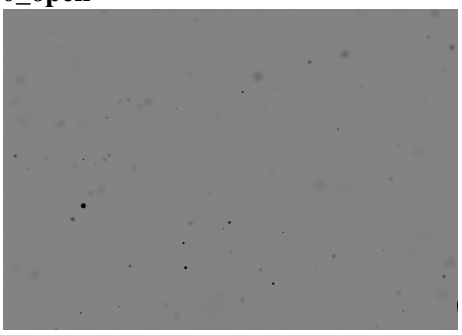

VE_30_open

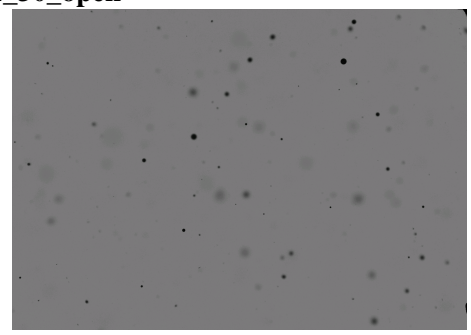

VE_40_open

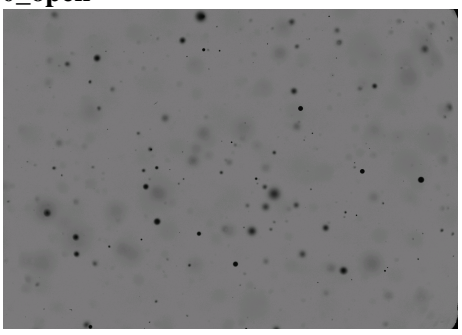

SALT_20_open

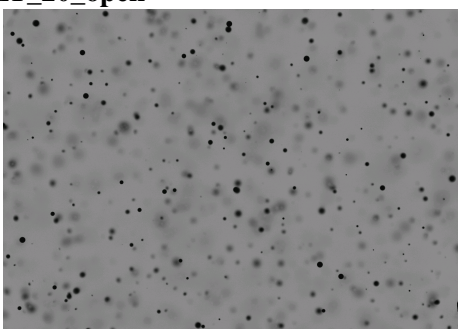

SALT_30_open

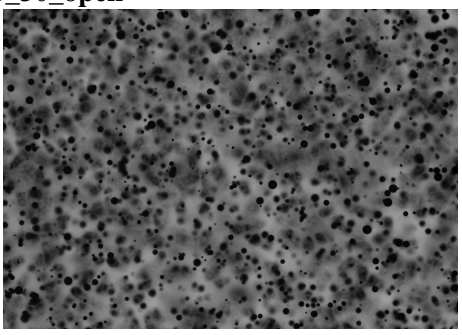

VE_30_pulsed_open

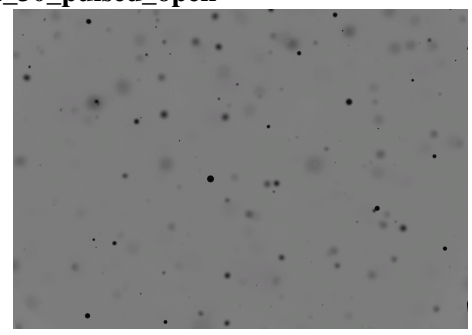

TRITON43_40_open

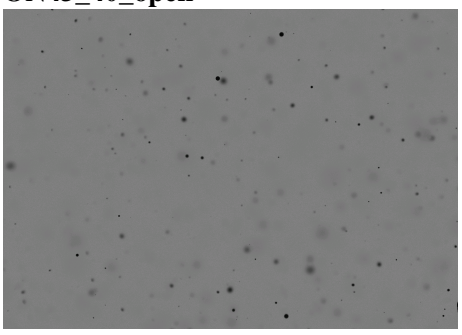

TRITON216_40_open

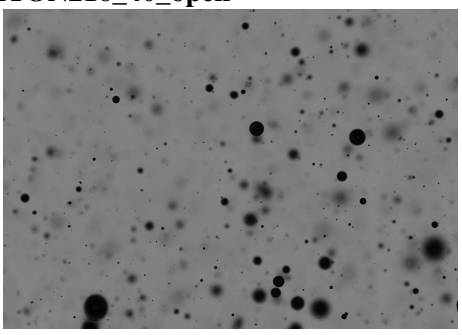

BUTANOL_30_open

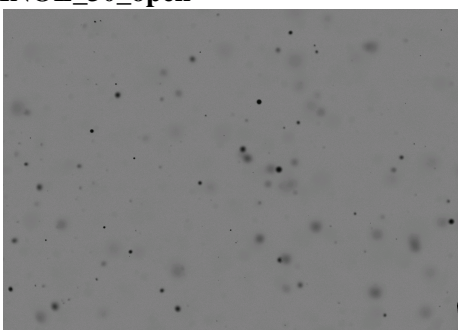

GLYCEROL_20_open

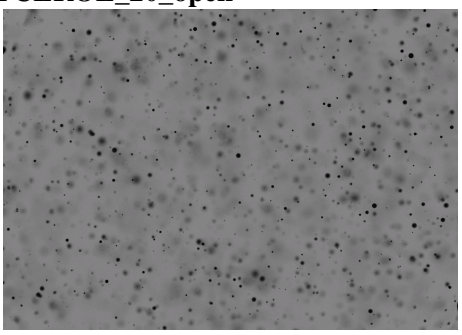

Figure 6.1.: Sample images of bubble measurement at lower left bulk position. Images are taken from *basler acA2000* camera and are normalized.

7. Data Processing

This chapter describes the processing and the first evaluation steps of the acquired bubble data. This processing produces position resolved bubble size distributions and velocity distributions from the acquired image data. The algorithm used for calculating the bubble size distributions was basically developed in the author's diploma thesis [53] and is based on [29]. Here the essential parts are described - for more detailed explanation, please refer to [53]. Afterward the algorithm for calculating the velocity distributions is described.

In fig. 7.1 an overview of the algorithm is shown in a flowchart. It is split in three major parts - the pre-processing, processing and the post-processing. The pre-processing improves image quality and normalizes the data. The processing detects and extracts the bubble features and the post-processing uses the extracted bubble features to calculate statistical values, such as the bubble density distribution. Pre-processing and processing are described in this chapter, post-processing is described in the next chapter 8.2 Evaluation.

7.1. Image Normalization

In this processing step all images are normalized to values ideally ranging from 0.0 (background) to 1.0 (object). Therefore a 2-point calibration with a dark image g_Z and an illuminated images without bubbles, called zero image g_Z, is performed. The dark image is recorded with no illumination to compensate for the fixed pattern noise of the camera. The dark images were calculated as the average of 100 single images to reduce the statistical error. The zero image was calculated from the measurements itself, since the manual translation stages could not be positioned in a reproducible way at the needed accuracy, so that the zero images g_Z had to be calculated for each position independently. This was done by using the measurement sequences itself. For one position the maximum for each pixel over all sequences was determined. For each pixel the mean values over all sequences were calculated, whereby only values greater than 70% of the maximum were accounted for. Thus the zero image for each position is given by:

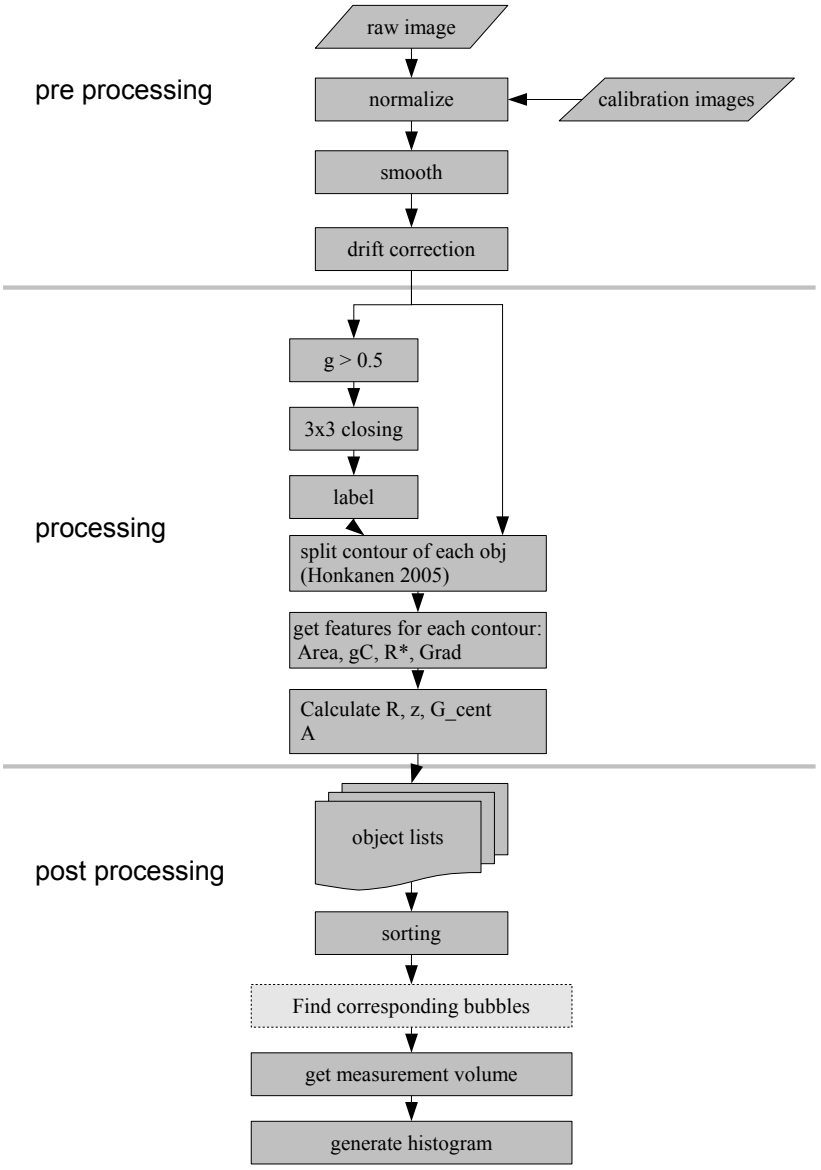

Figure 7.1.: Flowchart of the bubble detection in the image data. It consists out of three major parts: the pre-processing, the processing and the post-processing.

$$g_D(x,y) = \frac{1}{|M(x,y)|} \sum_{i \in M(x,y)} g(x,y,t_i) \tag{7.1}$$

$$M(x,y) = \left\{ i \in \mathbb{N} \,|\, g(x,y,t_i) > 0.7 \max_j (g(x,y,t_j)) \right\} \tag{7.2}$$

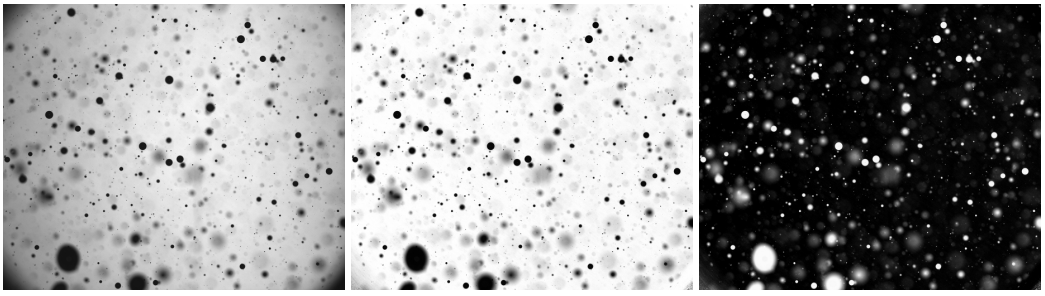

Figure 7.2.: Normalization of raw images: *left*: raw image from camera - *center*: normalized image, the dark image was subtracted and the result was divided by the zero image - *right*: inverted normalized image

The normalized image $n^*(x, y)$ then results from the raw image $g(x, y)$ by:

$$n^*(x, y) = \frac{g(x, y) - g_D(x, y)}{g_Z(x, y) - g_D(x, y)}. \tag{7.3}$$

To remove high frequency noise a binomial filter with width 8 is applied. The result of this step is shown in fig. 7.2 (center).

Due to high particle densities, it is common that the average gray value level of the background increases and the level of the objects decreases for the normalized images[1]. To compensate for that, a simple gray value scaling, here called drift correction, is applied. The histogram peak of the background has a value of 0.0 and the maximum value of the image is at 1.0 . This is realized by a simple linear rescaling of the gray values:

$$n(x, y) = 1 - \frac{n^*(x, y) - \min(n^*(x, y))}{\mu_n - \min(n^*(x, y))}. \tag{7.4}$$

Here the mean value of the background μ_n is calculated as the center of gravity of the histogram peak of the image. The center of gravity calculation was restricted to bins, whose count was higher than $2/3$ of the maximum count.

7.2. Bubble Detection

The next steps of the processing in fig. 7.1 are described in this section. Mischler and Jähne [54] discuss three different approaches of evaluating these kind of bubble images. Two algorithms require the bubbles to be large enough to produce a core shadow in the image, i.e. that the intensity

[1] for raw images the opposite is true, because of the first minus in eq. 7.4.

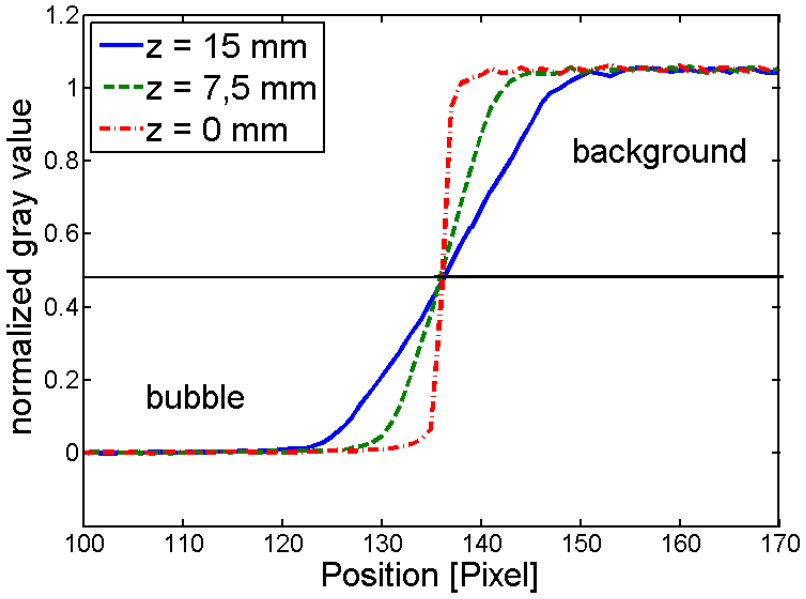

Figure 7.3.: Illustration of the gray values produced by edges in different distances z to the optics. The gradient decreases with increasing distance from focal plane. There is a gray value for which the position of the edge does not move (intersection of the curves).

drops ideally to zero in the center of the image of the bubble. The difference between those two algorithms is the method of determining the radius and the distance from the focal plane. The first uses integral measures like the total area of the bubble and its mean gray value, whereas the second one uses circular fits on the contour of the bubbles. This enables the use of a method introduced by Honkanen et al. [29] to detect overlapping bubbles by splitting the contour on points of high curvature.

The last algorithm tries to detect the bubbles even if they are further out of focus. This method introduces a larger error, but is able to detect smaller bubbles. Since two cameras with two different resolution ranges are used, this features gives no advantage for these measurements. And because high bubble densities are expected, the feature of splitting overlapping bubbles is preferred over the slightly more robust detection of the first algorithm. In the following this algorithm is described shortly, for in detail description and explanation of the other algorithms, see [53, 54].

Segmentation at Half Maximum is the first step. This is motivated by the telecentricity of the imaging system, see section 3.2. To understand the nature of the imaging, it is modeled in the geometric approximation and the properties are discussed afterward. In this approximation the image $n_z(\vec{x})$ is given by a convolution of the object with the point spread function (PSF) $H_z(\vec{x})$

of the optical system:

$$n_z(\vec{x}) = O(\frac{\vec{x}}{2R}) * H_z(\vec{x}) \tag{7.5}$$

Here O denotes the object function, which is scaled by a arbitrary radius R. The PSF $H_z(\vec{x})$ models the optical system as a linear space invariant system. This function changes with depth z, what is responsible for defocus in the final image. Since a geometric approximation is used, this function can be determined by energy conservation to:

$$H_{z,\text{ geometric}}(|\vec{x}|) = \frac{1}{\pi(z\tan\alpha)^2}\,\mathrm{Circ}(\frac{|\vec{x}|}{2z\tan\alpha}) \tag{7.6}$$

with

$$\mathrm{Circ}(x) = \begin{cases} 1 & |x| < \frac{1}{2} \\ 0 & \text{else} \end{cases} \tag{7.7}$$

The effects of diffraction and aberrations of the optics are neglected in this discussion, since they are not needed for understanding the concept and have little effect on the final results in the processing [53].

With this formulation features can be derived, which enable a reliable determination of radius and depth of the bubbles. The step function Θ is introduced

$$\Theta(x) = \begin{cases} 1 & x > 0 \\ \frac{1}{2} & x = 0 \\ 0 & x < 0 \end{cases} \tag{7.8}$$

to verify this. With the assumption, that the radius of the bubble is much larger than the PSF, the image of an edge at x = 0 can be described in one dimension by a step function:

$$n(x) = \int_{-\infty}^{+\infty} \Theta(x')H_Z(x-x')dx' \quad . \tag{7.9}$$

The value at the edge itself (x = 0) will reduce to a fixed value - in case of normalized images to 0.5:

$$n(0) = \int_{-\infty}^{+\infty} \Theta(x') H_Z(-x') dx' = \int_{0}^{+\infty} H_Z(-x') dx' = 0.5 \quad . \tag{7.10}$$

This means, that gray values of 0.5 denote positions of edges in the image, regardless of the distance z from the image plane. Therefore no intrinsic error is introduced to the radius determination of the bubbles. In fig. 7.3, this is shown for three different depths on real data. This property is used to detect the borders in the image, which will be used for further processing.

To extract these borders from the image, a global threshold is applied to the normalized image. This threshold was chosen to be 0.48, i.e. slightly lower than calculated, because the maximum intensity tended to be below 1. This threshold was found to be the best fitting value for the edge position not to move, see fig. 7.3. Having applied the threshold, the resulting binary image was filtered with a morphological closing [32] and was labeled afterward. That means that each connected structure in the image was assigned a number. To decide whether pixels are connected or not, the 8-neighborhood has been used. For each labeled object the contour was extracted by the built-in function *ObjContour* of *Herisko*®. These contours were used as input for the next step - the overlapping bubble detection.

Intensity at the Object Center was used as the threshold parameter for the depth. The reason for this choice can be explained by eq. (7.5). Evaluation of this equation in the object center distinguishes two cases:

$$n(0) = \int_A \mathrm{Circ}(\frac{\vec{x}'}{2r_{Obj}}) H_Z(-\vec{x}') d\vec{x}' = 2\pi \int_0^{r_{Obj}} r H_Z(r) dr \begin{cases} = 1 & r_{\mathrm{Obj}} > r_{\mathrm{PSF}} \\ < 1 & r_{\mathrm{Obj}} < r_{\mathrm{PSF}} \end{cases} \tag{7.11}$$

Here $x = 0$ denotes the center of the object. For bubbles, which are larger than the PSF, the central value should reach the maximum. In the other cases the value will be lower. Due to defocus the size of the PSF is depth dependent. Therefore the maximal depth, for which the central value reaches the maximum, is radius dependent. This can be seen, e.g. on the calibration curves in section 5.1.2. In this thesis a threshold value for the central intensity of 0.92 was chosen.

7.3. Splitting of Overlapping Bubbles

This approach is based on the method used by Honkanen et al. [29] and was implemented in Mischler [53]. The idea of this algorithm is to seperate overlapping bubbles. Since the image of a single bubble is a convex object, its outline has a positive curvature on all locations. Two overlapping bubbles produce a point with negative curvature, when their contours cross (as long as the centers are not too close). This can for example be seen in fig. 7.4.

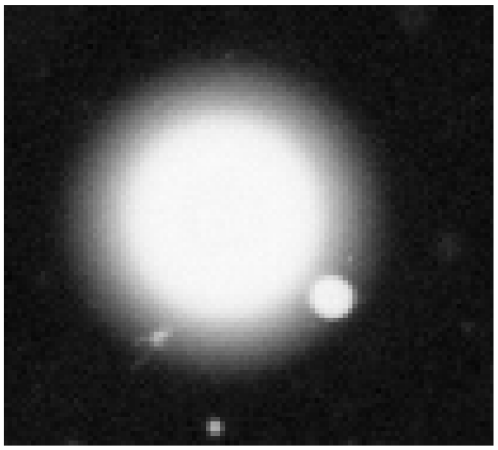

Figure 7.4.: Image of two overlapping bubbles. Taken from Mischler [53]

To detect the points of negative curvature, the contour is smoothed with the help of Fourier Descriptors (FD). It is derived to find local extrema with negative second derivative, i.e. curvature. An overview of these steps is given in fig. 7.6.

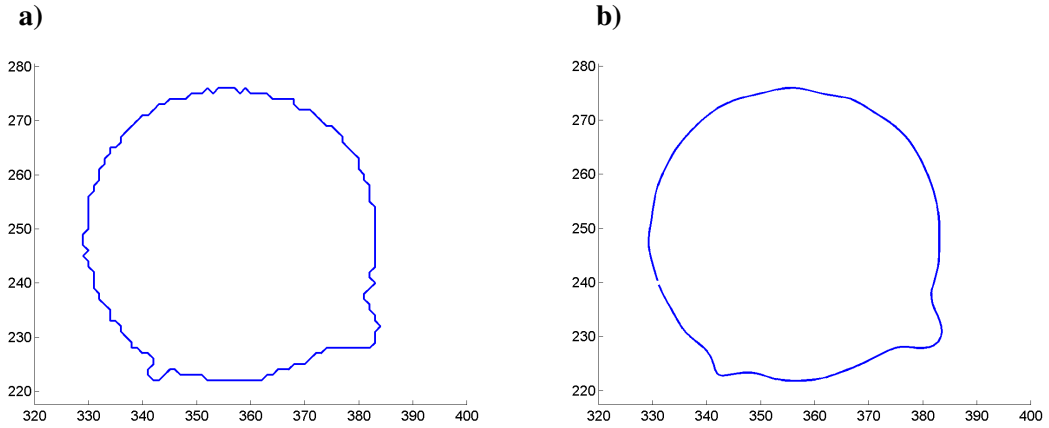

Figure 7.5.: Smoothening by Fourier Descriptors: **a)** Contour of an object. Due to the discrete nature of pixels, this contour is discontinuous. **b)** Smoothed contour by setting higher order FDs to zero. Taken from Mischler [53]

To calculate the FD $\hat{k}_r$ of a two dimensional curve k_s with S points, the two dimensional coor-

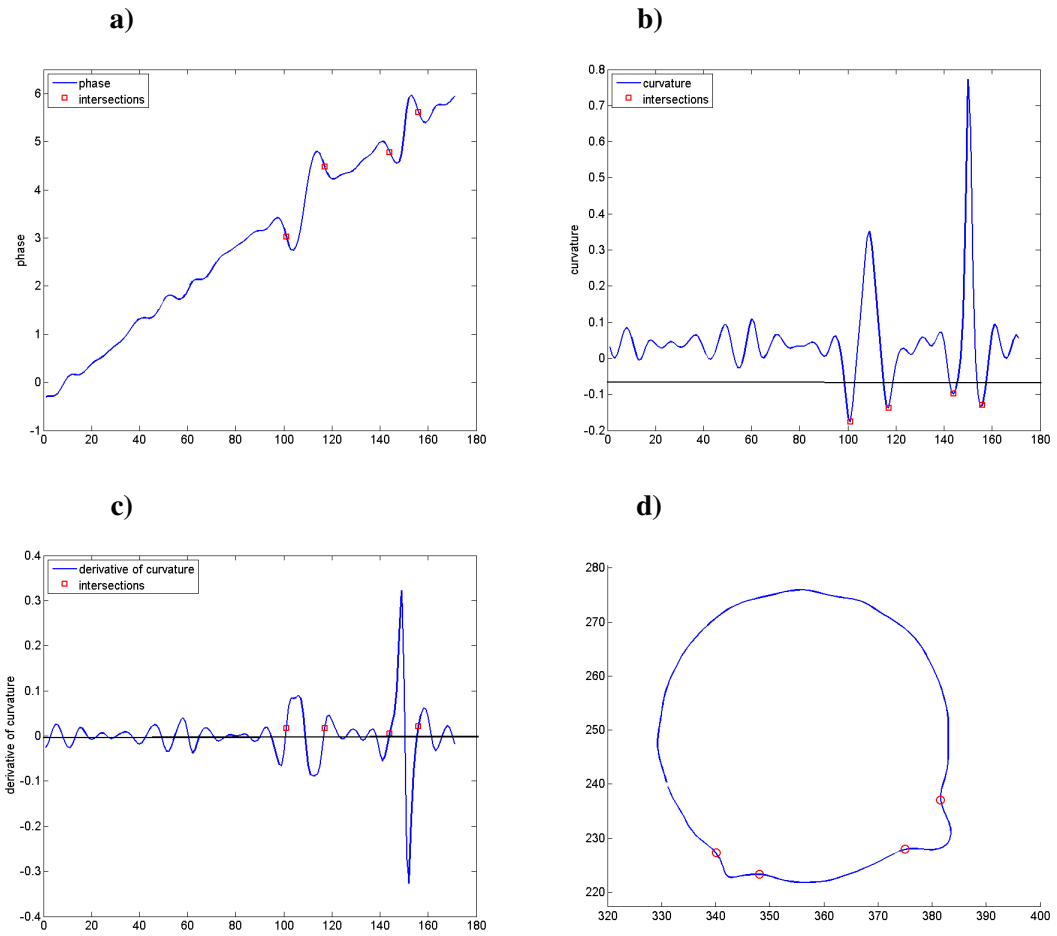

Figure 7.6.: Detection of points of negative curvature: **a)** Angle of the tangent to the smoothed contour. **b)** Calculated curvature of the contour. The line shows the threshold value κ_c for selecting a relevant point **c)** Derivative of the curvature to detect local extrema by detecting the zero crossings. **d)** Result from the detection algorithm. Taken from Mischler [53]

dinates are seen as points in the complex plane. Then the FDs of the curve are given by:

$$\hat{k}_r = \frac{1}{S}\sum_{s=0}^{S-1} k_s \, e^{-\frac{2\pi r s}{S} i}, \tag{7.12}$$

with i being the imaginary unit and k being an index running from 0 to $S-1$. To smooth the curve, higher order FDs are set to zero, since they represent high frequencies or variations in the positions. Honkanen et al. [29] report the following term to determine the cutting FD k_c, which is the largest FD to use:

$$k_c = \frac{1.6S}{\sqrt{S+30}} \tag{7.13}$$

In fig. 7.5 the effect of smoothing the outline by this method is shown on the example of the contour of the bubble in image 7.4.

To get the curvature, the angle of a tangent to the smoothed curve is calculated by:

$$\phi_t = \arg \frac{\partial k_s}{\partial s}\Big|_t = \arg \widehat{irk_r}\Big|_t$$

.

The multiplication with ir in the Fourier space corresponds to the derivation in normal space. Then the curvature κ_s at position s is given by:

$$\kappa_s = \frac{d\phi_{s'}}{ds'}\Big|_s = \frac{d\phi_t}{dt}\frac{dt}{ds}\Big|_s = \frac{d\phi_t}{dt}\frac{1}{|\frac{dk_t}{dt}|}\Big|_s$$

To each segment a circular fit is performed. The results for the individual center points are compared to cluster segments, which belong to the same bubble. As a criteria the ratio ϵ_K of the differences in radius Δr and center point position Δx is used:

$$\epsilon_K = \frac{\Delta x}{\Delta r} \tag{7.14}$$

A value of $\epsilon_K = 0.3$ was found to be most suitable. The circle fitting was realized by a direct algebraic least square calculation [53].

7.4. Algorithm for Velocity Distributions

The algorithm for calculating the bubble velocities is identical to the algorithm described before, except one additional step - finding bubble correspondences in subsequent images. So the description is limited to this additional step. Goal of this procedure is to identify bubbles found in the first image in the second image. A metric in the $\vec{x} = (x, y, r)$-space is defined, which considers

the spatial distance and the radius of the bubbles:

$$d(\vec{x}_A, \vec{x}_B) = \sqrt{(x_A - x_B)^2 + (y_A - y_B)^2 + 3\,(r_A - r_B)^2} \tag{7.15}$$

The coefficient at the radius term leads to a stronger weight for the difference in the radius dimension. To get the mapping between the bubbles of two subsequent images, the distance matrix of the bubbles of both images is calculated. This matrix is scanned row by row and for each row the entry with the lowest value is selected as the corresponding bubble. Bubbles , which have already been selected, are excluded from further mapping. A threshold of 1200 px is chosen as a maximum allowed distance between bubbles. If only values larger are detected for an object, it is considered unmatched. This can happen if the bubble left the image or was occluded.

This approach is not optimal, but has a low computational cost. For comparison reasons an algorithm for minimizing the total distance for one image pair was tested. This algorithm has a reasonable computing time for small images and few bubbles (~ 250), but was not usable for bubble counts in actual measurement conditions. The advantage was not significant and could be balanced by statistics in the velocity evaluation step.

8. Evaluation

In the first part of this chapter the evaluation of the gas concentration data is described. In the second part further evaluation of the previously obtained bubble size and velocity data is explained. In the last part of this chapter the data of both measurements is merged into different models.

8.1. Gas Exchange Evaluation

The first goal is to get the transfer velocities for different tracers out of the experimental concentration data. Therefore a model is needed.

For the closed invasion measurements eq. (2.12) was used to calculate the transfer velocities from the determined characteristic exchange times τ_{exp} for the different tracers. For these experiments a fit of an ordinary exponential function with offset suffices to determine τ_{exp} from the concentration time series. This can be seen by comparison to the solution for the concentrations given in eq. (2.11).

For the open evasion measurements eq. (2.14) was used to calculate the transfer velocities from the determined characteristic exchange times τ_{exp} for the different tracers. In this case there are two characteristic times $\tau_{1,2}$ in the solution for the air side of the concentration $c_a(t)$, but only one - τ_2 - in the solution for the water sided concentration $c_w(t)$. Since only the water sided concentration was measured in this case, a fit of an ordinary exponential function with offset is sufficient in this case, too. Compare to the solution given in eq. (2.13).

The fit is performed as a standard least squares minimization of the relative deviations of model and measurement:

$$\min_{\vec{p}} \sum_{i=0}^{i_{\max}} \left\| \frac{f(t_i, \vec{p}) - c_i}{c_i} \right\| \tag{8.1}$$

$$\vec{p} = (p_0, p_1, p_2) \tag{8.2}$$

$$f(t, \vec{p}) = p_0 + p_1 \exp\left(-\frac{t}{p_2}\right) \tag{8.3}$$

The relative error was chosen because the data covers several orders of magnitude. Taking absolute values would ignore measured data points for low concentrations. The fit was done by the built in function *lsqnonlin* of *Matlab*®.

To get a reliable fit, it is necessary to assure that the model can be applied to the experiment. Pressure and temperature were checked to be in the range previously defined in section 5.2.2 to assure measurement accuracy. Whenever problems occurred, the data was excluded from the fits.

As discussed in section 5.2.2 it is necessary to exclude the data, while the system is adapting to the gas stream. So after each switch of the probe inlet a time period of $5 \times \tau_{\text{MIMS}}$ was excluded for the respecting tracer. That includes particularly the beginning of the evasion measurements.

To calculate the transfer velocity eq. (2.12) resp. eq. (2.14) were applied.

8.2. Bubble Spectra Evaluation

In this section the post processing of the bubble and velocity data is described, which yield radius resolved radius, area and volume densities as well as the velocity distributions at each sampled position. Therefore the model described in section 2.3 is converted to a discrete formulation to be able to use it with the measured data.

8.2.1. Discretization of Coordinates and Distributions

Since the size and velocity distributions can only be measured at discrete positions, the model described in section 2.3 has to be adapted to discrete measurements. The important terms are eq.

(2.52) and eq. (2.53), which need to be reformulated. The coordinates and notations are shown in fig. 8.1. The form of the equations is matched to the sampling positions $(x_i, y_j) = x_{i,j}$ chosen in the experiment, which is described in section 6.1.3. The vertical sampling distance $\Delta x_k = \Delta x$ was constant, whereas the horizontal position Δy_k was unequally spaced. Δz denotes the thickness of the water tank.

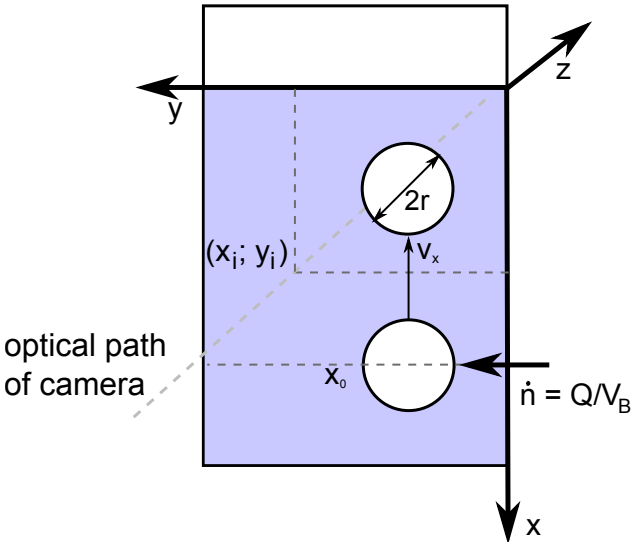

Figure 8.1.: Model for gas exchane in the bubble tank.

To calculate the bubble density spectra, the bubble data from the previous processing step is analyzed. Therefore the bubble data is binned in radius intervals I_k. Because smaller bubbles usually occur more frequent than big bubbles, these intervals are chosen to be larger for bigger radii to ensure a minimum count in each bin to yield good statistics. The radius bin boundaries for a mean radius r_k are defined as following:

$$r_k = r_0 A^{k+0.5}$$

$$r_{k,min} = r_0 A^k \qquad r_{k,max} = r_0 A^{k+1}$$

with the radius boundaries of each bin $r_{k,min}$ and $r_{k,max}$. The bin interval grows by a factor of A each bin b:

$$I_k = [r_{k,min}; r_{k,max})$$

$$|I_k| = r_0(A-1)A^k$$

r_0 and A are chosen in accordance to the following constraints: The minimum and maximum radius are chosen to be $r_{\text{min}} = 3\,px$ and $r_{\text{max}} = 250\,px$ for both cameras. The number of bins for the velocimetry camera was set to 20, whereas the high resolution camera the number of bins was set to 10 because this camera usually imaged fewer bubbles.

Simple histograms of the radii were not used, since this would underestimate the bubble count for smaller particles, which can be occluded by bigger bubbles. This can be corrected by sorting all detected particles in a single image descendant by size and introducing effective measurement areas $A_{\text{eff},i}$:

$$A_{\text{eff},i} = A - \sum_{i<j} A_j, \tag{8.4}$$

The measurement area for bubble i $A_{\text{eff},i}$ is the total image area minus the sum of the segmented areas A_j that are covered with bigger bubbles. If all areas had the same size, the particle area density would be n/A, where n is the number of detected objects in the desired radius interval. With varying measurement areas, all effective measurement areas $A_{\text{eff},i}$ of objects within this radius interval are added inversely, to get the density Ψ_{in}:

$$\Psi_{\text{in}} = \frac{1}{A_{\text{1,eff}}} + \frac{1}{A_{\text{2,eff}}} + ... + \frac{1}{A_{\text{n,eff}}} \approx \frac{n}{A} \quad \text{, for small bubbles} \tag{8.5}$$

This number is the area density. All effective measurement areas of bubbles in a radius interval at one position were summed up. To yield a volume density the result is divided by the effective measurement depth for that radius range and is normalized to the number of images and the width of the radius interval I_k. The maximal depth $z_{\max}$ was determined by calibration, see section 5.1.2. The calculated bubble size densities for both cameras are combined by taking the values of the high resolution camera for radii smaller than $200\,\mu\text{m}$ and taking the values basing on data of the velocimetry data for larger radii. From the total bubble densities Ψ_{in}, which are measured, the local source bubble densities Ψ, which are needed for the gas exchange calculations, are estimated:

$$\Psi(x_i, y_j, r_k) = \Psi_{\text{in}}(x_i, y_j, r_k) - \sum_{l>i} \Psi_{\text{in}}(x_l, y_j, r_k) \tag{8.6}$$

This calculation assumes that all bubbles below a position x_i rise vertically and add to the distribution above. The local source bubble densities give the number of bubbles, which start to exchange gas at this position.

The radius distributions $\Psi_{\text{in}}(x_i, y_j, r_k)$ imply the area and volume distribution $\Psi_{A,in}$ and $\Psi_{V,in}$ over the radii:

$$\Psi_{A,\text{in}}(x_i, y_j, r_k) = 4\pi r_k^2 \Psi_{\text{in}}(x_i, y_j, r_k) \tag{8.7}$$

$$\Psi_{V,\text{in}}(x_i, y_j, r_k) = \frac{4}{3}\pi r_k^3 \Psi_{\text{in}}(x_i, y_j, r_k) \tag{8.8}$$

The residence times of the bubbles were calculated through the measured velocity distributions. To get the velocity distribution a histogram for each position and radius interval I_k was calculated with the velocity data associated to each bubble. The mean value of this distribution is used as the velocity for the radius r_k. To calculate the local residence times $\tau_{\text{res}}(x_i, y_j, r_k)$ for a certain position and radius the following equation was used:

$$\tau_{\text{res}}(x_i, y_j, r_k) = \frac{\Delta s}{v(x_i, y_j, r_k)} \tag{8.9}$$

with $v(x_i, y_j, r_k)$ being the measured total planar velocity at position (x_i, y_j) for the radius r_k. For the travel distance Δs the average distance of the sampled positions (x_i, y_j) was assumed. Since the total residence times $\tau_{\text{res,in}}(x_i, y_j, r_k)$ are needed to calculate the amount of transferred gas for each bubble, the local residence times are integrated resp. summed up. For each position (x_i, y_j) the times of all positions above that position are added:

$$\tau_{\text{res,in}}(x_i, y_j, r) = \sum_{l \leq i} \tau_{\text{res}}(x_l, y_j, r) \tag{8.10}$$

This approach assumes that all bubbles rise vertically and pass each sampling position just once. This may not be the case for looping traces of bubbles, which can occur in presence of strong currents as produced by the jet [56]. This leads to an underestimation of the residence times and therefore an underestimation for the transfer velocities.

Values for the rise velocity, which could not be determined, are calculated by linear interpolation in the radius domain. For values outside of the measured radius range, the last measured radius is chosen. A second linear interpolation step is done in the spatial domain for the residence times.

Discretization of the Model

Here equations (2.52) and (2.53) are recalled:

$$Q_{\text{tot}} = \int_{V_0} \int_{0}^{r_{\text{max}}} \frac{\Psi(x_0, r) V_b(r)}{\tau_{\text{res}}(x_0, r)} dr dV_0$$

$$\lambda_{\text{tot}} = \frac{1}{Q_{\text{tot}}} \int_{V_0} \int_{0}^{r_{\text{max}}} \frac{\Psi(x_0, r) V_b(r)}{\tau_{\text{res}}(x_0, r)} \lambda(x_0, r) dr dV_0$$

The integrals are converted to discrete sums with the sampling coordinates $x_{i,j}$:

$$x_{i,j} = (x_i, y_j) = (i\Delta x, \sum_{k<j} \Delta y_k) \tag{8.11}$$

$$\Delta V_{i.j} = \Delta x \frac{\Delta y_j + \Delta y_{j+1}}{2} \Delta z \tag{8.12}$$

with $\Delta V_{i.0} = \Delta y_0 + \frac{1}{2}\Delta y_1$ and $\Delta V_{i.j_{\text{max}}} = \Delta y_{\text{max}} + \frac{1}{2}\Delta y_{\text{max}-1}$.

$$\Psi(x_{i,j}, r) = \Psi(\vec{x}_{i,j}, r) dV = \Psi(\vec{x}, r) \delta(x - x_{i,j}) \Delta V_{i,j} dV \tag{8.13}$$

$$Q_{\text{tot}} = \sum_{i=0,j=0}^{i_{\text{max}}, j_{\text{max}}} \sum_{k=0}^{k_{\text{max}}} \frac{\Psi(x_{i,j}, r_k) V_b(r_k)}{\tau_{\text{res,i}}(x_{i,j}, r_k)} \Delta r_k \Delta V_{i,j} \tag{8.14}$$

$$\lambda_{\text{tot}} = \frac{1}{Q_{\text{tot}}} \sum_{i=0,j=0}^{i_{\text{max}}, j_{\text{max}}} \sum_{k=0}^{k_{\text{max}}} \frac{\Psi(x_{i,j}, r_k) V_b(r_k)}{\tau_{\text{res,i}}(x_{i,j}, r_k)} \lambda(x_{i,j}, r_k) \Delta r_k \Delta V_{i,j} \tag{8.15}$$

In this form it is possible to use the measured bubble size and velocity data in the model established in section 2.3. These expressions are evaluated with the data taken at the experiments and used in the equations (2.70) and (2.71) for the transfer velocities for comparison with the measured transfer velocities.

9. Results and Discussion

In the first part of this section the results of the calculations of the transfer velocities based on the bubble measurements are discussed. Here, the experimental transfer rates are anticipated to discuss the results of the calculations. In the second part the gas exchange measurements are presented and discussed. This chapter closes with a comparison of the results with existing models and a proposal of a parametrization basing on the modeling given in section 2.3.

9.1. Calculated Transfer Velocities

Measurements of the bubble size, area and volume distributions were conducted at 11 different depths and 6 horizontal positions (see section 6.1). Here, three exemplary positions are presented for detailed discussion. These three positions are horizontally in the middle ($x \approx 300\,\mathrm{mm}$) at the bottom ($y = 1100\,\mathrm{mm}$), middle ($y = 700\,\mathrm{mm}$) and top ($y = 200\,\mathrm{mm}$) of the tank. The bottom position represents the *bulk* distribution, the middle one represents a *developed jet* distribution and the top position represents a *rising* distribution.

Data from the deionized water experiments are discussed in full and interesting effects are presented for the other measurements. In appendix C.1 results for all conditions are shown.

Deionized Water In figures 9.1 and 9.2 the radius, area and volume densities for all jet energies are shown. At all conditions the same inward gas volume flux was used. Looking at the radius distribution the number density for all radii is arranged in the expected order. At the conditions with the highest energy deposit in the tank the most bubbles are generated. In table 6.3 the values for the jet energies for all conditions are given. The energies of the presented conditions differ roughly by a factor of 3 for adjacent conditions. For a higher jet energy, the number of large bubbles produced is higher in general, and also more of the large bubbles are taken to the bulk, i.e. deeper into the tank. Fig. 9.3 shows a spatial total volume distribution of the three conditions,

which show the different depth distribution of the bubbles. The peak around $1500\,\mu m$ for the high energy condition VE_40, with a kinetic jet energy of $9.1\,W$, represents the large bubbles, which are generated and entrained by the jet. For lower jet energies these bubbles are less likely to be produced and also the current generated by the jet is not capable of overcoming the buoyancy of the big bubbles. For small bubble radii below $\sim 100\,\mu m$ only the low energy condition shows a different behavior. The fact that the density distributions for high jet energies do not change with energy could hint on a maximum bubble concentration, at least for deionized water conditions. This can be attributed to an effect in the energy distribution in the break up process of bubbles. Another possibility is that the dependence of the number density on the input energy is so weak for high energies, that this effect could not be resolved. Looking at the area distribution for the *rising* and *bulk* position no dominant radius range can be identified. All radii contribute to the bubble surface area distribution in the same order of magnitude. For gas exchange in the limiting case of low soluble tracers this is an important value (see eq. (2.34)). This means, in this limiting case all bubbles have to be considered with respect to their area. At the *jet* position a dominant contribution of the large bubbles to the area distribution and therefore to the gas transfer can be identified. For low jet energies the largest bubbles contributing have a radius of $400\,\mu m$, whereas the maximum radius is about $5000\,\mu m$ for the higher jet energies. For the volume distribution a general emphasis of the larger bubbles ($> 500\,\mu m$) can be seen. This means that especially for high soluble gases the big bubbles are important at these conditions, compare to eq. (2.32). To which extent the areas resp. volumes in a certain radius range affect the gas exchange is addressed more detailed below, where λ, which considers the residence times, is discussed.

In fig. 9.4 the measured velocity distributions vs. r for three sampling positions are shown. The velocity component of the bubbles in the optical object plane is plotted. The velocity perpendicular to the plane could not be measured reliably (see depth resolution in Mischler and Jähne [54]). Due to the tank geometry, this component is symmetrically distributed around zero, so it will average to zero in the statistics. At the *bulk* position the rise velocity is almost independent of radius. This can be explained by the fact that the movement in this region is governed by the global current in the tank induced by the jet. This current is stronger for higher energy inputs, which describes the rising velocity among the conditions. Larger bubbles at this position are arriving at their initial depth and therefore just start accelerating to their terminal velocity. This explains the tendency to smaller velocities for larger bubbles.

The highest velocities occur for big bubbles at the *rising* position, since these bubbles have reached their terminal velocity. This terminal velocity has a value in the range of $300\,mm/s$ to $400\,mm/s$ for bubbles with a radius larger than $\sim 700\,\mu m$. This agrees with measurements of Alves et al. [2]. The fact that the rise velocity drops after reaching a maximum for growing radii is explained by the onset of bubble surface deformations and oscillations, which increase the form drag of the bubble. This velocity is the same for all energy inputs as expected. For the *rising* position the small bubbles in the high jet energy condition seem to be faster than in the low jet

energy conditions, which could be explained by the larger number of big bubbles which create an uprising current. Small bubbles at the *developed jet* position have the same velocities in all conditions. Larger bubbles are faster for higher energy inputs, which can be attributed to the faster jet flow the bubbles are located in.

The integrated residence times $\tau_{\mathrm{res,i}}$ are calculated from the velocity distributions using eq. (8.10). Since these times describe the average time a bubble spends under water, the times will be generally higher for positions deeper below the water surface. This is reproduced by the values shown in fig. 9.4, which shows the residence times for all VE conditions at three positions. At all positions the residence times of small bubbles are higher for low energy inputs, since they have low rise velocities, which are increased by the global jet current for higher jet energies. Values for bubbles smaller than the resolution limit of the velocimetry camera are taken from the smallest measured radius. Residence times decrease with increasing radius in general, due to their increasing rise velocity.

In fig. 9.5 the bubble concentration equilibration parameter λ (eq. (8.15)) for two different solubilities α is shown at the sampling positions. The parameter is 0 for bubbles, which equilibrate completely with the surrounding water, and is 1 for bubbles, for which the gas concentration within the bubbles does not change while passing through the water. The process of equilibration depends on solubility – gases with high solubility equilibrate faster – , on the radius r, on the transfer velocity $k_b(r)$ of a single bubble of radius r and the residence time $\tau_{\mathrm{res,i}}$ of that bubble. Here, the dirty case model of Frössling [23] for the transfer velocity is shown, see eq. (2.26). Larger bubbles have a larger capacity for trace gases and therefore take longer to equilibrate. The calculated λ show a clear dependency on solubility. At the *bulk* position all bubbles come into full equilibrium for gases with the solubility $\alpha = 1$ and a radius smaller than $\sim 800\,\mu\mathrm{m}$. This can be attributed to long residence times. That means the gas exchange in this region mediated by small bubbles for a gas with high solubilities can be determined by the volume flux alone. A transient radius of $\sim 1000\,\mu\mathrm{m}$ can be defined for these tracers, for which the bubbles exchanged $50\,\%$ of their tracer content ($\lambda = 0.5$). For gases with lower solubilities, e.g. $\alpha = 0.01$, the transient radius of $\sim 50\,\mu\mathrm{m}$ can be found. Lowering the solubility corresponds to an increase in the tracer capacity of a bubble. Hence the bubbles need a longer time to come into equilibrium, which explains the shifted radius of transition. The residence times at the *rising* position are significantly lower, so that the bubbles exchange gas for a shorter period of time and therefore are less likely to reach equilibrium. Fig. 9.5 shows a radius of transition of $\sim 300\,\mu\mathrm{m}$ for the gases with the higher solubility $\alpha = 1$ and a radius of transition in the range of $2\,\mu\mathrm{m}$ to $20\,\mu\mathrm{m}$ for gases with lower solubilities like $\alpha = 0.01$. For all positions the radius of transition is lower for the high energetic case. This is explained by the significantly shorter residence times of the bubbles in this case, since all other parameters are shared by the calculation. The values at the *jet* position lie in between the preceding ones.

The transfer velocities are calculated using the equations given in section 8.2.1. For the deionized water condition these are shown in fig. 9.6. In these plots the measured transfer velocities of the evasion measurements (see next section 9.2) are also shown as data points. The transfer velocities are calculated for two different assumptions for the transfer velocity of single bubbles $k_b(r)$ - the clean case using Higbie's equation [13] and the dirty case after Frössling [23], see eq. (2.25) and eq. (2.26), respectively. The lower group of the curves represents the direct calculation of the transfer rates, whereas the upper group is rescaled to match the asymptote for high solubilities, compare to eq. (2.32). This asymptote is determined using a least square fit for the high soluble tracers used in each experiment, this will be discussed in section 9.2. It can be seen in fig. 9.6 that the direct calculations are at least by a factor of 5 below the actual measured values. It is expected that the calculated transfer rates are lower because it is likely that not all bubbles at all locations could be measured. For positions capturing the jet entry point the bubble densities are that high, that extended dark areas are imaged, in which it is not possible to detect any individual objects. The compensation by introducing effective measurement areas, see section 8.2, works only in cases the occluded areas are rare and not if these are the common case. Since in these areas the largest fraction of the volume flux is located, this leads to a massive underestimation in the bubble counts. The attempt to correct for that afterward by simple scaling fails as can be seen in fig. 9.6, since this approach assumes that the general shape of the measured bubble size distribution is correct, but only the absolute value is underestimated. This is obviously wrong because the size distribution measurements, which are performed at the jet positions, are only able to capture small bubbles, which appear in occasionally bright parts of the images. This means that large bubbles are likely to be missed and the number of small bubbles is underestimated. Recalling the discussion of the parameter λ in the section 2.3, adding more small bubbles to a given distribution, the transition between the low and high solubility case shifts to lower values for α, or adding larger bubbles the transition is shifted to higher solubilities. This means, to correct for the missing bubbles for the lowest energy case VE_20, the transition has to be shifted to higher solubilities, i.e. larger bubbles are missing to describe the measured data correctly. For both higher jet energy cases the situation is the other way round, here small bubbles are missing to shift the transition to lower solubilities. For the high jet energy cases VE_30 and VE_40 this is true for both calculations using the clean and the dirty case. In the low jet energy condition the scaled calculation using the dirty model describes the absolute values of the measured data more accurately. Though the shape of the calculated transition is not reproducing the measured data satisfactory. This can be explained by a erroneous ratio between small and big bubbles, which is likely to occur as described before.

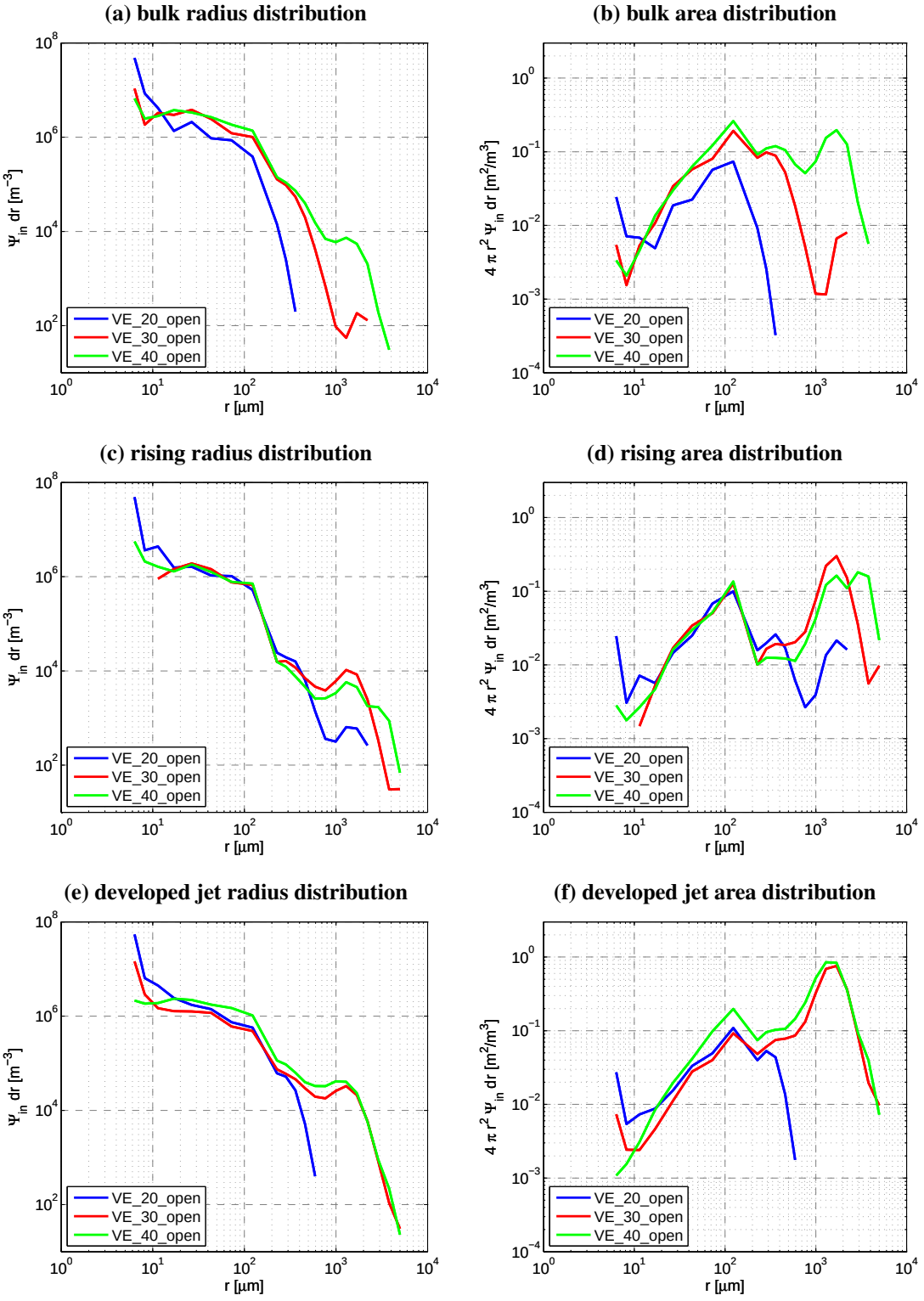

Figure 9.1.: Measured radius and area densities for all VE (deionized water) conditions are shown. Three representative sampling positions are shown.

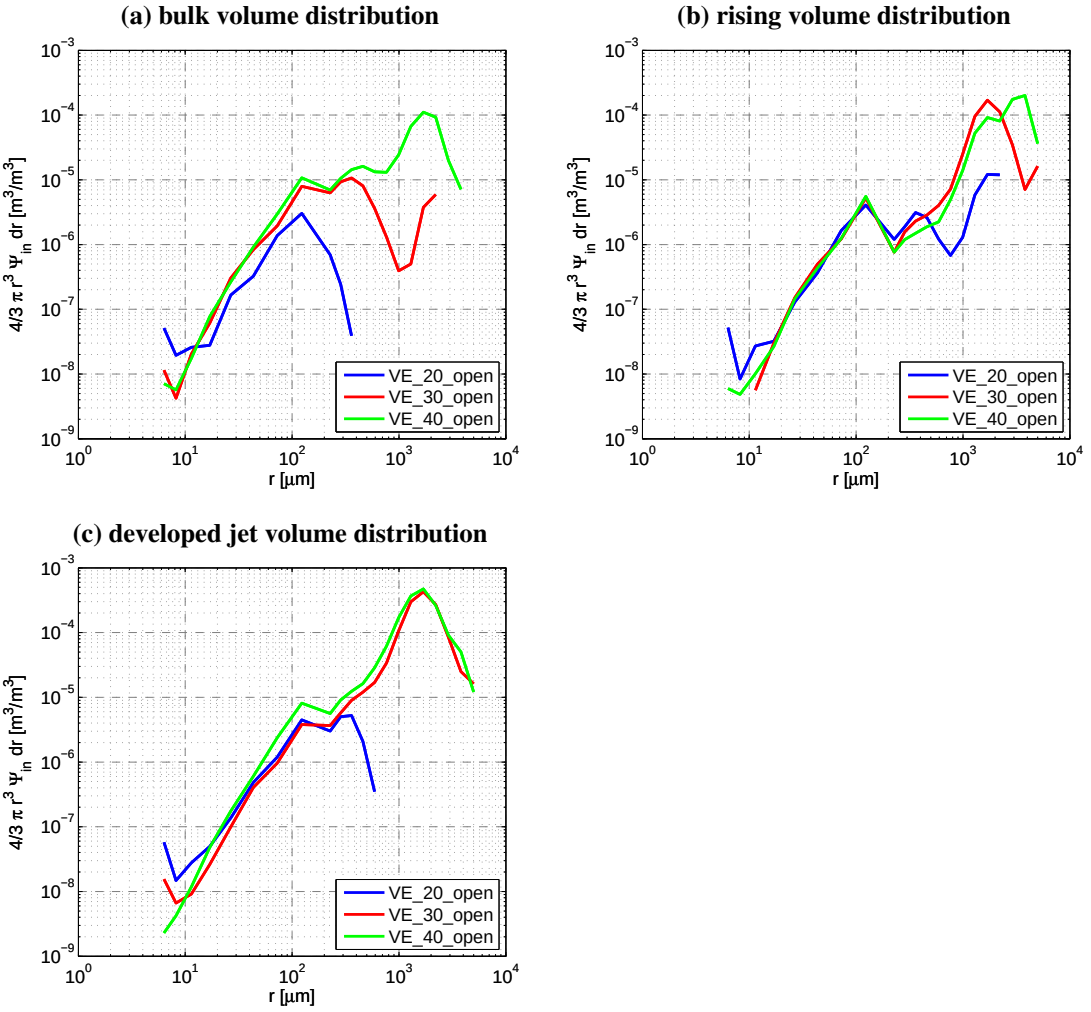

Figure 9.2.: Volume densities for all VE (deionized water) conditions are shown. Three representative sampling positions are shown.

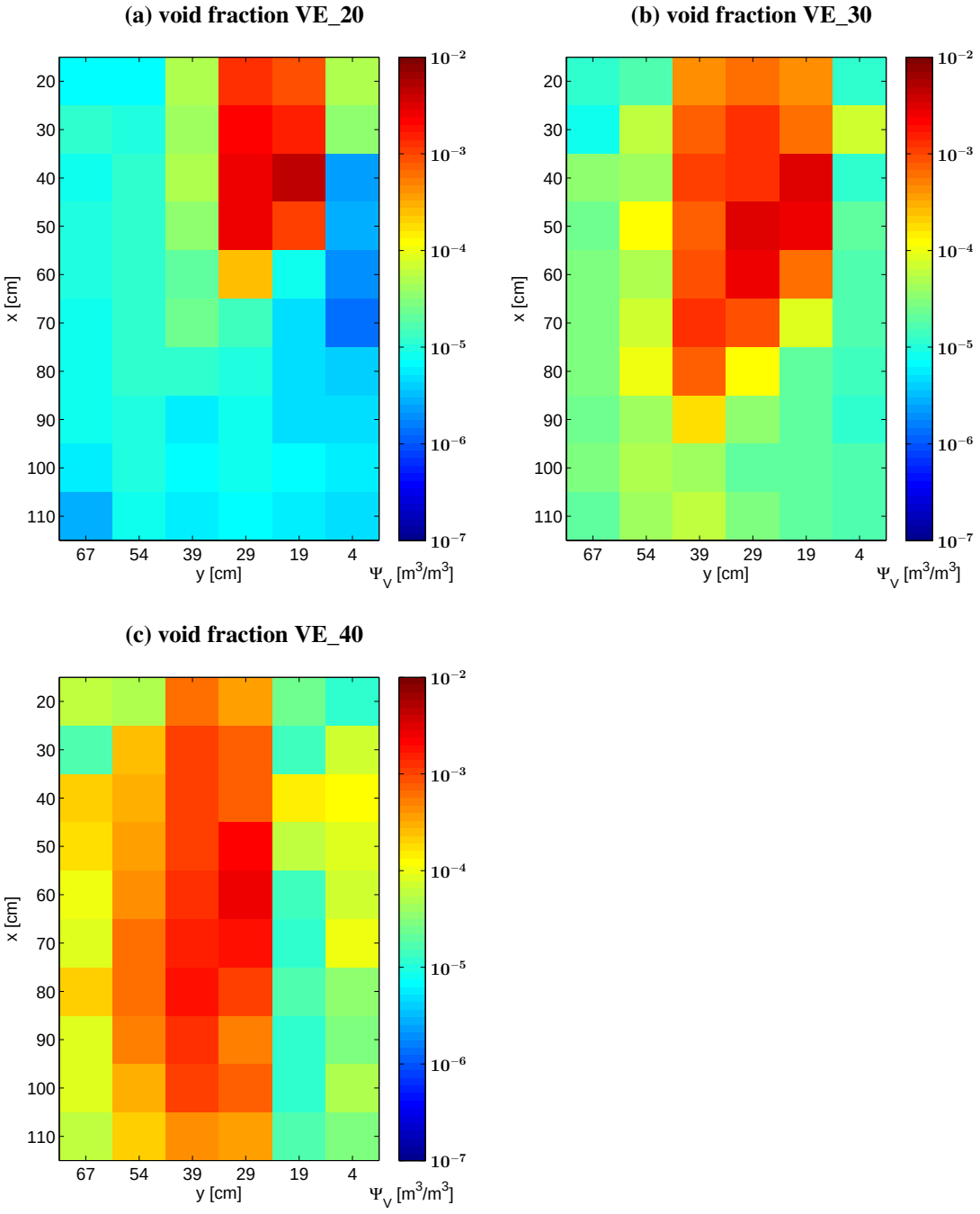

Figure 9.3.: Spatial distribution of the void fraction in the VE cases.

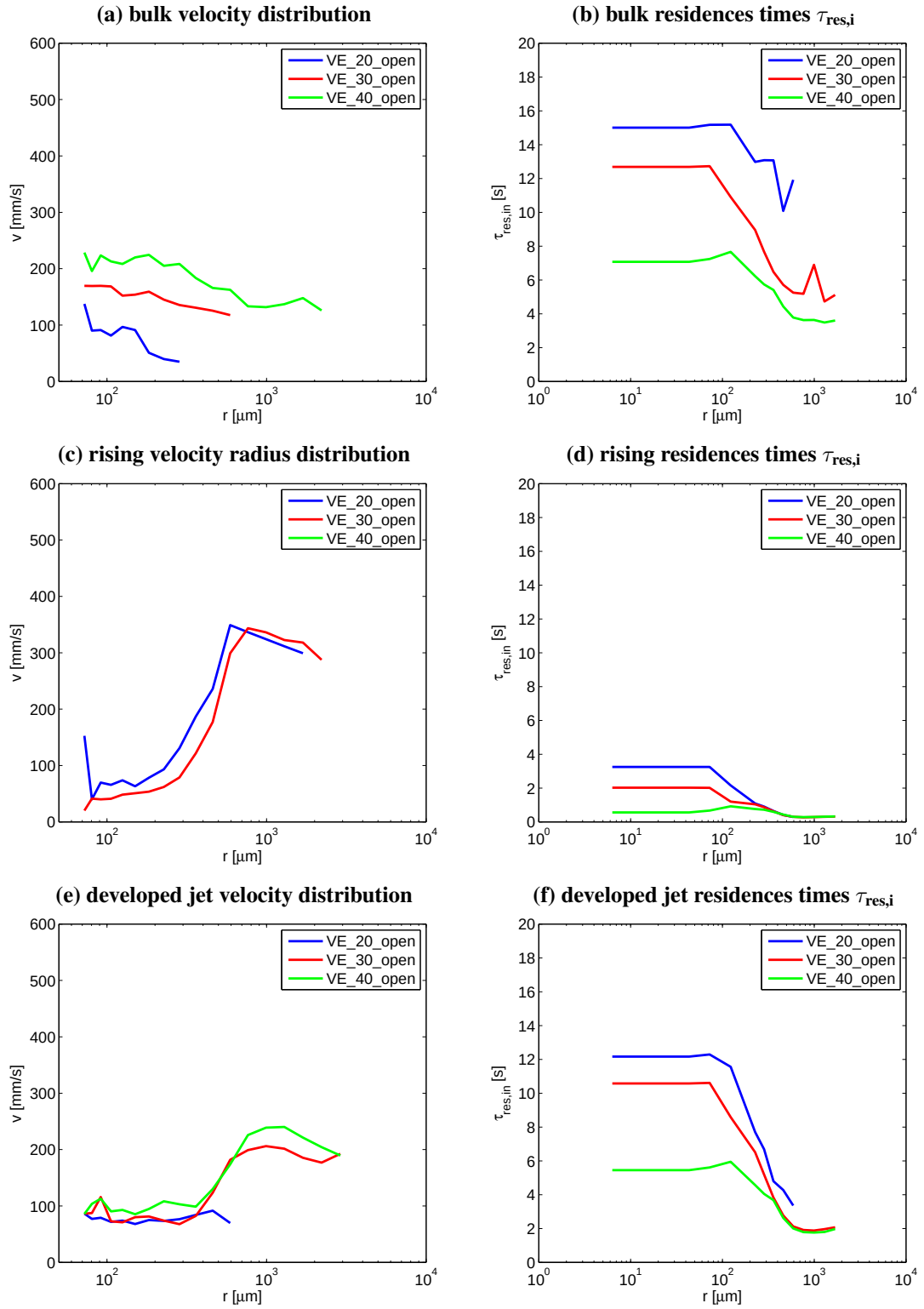

Figure 9.4.: Measured velocities v and residences times $\tau_{res,i}$ for bubbles with radius r. Three sampling positions are shown.

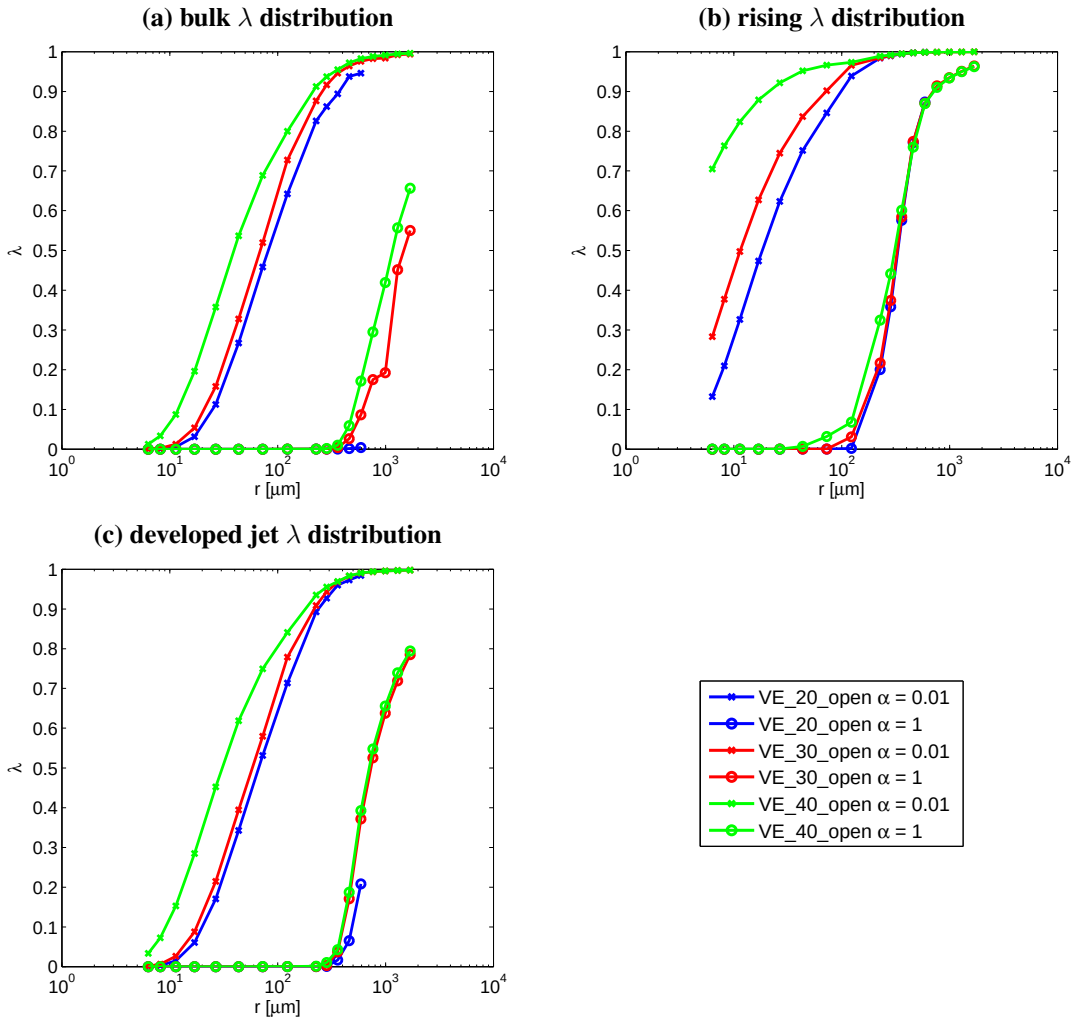

Figure 9.5.: Derived equilibration parameters λ for two different solubilities for three sampling positions in the tank. The calculation is based on eq. (8.15) using the calculated residence times $\tau_{\text{res,i}}$ and the model of a radius dependent transfer velocity for a single bubble k_b in the dirty case, see eq. (2.26)

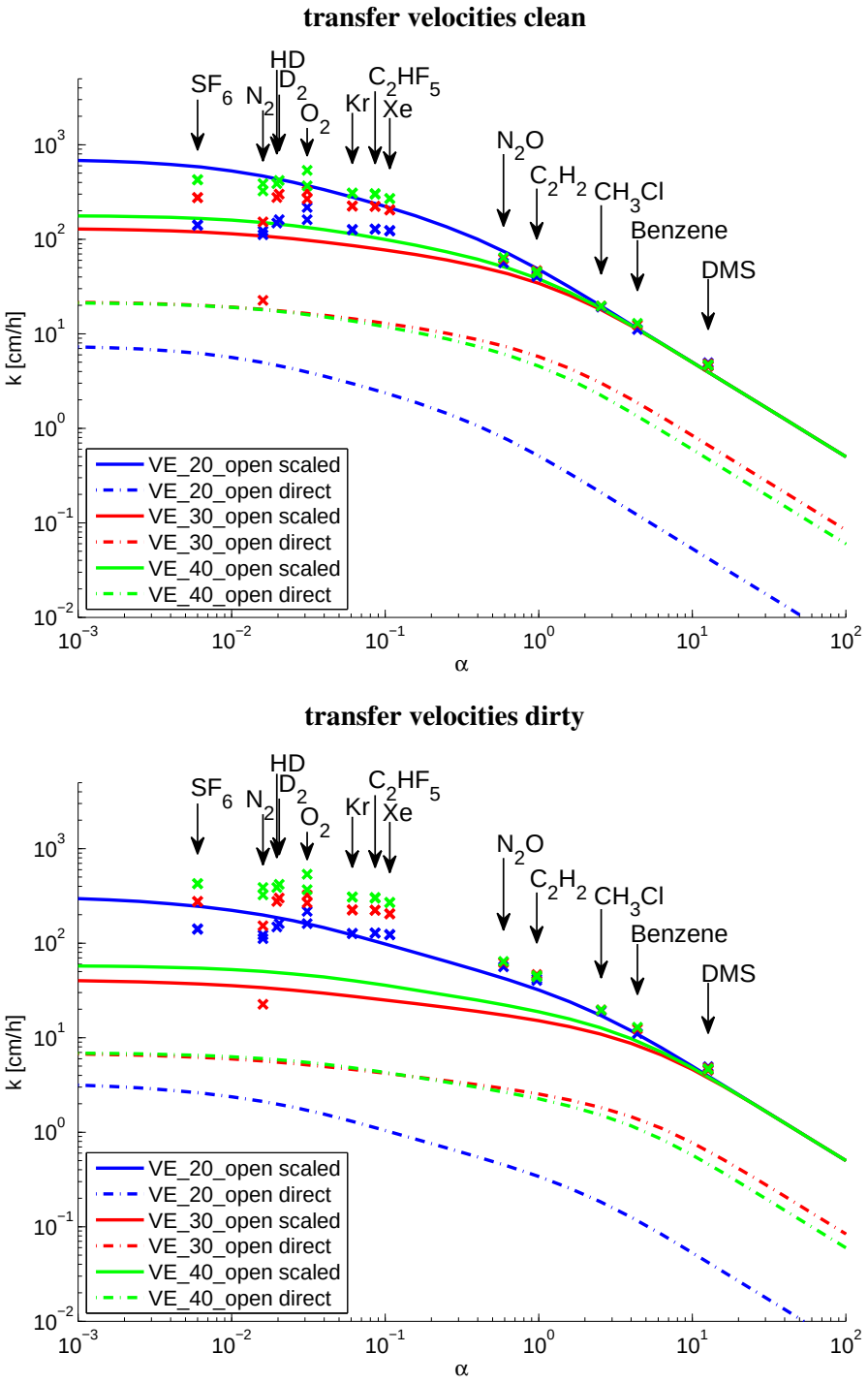

Figure 9.6.: The calculated transfer velocities for all conditions are shown. Measured transfer velocities acquired using the open configuration are plotted additionally. The lower curves represent the direct calculation, whereas the upper curves are calculated by scaling the direct calculation to the known high solubility asymptote.

Other Conditions In analogy to the evaluation shown here for the VE cases, evaluated bubble size, area, volume, residence time spectra and transfer velocities are shown in appendix C. Here, the special features of each condition are presented and new effects, which did not occur for the preceding conditions are discussed.

The actual fraction of the gas volume flux, which could be reconstructed by using the data from the bubble measurements, can be determined by comparing the calculated transfer velocities with the measured transfer velocities in the high solubility limit. The fractions are shown in fig. 9.7 for all experimental conditions. Except for the SALT_30 case, which captured $\sim 45\,\%$ of the flux, and the VE_20 and the VE_30_pulsed case, which captured below $5\,\%$, the measurements captured around $20\,\%$ of the actual volume gas flux through the bubble tank. This leads to an underestimation of the calculated gas transfer yielding a transfer velocity lower than this percentage. The high captured fraction for SALT_30 originates from the high fraction of small bubbles in the distribution. Therefore fewer large bubbles are present, which disturb the measurement. The reason for the low reconstructed fluxes for the other conditions is that at the low jet energies most of the gas flux is associated to big non spherical bubbles in high bubble density regions near the water surface, which are hard to capture for the bubble detection algorithm.

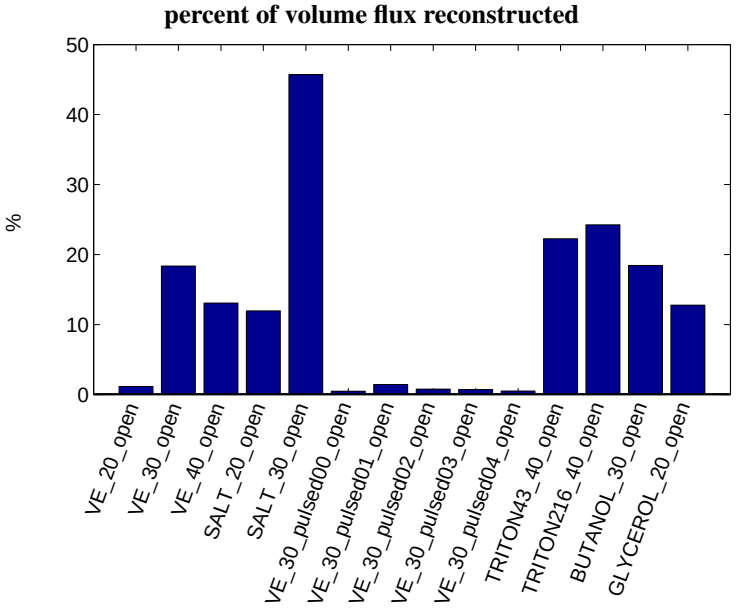

Figure 9.7.: Overview of the captured fraction of the flux, which could be reconstructed through the bubble size and velocity measurements. The total flux was determined through a fit in the high solubility limit to the experimental data, see section 9.2.

For the SALT_30 conditions an analysis analogous to the one done for the VE case, shows that in these conditions small bubbles are missing in the bubble distribution, whereas the general shape of the distribution of bubbles (scaled distribution) for the SALT_20 case describes the measured transfer velocities quite well. In all remaining conditions it turns out, that small bubbles are miss-

ing in the volume flux. This could be due to the limits of the measurement method as described before or a problem in the evaluation strategy. For calculating the local bubble source distributions Ψ, it is assumed that all bubbles rise strictly vertical, see eq. (8.6). Since this is not the case and the bubbles distribute in different directions, i.e. to different sampling locations than the one above, this can lead to an over correction of the densities. In this case this is a cause for a lack in mostly small bubbles because larger bubbles have a stronger directionality due to their stronger buoyancy.

In the figures 9.8 - 9.9 all conditions are compared regarding the measured total area and volume resp. their ratio to the water surface A. The largest gas hold up (air fraction in the water bulk) is generated in the SALT_30 condition due to small bubbles, which stay longer in the water than big bubbles. Considerable volumes of gas can be entrained by bubbles, in this condition $\sim 100\,\mathrm{l/m^2}$ of gas are submerged into the water. It is remarkable that in this condition the bubble surface area is 10 times larger than the water surface, which alone enhances the gas transfer by this factor in the low solubility limit, without regarding additional effects like increased turbulence. For all other cases the bubble area was at least in the same order as the water surface. In general additives in the water increase the bubble surface and the gas hold up. The VE conditions show the expected behavior, with increasing jet energy the area and the volume increases too. While the ratio of the volume of VE and SALT is $2-3$, the ratio of the areas amounts to $\sim 4-5$. A measure to compare these ratios is the so called Sauter radius $r_{32} = 3\frac{V_{\mathrm{tot}}}{A_{\mathrm{tot}}}$. It is defined as the radius of a spherical particle with the same ratio of volume and area as measured in the distribution. This means a bubble cloud with the same volume as measured in the distribution, but consisting only of bubbles with the Sauter radius, would give the same value for the area as was measured in the distribution. The Sauter radii for all conditions are shown in fig. 9.10. The presented Sauter radii match the bubble scene seen at the different conditions. With increasing jet energies the radius decreases because more energy is available to disrupt bubbles. With additives like salt, surfactants or alcohols the radius is decreased as well. This means the additives promote bubble break up or suppress bubble coalescence. Literature supports the hypothesis of suppressing the coalescence [14]. For the VE_30_pulsed condition this radius changes over time. The data for the pulsed measurement is divided in 2 s intervals for a pulse period of 10 s. The radius is largest at 6 s after the start of the bubble injection. At this time also the maximum for the total volume is reached. That delay can be accounted to the time needed for the bubble generator to establish the gas flow and to the time needed for the bubbles to reach their terminal depth.

In fig. 9.11 the transfer velocities are shown in the limit of low solubilities. The values in this plot are almost proportional to the values for the total bubble surface area because in this limit the transfer is proportional to the additional bubble surface multiplied by a radius dependent transfer velocity for single bubbles, see eq. (2.34). This dependency is responsible for the small deviations from proportionality.

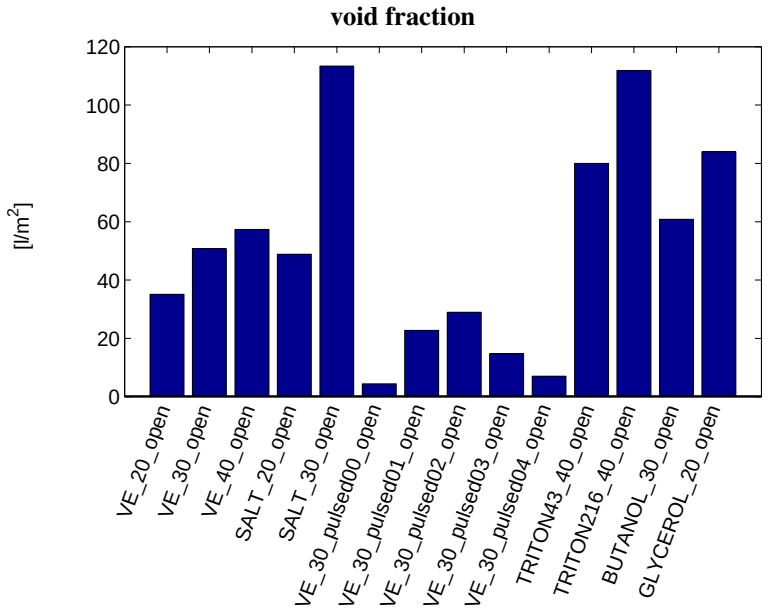

Figure 9.8.: Total reconstructed bubble volume for all measurement conditions normalized to the water surface area of the tank.

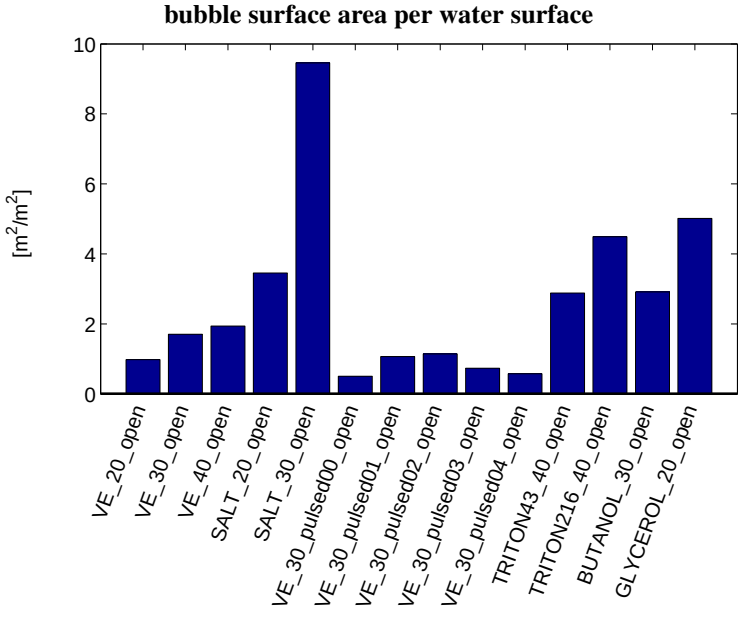

Figure 9.9.: Total reconstructed bubble surface area for all measurement conditions normalized to the water surface area of the tank.

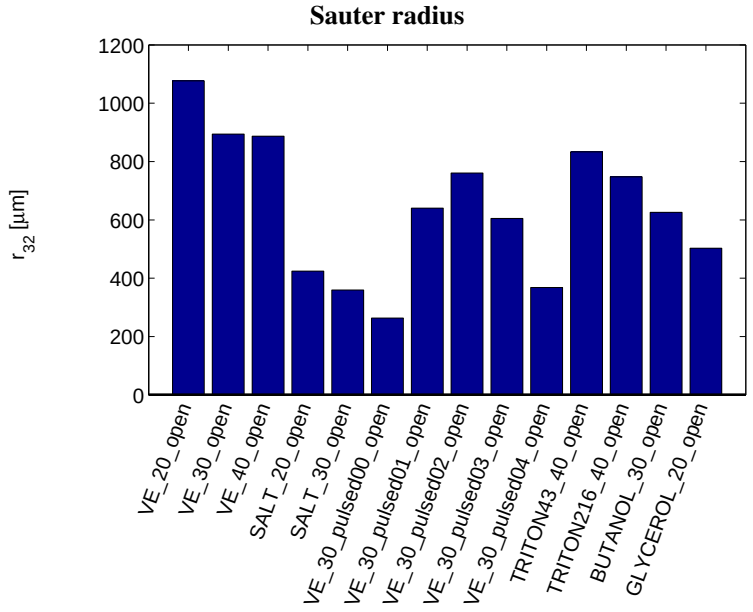

Figure 9.10.: The Sauter radius for all experimental conditions. The radius gives the mean radius of a spherical bubble, which matches the ratio of total volume and total area. $r_{32} = 3\frac{V_{\text{tot}}}{A_{\text{tot}}}$

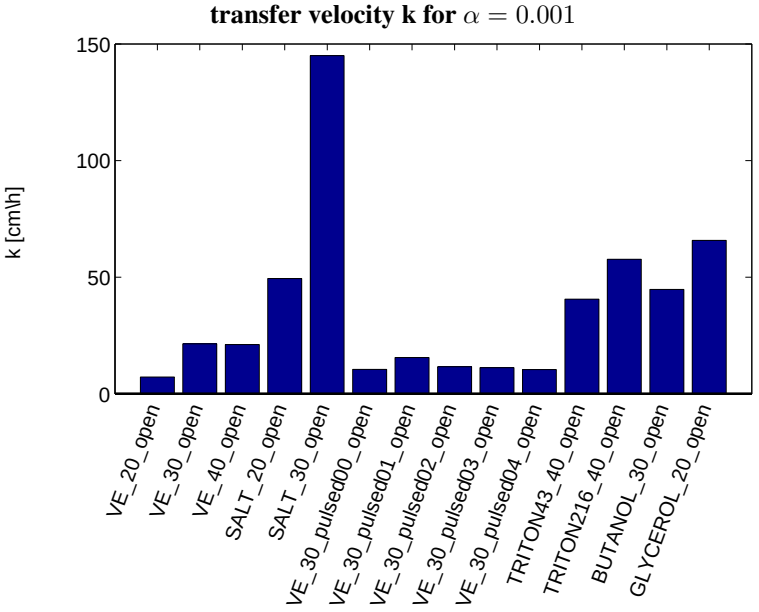

Figure 9.11.: Calculated transfer velocities for the low solubility limit for all experimental conditions.

9.2. Measured Transfer Velocities

In this section the measured transfer velocities for all conditions are discussed. The limiting cases are addressed, which is followed by the application of existing models and their comparison. A parametrization based on the modeling in this thesis is proposed. The section is closed by the discussion of interesting aspects, which seem promising to be investigated in further experiments.

The time series measured in the closed configuration for invasion measurements, while saturating the water with tracers for the evasion experiments proofed to be associated with a large experimental errors. An example for a time series is shown in fig. 9.12 for the VE_30_closed condition for D_2 and Benzene. It can be seen that few data points were available for fitting the temporal evolution, which caused a large scatter in the data, see fig. 9.13. The error results from the switching of the inlets. As discussed in section 5.2.2 large air concentrations, which were measured before switching the inlet to the waterside spoil the measurement. A compromise between waiting for the spectrometer to accommodate to the concentration and capturing the changes in concentration was made with an inlet switch time of 10 min. This proofed to be too fast for most gases to get reliable fits for the time series. Since the time series of water sided concentrations for the evasion measurements are far more reliable, the data from the invasion measurements were not used for further discussion, except for a check of asymmetry effects in section 9.2.2.

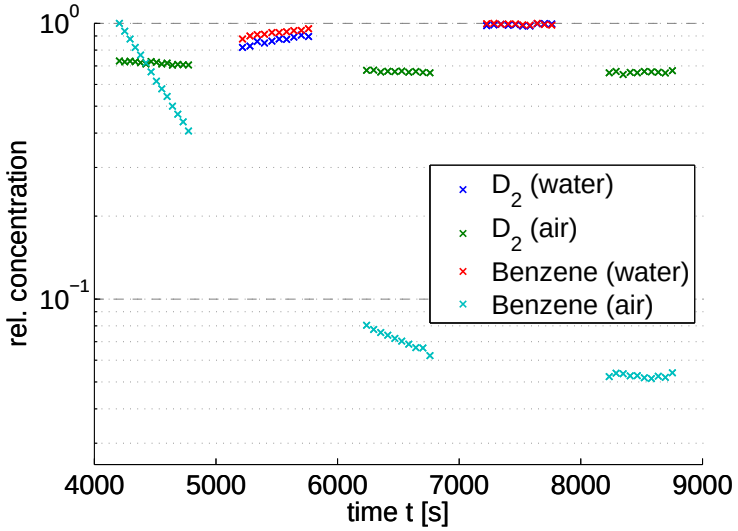

Figure 9.12.: Time series for the concentrations of D_2 and Benzene at VE_30_closed conditions. Shown are the concentrations measured in the air and the water phase for two tracers. The airside concentration is decreasing, while the waterside concentration is increasing, due to invasion. It can be seen that few data points were available for fitting the temporal evolution, which cause a large scatter in the data.

Examples of time series as well as the measured transfer velocities are shown in fig. 9.14 and 9.15 for the closed configuration shown before (With CH_3Cl in place of Benzene). The constant region for D_2 at times $> 1 \times 10^4$ s represents the resolution limit of the spectrometer resp. the

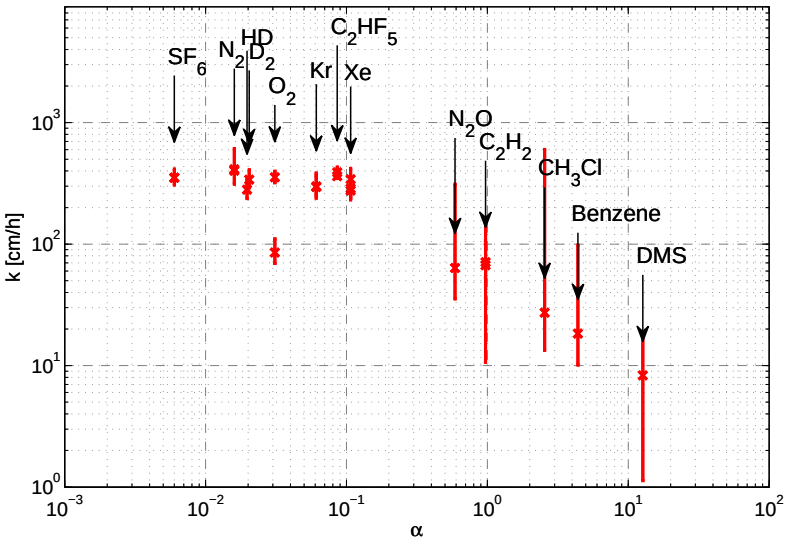

Figure 9.13.: Measured transfer velocities for VE_30_closed conditions. The determined transfer velocities were associated with a big scatter.

background concentration for mass 4 u, which probably is the natural Helium 4 concentration in the air. An overview over all measured transfer velocities for all conditions is given in fig. 9.16. Shown is the dependency of the transfer velocity on the solubility α and on the diffusivity D for tracers for which the low solubility limit can be assumed (SF_6, N_2, HD, D_2). In this limit the transfer velocity should not depend on the solubility but only on D, see eq. (2.34). The behavior in this limit is fitted using the following simple parametrization:

$$k_{\text{bub}} = c\, D^n \tag{9.1}$$

For the fit D was used in units of $10^{-5}\,\text{cm}^2/\text{s}$. The unit of c and therefore k_{bub} is cm/h. The parameter c will give the transfer velocity of a tracer with diffusivity $1 \times 10^{-5}\,\text{cm}^2/\text{s}$ in the low solubility limit. To model the high solubility case eq. (2.32) was used with one free parameter, $\frac{Q}{A} = Q^*$, which is an air sided transfer velocity, that is divided by α to yield a water sided transfer velocity as it is measured in this experiment:

$$k_{\text{bub}} = \frac{1}{\alpha} Q^* \tag{9.2}$$

The results of the asymptotic fits eq. (9.1) and eq. (9.2) are shown in tab. 9.1 and in fig. 9.16. Since the diffusivities of HD and D_2 are not known, they were calculated through a square root

dependence on the molecular mass from the diffusivity of H_2, see section 5.2.1. To test the influence of these diffusivities the fit was performed again with both diffusivities set to the value of H_2. The true values should be between those two extreme cases. The impact on the fit parameter n was $\sim 10\,\%$. By the intersection of the fitted parametrizations for both limiting cases a solubility for transition α_t can be defined. This solubility describes if a tracer is controlled by the volume flux (high α) or by the bubble area (low α) or has an intermediate behavior. Since the fitted parameters for n are mostly below 0.5, though a value in the range 0.5 - 0.66 is expected, the fit was performed again with fixed $n = 0.5$, which had no significant effect on $\alpha_t (< 1\,\%)$. This hints at a $D^{0.5}$ dependency for the transfer velocity at bubble surfaces.

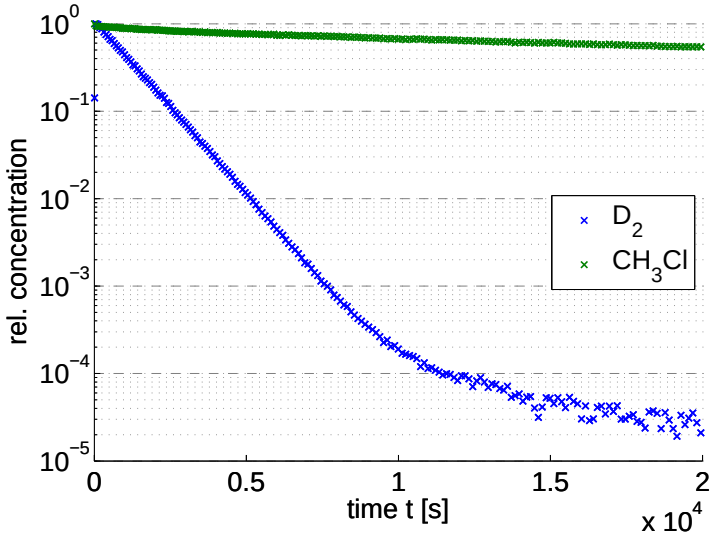

Figure 9.14.: Time series for the concentrations of D_2 and Benzene at VE_30_open conditions.

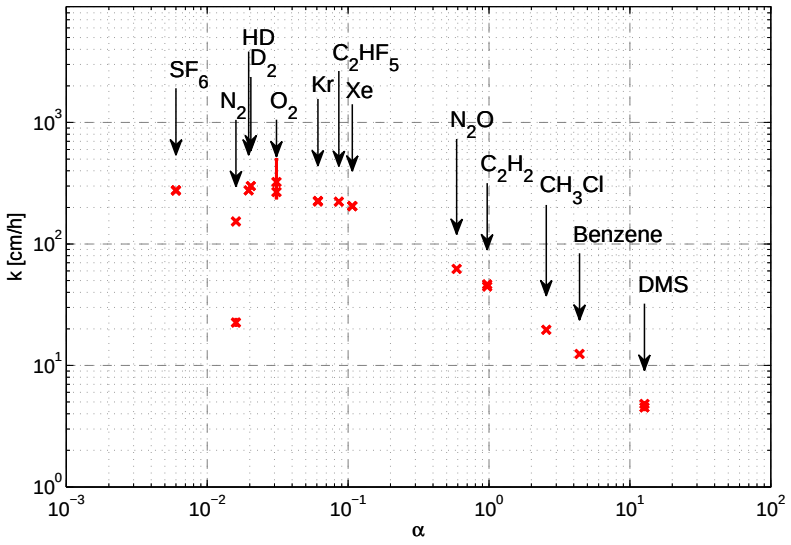

Figure 9.15.: Measured transfer velocities for VE_30_open conditions. The outlier data point for N_2 is caused by a leakage of ambient air into the tank.

As mentioned above the parameter c gives the transfer velocity in the low solubility limit for

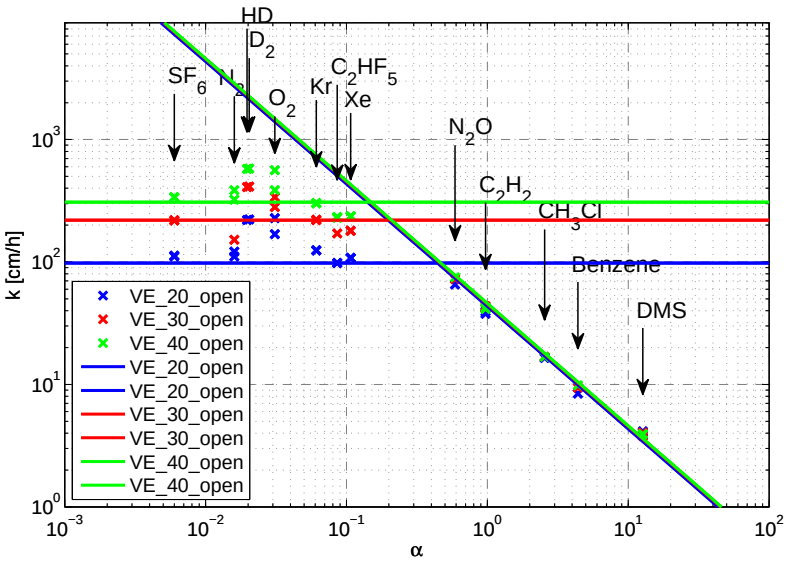

Figure 9.16.: Asymptotes of k_{bub} for all VE conditions. Plots of other conditions can be found in appendix C.2

Experiment	Low solubilities			High solubilities		α_t
	c [cm/h]	n	rms error [%]	Q^* [cm/h]	rms error [%]	
VE_20	88.99 ± 19.20	0.54 ± 0.24	41.45	43.47 ±4.30	27.14	0.44
VE_30	199.20 ± 9.66	0.53 ± 0.05	6.04	45.29 ±2.84	17.30	0.21
VE_40	284.54 ± 48.88	0.42 ± 0.19	34.04	45.88 ±2.42	14.56	0.15
SALT_20	346.01 ± 39.29	0.35 ± 0.12	23.13	46.85 ±1.42	8.42	0.13
SALT_30	754.88 ± 93.79	0.21 ± 0.13	21.65	39.61 ±2.38	16.57	0.05
VE_30_pulsed	180.79 ± 3.99	0.34 ± 0.02	2.81	40.08 ±6.37	57.71	0.21
TRITON43_40	289.70 ± 33.39	0.44 ± 0.13	23.41	39.60 ±3.38	23.48	0.13
TRITON216_40	270.58 ± 55.10	0.43 ± 0.23	39.22	44.94 ±2.07	12.73	0.15
BUTANOL_30	402.07 ± 28.52	0.36 ± 0.08	14.83	36.28 ±2.96	22.49	0.08
GLYCEROL_20	133.90 ± 27.97	0.53 ± 0.23	40.21	51.55 ±5.17	27.52	0.35

Table 9.1.: Values for the parameters of the asymptotic fits and the transition value for the solubility α_t. The low solubility case used the parametrization given in eq. (9.1). In the high solubility case eq. (9.2) was used. Fixing n to 0.5 has no noticeable impact on α_t (below 1 percent).

a tracer with the diffusivity $D = 1 \times 10^{-5}\,\text{cm}^2/\text{s}$. By comparing this parameter it is possible to quantify the effects of the kinetic jet energy and the different additives can be quantified. The ratio of the transfer velocities of fresh and salt water conditions amount to a factor of ~ 4 due to increased bubble surface. The influence of the surfactants on the transfer velocity is lower than $5\,\%$. The addition of $\sim 20\,\text{ppm}$ (vol) of n-butanol shifted the bubble distribution to lower radii in a way that the transfer increased by one third. A lower value for α_t is an indication for the bubble distribution being dominated by small bubbles. This can be seen by comparing with the salt water condition, where α_t was a factor of 3 lower, and the bubble distribution was shifted towards smaller radii, too, see fig. .42.

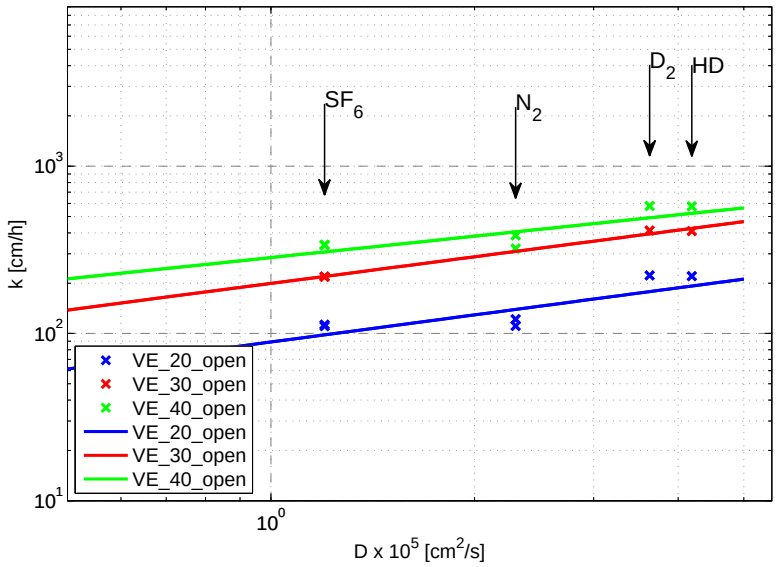

Figure 9.17.: D dependency of k_{bub} for all VE conditions. Plots of other conditions can be found in appendix C.2

Statistical Error

To test the deviations in the determined transfer velocity one condition was repeated at the same conditions and the relative deviations between both runs were calculated. The results for the transfer velocities are given in table 9.2. The total rms error of the given tracers results in 1.7 %.

The tracers, which are not given in the table could not be evaluated, because of a leakage problem in the reference experiment.

9.2.1. Comparison to Models

In this section the measured data is compared to the models presented in section 2.2. All fits are performed to minimize the relative RMS error of the modeled data to the measured transfer velocities using the *MATLAB*® function *lsqnonlin*. The errors are estimated using 70 % confidence intervals to be comparable to standard deviations. In fig. 9.18 the fits of the model of Keeling [37], see eq. (2.37), are shown, the estimated values for the parameters are listed in table 9.3. The tracers used for performing this fit were the following: N_2, N_2O, HD, D_2, C_2H_2, CH_3Cl, Kr, C_2HF_5, Xe, SF_6, Benzene and DMS. In the VE_30 condition N_2 was excluded because there was a leakage problem rendering this tracer unusable. For the condition VE_30_pulsed the tracers N_2, Benzene and DMS were excluded because the high soluble species changed their concentration

Tracer	k_1[cm/h]	k_2[cm/h]
SF_6	280	277
SF_6	280	275
HD	287	276
D_2	315	300
Kr	218	226
Kr	218	224
Xe	201	205
Xe	201	204
Xe	201	205
C_2HF_5	223	223
C_2HF_5	223	223
C_2H_2	46.4	46.5
C_2H_2	43.5	44.5
CH_3Cl	20.5	19.6
Benzene	14.0	12.4
DMS	5.83	4.82
DMS	5.23	4.51

Table 9.2.: Summary of two experiments at the same conditions (30 Hz jet 1000 ml/min air flow rate). The second experiment is condition VE_30.

only about $1\,\%$, which was in the order of the measurement accuracy of the mass spectrometer and therefore yielded an unreliable fit. It is apparent that this parametrization produces a large deviation of modeled to measured data, because the functional form does not allow to describe both limiting cases at the same time. Therefore, a fit yields an intermediate solution, which does neither describes the low solubility nor the high solubility case in an appropriate way. Applying the fit to only the low solubility or the high solubility regime has no benefits over using the direct physically motivated equations for the limiting cases described in the previous section 9.2. The model used by Asher et al. [4], see eq. (2.38), is fitted to the experimental data using the same tracers as before. The model gives a better approximation than the Keeling model, but still fails to reproduce both asymptotes correctly at the same time. The same explanations as before apply, but here a better fit performance is traded for an additional fit parameter. Due to the bad performance of these models a physical interpretation of the fit parameters is not reasonable.

The model of Woolf et al. [72] is fitted to the measured transfer velocities in three different variations: The first variation uses the parametrization as given by Woolf et al. [72] and shown in eq. (2.39). The entire integral term is used as a parameter in the fit procedure. In the second variation an explicit D^n dependence is introduced by a factor to the integral term, which yields:

$$k_{\text{bub}} = X\frac{Q}{\alpha}(1+(X\chi)^{\frac{1}{f}})^{-f} \quad \text{with} \quad \chi = \frac{AQ}{\alpha D^n \int j\mathrm{d}A_b} \quad \text{and} \quad X = \frac{\alpha\dot{V}_z}{\alpha\dot{V}_z + Q} \tag{9.3}$$

Experiment	Keeling			
	c [cm/h]	m	n	rms error [%]
VE_20	13.49 ± 2.85	-0.43 ± 0.04	0.77 ± 0.37	183.91
VE_30	16.20 ± 3.34	-0.54 ± 0.04	0.97 ± 0.34	176.60
VE_40	18.73 ± 3.77	-0.59 ± 0.04	0.84 ± 0.34	176.95
SALT_20	19.63 ± 4.07	-0.61 ± 0.04	0.83 ± 0.35	185.57
SALT_30	21.25 ± 4.74	-0.72 ± 0.04	0.77 ± 0.38	189.30
VE_30_pulsed	26.62 ± 4.94	-0.41 ± 0.04	0.72 ± 0.25	102.37
TRITON43_40	17.11 ± 3.27	-0.60 ± 0.04	0.88 ± 0.31	169.87
TRITON216_40	18.15 ± 3.85	-0.59 ± 0.04	0.84 ± 0.36	183.41
BUTANOL_30	15.94 ± 3.45	-0.68 ± 0.04	0.89 ± 0.34	190.63
GLYCEROL_20	17.19 ± 3.31	-0.46 ± 0.04	0.79 ± 0.33	168.87

Table 9.3.: Fitted parameter using the parametrization of Keeling [37], see eq. (2.37). ($k_{\text{bub}} = c\alpha^m D^n$, D is in units of $10^{-5}\,\text{cm}^2/\text{s}$)

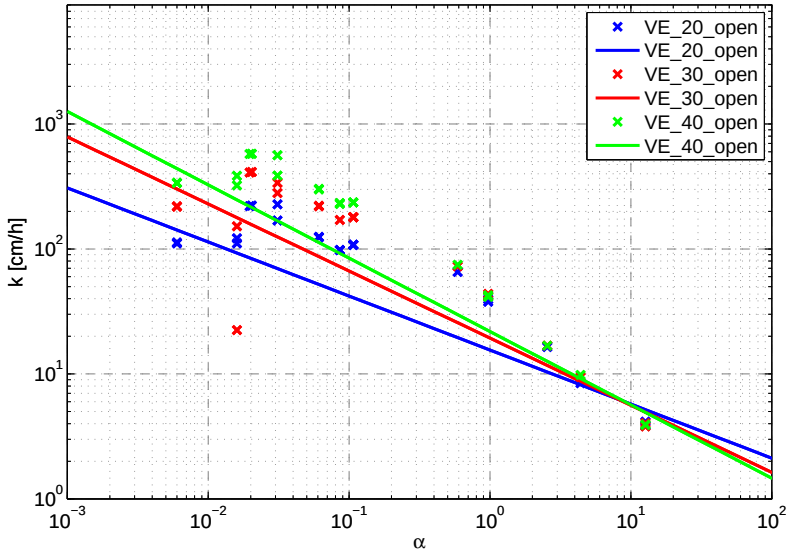

Figure 9.18.: Fits of the Keeling model to the experimental data for all VE conditions.

The third variant fixes the values for the interstitial water fraction $X = 1$ and the parameter modeling the shape of the transition $f = 1$. This is done to check the impact of the concept of interstitial water on the modeling. The resulting fit parameters are shown in tab. 9.5 and the curves are shown for the first variant as given by Woolf et al. [72] in fig. 9.21. An overview of all fit performances is given in fig. 9.23. The second variant performs best, which is to be expected due to the largest number of degrees of freedom. The performance of the first and third variant can be considered equal, which challenges the impact of the interstitial water to the model and therefore for the process in bubble mediated gas exchange. This is supported by the determined values for X in the first and second case because they all are statistical compatible with $X = 1$. In the first place the integral term considers the surface contributing to the gas exchange. The ratios of this fit parameter are consistent to the ratios of the transfer rates in the low solubility case.

Experiment	Asher				
	c_1 [cm/h]	c_2 [cm/h]	m	n	rms error [%]
VE_20	-7.88 ± 3.43	34.43 ± 4.70	-0.73 ± 0.06	-0.12 ± 0.06	105.56
VE_30	-63.37 ± 38.62	96.39 ± 38.75	-0.92 ± 0.04	0.01 ± 0.02	50.16
VE_40	-162.74 ± 280.63	201.02 ± 280.89	-0.96 ± 0.06	-0.01 ± 0.02	75.77
SALT_20	-247.74 ± 762.77	286.78 ± 763.19	-0.97 ± 0.08	-0.00 ± 0.01	95.60
SALT_30	-494.31 ± 6987.12	531.47 ± 6991.53	-0.99 ± 0.17	0.00 ± 0.07	143.27
VE_30_pulsed	-5.04 ± 2.03	36.29 ± 3.14	-0.65 ± 0.06	0.18 ± 0.10	52.02
TRITON43_40	-240.19 ± 611.05	274.36 ± 611.39	-0.98 ± 0.06	-0.00 ± 0.01	68.77
TRITON216_40	-209.64 ± 493.69	247.93 ± 493.93	-0.97 ± 0.07	-0.01 ± 0.02	83.55
BUTANOL_30	-332.59 ± 2036.26	364.74 ± 2038.19	-0.98 ± 0.10	0.01 ± 0.04	105.83
GLYCEROL_20	-11.71 ± 4.74	44.27 ± 5.93	-0.76 ± 0.05	-0.08 ± 0.05	88.84

Table 9.4.: Fitted parameter using the parametrization of Asher et al. [4], see eq. (2.38). ($k_{\text{bub}} = \frac{c_1}{\alpha} + c_2 \alpha^m D^n$, D is in units of $10^{-5}\,\text{cm}^2/\text{s}$)

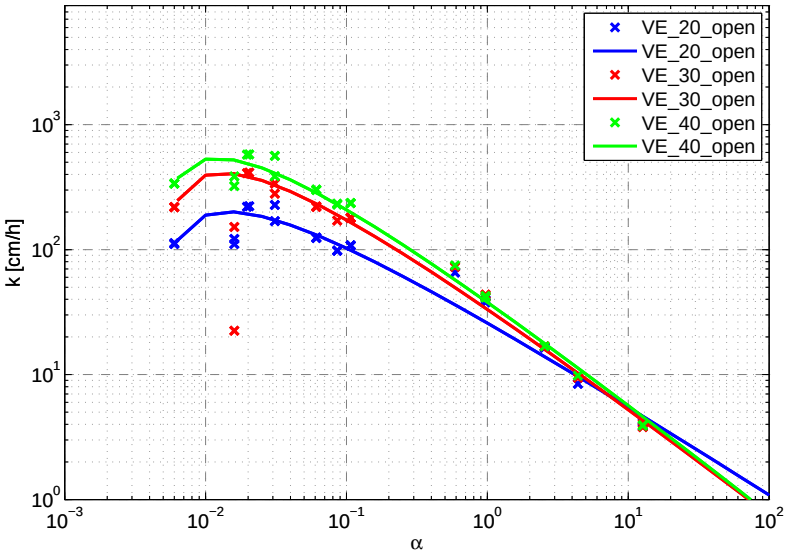

Figure 9.19.: Fits of the Asher model to the experimental data for all VE conditions.

For a comparison the data was fitted with the model presented in this thesis, see eq. (2.64) and eq. (8.15), with two different approaches. In the first approach, the same processing as used for calculating the transfer velocities was fed with a synthetically generated normally distributed radius distribution with mean radius r and width σ_r. This distribution was used as a spatial homogenous bubble source distribution. For the individual bubble velocities the measured values were used, whereas the transfer velocities for single bubbles k_b were assumed according to the clean and dirty parametrization given by Higbie's equation [13] resp. Frössling [23]. The parameters r and σ_r for the best fitting radius distribution are given in table 9.6. These models perform better than the model of Woolf et al. [72], which is probably caused by the additional information input of the spatial velocity distribution. No errors could be given for these parameters since the discrete nature of the sampling domain leads to a noncontinuous residual of the fitted model. This leads to inaccurate derivatives, which are needed to calculate the confidence intervals. This is also the reason for using a brute force approach to fit the distribution, that means many combinations for r

and σ_r were used as starting values for the fit and the combination with lowest error was chosen.

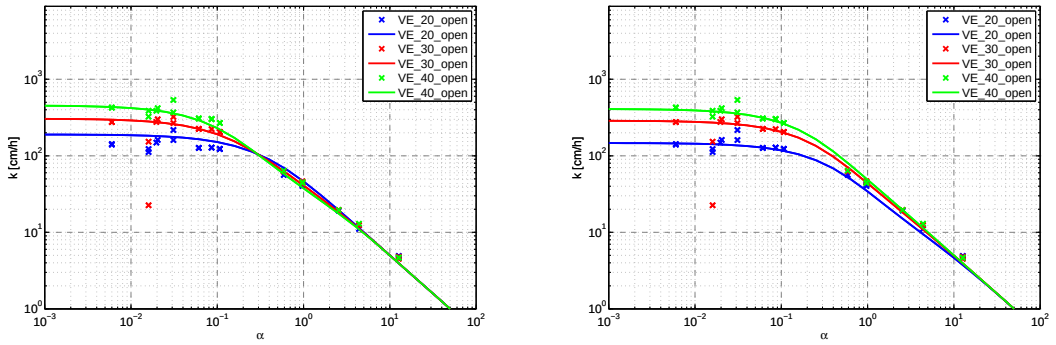

Figure 9.20.: Fits of the presented model to the experimental data for all VE conditions. *left*: clean case *right*: dirty case

To get a simple analytic form of an parametrization in agreement to the presented modeling in this thesis eq. (2.73) was used. To remove the integration over r it was assumed, that the distribution consists only of bubbles with one radius – the transfer equivalent radius. The division of τ and r in the exponential function in λ was combined to a single parameter α_t, which equals the transition solubility discussed in the previous section. The explicit D dependence was modeled by an exponent n. This yields the parametrization used:

$$k_{\text{bub}} = \frac{1}{\alpha}\frac{Q}{A}(1 - \exp(-D^n \frac{\alpha}{\alpha_t})) \tag{9.4}$$

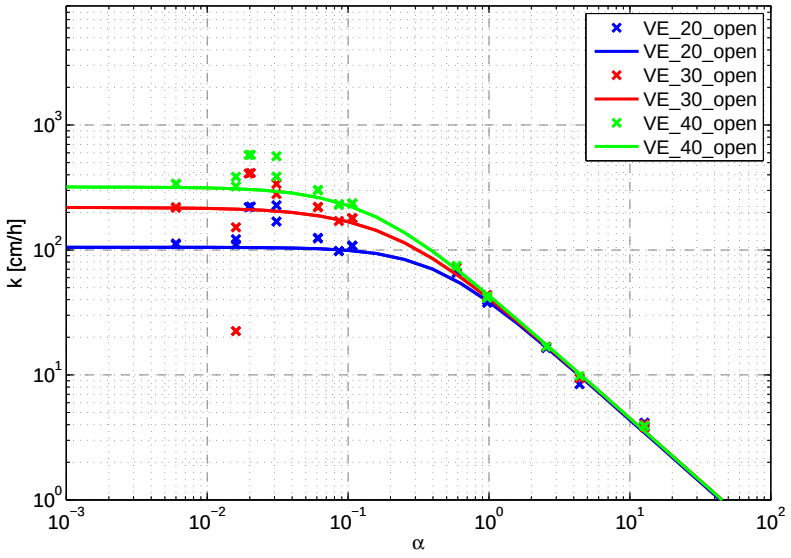

Figure 9.21.: Fits of the extended Woolf model to the experimental data for all VE conditions.

The parametrization performs better than the model proposed by Woolf et al. [72], but slightly worse than the modified version with explicit D dependence, see fig. 9.23. This doubts again

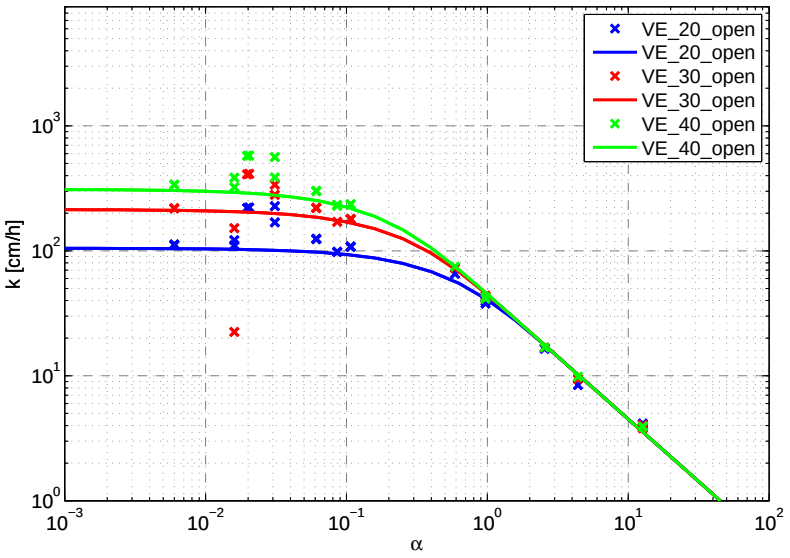

Figure 9.22.: Fits of the presented general model to the experimental data for all VE conditions.

the necessity of the interstitial water term in the model of Woolf et al. [72]. The exponent n for the diffusivity dependence in all models with correct physical approaches are compatible with a value of 0.5, though they show a tendency to even lower values. Since there are theoretical considerations contradicting values of n smaller than 0.5, this hints at a $D^{0.5}$ dependence of the transfer velocities at bubble surfaces.

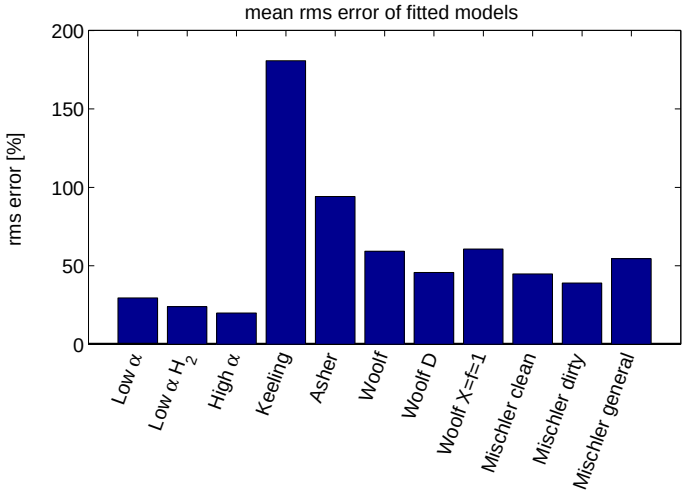

Figure 9.23.: Mean rms error for the used models. Low α denotes the asymptotic fit in the low solubility case. For Low α H_2 the values for the diffusion coefficients for HD and D_2 have been replaced by H_2. High α denotes the asymptotic case for high solubilities.

Experiment	Woolf				
	X	$\int j \mathrm{d}A_b$	f	n	rms error [%]
VE_20	1.00 ± 0.09	12.57 ± 0.87	0.71 ± 0.20	0	60.01
VE_30	1.00 ± 0.07	25.11 ± 2.45	0.75 ± 0.17	0	52.76
VE_40	1.00 ± 0.06	38.99 ± 2.99	0.77 ± 0.12	0	49.57
SALT_20	1.00 ± 0.10	45.43 ± 5.85	0.81 ± 0.19	0	77.30
SALT_30	0.90 ± 0.06	74.16 ± 6.80	0.32 ± 0.17	0	69.65
VE_30_pulsed	1.00 ± 0.31	22.36 ± 4.86	1.17 ± 0.41	0	73.90
TRITON43_40	0.86 ± 0.05	40.03 ± 3.30	0.76 ± 0.13	0	52.14
TRITON216_40	0.99 ± 0.06	37.13 ± 2.63	0.70 ± 0.12	0	48.57
BUTANOL_30	0.82 ± 0.04	52.46 ± 3.73	0.62 ± 0.10	0	47.13
GLYCEROL_20	1.00 ± 0.11	18.43 ± 1.74	0.77 ± 0.21	0	67.78
VE_20	0.97 ± 0.07	10.26 ± 0.80	0.61 ± 0.18	0.40 ± 0.11	44.42
VE_30	1.00 ± 0.03	20.74 ± 0.91	0.78 ± 0.07	0.56 ± 0.05	18.39
VE_40	1.00 ± 0.04	31.24 ± 2.55	0.71 ± 0.10	0.39 ± 0.09	34.47
SALT_20	1.00 ± 0.09	35.99 ± 5.95	0.76 ± 0.18	0.41 ± 0.19	67.26
SALT_30	0.90 ± 0.06	70.78 ± 12.68	0.31 ± 0.18	0.07 ± 0.23	69.46
VE_30_pulsed	1.00 ± 0.24	18.30 ± 3.51	1.21 ± 0.33	0.62 ± 0.20	53.14
TRITON43_40	0.86 ± 0.03	31.53 ± 2.43	0.72 ± 0.09	0.44 ± 0.09	32.68
TRITON216_40	0.98 ± 0.04	30.09 ± 2.66	0.62 ± 0.10	0.35 ± 0.11	37.54
BUTANOL_30	0.83 ± 0.03	42.26 ± 2.76	0.61 ± 0.07	0.40 ± 0.08	28.21
GLYCEROL_20	1.00 ± 0.08	14.36 ± 1.58	0.68 ± 0.20	0.46 ± 0.14	51.92
VE_20	1.00	11.68 ± 1.00	1.00	0.36 ± 0.13	56.92
VE_30	1.00	23.10 ± 1.13	1.00	0.60 ± 0.08	29.12
VE_40	1.00	36.98 ± 3.08	1.00	0.37 ± 0.13	46.90
SALT_20	1.00	42.04 ± 5.53	1.00	0.41 ± 0.20	72.67
SALT_30	1.00	96.13 ± 20.18	1.00	0.12 ± 0.33	95.18
VE_30_pulsed	1.00	15.85 ± 1.73	1.00	0.61 ± 0.18	57.09
TRITON43_40	1.00	35.09 ± 2.92	1.00	0.45 ± 0.13	46.86
TRITON216_40	1.00	37.10 ± 3.58	1.00	0.30 ± 0.15	53.86
BUTANOL_30	1.00	48.88 ± 5.44	1.00	0.45 ± 0.17	60.25
GLYCEROL_20	1.00	16.88 ± 1.65	1.00	0.40 ± 0.15	61.57

Table 9.5.: Fitted values for the parametrization originally proposed by [71] and reformulated with an explicit D dependency in eq. (9.3). Values for $\frac{Q}{A}$ were taken from the fit in the high solubility asymptote, eq. (9.2). Values without errors denote fixed parameters for the fitting procedure.

Experiment	clean case			dirty case		
	r [µm]	σ_r [µm]	rms error [%]	r [µm]	σ_r [µm]	rms error [%]
VE_20	878.37	12.34	16.18	407.77	12.54	32.50
VE_30	527.06	23.56	13.00	321.96	5.57	10.11
VE_40	517.79	17.88	34.55	258.51	19.20	20.72
SALT_20	410.73	9.63	70.26	251.26	31.79	35.56
SALT_30	322.94	6.34	83.85	186.65	13.75	75.90
VE_30_pulsed	539.02	5.76	164.85	325.45	17.92	137.66
TRITON43_40	493.86	14.14	14.20	304.62	56.84	27.65
TRITON216_40	514.75	22.97	40.08	268.68	35.48	23.39
GLYCEROL_20	771.15	5.02	37.99	291.91	55.33	44.31
BUTANOL_30	409.56	10.96	34.81	324.10	14.26	42.34

Table 9.6.: Assumed Gaussian radius distribution with mean r and width σ_r. To calculate the transfer velocity the measured τ distributions and modeled k_b are used. Values for the *transfer equivalent radius* determined by a fit of the model described in section 8.2.1 for clean and dirty conditions. An reliable error estimate was not possible, since the discrete nature of the radius sampling leads to unstable derivatives needed for error estimation.

Experiment	general		
	α_t	n	rms error [%]
VE_20	0.44 ± 0.03	0.37 ± 0.11	49.33
VE_30	0.23 ± 0.01	0.57 ± 0.06	23.04
VE_40	0.15 ± 0.01	0.42 ± 0.09	35.91
SALT_20	0.14 ± 0.02	0.46 ± 0.17	66.51
SALT_30	0.06 ± 0.01	0.11 ± 0.24	76.56
VE_30_pulsed	0.35 ± 0.05	0.63 ± 0.24	75.96
TRITON43_40	0.16 ± 0.02	0.51 ± 0.15	62.07
TRITON216_40	0.15 ± 0.01	0.35 ± 0.10	39.67
BUTANOL_30	0.12 ± 0.01	0.48 ± 0.16	64.48
GLYCEROL_20	0.32 ± 0.02	0.45 ± 0.12	51.64

Table 9.7.: Fitted values for the general parametrization proposed in eq. (9.4). Values for $\frac{Q}{A}$ were taken from the fit in the high solubility asymptote, eq. (9.2).

9.2.2. Super-Saturation and Asymmetry

As far as super-saturation of the water phase is concerned, see eq. (2.30), the conducted experiments are not suitable for validation. As stated in section 2.2.1 the super-saturation can be seen as a change in effective solubility. Since the magnitude of super-saturation is expected to be in an order of a few percent [72], the uncertainty of the available solubility data covers this effect. A suitable experiment to resolve this effect would use a setup in a closed configuration. There it would be possible to compare the equilibrium concentration without bubbles with the steady state concentrations with enabled bubble generator. It would take a very long time to reach equilibrium concentration. Even then it would be doubtful if the measurement accuracy is good enough to resolve the effect. Therefore it was decided not to perform these measurements.

Regarding the asymmetry of transfer velocities of invasion and evasion, no reliable statement can be made. Expected asymmetries are in the range of about $1\,\%$ to $3\,\%$ according to Bowyer and Woolf [8]. Due to significant inaccuracies in the invasion measurements, see section 9.2, the asymmetric effects could not be verified. An example of the relative differences between invasion an evasion measurements for two conditions are shown in fig. .51. The results for other conditions are shown in the appendix C.3. A mean asymmetry was calculated from tracers, which have an error below $15\,\%$ and an absolute deviation below $15\,\%$. Data for other tracers was considered erroneous, due to problems in the measurement resp. evaluation of the invasion data. The data for the VE_30 conditions was the only one among the measurements, having the same conditions for invasion and evasion, which yields a significant value for the asymmetry. For all other conditions a vanishing asymmetry was compatible with the result.

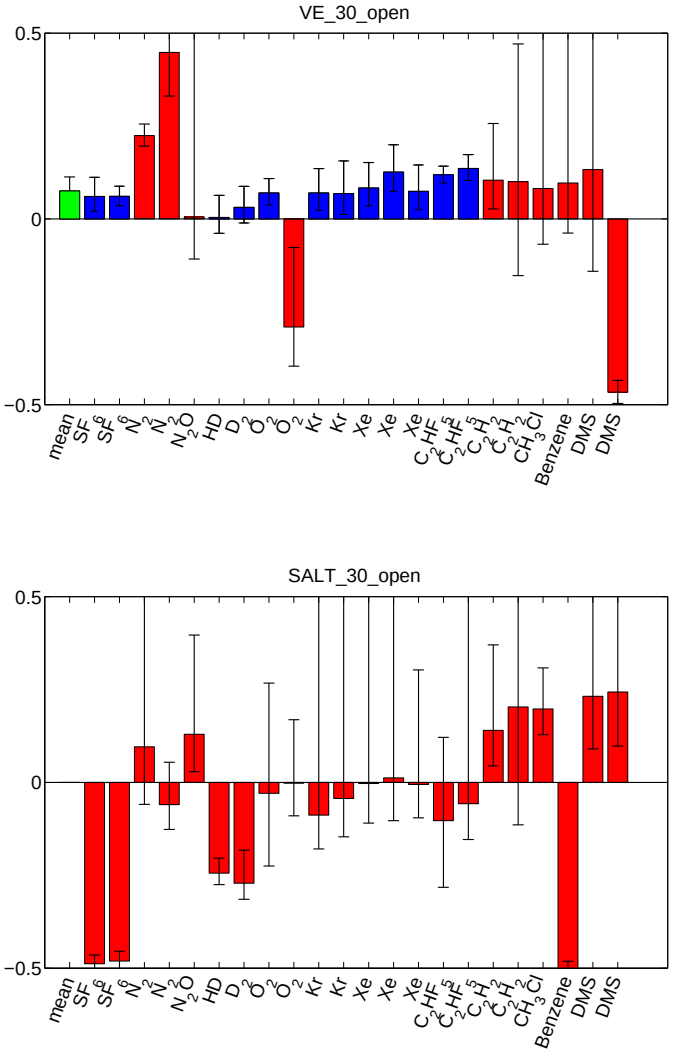

Figure 9.24.: Relative enhancement of invasion over evasion measurements. Blue bars denote measurements used for mean calculation. Red bars are excluded due to a errors larger than $15\,\%$ or a deviation larger than $15\,\%$, which are attributed to experimental problems of the invasion measurement. *top*: VE_30 *bottom*: SALT_30

10. Conclusion and Outlook

10.1. Conclusion

An experiment to investigate bubble mediated gas exchange for tracers in a wide range of solubilities and diffusivities was designed. Therefore a quadrupole mass spectrometer with membrane inlet was put into operation and was integrated at an experimental bubble tank, see section 4.1. The gas injection, extraction and measuring procedure was automated to a large extent. The spectrometer was characterized regarding the selected tracer used in these experiments, see section 5.2.2. An optical bubble size distribution measurement setup consisting of two cameras including illumination, was attached to the tank to capture the bubble characteristics during systematic measurements, see section 5.1.1. Measurements covering different kinetic energies for the water jet entraining the bubbles were conducted. Several additives to the waters were tested. To investigate the different impacts of bubbles in fresh and sea water, the experimental conditions include measurements with NaCl dissolved in the water. To model the effect of contamination with surfactants measurements with the surface active substance Triton X-100 were conducted. Additional measurements with n-butanol and glycerol were performed to explore the effect of different surface tension and viscosity. It proved that the effect of surface tension cannot be studied by the addition of butanol. Small amounts of n-butanol alter the bubble distribution massively, due to a bubble coalescence suppression effect, which covers the effects of surface tension, see section 6.2.1.

The comparison of the acquired transfer velocity data with existing models shows that simple power law dependencies used to model the diffusivity and solubility dependence, used for example by Asher et al. [4], are not capable of describing the transfer dependency over the whole range of solubilities. This originates from the incapability of this functional form to reproduce the correct asymptotic behaviors. The model proposed by Woolf et al. [72] eliminates this shortcoming. It was found that this model performs best in describing the transfer velocity data measured in this thesis. Anyhow its functional form is not motivated by physical principles and it could not be excluded that this model over fits the measured data. The conclusion of Woolf et al. [72], that the interstitial water plays a significant role for gas exchange in bubble clouds could not be verified. In this thesis a general model, which is derived using physical concept, is proposed, see section

9.2.1. It performs slightly worse ($45.7\,\%$ vs. $54.6\,\%$ rms error over all conditions). It introduces two parameters. α_t is the solubility at which the transition between the two limiting cases of bubble mediated gas exchange can be located. For lower solubilities the gas transfer is governed by the surface area of the bubbles, for larger solubilities the amount of gas transported depends on the volume flux carried by the bubbles. This parameter was found to be in the range of 0.05 - 0.44 for all conditions, whereas α_t was a factor of ~ 3 lower for conditions using salt water, see section 9.2.1. This means for example that the gas exchange for a gas like CO_2 with a solubility of $\alpha_{CO_2} \approx 0.83$ is completely controlled by the volume flux of entrained air. For gases in the low solubility limit the difference of the transfer velocities of fresh and salt water conditions amount to a factor of ~ 4. The influence of the surfactants on the transfer velocity was found to be lower than $5\,\%$. The addition of $\sim$ 20ppm of butanol altered the bubble distribution in a way that the transfer increased by one third. The fit of the exponent of the diffusivity D in the model of Woolf et al. [72] and the model presented here give strong indication that the transfer velocity at bubble surfaces scales as $D^{0.5}$ or weaker, see section 9.2.1.

With the bubble measurement setup it was only possible to detect $\sim\ 20\,\%$ or less of the bubble volume flux in conditions with deionized water. In conditions using salt water it was possible to measure up to $\sim\ 45\,\%$ of the bubble volume flux. Problems occurred mostly in high density regions located near to the point of air entrainment. The major fraction of gas transfer happens at these regions of the bubble cloud. This challenges the simulation of the influence of bubbles, generated by breaking events by adding bubble aerators to wave tanks during gas exchange measurements. Since Woolf et al. [72] used bubble aerators with low bubble densities compared to this measurements, they were able to reconstruct the gas flux almost completely. His conclusion that accurate bubble distribution measurements will allow for the calculation of the bubble mediated gas transfer can still be supported, though it is doubtful that measurements can be sufficiently accurate at high bubble densities with existing methods. Measurements in salt water seem more promising due to fewer large bubbles.

10.2. Outlook

The experiments could be conducted in a range of temperatures to investigate its combined effect on gas transfer and with respect to the specific effects, like influence on solubility, viscosity, diffusivity and surface tension.

To determine the magnitude of super-saturation and asymmetric transfer different experimental processes could be used. Invasion experiments in a closed configuration with and without bubbles

could be used to measure super-saturation effects. Asymmetric transfer is measurable by comparing invasion and evasion experiments, if the error in the invasion experiments could be reduced significantly. This could be achieved by either reducing the high accommodation times after inlet switching of the mass spectrometer or by using only one inlet during an experiment.

The problems of detecting bubbles at high bubble densities can be avoided by using a different bubble generation mechanism, e.g aeration devices for aquariums. If high densities at the gas entry points are avoided, it is likely that the whole bubble flux can be captured. This enables a more accurate investigation of the models for bubble mediated gas transfer. This approach has the disadvantage that the bubble generation process is not adapted from wave breaking, what may alter the resulting transfer rates.

Experiments for measuring the solubilities and diffusion coefficients for the tracers used in the thesis are in preparation by Jähne [34]. This will help to reduce the errors in determining the α and D dependencies of bubble mediated gas transfer.

Bibliography

[1] Alaee, M., Donelan, M. A., and Strachan, W. M. J.: Wind and wave effects on mass transfer velocities of halomethanes and SF_6 measured in a gas transfer flume, in: Air-Water Gas Transfer, Selected Papers, 3rd Intern. Symp. on Air-Water Gas Transfer, edited by Jähne, B. and Monahan, E., pp. 617–626, AEON, Hanau, doi: 10.5281/zenodo.10571, 1995.

[2] Alves, S., Orvalho, S., and Vasconcelos, J.: Effect of bubble contamination on rise velocity and mass transfer, Chemical Engineering Science, 60, 1–9, URL http://www.sciencedirect.com/science/article/B6TFK-4DB5576-6/2/a8d543a276dca02cf7923e7bfa34c30e, 2005.

[3] Asher, W. E., Karle, L. M., Higgins, B. J., Farley, P. J., Leifer, I. S., and Monahan, E. C.: The effect of bubble plume size on the parameterization of air-seawater gas transfer velocities, in: Air-Water Gas Transfer, Selected Papers, 3rd Intern. Symp. on Air-Water Gas Transfer, edited by Jähne, B. and Monahan, E., pp. 227–238, AEON, Hanau, doi: 10.5281/zenodo.10571, 1995.

[4] Asher, W. E., Karle, L. M., Higgins, B. J., Farley, P. J., Monahan, E. C., and Leifer, I. S.: The influence of bubble plumes on air-seawater gas transfer velocities, J. Geophys. Res., 101, 12 027–12 041, doi: 10.1029/96JC00121, 1996.

[5] Baldy, S. and Bourguel, M.: Bubbles Between the Wave Trough and Wave Crest Levels, J. Geophys. Res., 92, 2919–2929, URL http://dx.doi.org/10.1029/JC092iC03p02919, 1987.

[6] Balschbach, G.: Verschiedene Verfahren zur Visualisierung und Größenbestimmung von Gasblasen in Wasser, Diplomarbeit, Institut für Umweltphysik, Fakultät für Physik und Astronomie, Univ. Heidelberg, 1994.

[7] Bell, R. J., Short, R. T., van Amerom, F. H. W., and Byrne, R. H.: Calibration of an in situ membrane inlet mass spectrometer for measurements of dissolved gases and volatile organics in seawater, Environ. Sci. Technol., 41, 8123–8128, doi: 10.1021/es070905d, 2007.

[8] Bowyer, P. and Woolf, D.: Gas exchange and bubble-induced supersaturation in a wind-wave tank, J. Atmos. Oceanic Technol., 17, 1925–1936, doi: 10.1175/JTECH-1666.1, 2004.

[9] Broecker, H. C.: Effects of bubbles upon the gas exchange between atmosphere and ocean, in: Berichte aus dem Sonderforschungsbereich 94 Meeresforschung - Symposium on Capillary Waves and Gas Exchange, Trier July 2–6, 1979, edited by Broecker, H. C. and Hasse, L., 17, pp. 127–139, Univ. Hamburg, 1980.

[10] Broecker, H. C. and Hasse, L., eds.: Proceedings Symposium on Capillary Waves and Gas Exchange, Trier July 2–6, 1979, no. 17 in Berichte aus dem Sonderforschungsbereich 94 Meeresforschung, Universität Hamburg, 1980.

[11] Buckingham, M. J., Potter, J. R., and Epifanio, C. L.: Seeing Underwater with Background Noise, Scientific American, 274, 86–90, doi: 10.1038/scientificamerican0296-86, URL http://dx.doi.org/10.1038/scientificamerican0296-86, 1996.

[12] Chanson, H., Aoki, S., and Hoque, A.: Bubble Entrainment and Dispersion in Plunging Jet Flows: Freshwater vs. Seawater, Journal of Coastal Research, 22, 664–677, doi: 10.2112/03-0112.1, URL http://www.jcronline.org.pinnacle.allenpress.com/doi/abs/10.2112/03-0112.1, 2006.

[13] Clift, R., Grace, J. R., and Weber, M. E.: Bubbles, Droops and Particles, chap. 7. Ellipsoidal fluid particles, pp. 169–202, Academic Press, 1978.

[14] Craig, V. S. J.: Bubble coalescence and specific-ion effects, Current Opinion in Colloid & Interface Science, 9, 178 – 184, doi: DOI:10.1016/j.cocis.2004.06.002, URL http://www.sciencedirect.com/science/article/B6VRY-4CXN0NJ-1/2/ffaa1cb3f6f2d5d4cba2cb75574bc33c, 2004.

[15] Crank, J.: The Mathematics of Diffusion, Clarendon Press, Oxford, 2nd edn., 1975.

[16] Davis, G. E.: Scattering of Light by an Air Bubble in Water, J. Opt. Soc. Am., 45, 572–581, 1955.

[17] de Leeuw, G., Kunz, G. J., Caulliez, G., Woolf, D. K., Bowver, P., Leifer, I., Nightingale, P., Liddicoat, M., Rhee, T., Andreae, M. O., Larsen, S., Hansen, F. A., and Lun, S.: LUMINY - an overview, in: Gas Transfer at Water Surfaces, edited by Saltzman, E., Donelan, M., Drennan, W., and Wanninkhof, R., vol. 127 of *Geophysical Monograph*, pp. 291–294, American Geophysical Union, doi: 10.1029/GM127p0291, 2002.

[18] Degreif, K. and Jähne, B.: Gas exchange experiments using time resolved UV-spectroscopy, in: Verhandlungen der Deutschen Physikalischen Gesellschaft, Spring Conference, Munich, 22.-26.03.2004, Deutsche Physikalische Gesellschaft, URL http://old.dpg-tagungen.de/archive/2004/up_15.html, 2004.

[19] El Hammoumi, M., Achard, J. L., and Davoust, L.: Measurements of air entrainment by vertical plunging liquid jets, Experiments in Fluids, 32, 624–638,

doi: 10.1007/s00348-001-0388-1, URL http://dx.doi.org/10.1007/s00348-001-0388-1, 2002.

[20] EMVA 1288 Working Group: EMVA Standard 1288 - Standard for Characterization of Image Sensors and Cameras, doi: 10.5281/zenodo.10696, URL www.standard1288.org, 2010.

[21] Farmer, D. M., Vagle, S., and Booth, D.: A Free-Flooding Acoustical Resonator for Measurement of Bubble Size Distributions, J. Atmos. Oceanic Technol., 15, 1132–1146, 1998.

[22] Favre, E., Schaetzel, P., Nguygen, Q., Clément, R., and Néel, J.: Sorption, diffusion and vapor permeation of various penetrants through dense poly(dimethylsiloxane) membranes: a transport analysis, Journal of Membrane Science, 92, 169 – 184, doi: http://dx.doi.org/10.1016/0376-7388(94)00060-3, URL http://www.sciencedirect.com/science/article/pii/0376738894000603, 1994.

[23] Frössling, N.: Über die Verdunstung fallender Tropfen., Gerlands Beiträge zur Geophysik, 52, 170–216, 1938.

[24] Garbe, C. S., Rutgersson, A., Boutin, J., Delille, B., Fairall, C. W., Gruber, N., Hare, J., Ho, D., Johnson, M., de Leeuw, G., Nightingale, P., Pettersson, H., Piskozub, J., Sahlee, E., Tsai, W., Ward, B., Woolf, D. K., and Zappa, C.: Transfer across the air-sea interface, in: Ocean-Atmosphere Interactions of Gases and Particles, edited by Liss, P. S. and Johnson, M. T., pp. 55–112, Springer, doi: 10.1007/978-3-642-25643-1_2, 2014.

[25] Garrett, C., Li, M., and Farmer, D.: The Connection between Bubble Size Spectra and Energy Dissipation Rates in the Upper Ocean, J. Phys. Oceanogr., 30, 2163–2171, doi: 10.1175/1520-0485(2000)030<2163:TCBBSS>2.0.CO;2, URL http://journals.ametsoc.org/doi/abs/10.1175/1520-0485%282000%29030%3C2163%3ATCBBSS%3E2.0.CO%3B2, 2000.

[26] Geißler, P.: Depth-from-Focus zur Messung der Größenverteilung durch Wellenbrechen erzeugter Blasenpopulationen, Dissertation, IWR, Fakultät für Physik und Astronomie, Univ. Heidelberg, 1998.

[27] Gross, J. H.: Mass Spectrometry — A textbook, Springer Berlin Heidelberg, Heidelberg, doi: 10.1007/978-3-642-10711-5, 2011.

[28] Hinze, J. O.: Fundamentals of the hydrodynamic mechanism of splitting in dispersion processes, AIChE Journal, 1, 289–295, doi: 10.1002/aic.690010303, URL http://dx.doi.org/10.1002/aic.690010303, 1955.

[29] Honkanen, M., Saarenrinne, P., Stoor, T., and Niinimaki, J.: Recognition of highly overlapping ellipse-like bubble images, Meas. Sci. Technol., 16, 1760–1770,

doi: 10.1088/0957-0233/16/9/007, URL http://dx.doi.org/10.1088/0957-0233/16/9/007, 2005.

[30] IPCC: Climate Change 2007: The Physical Science Basis. Contribution of Working Group I to the Fourth Assessment Report of the Intergovernmental Panel on Climate Change, Cambridge University Press, Cambridge, United Kingdom and New York, NY, USA, URL http://www.ipcc.ch/, 2007.

[31] Jähne, B.: Zur Parametrisierung des Gasaustauschs mit Hilfe von Laborexperimenten, Dissertation, Institut für Umweltphysik, Fakultät für Physik und Astronomie, Univ. Heidelberg, doi: 10.5281/zenodo.10443, URL http://www.ub.uni-heidelberg.de/archiv/16796, iUP D-145, Link Nationalbibliothek http://d-nb.info/810123614, 1980.

[32] Jähne, B.: Digital Image Processing, Springer, Berlin, 6 edn., doi: 10.1007/3-540-27563-0, 2005.

[33] Jähne, B.: Air-sea gas exchange, in: Encyclopedia Ocean Sciences, edited by Steele, J. H., Turekian, K. K., and Thorpe, S. A., pp. 3434–3444, Elsevier, doi: 10.1016/B978-012374473-9.00642-1, invited, 2009.

[34] Jähne, B.: Simultaneous measurements of solubilities and diffusion coeffcients of volatile species in liquids, in: 7th SOPRAN Annual Meeting, Bremen, Germany, 25-26 March 2014, doi: 10.5281/zenodo.10409, 2014.

[35] Jähne, B., Fischer, K. H., Ilmberger, J., Libner, P., Weiss, W., Imboden, D., Lemnin, U., and Jaquet, J. M.: Parameterization of air/lake gas exchange, in: Gas transfer at water surfaces, edited by Brutsaert, W. and Jirka, G. H., pp. 469–476, Reidel, Hingham, MA, doi: 10.1007/978-94-017-1660-4_42, 1984.

[36] Jähne, B., Wais, T., and Barabas, M.: A new optical bubble measuring device; a simple model for bubble contribution to gas exchange, in: Gas transfer at water surfaces, edited by Brutsaert, W. and Jirka, G. H., pp. 237–246, Reidel, Hingham, MA, doi: 10.1007/978-94-017-1660-4_22, 1984.

[37] Keeling, R. F.: On the role of large bubbles in air-sea gas exchange and supersaturation in the ocean, J. Marine Res., 51, 237–271, doi: 10.1357/0022240933223800, 1993.

[38] Kim, Y.-K., Irikura, K., Rudd, M., Ali, M., Stone, P., Chang, J., Coursey, J., Dragoset, R., Kishore, A., Olsen, K., Sansonetti, A., Wiersma, G., Zucker, D., and Zucker, M.: NIST Electron-Impact Cross Section Database for Ionization and Excitation [Online]. Available: http://www.nist.gov/pml/data/ionization/, 2014.

[39] Koga, M.: Bubble entrainment in beaking wind waves, Tellus, 34, 481–489, doi: 10.1111/j.2153-3490.1982.tb01836.x, 1982.

[40] Kralchevsky, P. A., Danov, K. D., and Denkov, N. D.: Chemical Physics of Colloid Systems and Interfaces, in: Handbook of Surface and Colloid Chemistry, edited by Birdi, K. S., chap. 7, pp. 197–377, Taylor & Francis Ltd., 3rd edn., 2008.

[41] Krall, K. E.: Laboratory Investigations of Air-Sea Gas Transfer under a Wide Range of Water Surface Conditions, Dissertation, Institut für Umweltphysik, Fakultät für Physik und Astronomie, Univ. Heidelberg, URL http://www.ub.uni-heidelberg.de/archiv/14392, 2013.

[42] Kräuter, C.: Aufteilung des Transferwiderstands zwischen Luft und Wasser beim Austausch flüchtiger Substanzen mittlerer Löslichkeit zwischen Ozean und Atmosphäre, Diplomarbeit, Institut für Umweltphysik, Fakultät für Physik und Astronomie, Univ. Heidelberg, URL http://www.ub.uni-heidelberg.de/archiv/13010, 2011.

[43] LaPack, M. A., Tou, J. C., and Enke, C. G.: Membrane mass spectrometry for the direct trace analysis of volatile organic compounds in air and water, Analytical Chemistry, 62, 1265–1271, doi: 10.1021/ac00212a013, URL http://pubs.acs.org/doi/abs/10.1021/ac00212a013, 1990.

[44] Leifer, I. and De Leeuw, G.: Bubble mesurements in breaking-wave generated bubble plumes during the LUMINY wind-wave experiment in: Gas Transfer at Water Surfaces, edited by Donelan, M. A., Drennan, W. M., Saltzman, E. S., and Wanninkhof, R., vol. 127 of *Geophysical Monograph*, pp. 303–309, doi: 10.1029/GM127p0303, 2002.

[45] Leifer, I., De Leeuw, G., and Cohen, L. H.: Optical Measurement of Bubbles: System Design and Application, J. Atmos. Oceanic Technol., 20, 1317–1332, doi: 10.1175/1520-0426(2003)020<1317:OMOBSD>2.0.CO;2, URL http://journals.ametsoc.org/doi/abs/10.1175/1520-0426%282003%29020%3C1317%3AOMOBSD%3E2.0.CO%3B2, 2003.

[46] Lim, H.-J., Chang, K.-A., Su, C. B., and Chen, C.-Y.: Bubble velocity, diameter, and void fraction measurements in a multiphase flow using fiber optic reflectometer, Rev. Sci. Instrum., 79, 125105, doi: 10.1063/1.3053271, URL http://link.aip.org/link/?RSI/79/125105/1, 2008.

[47] Loewen, M. R. and Melville, W. K.: A model of the sound generated by breaking waves, Journal of the Acoustical Society of America, 90, 2075–2080, doi: 10.1121/1.401634, 1991.

[48] Maiß, M.: Modelluntersuchung zum Einfluss von Blasen auf den Gasaustausch zwischen Atmosphäre und Meer, Diplomarbeit, Institut für Umweltphysik, Fakultät für Physik und Astronomie, Univ. Heidelberg, iUP D-215, 1986.

[49] McGillis, W. R., Bock, E. J., and Frew, N. M.: Mass transfer from gas bubbles in fresh and seawater, in: Air-Water Gas Transfer, Selected Papers, 3rd Intern. Symp. on Air-Water

Gas Transfer, edited by Jähne, B. and Monahan, E., pp. 363–372, AEON, Hanau, doi: 10.5281/zenodo.10571, 1995.

[50] Memery, L. and Merlivat, L.: Modelling of gas flux through bubbles at the air-water interface, Tellus B, 37B, 272–285, doi: 10.1111/j.1600-0889.1985.tb00075.x, 1985.

[51] Merlivat, L. and Memery, L.: Gas exchange across an air-water interface: experimental results and modeling of bubble contribution to transfer, J. Geophys. Res., 88, 707–724, doi: 10.1029/JC088iC01p00707, 1983.

[52] Mesarchaki, E., Kräuter, C., Krall, K. E., Bopp, M., Helleis, F., Williams, J., and Jähne, B.: Measuring air-sea gas exchange velocities in a large scale annular wind-wave tank, Ocean Sci. Discuss., 11, 1643–1689, doi: 10.5194/osd-11-1643-2014, 2014.

[53] Mischler, W.: Entwicklung eines Experiments zur Messung von Blasendichten und blaseninduziertem Gasaustausch, Diplomarbeit, Institut für Umweltphysik, Fakultät für Physik und Astronomie, Univ. Heidelberg, 2010.

[54] Mischler, W. and Jähne, B.: Optical measurements of bubbles and spray in wind/water facilities at high wind speeds, in: 12th International Triennial Conference on Liquid Atomization and Spray Systems 2012, Heidelberg (ICLASS 2012), doi: 10.5281/zenodo.10957, 2012.

[55] Mächler, L., Brennwald, M. S., and Kipfer, R.: Membrane inlet mass spectrometer for the quasi-continuous on-site analysis of dissolved gases in groundwater, Environ. Sci. Technol., 46, 8288–8296, doi: 10.1021/es3004409, 2012.

[56] Nielsen, P.: The Motion of Suspended Particles, in: Coastal Bottom Boundary Layers and Sediment Transport, chap. 4, pp. 161–200, World Scientific Publishing Co., doi: 10.1142/9789812796035_0004, URL http://www.worldscientific.com/doi/abs/10.1142/9789812796035_0004, 1992.

[57] Patro, R., Leifer, I., and Bowyer, P.: Better bubble process modeling: improved bubble hydrodynamics parameterization, in: Gas Transfer at Water Surfaces, edited by Donelan, M. A., Drennan, W. M., Saltzman, E. S., and Wanninkhof, R., vol. 127 of *Geophysical Monograph*, pp. 315–320, doi: 10.1029/GM127p0315, 2002.

[58] Robb, W. L.: Thin silicone membranes - their permeation properties and some applications, Annals of the New York Academy of Sciences, 146, 119–137, doi: 10.1111/j.1749-6632.1968.tb20277.x, URL http://dx.doi.org/10.1111/j.1749-6632.1968.tb20277.x, 1968.

[59] Rodrigues, R. and Rubio, J.: New basis for measuring the size distribution of bubbles, Minerals Engineering, 16, 757 – 765, doi: http://dx.doi.org/10.1016/S0892-6875(03)00181-X, URL http://www.sciencedirect.com/science/article/pii/S089268750300181X, 2003.

[60] Rojas, G. and Loewen, M. R.: Fiber-optic probe measurements of void fraction and bubble size distributions beneath breaking waves, Exp. Fluids, 43, 895–906, doi: 10.1007/s00348-007-0356-5, 2007.

[61] Rudge, M. R. H.: Theory of the Ionization of Atoms by Electron Impact, Rev. Mod. Phys., 40, 564–590, doi: 10.1103/RevModPhys.40.564, URL http://link.aps.org/doi/10.1103/RevModPhys.40.564, 1968.

[62] Scott, J. C.: An optical probe for measuring water wave slopes, Journal of Physics E Scientific Instruments, 7, 747–749, doi: 10.1088/0022-3735/7/9/021, 1974.

[63] Stokes, M. and Deane, G.: A new optical instrument for the study of bubbles at high void fractions within breaking waves, Oceanic Engineering, IEEE Journal of, 24, 300 –311, doi: 10.1109/48.775292, 1999.

[64] Terray, E., Donelan, M., Agrawal, Y., Drennan, W., Kahma, K., Hwang, P., and Kitaigorodskii, S.: Estimates of Kinetic Energy Dissipation under Breaking Waves, J. Phys. Oceanogr., 26, 792–807, doi: 10.1175/1520-0485(1996)026<0792:EOKEDU>2.0.CO;2, 1996.

[65] Thomanek, K., Zielinski, O., Sahling, H., and Bohrmann, G.: Automated gas bubble imaging at sea floor - a new method of in situ gas flux quantification, Ocean Sci. Discuss., 7, 291–334, doi: 10.5194/osd-7-291-2010, URL http://www.ocean-sci-discuss.net/7/291/2010/, 2010.

[66] Tyroller, L.: Fractionation of Ne and Ar isotopes by molecular diffusion in water, Geochimica et Cosmochimica Acta, 136, 60–66, doi: 10.1016/j.gca.2014.03.040, 2014.

[67] Upstill-Goddard, R.: Simultaneous high-precision measurements of methane and nitrous oxide in water and seawater by single phase equilibration gas chromatography, Deep Sea Research Part I: Oceanographic Research, 43, 1669–1682, doi: 10.1016/S0967-0637(96)00074-X, 1996.

[68] Vasconcelos, J. M. T., Orvalho, S. P., and Alves, S. S.: Gas-liquid mass transfer to single bubbles: Effect of surface contamination, AIChE Journal, 48, 1145–1154, doi: 10.1002/aic.690480603, 2002.

[69] Wanninkhof, R., Asher, W., and Monahan, E.: The influence of bubbles on air-water gas exchange: results from gas transfer experiments during WABEX-93, in: Air-Water Gas Transfer, Selected Papers, 3rd Intern. Symp. on Air-Water Gas Transfer, edited by Jähne, B. and Monahan, E., pp. 239–254, AEON, Hanau, doi: 10.5281/zenodo.10571, 1995.

[70] Wetzel, R. C., Baiocchi, F. A., Hayes, T. R., and Freund, R. S.: Absolute cross sections for electron-impact ionization of the rare-gas atoms by the fast-neutral-beam method, Phys. Rev. A, 35, 559–577, doi: 10.1103/PhysRevA.35.559, 1987.

[71] Woolf, D.: Bubbles and their role in gas exchange, in: The sea surface and global change, edited by Liss, P. S. and Duce, R. A., chap. 6, Cambridge Univ Press, doi: 10.1017/CBO9780511525025.007, 1997.

[72] Woolf, D., Leifer, I., Nightingale, P., Rhee, T., Bowyer, P., Caulliez, G., de Leeuw, G., Larsen, S., Liddicoat, M., Baker, J., and Andreae, M.: Modelling of bubble-mediated gas transfer: Fundamental principles and a laboratory test, J. Marine Syst., 66, 71–91, doi: 10.1016/j.jmarsys.2006.02.011, 2007.

[73] Zhang, X.: Contribution to the global air-sea CO_2 exchange budget from asymmetric bubble-mediated gas transfer, Tellus B, 64, URL http://www.tellusb.net/index.php/tellusb/article/view/17260, 2012.

A. Full Solution for the Model of Gas Exchange in the Bubble Tank

The solution for the full coupled system of differential equations (2.59) was found by *Mathematica*® and is given by:

$$\begin{aligned} c_a(t) =& \frac{1}{\sqrt{\beta_1}} e^{-\frac{\beta_3 t}{2\alpha V_a V_w}} \Bigg(-\sinh(\beta_2 t)(V_w(A\alpha k_A(\alpha(c_{a_0}+c_{b_0})-2c_{w_0}) \\ & + Q(\alpha(c_{a_0}-2c_{b_0}\lambda+c_{b_0})+2c_{w_0}(\lambda-1)))+V_a(c_{b_0}-c_{a_0})(A\alpha k_A-\lambda Q+Q)) \\ & + c_{b_0}\sqrt{\beta_1}\sinh\left(\frac{1}{2}t\left(\frac{A\alpha k_A-\lambda Q+Q}{\alpha V_w}+\frac{A\alpha k_A+Q}{V_a}\right)\right) \\ & + c_{b_0}\sqrt{\beta_1}\cosh\left(\frac{\beta_3 t}{2\alpha V_a V_w}\right)+\sqrt{\beta_1}(c_{a_0}-c_{b_0})\cosh(\beta_2 t)\Bigg) \end{aligned} \tag{.1}$$

$$\beta_1 = (A\alpha k_A(\alpha V_w+V_a)+Q(\alpha V_w-\lambda V_a+V_a))^2-4\alpha Q V_a V_w(A\alpha k_A-\lambda Q+Q) \tag{.2}$$

$$\beta_2 = \frac{\sqrt{\beta_1}}{2\alpha V_a V_w} \tag{.3}$$

$$\beta_3 = A\alpha k_A(\alpha V_w+V_a)+Q(\alpha V_w-\lambda V_a+V_a) \tag{.4}$$

$$\begin{aligned} c_w(t) =& \frac{1}{2\sqrt{\beta_4}} e^{-\frac{t\beta_7}{2\alpha V_a V_w}} \Bigg((2\alpha c_{b_0}\sqrt{\beta_4}e^{\frac{\beta_7 t}{2\alpha V_a V_w}}-\alpha c_{b_0}\sqrt{\beta_4}e^{\beta_5 t} \\ & -\alpha c_{b_0}\sqrt{\beta_4}e^{\beta_6 t}+c_{w_0}\sqrt{\beta_4}e^{\beta_5 t}+c_{w_0}\sqrt{\beta_4}e^{\beta_6 t}-e^{\beta_5 t}\beta_8+e^{\beta_6 t}\beta_8\Bigg) \end{aligned} \tag{.5}$$

$$\begin{aligned} \beta_4 =& \alpha^2 V_w^2(A\alpha k_A+Q)^2+V_a^2(A\alpha k_A-\lambda Q+Q)^2 \\ & +2\alpha V_a V_w(A\alpha k_A-Q)(A\alpha k_A-\lambda Q+Q) \end{aligned} \tag{.6}$$

$$\beta_5 = \frac{\left(\lambda Q V_a+2\sqrt{\beta_4}\right)}{2\alpha V_a V_w} \tag{.7}$$

$$\beta_6 = \frac{\lambda Q}{2\alpha V_w} \tag{.8}$$

$$\beta_7 = (\alpha V_w+V_a)(A\alpha k_A+Q)+\sqrt{\beta_4} \tag{.9}$$

$$\begin{aligned} \beta_8 =& A\alpha k_A(V_a(\alpha(c_{b_0}-2c_{a_0})+c_{w_0})+\alpha V_w(\alpha c_{b_0}-c_{w_0})) \\ & +Q(\alpha c_{b_0}-c_{w_0})(\alpha V_w+(\lambda-1)V_a) \end{aligned} \tag{.10}$$

B. Technical Data

MIMS

pressure [torr]	Faraday		SEM	
	settle time [ms]	dwell time [ms]	settle time [ms]	dwell time [ms]
10^{-5}	6	20		
10^{-6}	6	20		
10^{-7}	6	20	6	20
10^{-8}	200	40	6	20
10^{-9}	1000	80	6	20
10^{-10}	2000	100	6	20
10^{-11}			200	40
10^{-12}			1000	100
10^{-13}			2000	1000

Table .1.: Default settle and dwell times for all pressure ranges

Tracer

D_2O 99.7 %

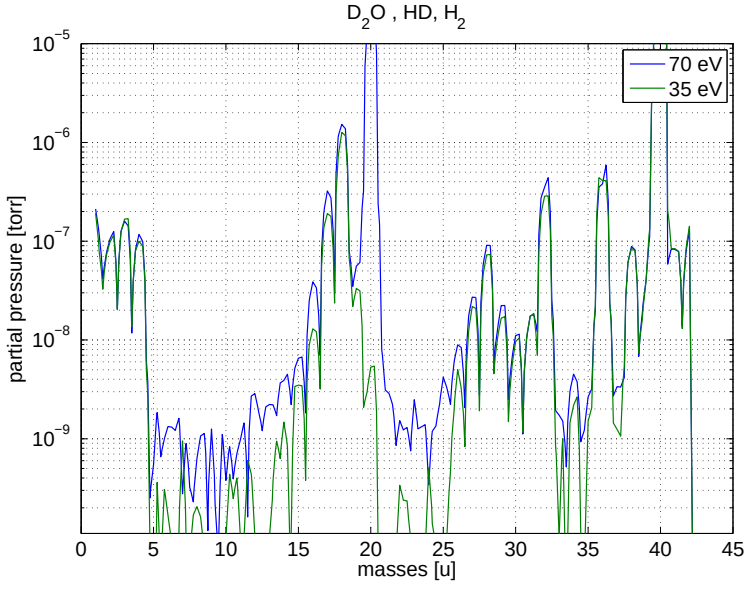

Figure .1.: Mass spectra for different ionization energies for D_2O

C_2H_2 Gas pureness 2.6. Bottled by *Air Liquide*. Data sheet available at: `http://www.airliquide.com/`

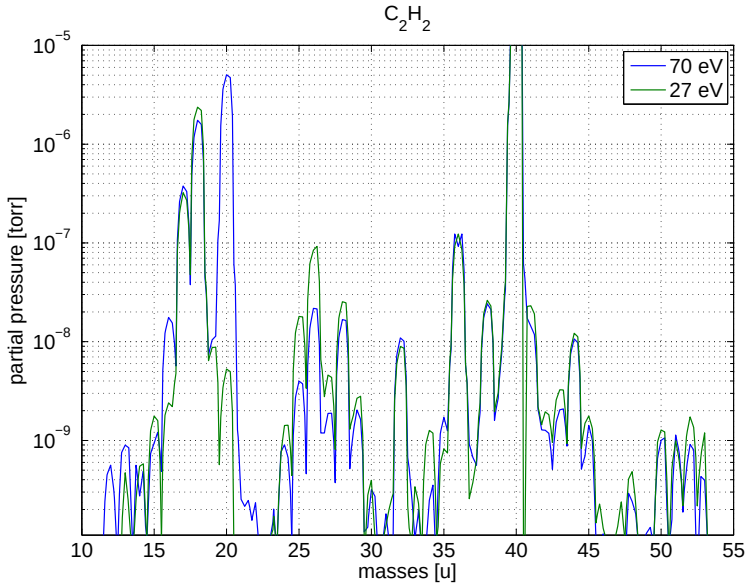

Figure .2.: Mass spectra for different ionization energies for C_2H_2

CHF_3 Bottled by *Tega*. Data sheet available at: `http://www.tega.de/`

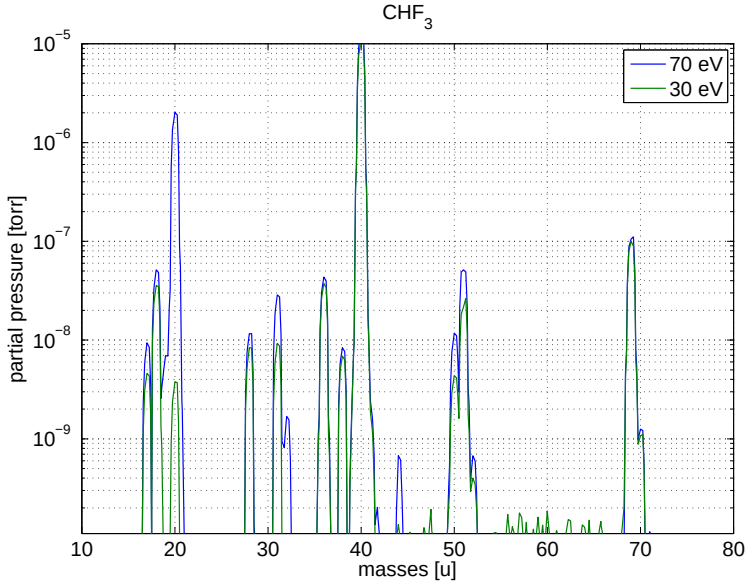

Figure .3.: Mass spectra for different ionization energies for CHF_3

CF_4 Bottled by *Tega*. Data sheet available at: `http://www.tega.de/`

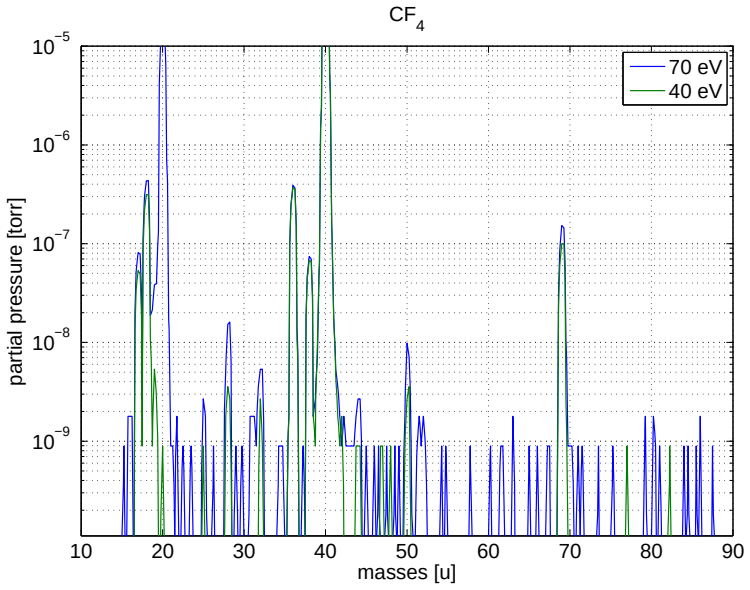

Figure .4.: Mass spectra for different ionization energies for CF_4

C_2HF_5 Bottled by *Tega*. Data sheet available at: `http://www.tega.de/`

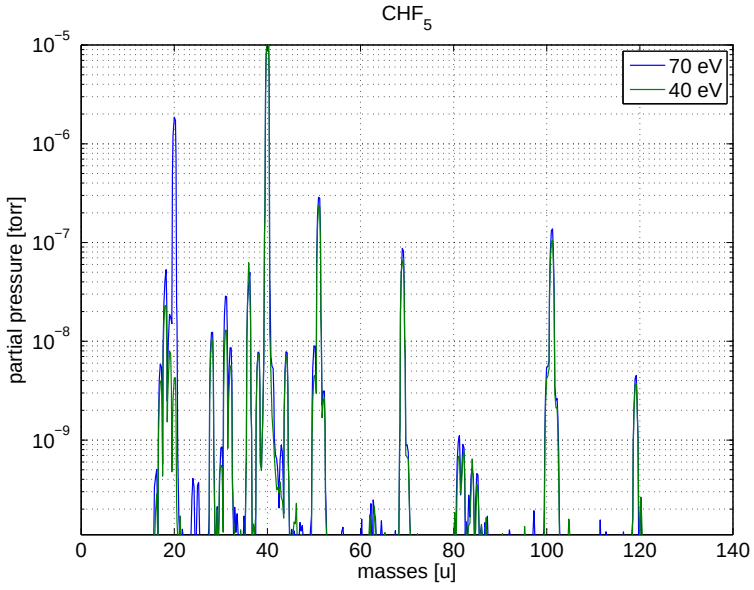

Figure .5.: Mass spectra for different ionization energies for C_2HF_5

Krypton Bottled by *Linde*. Data sheet available at: `http://www.linde-gas.com/`

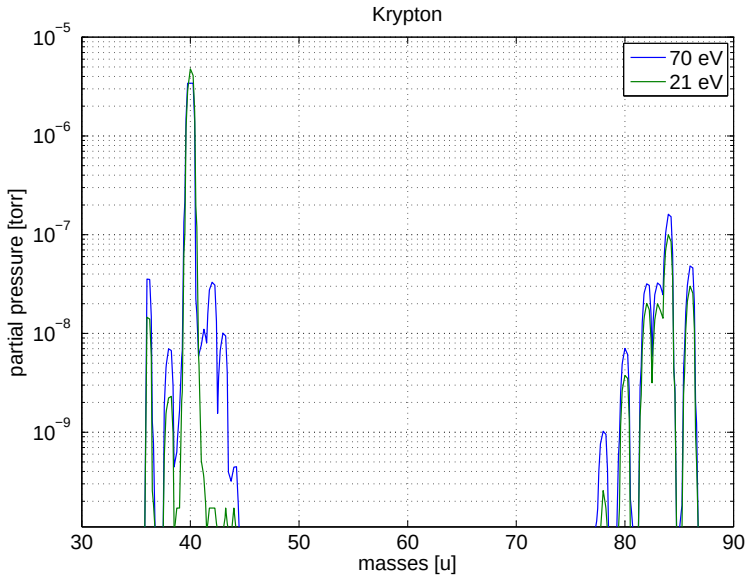

Figure .6.: Mass spectra for different ionization energies for Krypton

Xenon Bottled by *Linde*. Data sheet available at: `http://www.linde-gas.com/`

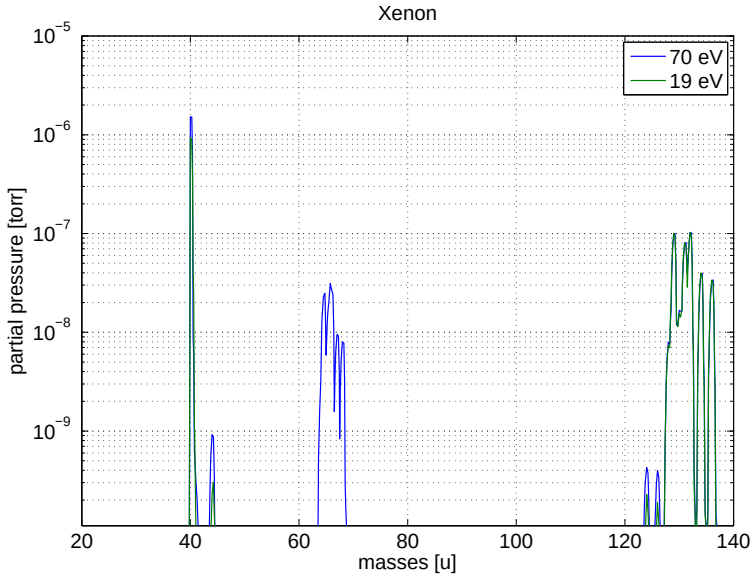

Figure .7.: Mass spectra for different ionization energies for Xenon

Neon Gas pureness 5.0. Bottled by *Air Liquide*. Data sheet available at: `http://www.airliquide.com/`

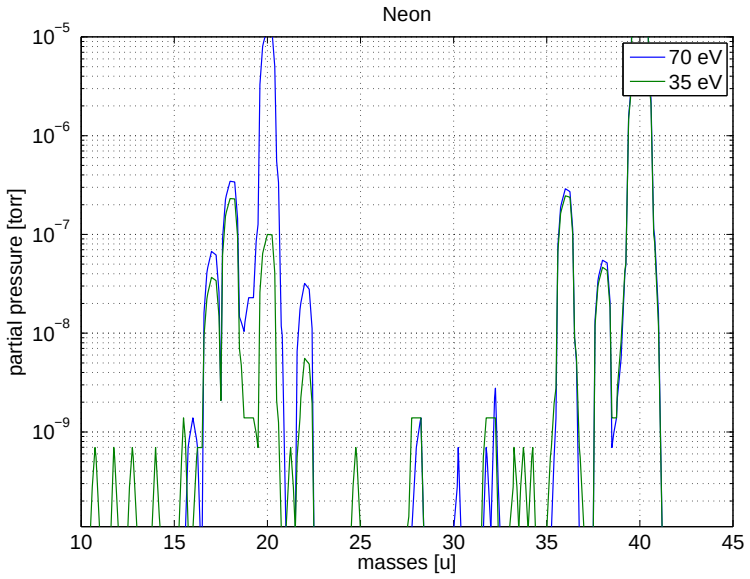

Figure .8.: Mass spectra for different ionization energies for Neon

Argon Gas pureness 5.0. Bottled by *Air Liquide*. Data sheet available at: `http://www.airliquide.com/`

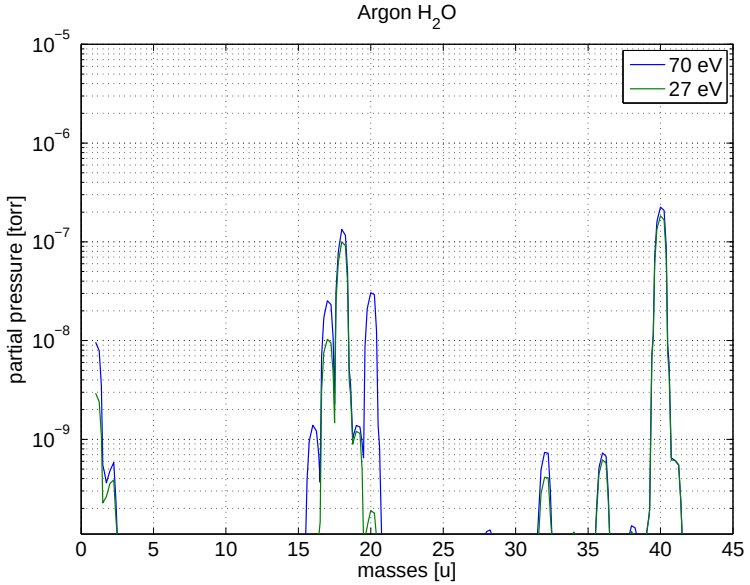

Figure .9.: Mass spectra for different ionization energies for Argon

N_2O Gas pureness 2.5. Bottled by *Air Liquide*. Data sheet available at: `http://www.airliquide.com/`

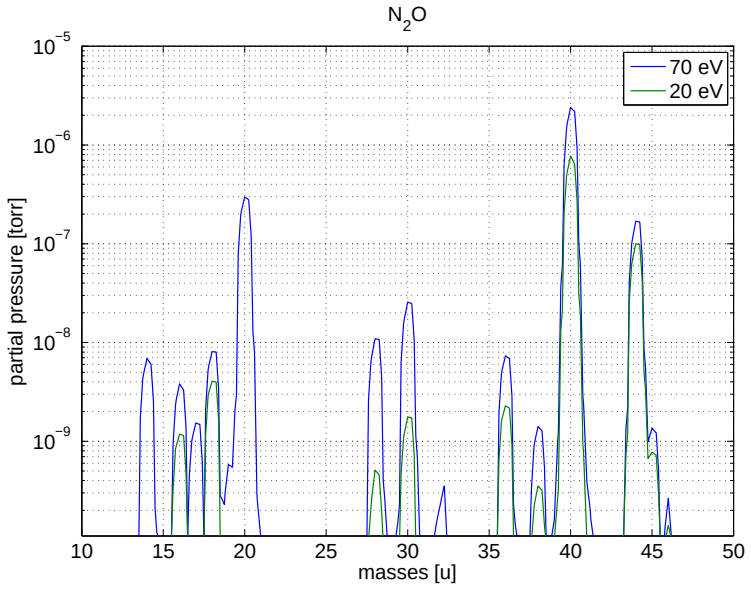

Figure .10.: Mass spectra for different ionization energies for N_2O

SF_6 Gas pureness 3.0. Bottled by *Air Liquide*. Data sheet available at: `http://www.airliquide.com/`

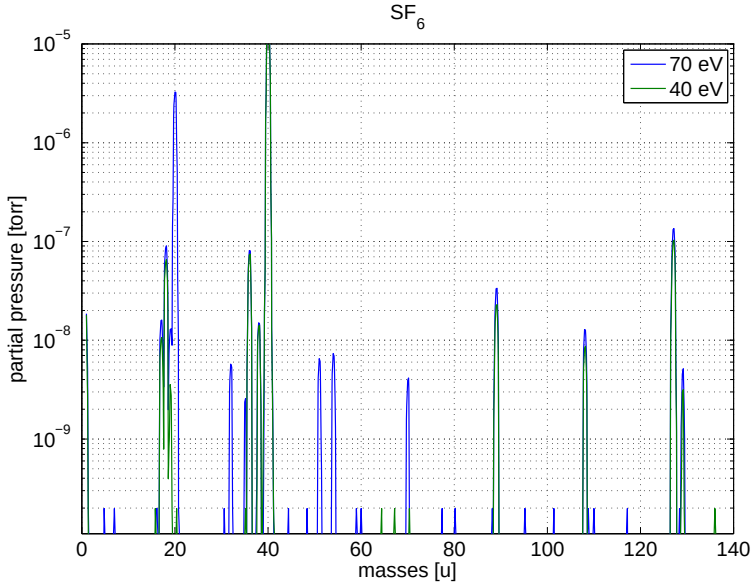

Figure .11.: Mass spectra for different ionization energies for SF_6

CH_3Cl Gas pureness 2.8. Bottled by *Air Liquide*. Data sheet available at: `http://www.airliquide.com/`

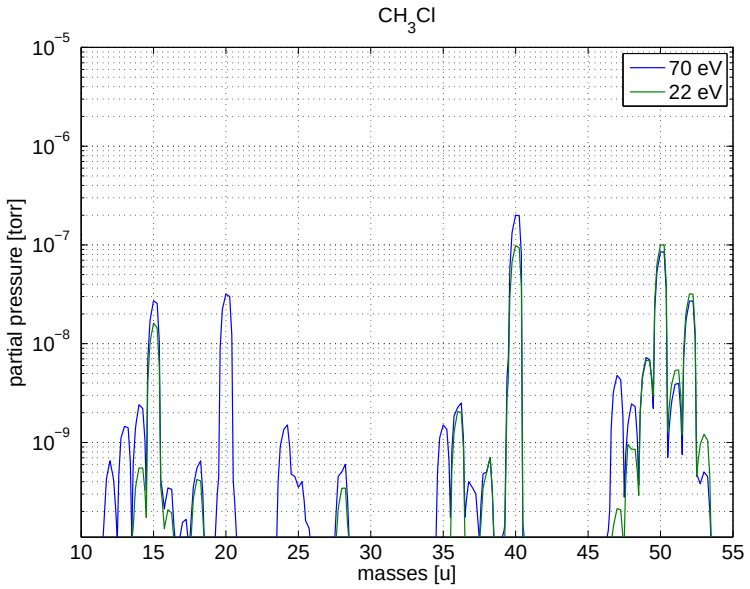

Figure .12.: Mass spectra for different ionization energies for CH_3Cl

Benzene Chemical grade p.a.

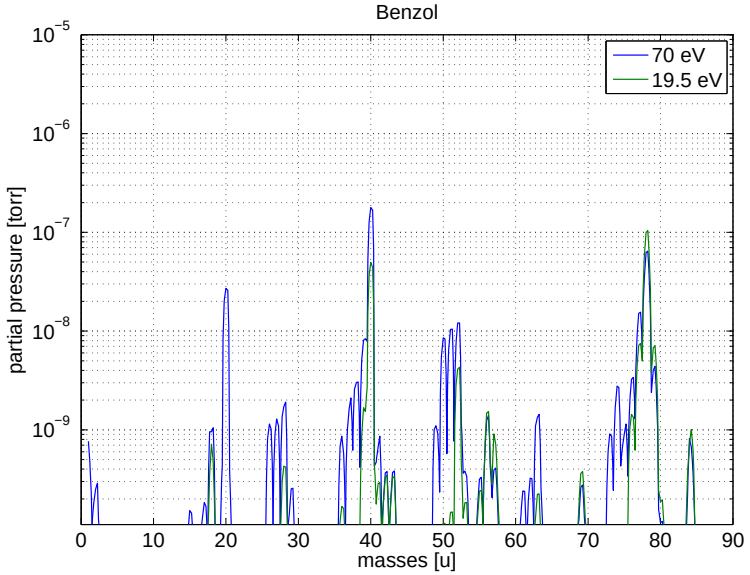

Figure .13.: Mass spectra for different ionization energies for benzene

DMS Chemical grade puriss. > 99.0 %. Produced by *Fluka*

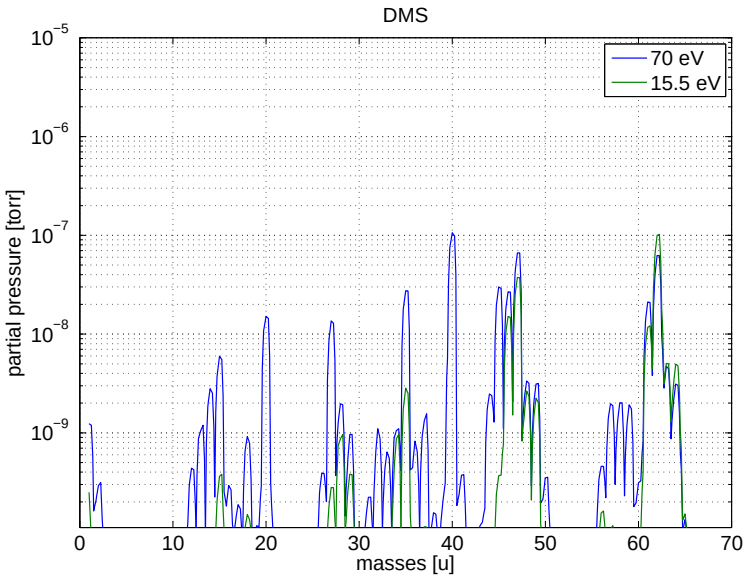

Figure .14.: Mass spectra for different ionization energies for DMS

-

C. Experimental Data

C.1. Bubble Properties

Pulsed Bubble Cloud

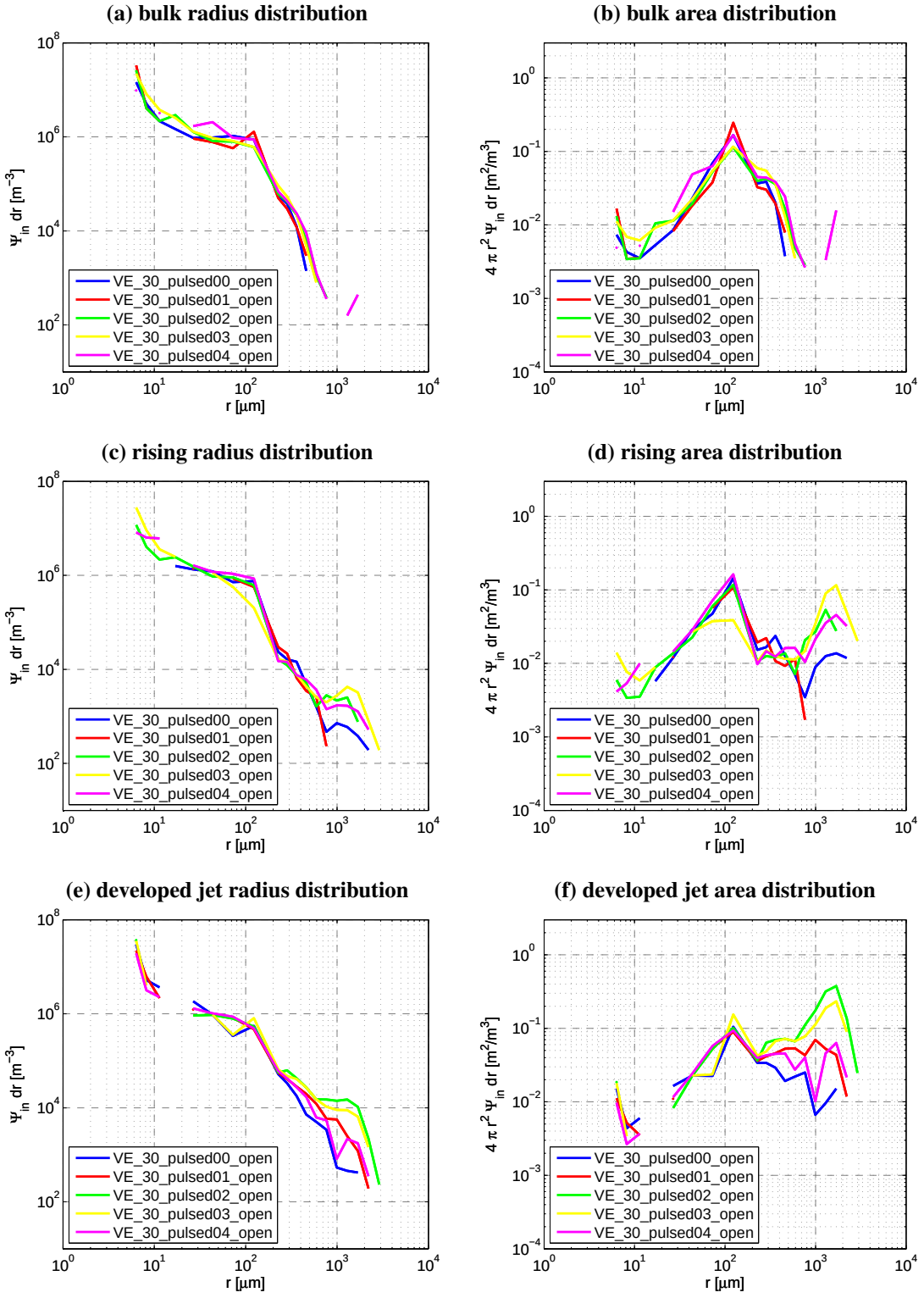

Figure .15.: Measured radius and area densities for all times in the VE_pulsed condition are shown. Three representative sampling positions are shown.

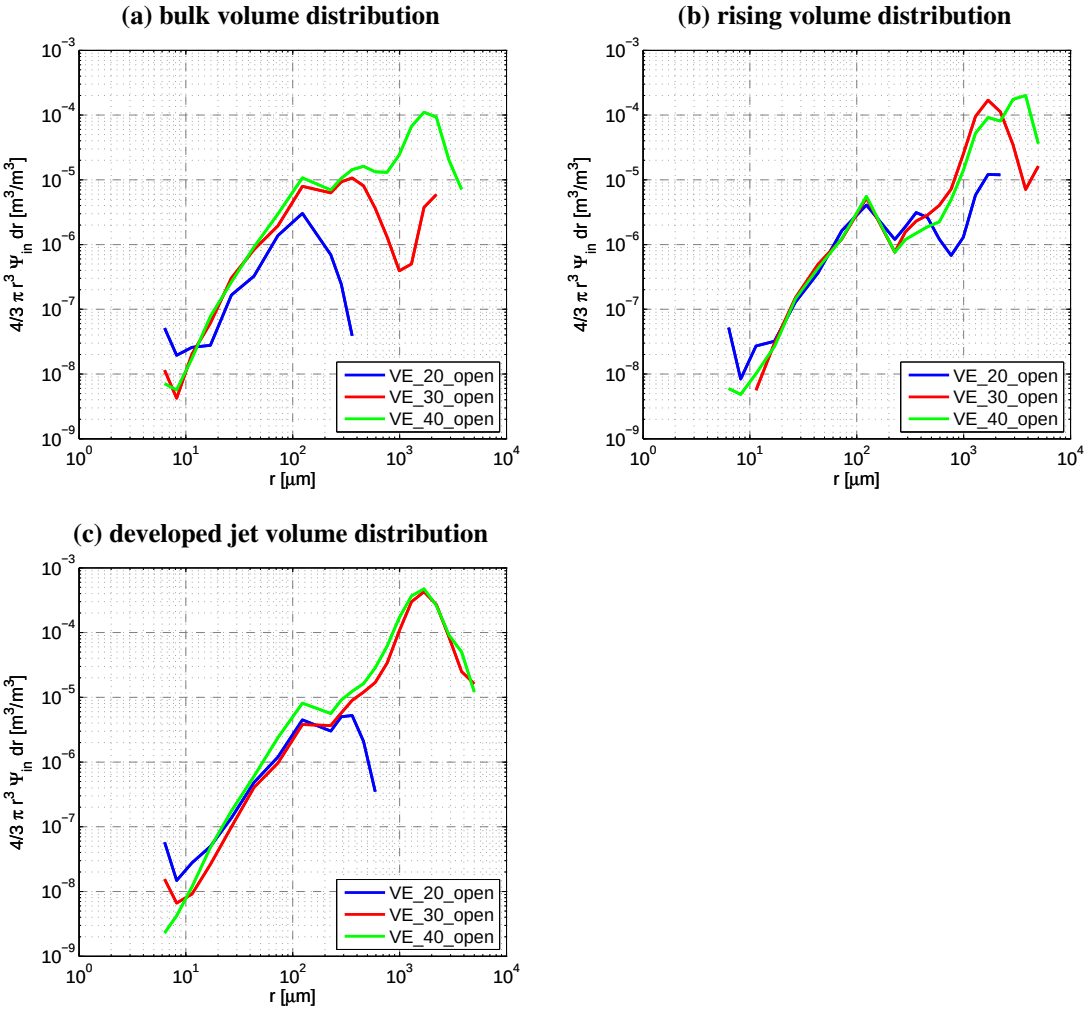

Figure .16.: Volume densities for all times in the VE_pulsed condition are shown. Three representative sampling positions are shown.

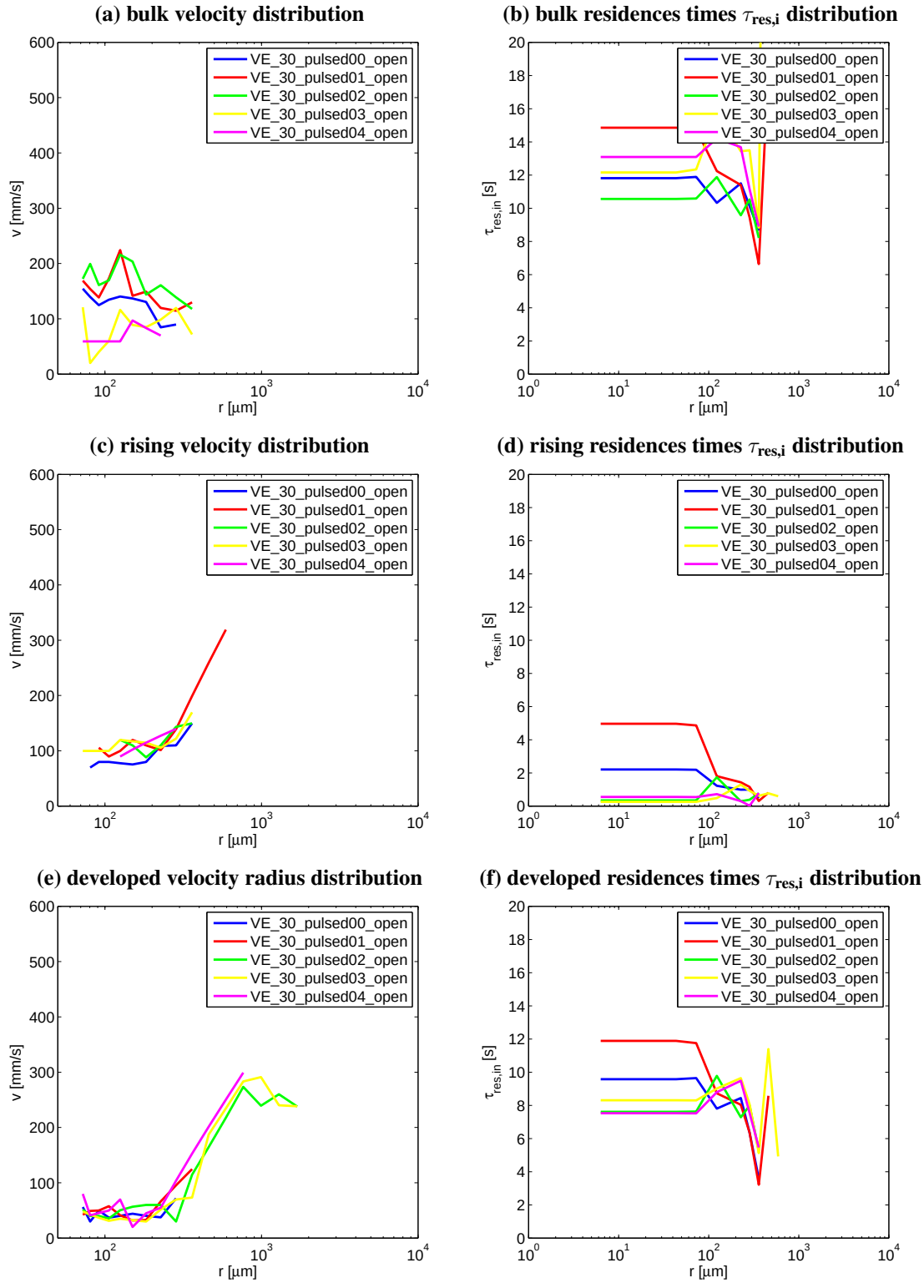

Figure .17.: Measured velocities v and residences times $\tau_{res,i}$ for bubbles with radius r. Three sampling positions are shown.

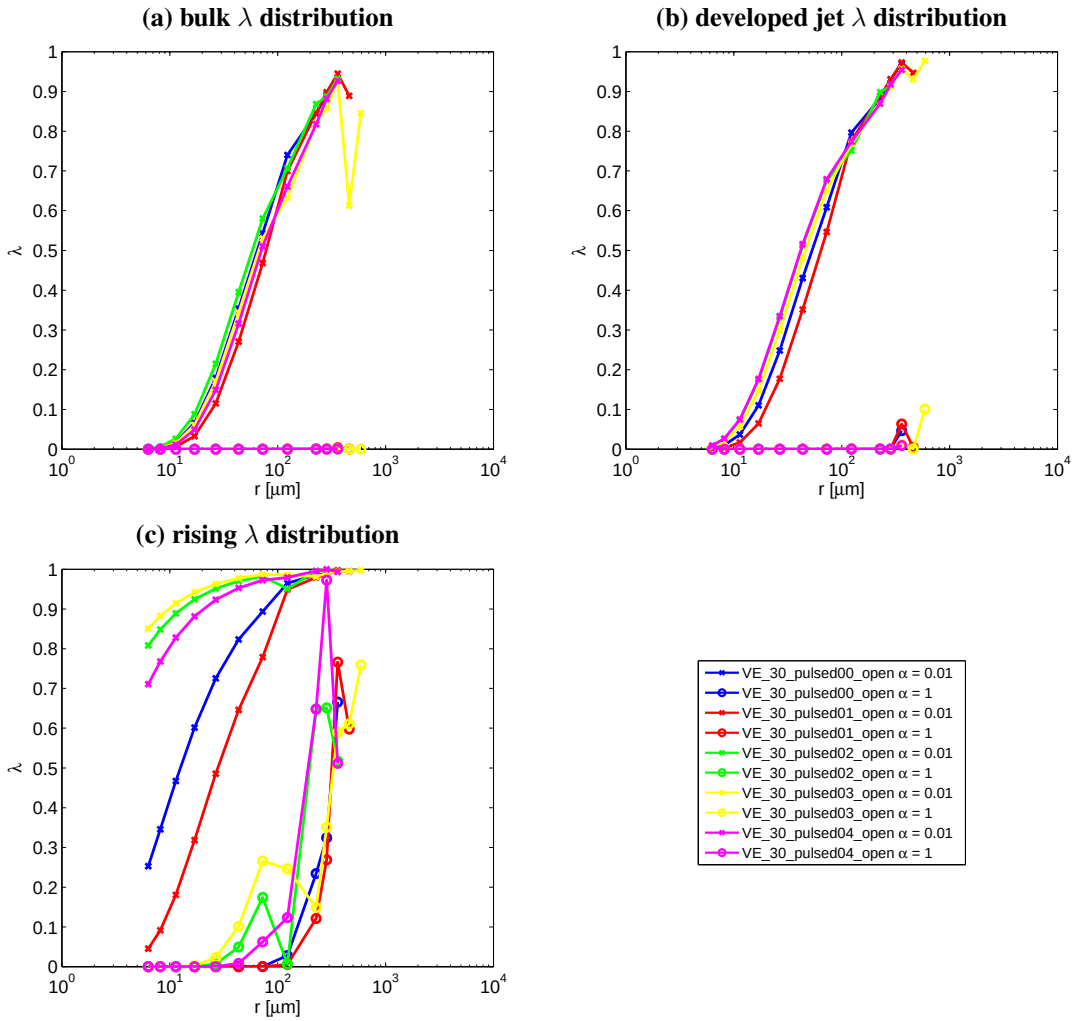

Figure .18.: Derived equilibration parameters λ for two different solubilities for three sampling positions in the tank. The calculation is based on eq. (8.15) using the calculated residence times $\tau_{res,i}$ and the model of a radius dependent transfer velocity for a single bubble k_b in the dirty case, see eq. (2.26)

transfer velocities clean

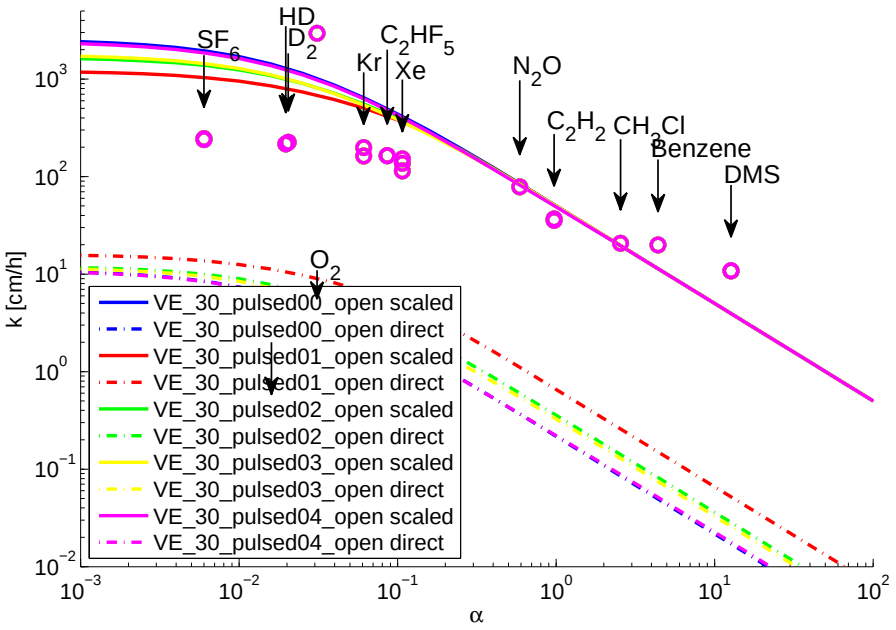

transfer velocities dirty

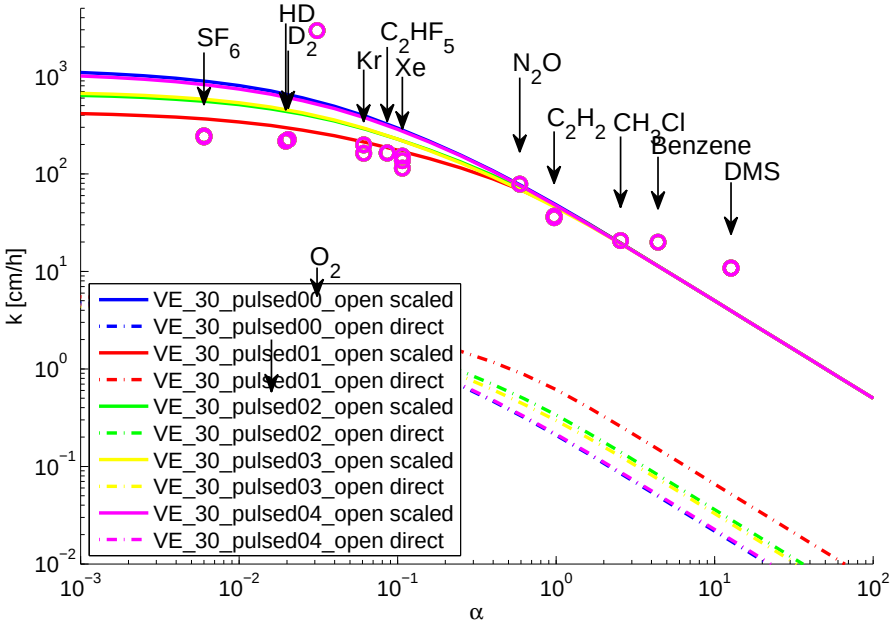

Figure .19.:

Salt water

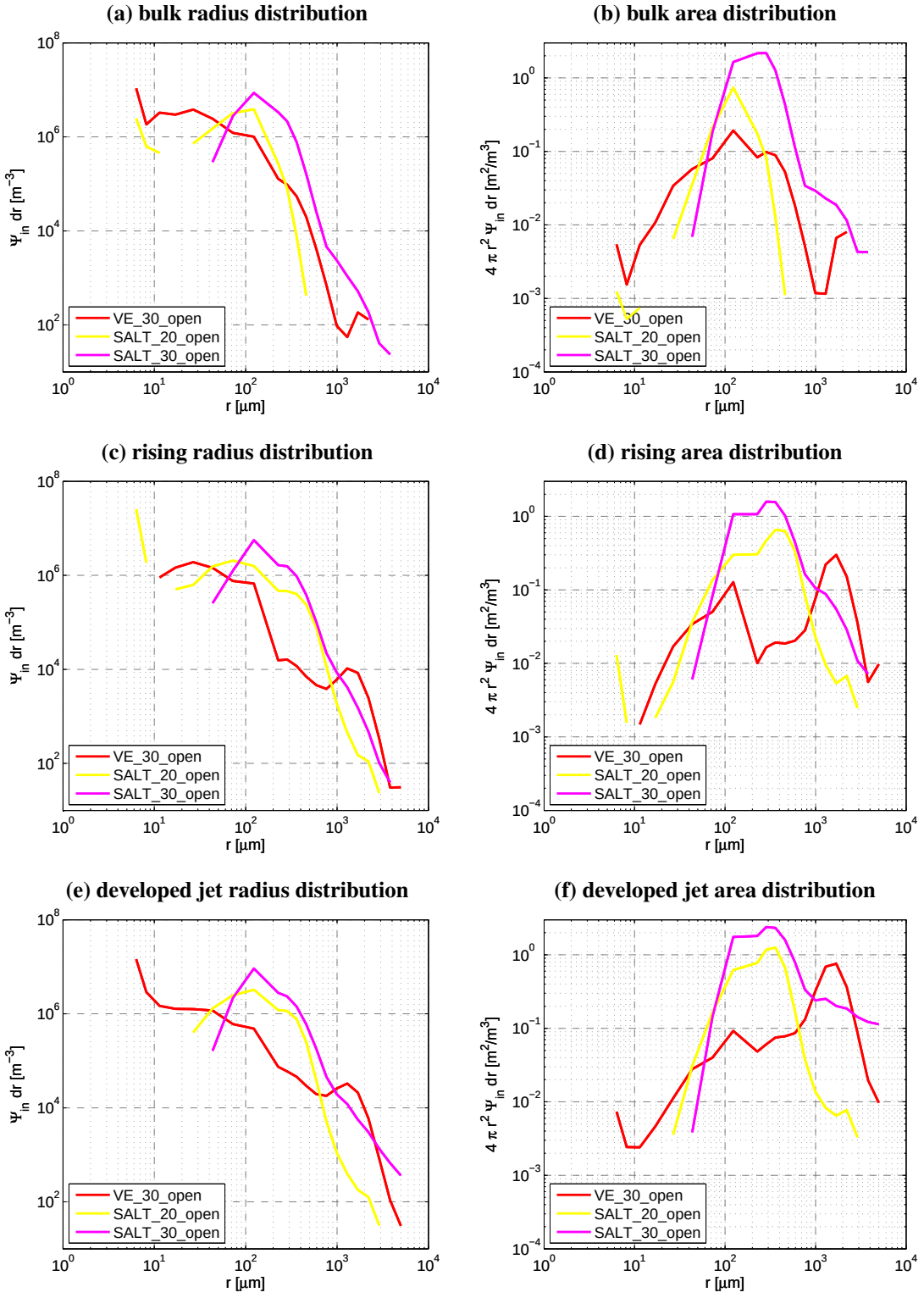

Figure .20.: Measured radius and area densities for all SALT conditions are shown. Three representative sampling positions are shown.

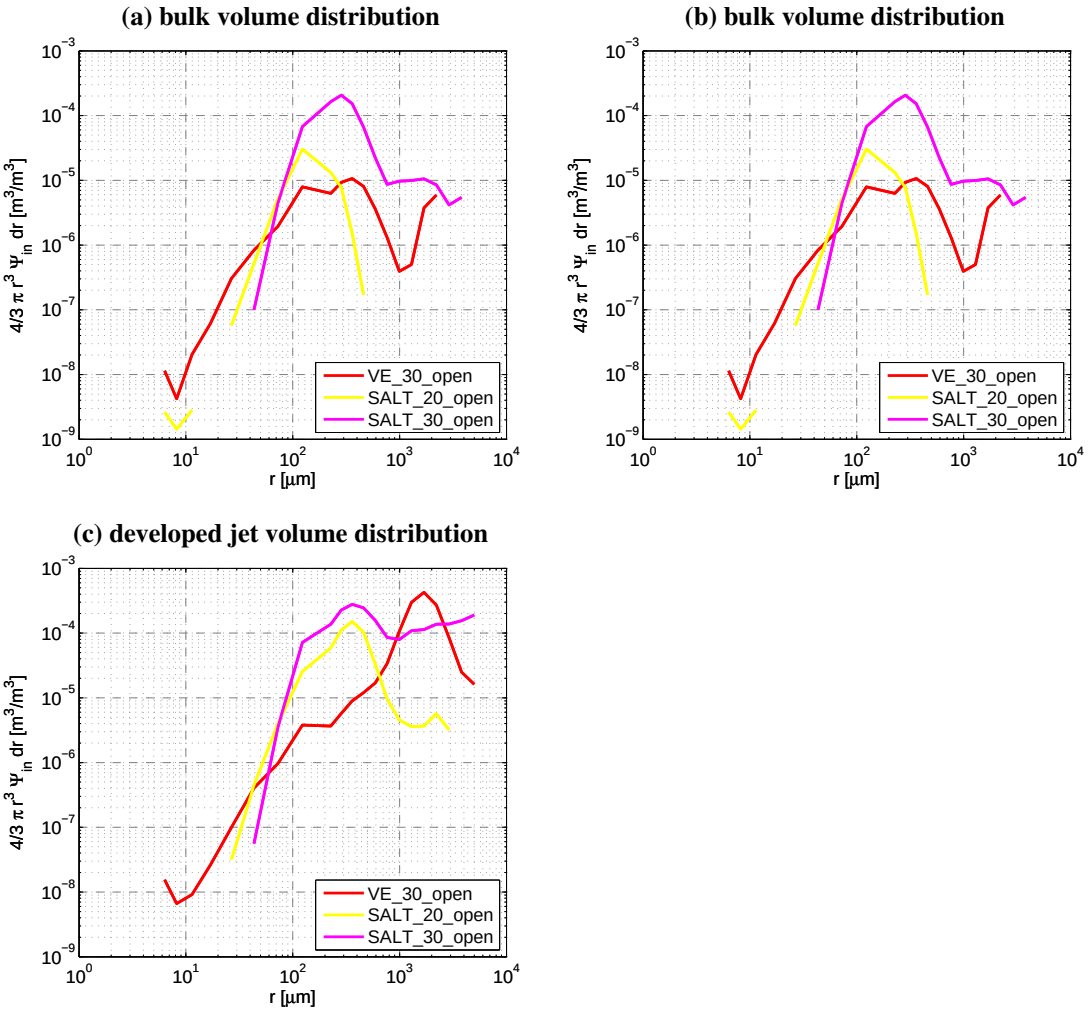

Figure .21.: Volume densities for all SALT conditions are shown. Three representative sampling positions are shown.

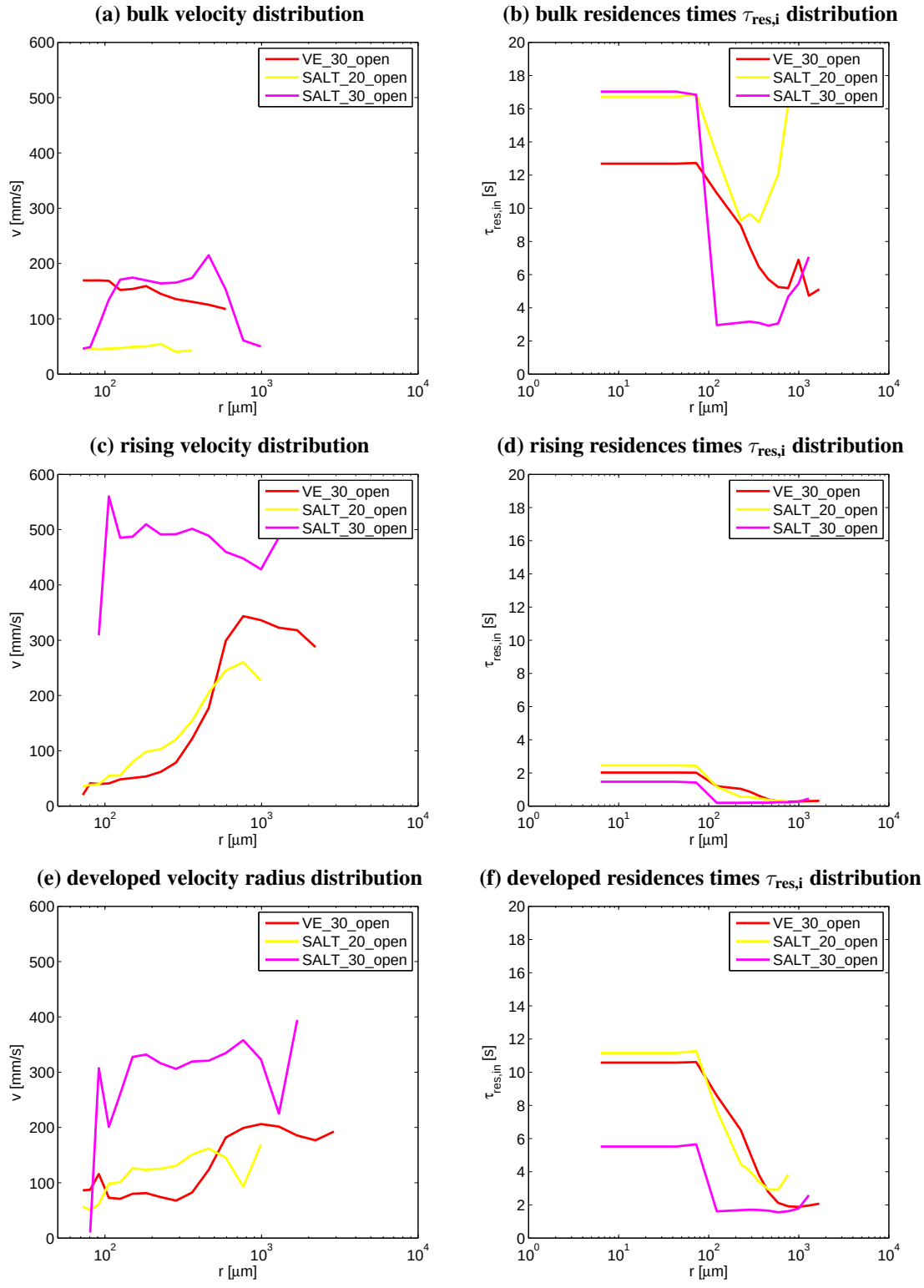

Figure .22.: Measured velocities v and residences times $\tau_{res,i}$ for bubbles with radius r. Three sampling positions are shown.

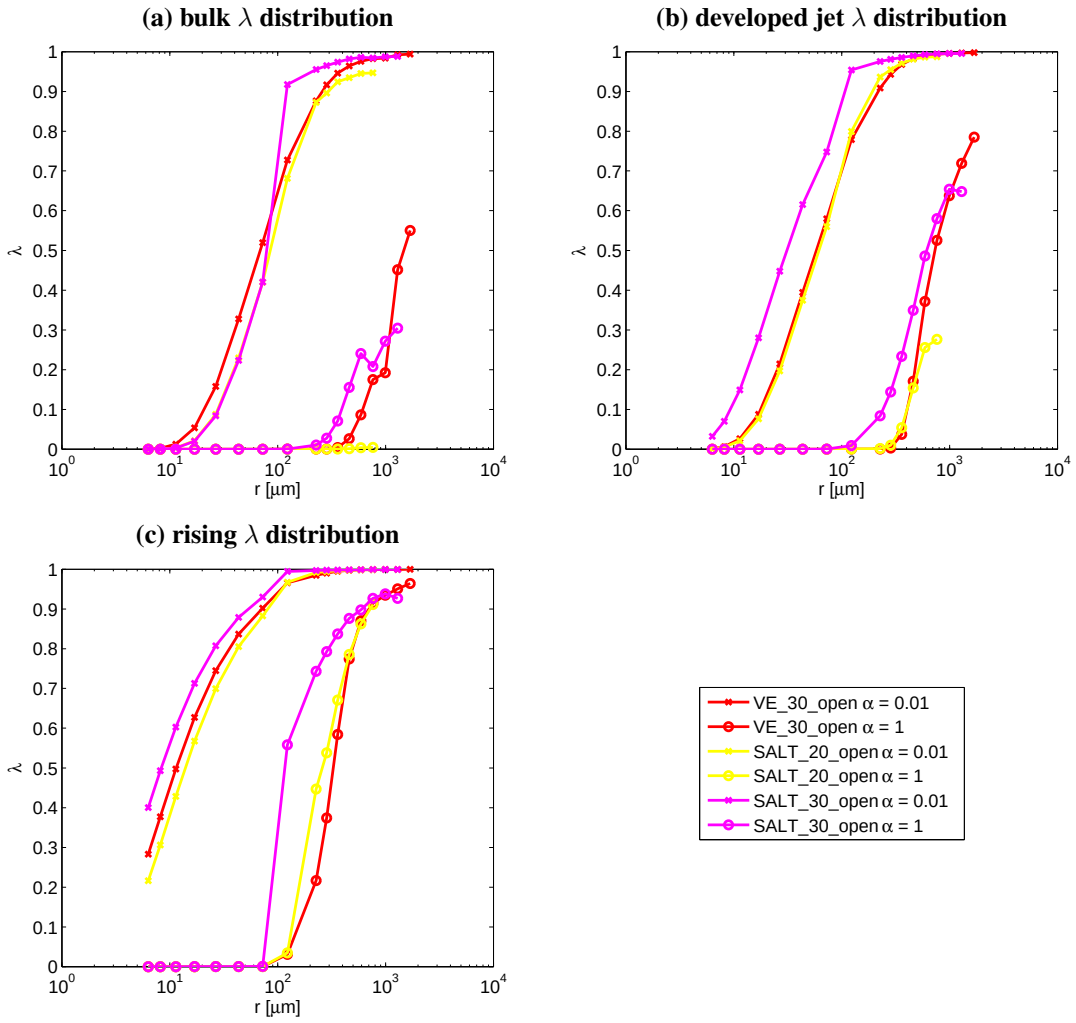

Figure .23.: Derived equilibration parameters λ for two different solubilities for three sampling positions in the tank. The calculation is based on eq. (8.15) using the calculated residence times $\tau_{\text{res,i}}$ and the model of a radius dependent transfer velocity for a single bubble k_b in the dirty case, see eq. (2.26)

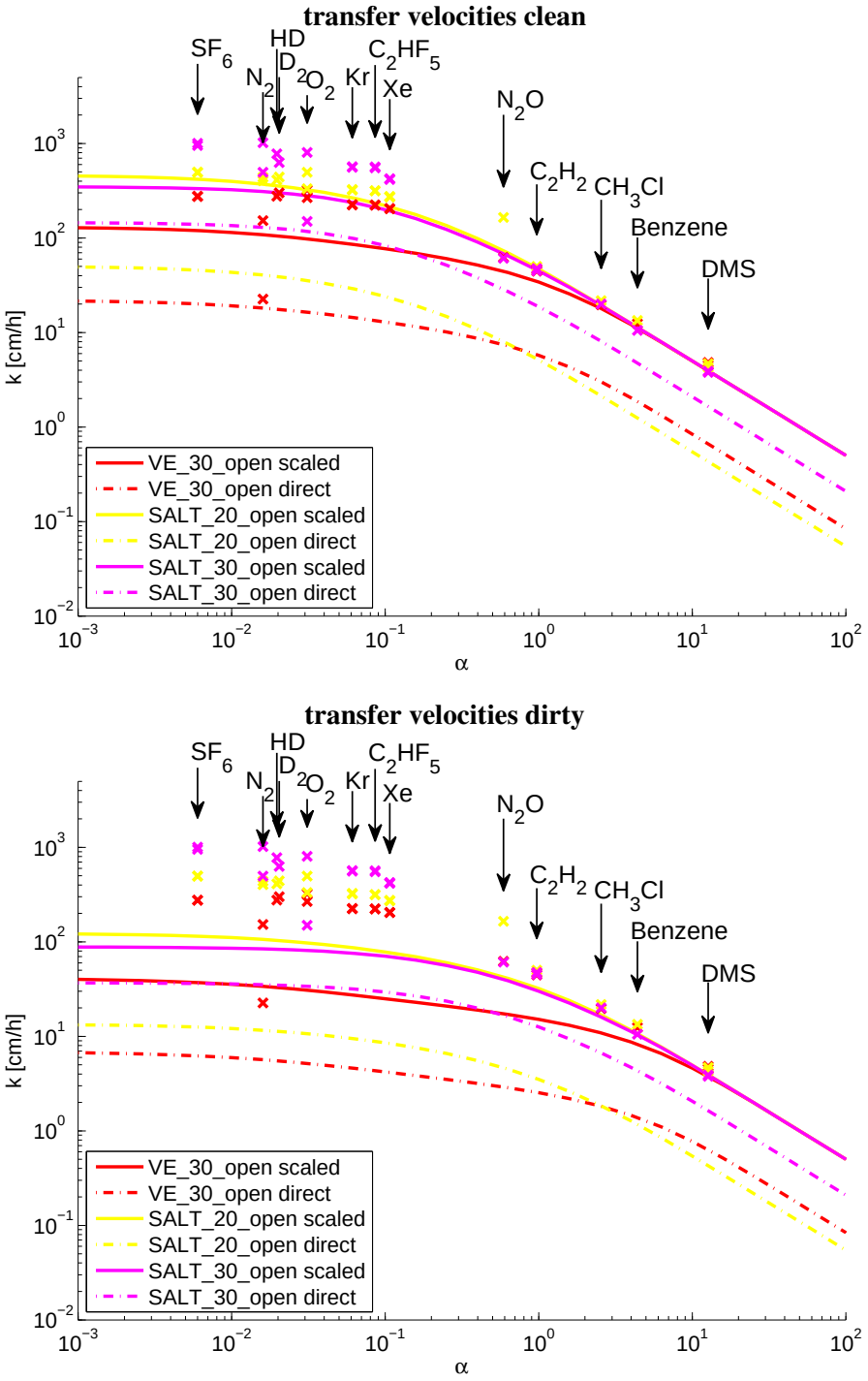
transfer velocities clean
SF6
HD
D2
N2
O2
Kr
C2HF5
Xe
N2O
C2H2
CH3Cl
Benzene
DMS
k [cm/h]
α
VE_30_open scaled
VE_30_open direct
SALT_20_open scaled
SALT_20_open direct
SALT_30_open scaled
SALT_30_open direct
transfer velocities dirty
SF6
HD
D2
N2
O2
Kr
C2HF5
Xe
N2O
C2H2
CH3Cl
Benzene
DMS
k [cm/h]
α
VE_30_open scaled
VE_30_open direct
SALT_20_open scaled
SALT_20_open direct
SALT_30_open scaled
SALT_30_open direct

Figure .24.:

Triton X

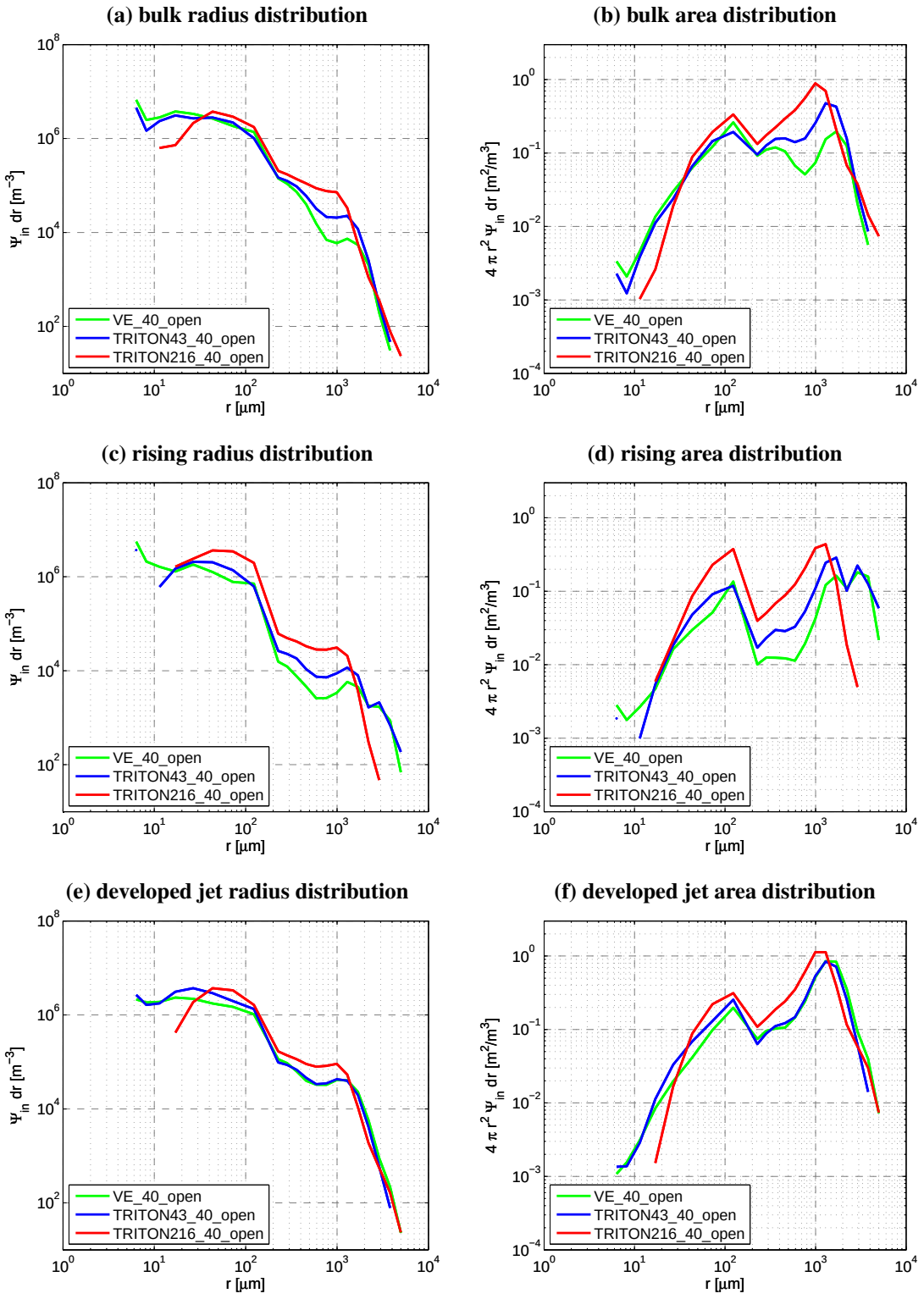

Figure .25.: Measured radius and area densities for all TRITON conditions are shown. Three representative sampling positions are shown.

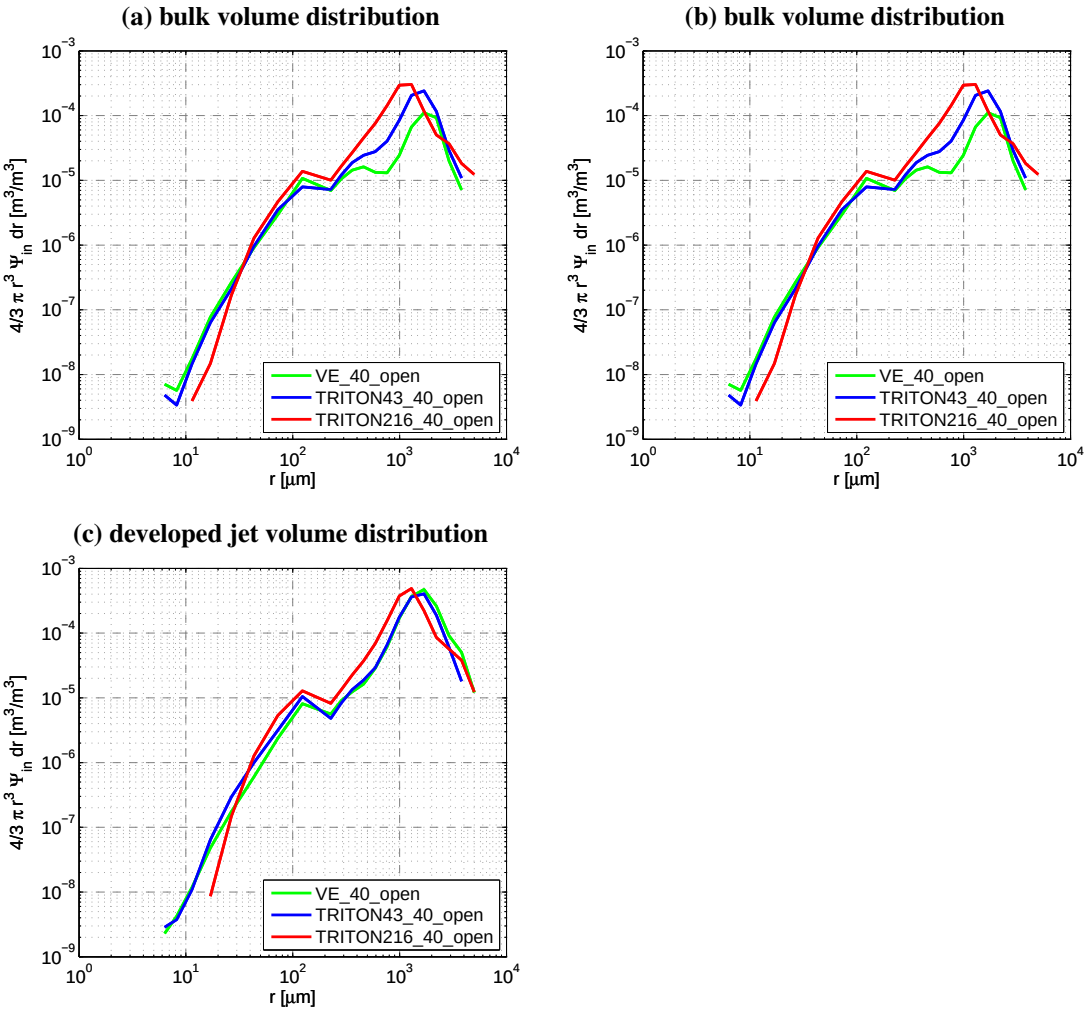

Figure .26.: Volume densities for all TRITON conditions are shown. Three representative sampling positions are shown.

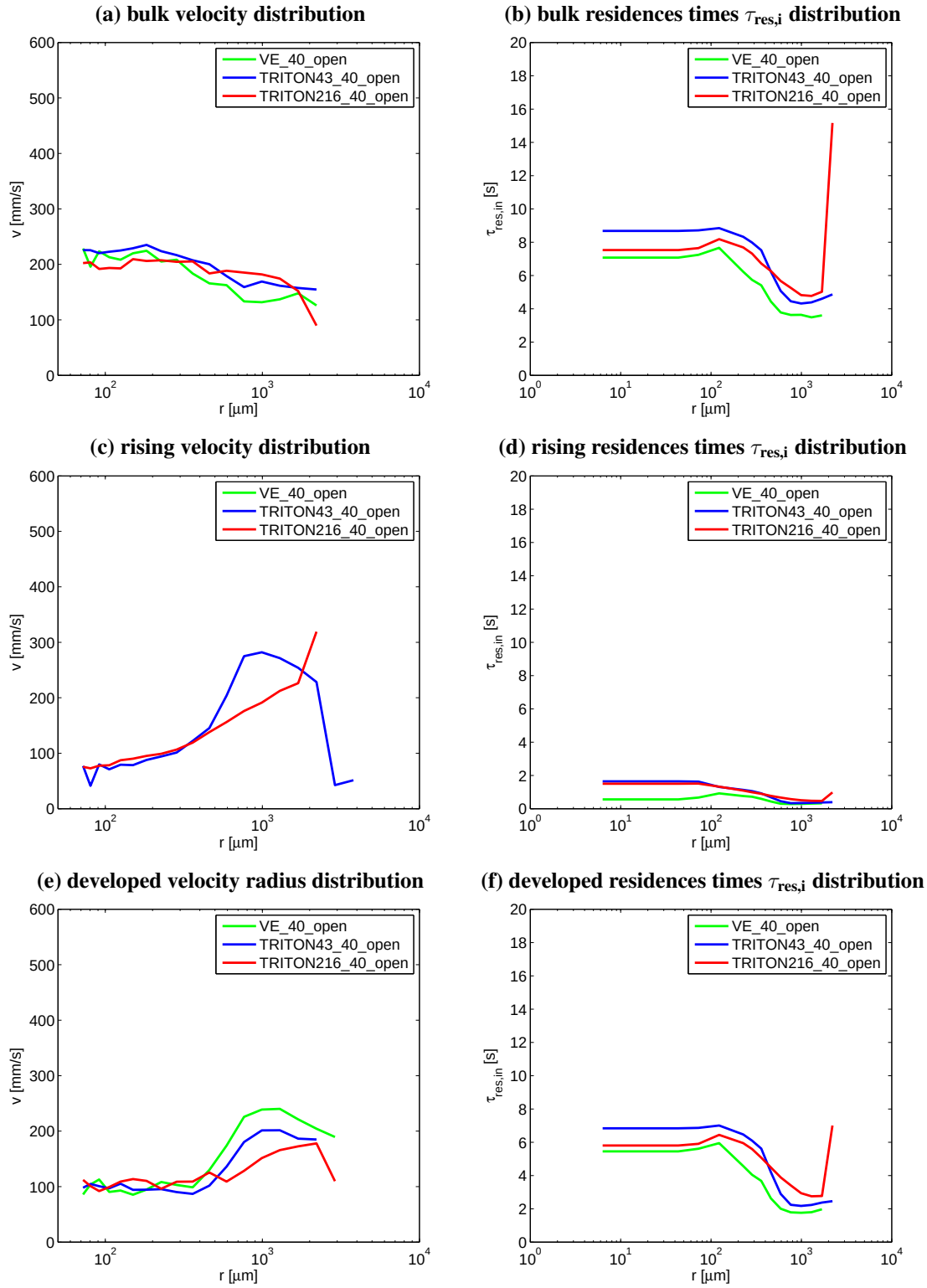

Figure .27.: Measured velocities v and residences times $\tau_{res,i}$ for bubbles with radius r. Three sampling positions are shown.

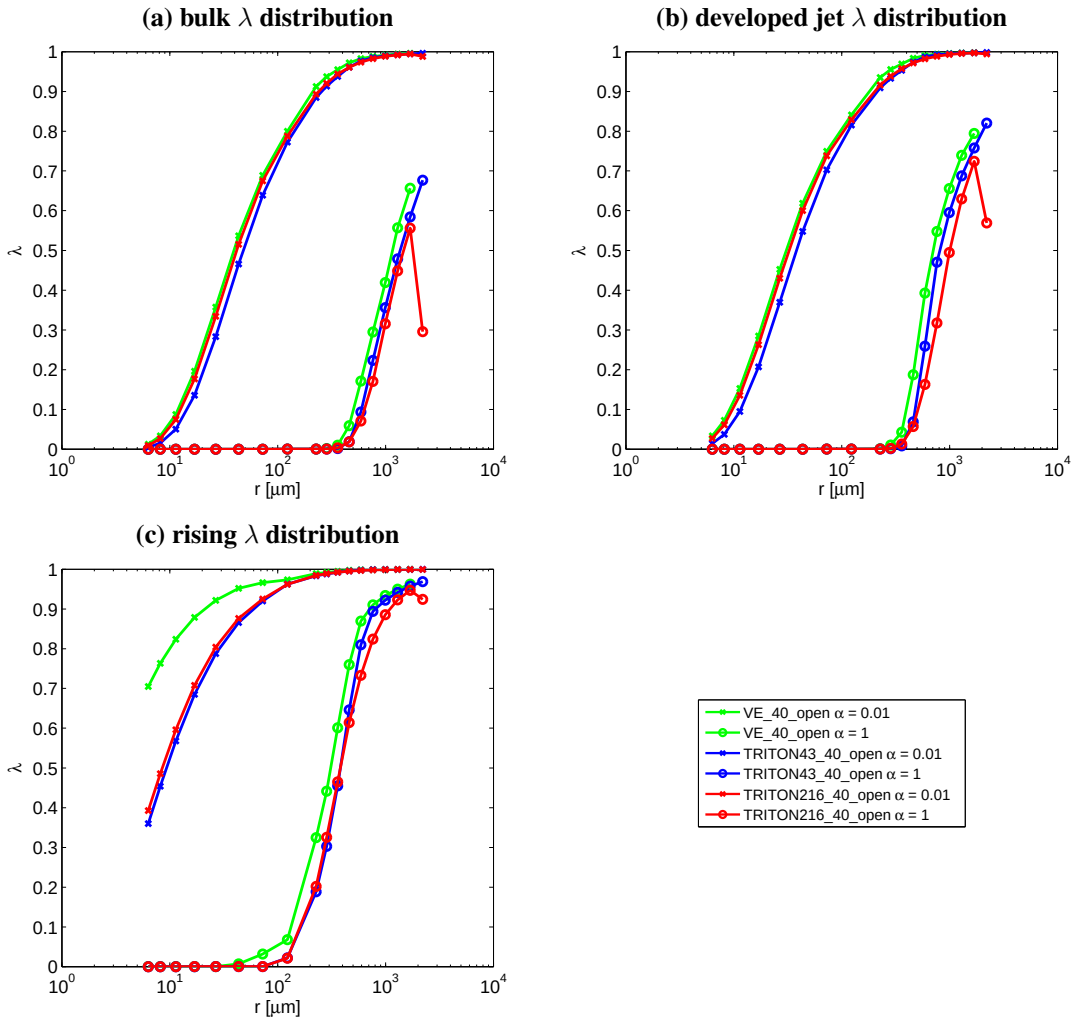

Figure .28.: Derived equilibration parameters λ for two different solubilities for three sampling positions in the tank. The calculation is based on eq. (8.15) using the calculated residence times $\tau_{res,i}$ and the model of a radius dependent transfer velocity for a single bubble k_b in the dirty case, see eq. (2.26)

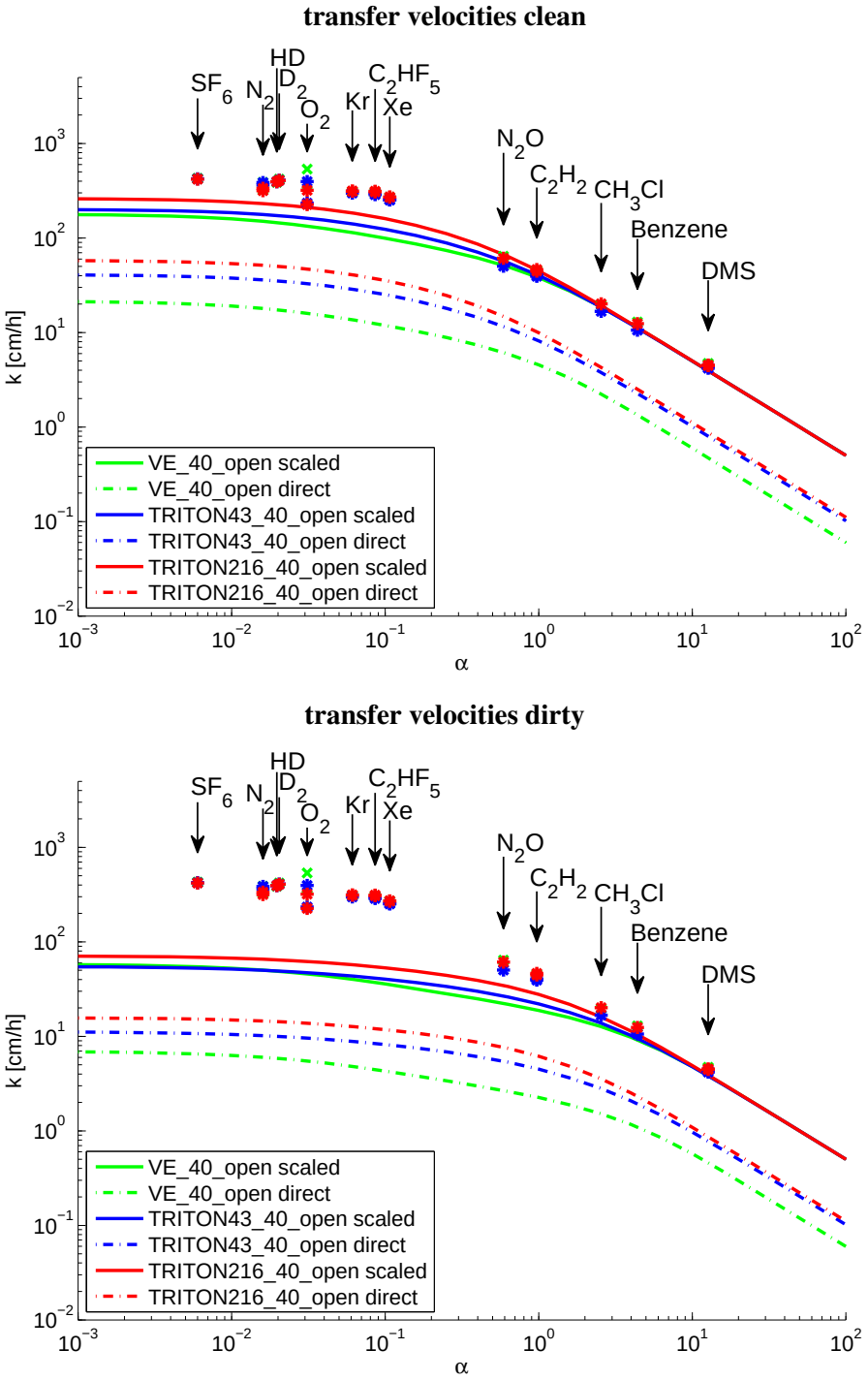
transfer velocities clean
SF6
HD
N2
D2
O2
Kr
C2HF5
Xe
N2O
C2H2
CH3Cl
Benzene
DMS
k [cm/h]
α
VE_40_open scaled
VE_40_open direct
TRITON43_40_open scaled
TRITON43_40_open direct
TRITON216_40_open scaled
TRITON216_40_open direct
transfer velocities dirty
SF6
HD
N2
D2
O2
Kr
C2HF5
Xe
N2O
C2H2
CH3Cl
Benzene
DMS
k [cm/h]
α
VE_40_open scaled
VE_40_open direct
TRITON43_40_open scaled
TRITON43_40_open direct
TRITON216_40_open scaled
TRITON216_40_open direct

Figure .29.:

Glycerol

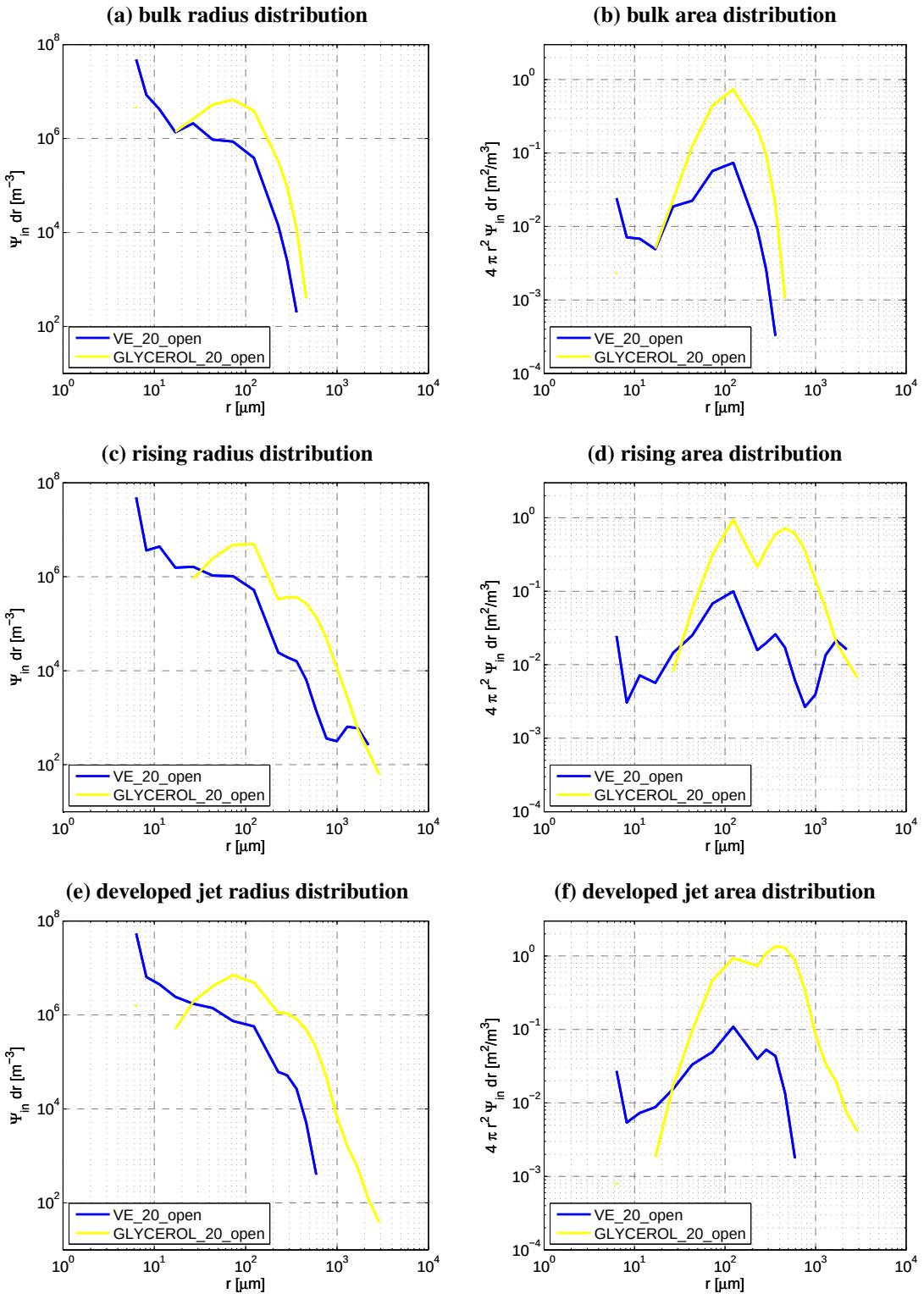

Figure .30.: Measured radius and area densities for the GLYCEROL conditions are shown. Three representative sampling positions are shown.

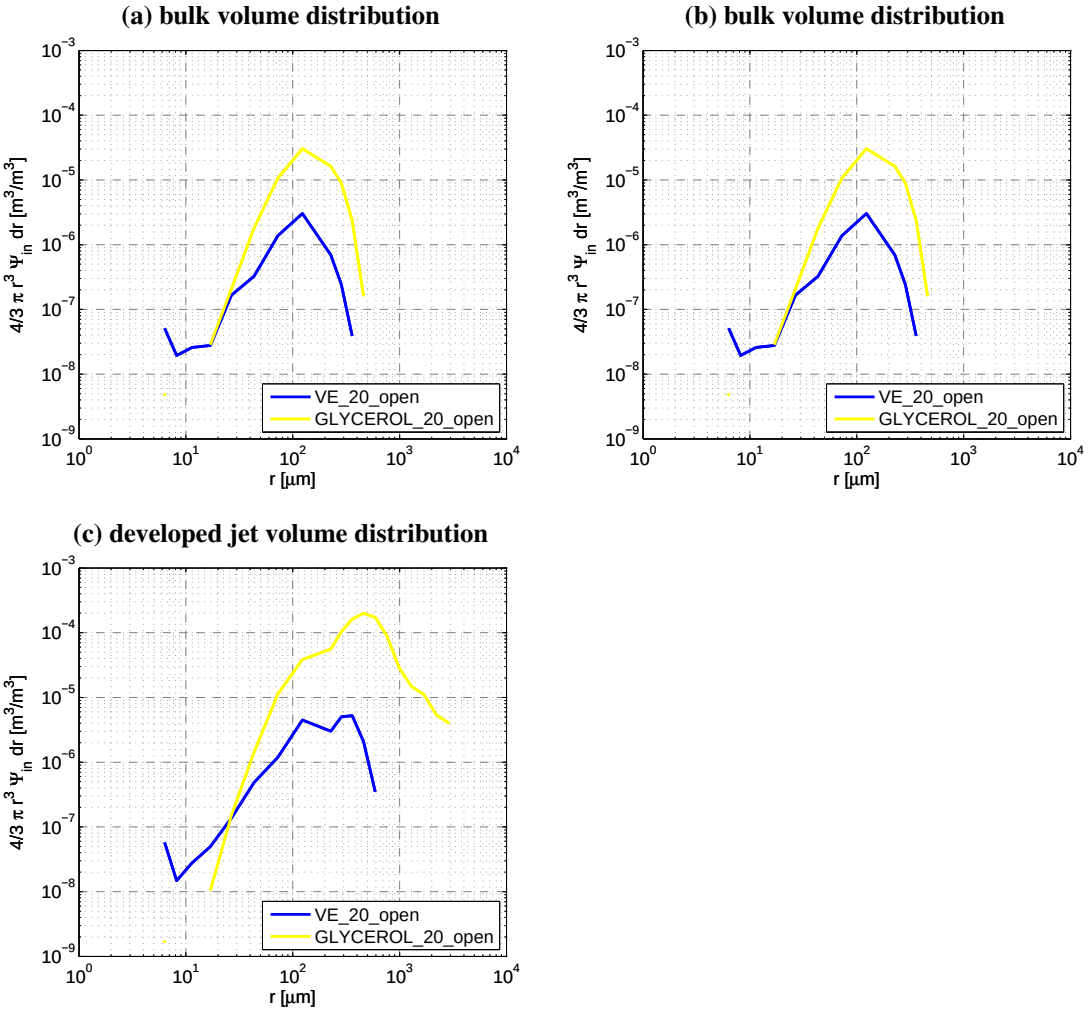

Figure .31.: Volume densities for the GLYCEROL conditions are shown. Three representative sampling positions are shown.

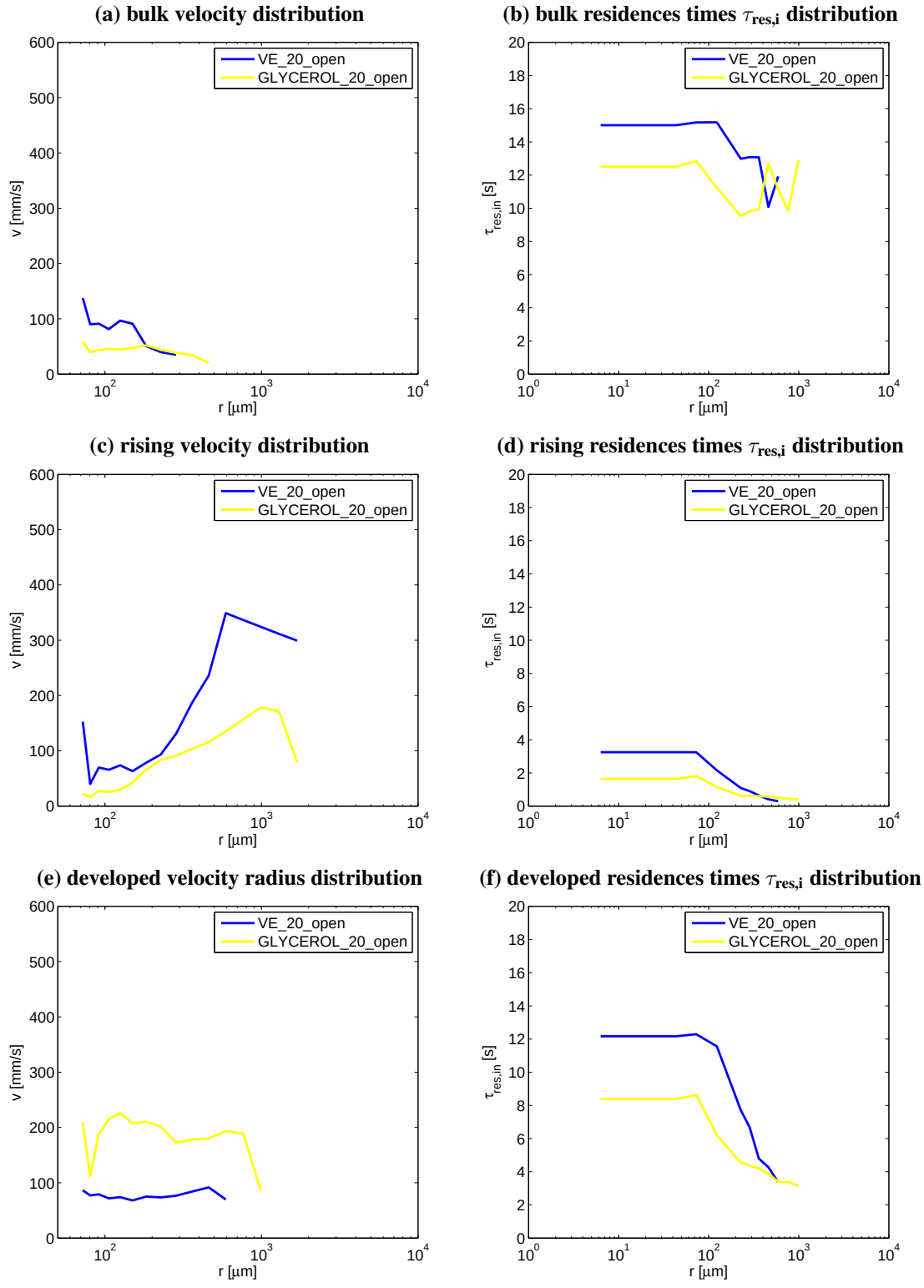

Figure .32.: Measured velocities v and residences times $\tau_{res,i}$ for bubbles with radius r. Three sampling positions are shown.

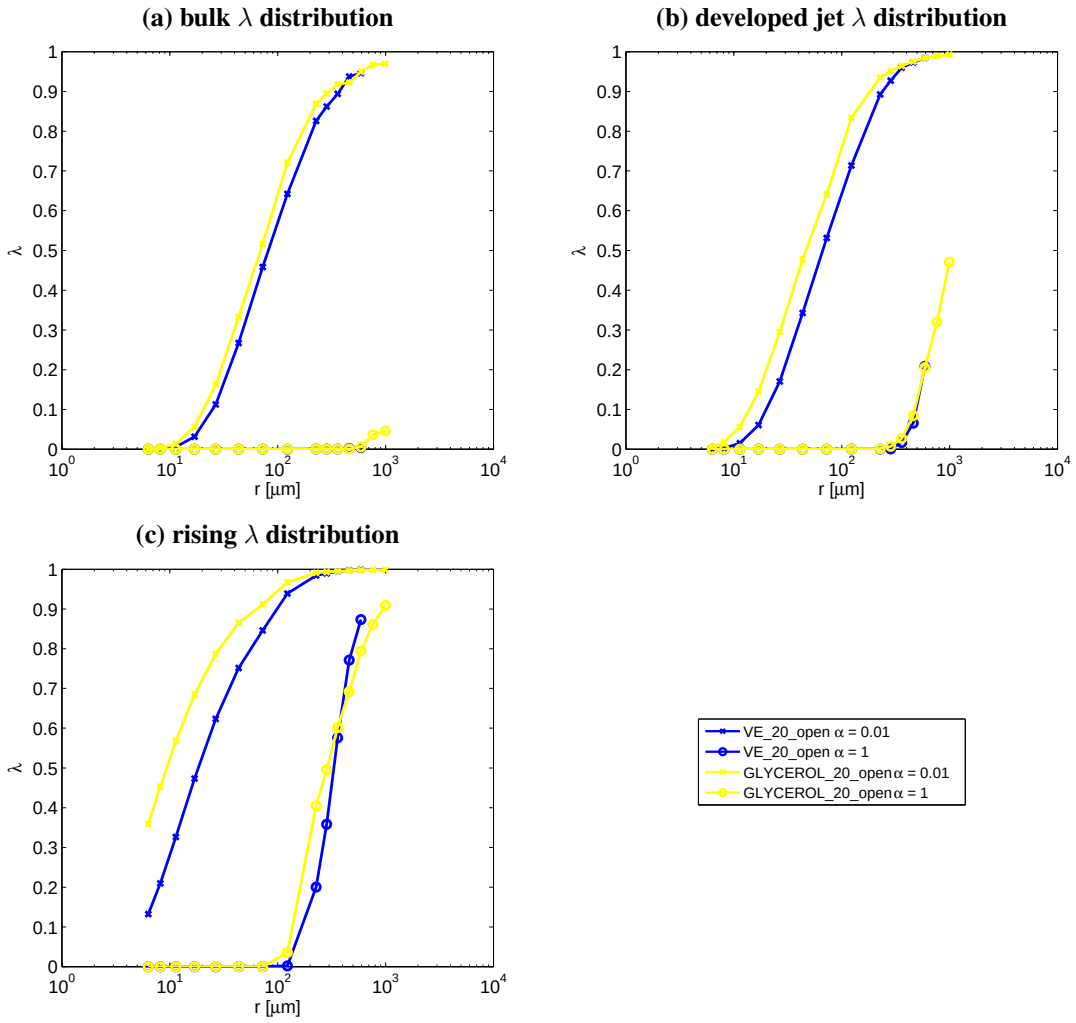

Figure .33.: Derived equilibration parameters λ for two different solubilities for three sampling positions in the tank. The calculation is based on eq. (8.15) using the calculated residence times $\tau_{res,i}$ and the model of a radius dependent transfer velocity for a single bubble k_b in the dirty case, see eq. (2.26)

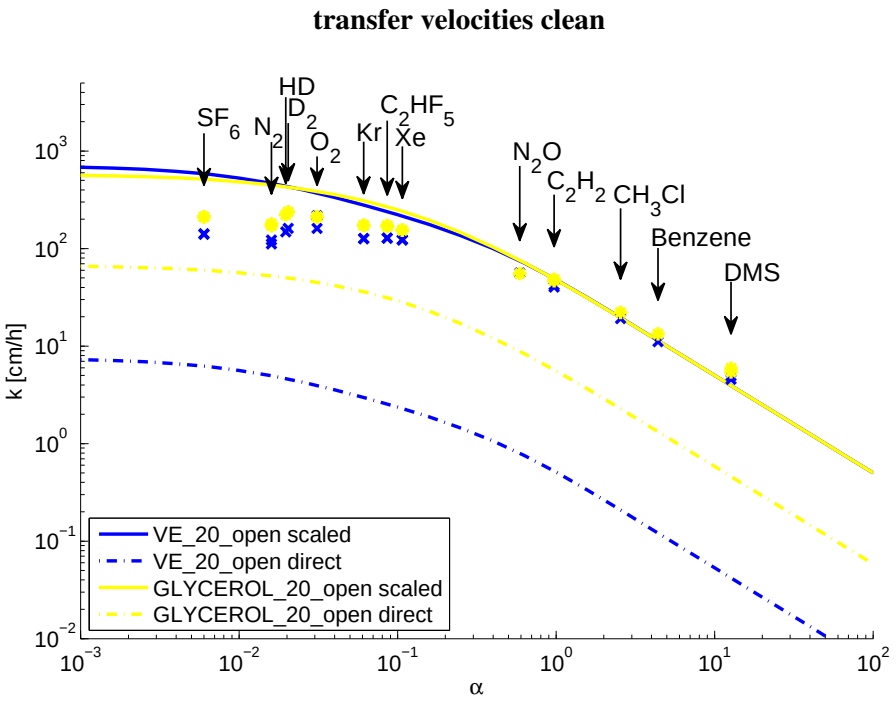
transfer velocities clean
HD
SF6
N2
D2
O2
Kr
C2HF5
Xe
N2O
C2H2
CH3Cl
Benzene
DMS
k [cm/h]
α
VE_20_open scaled
VE_20_open direct
GLYCEROL_20_open scaled
GLYCEROL_20_open direct

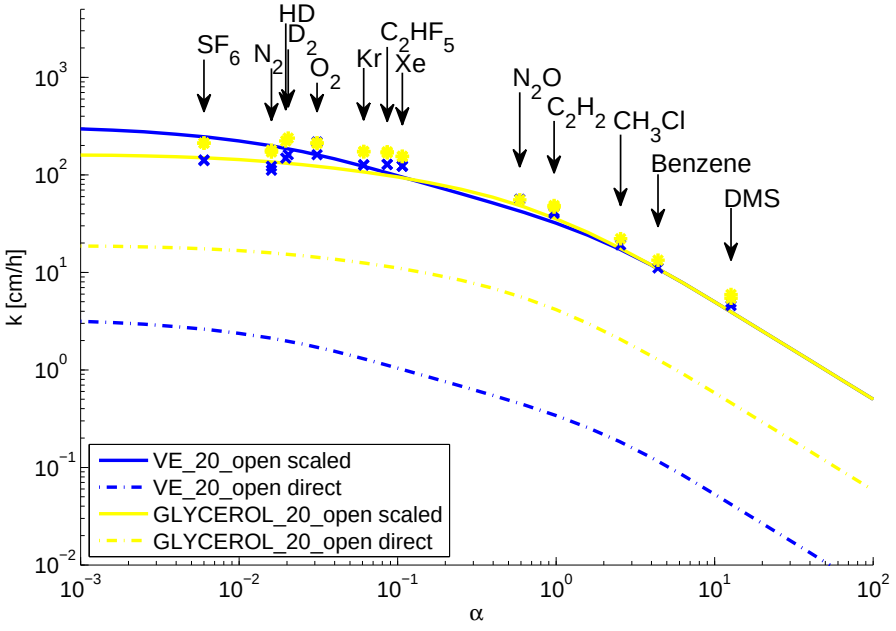
transfer velocities dirty
HD
SF6
N2
D2
O2
Kr
C2HF5
Xe
N2O
C2H2
CH3Cl
Benzene
DMS
k [cm/h]
α
VE_20_open scaled
VE_20_open direct
GLYCEROL_20_open scaled
GLYCEROL_20_open direct

Figure .34.:

Selection

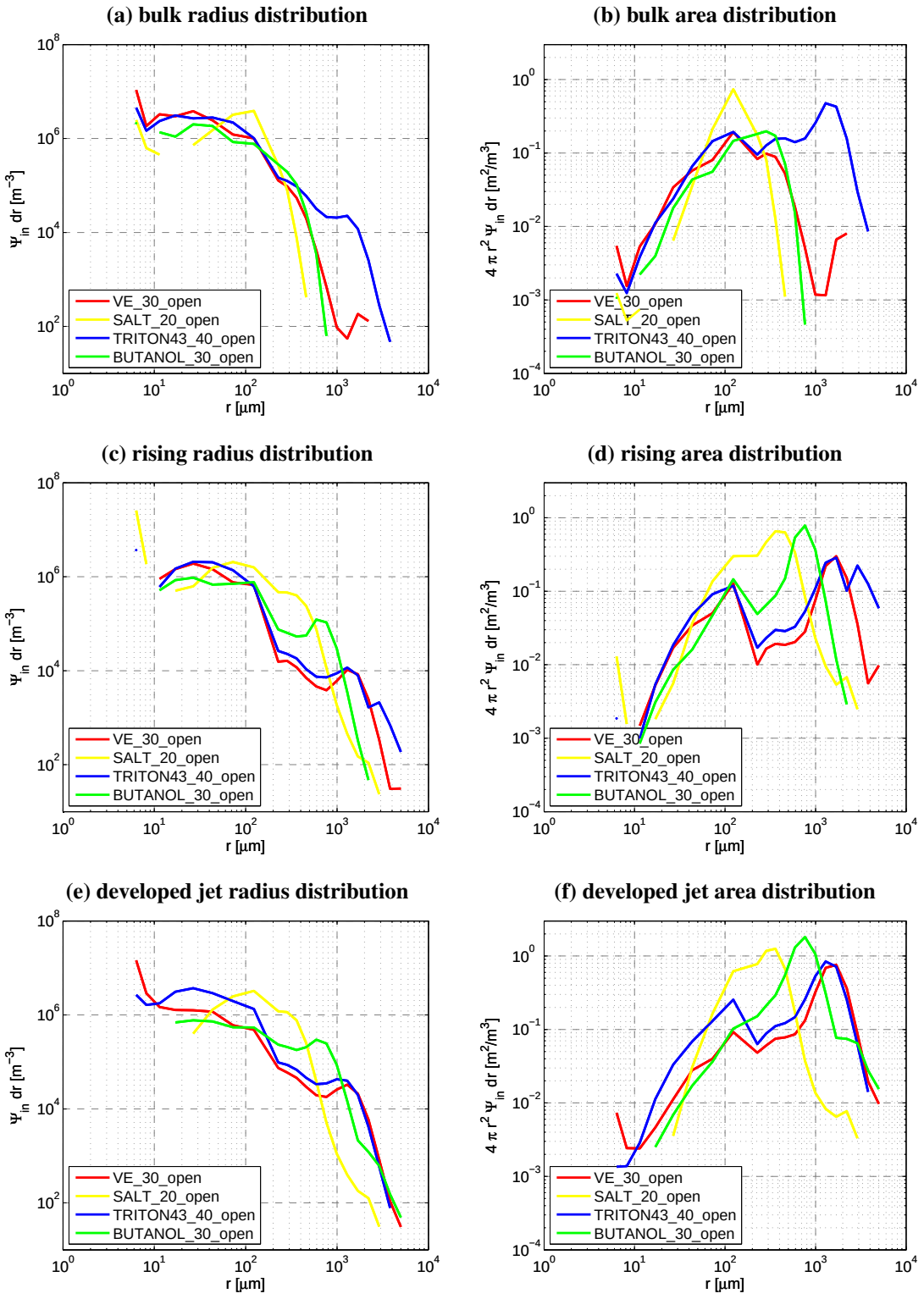

Figure .35.: Measured radius and area densities for a selection of conditions are shown. Three representative sampling positions are shown.

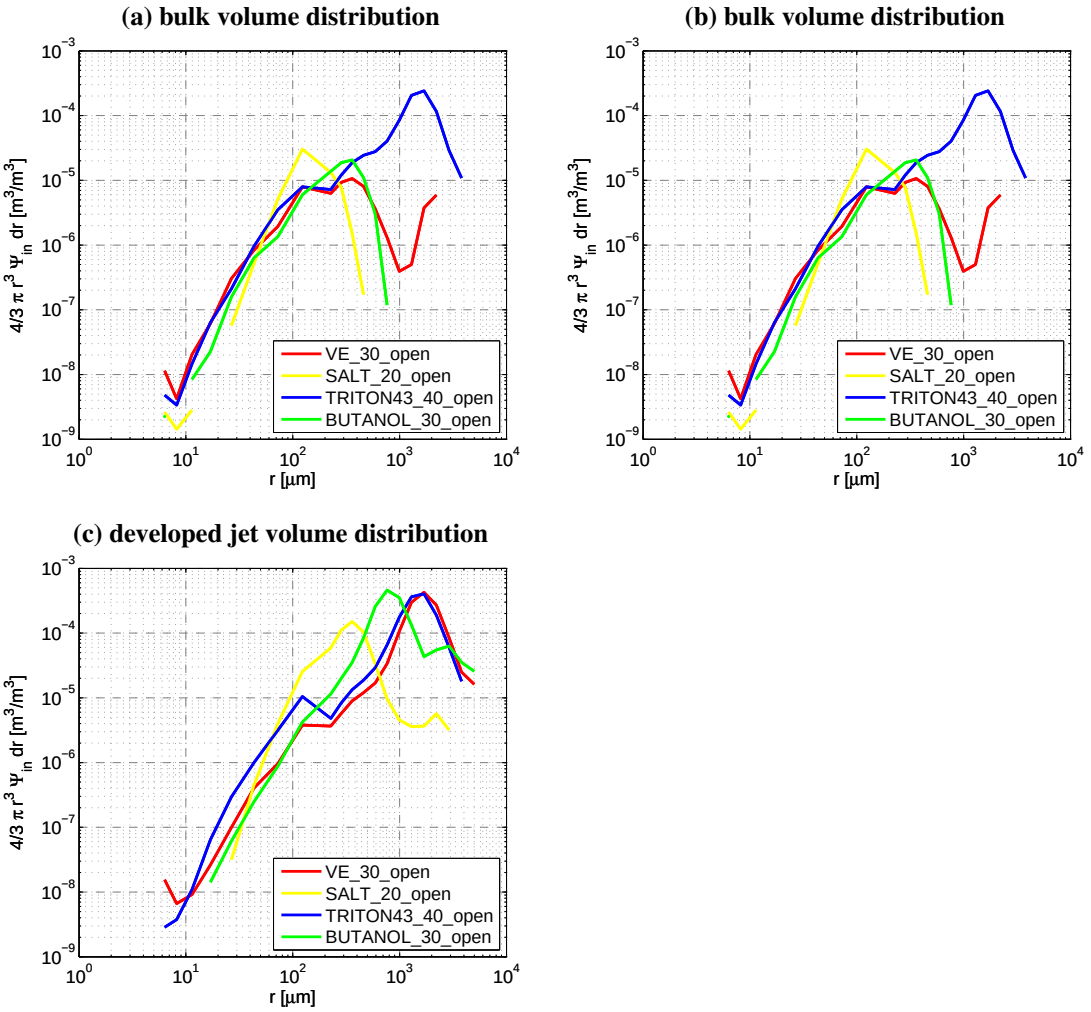

Figure .36.: Volume densities for a selection of conditions are shown. Three representative sampling positions are shown.

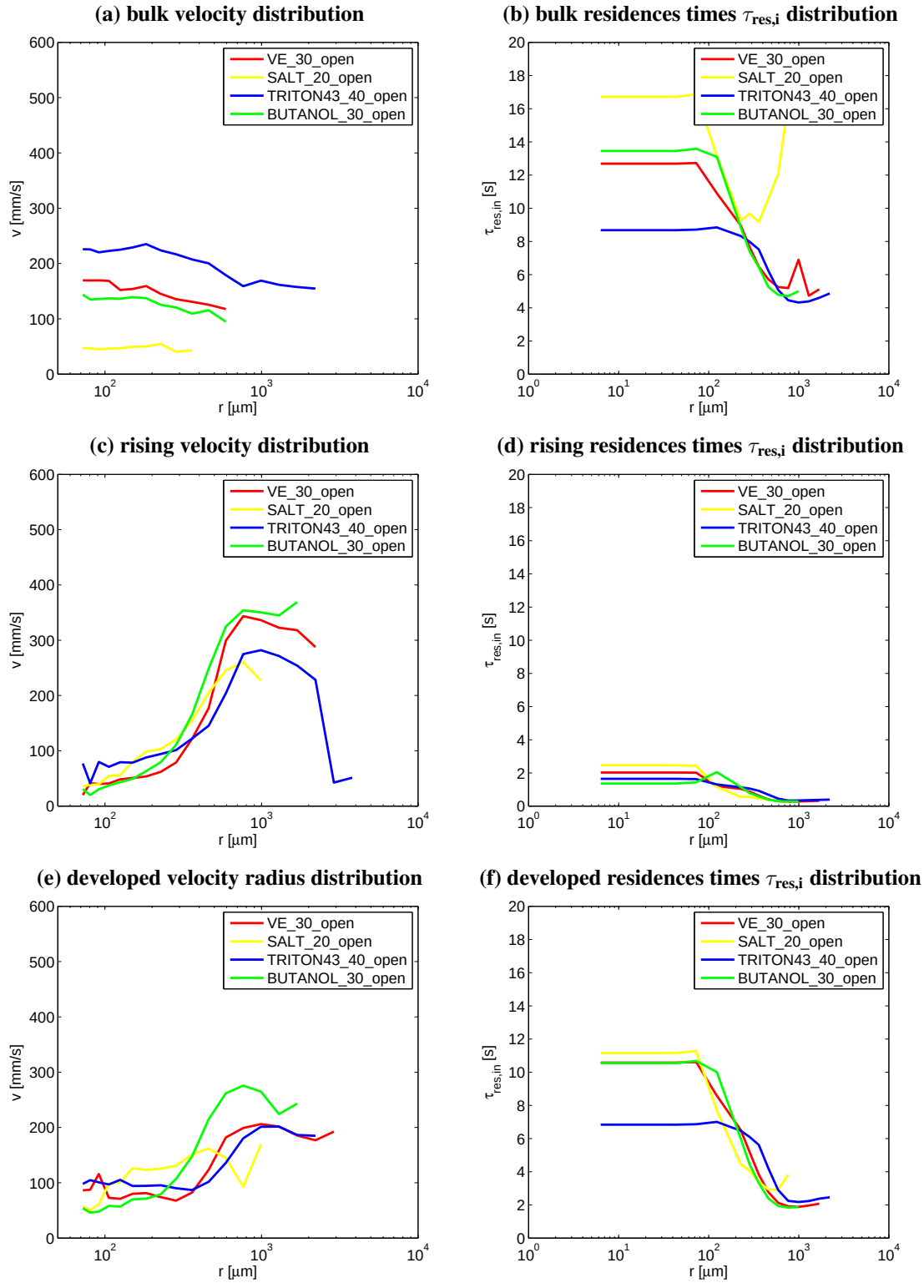

Figure .37.: Measured velocities v and residences times $\tau_{res,i}$ for bubbles with radius r. Three sampling positions are shown.

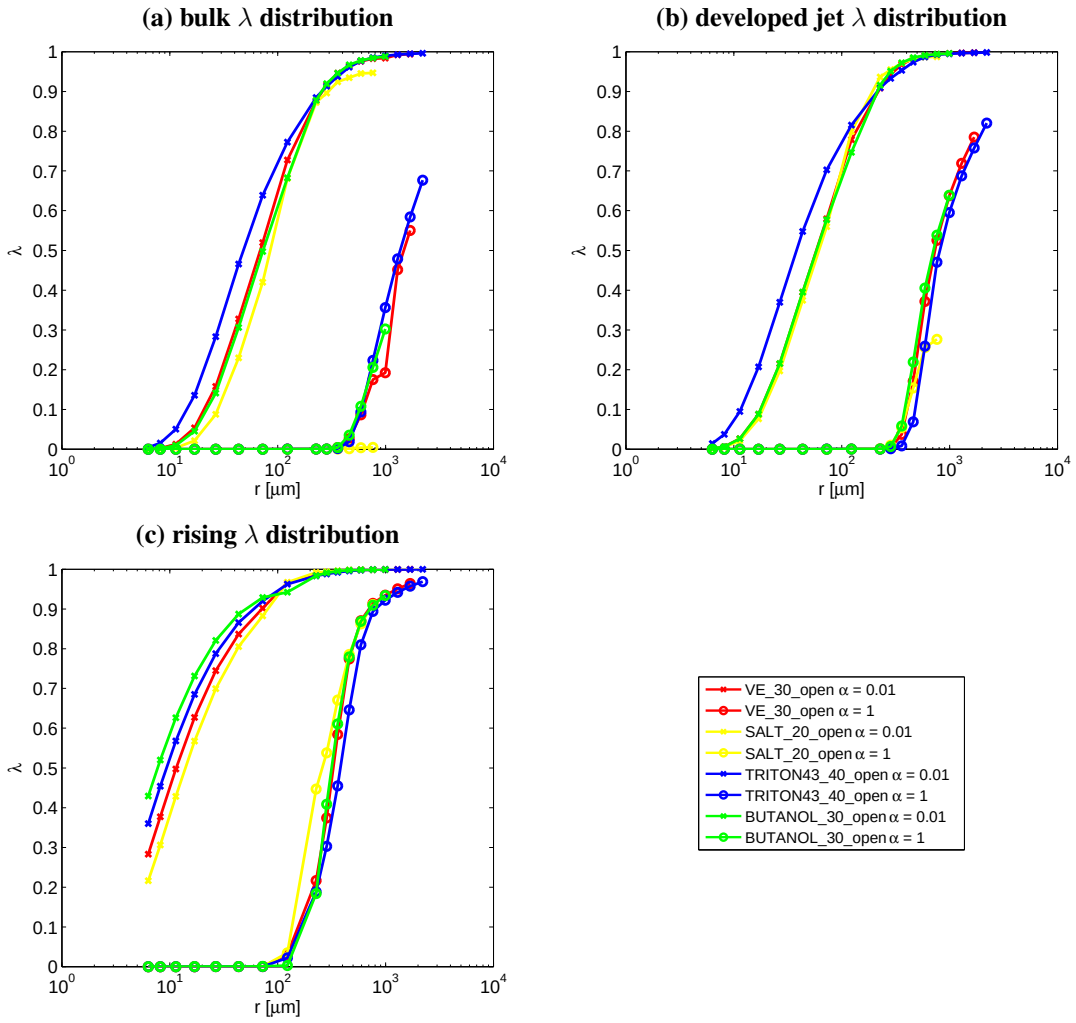

Figure .38.: Derived equilibration parameters λ for two different solubilities for three sampling positions in the tank. The calculation is based on eq. (8.15) using the calculated residence times $\tau_{\text{res,i}}$ and the model of a radius dependent transfer velocity for a single bubble k_b in the dirty case, see eq. (2.26)

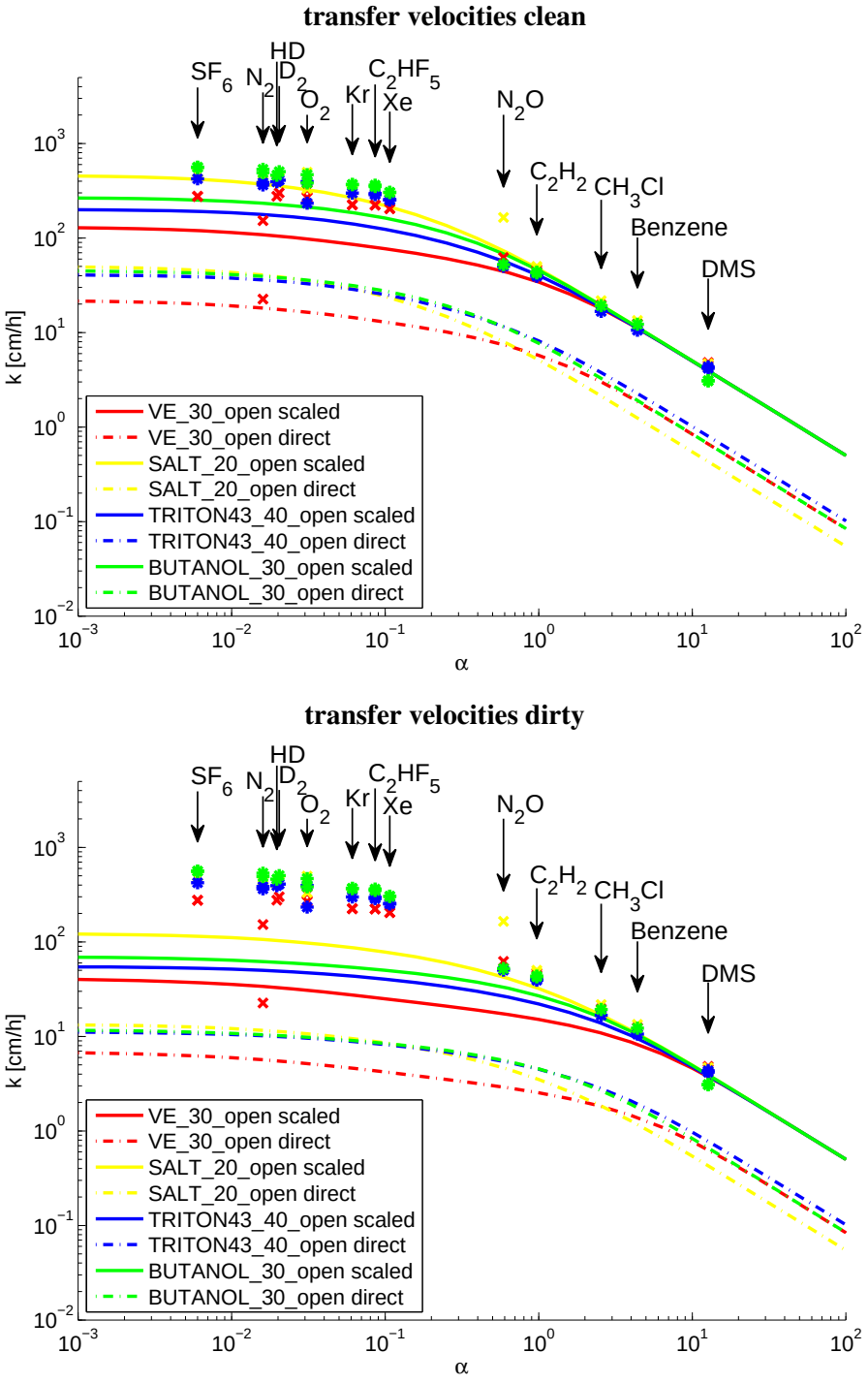
transfer velocities clean
SF6
HD
N2
D2
O2
Kr
C2HF5
Xe
N2O
C2H2
CH3Cl
Benzene
DMS
k [cm/h]
α
VE_30_open scaled
VE_30_open direct
SALT_20_open scaled
SALT_20_open direct
TRITON43_40_open scaled
TRITON43_40_open direct
BUTANOL_30_open scaled
BUTANOL_30_open direct
transfer velocities dirty
SF6
HD
N2
D2
O2
Kr
C2HF5
Xe
N2O
C2H2
CH3Cl
Benzene
DMS
k [cm/h]
α
VE_30_open scaled
VE_30_open direct
SALT_20_open scaled
SALT_20_open direct
TRITON43_40_open scaled
TRITON43_40_open direct
BUTANOL_30_open scaled
BUTANOL_30_open direct

Figure .39.:

C.2. Fitted Limiting Cases

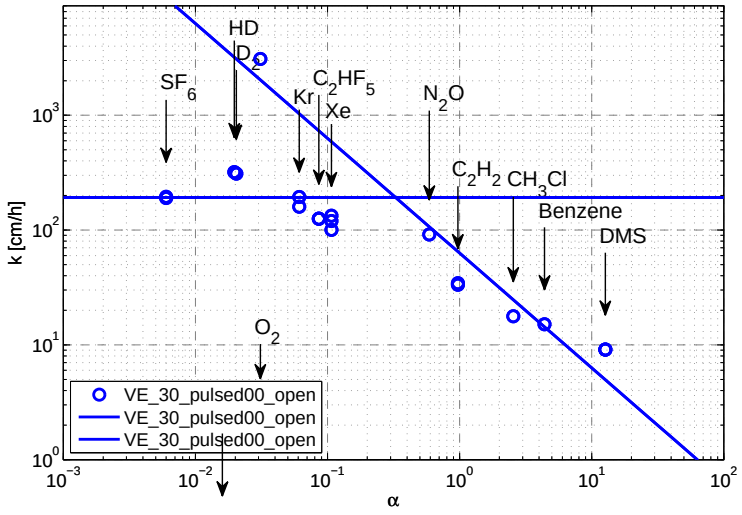

Figure .40.: Asymptotes of k_{bub} for the pulsed condition.

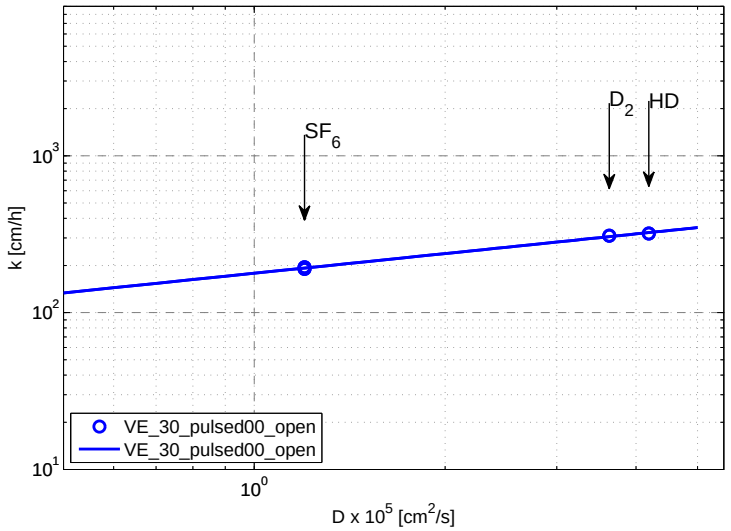

Figure .41.: D dependency of k_{bub} for the pulsed condition.

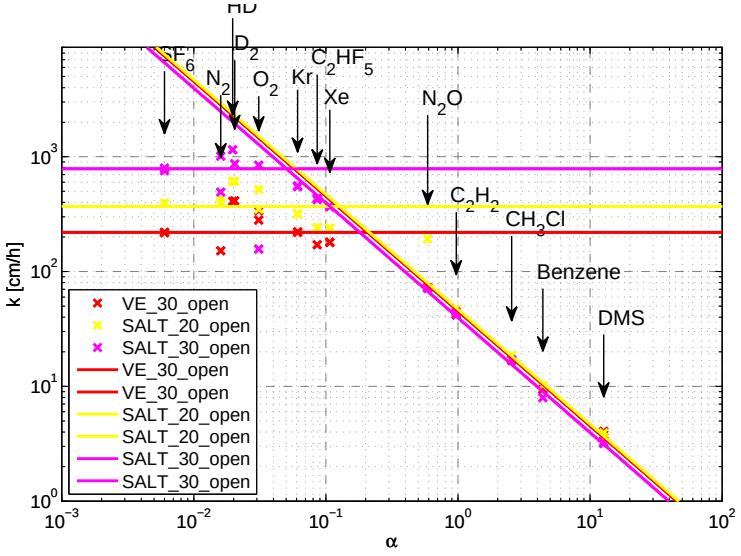

Figure .42.: Asymptotes of k_{bub} for all SALT conditions.

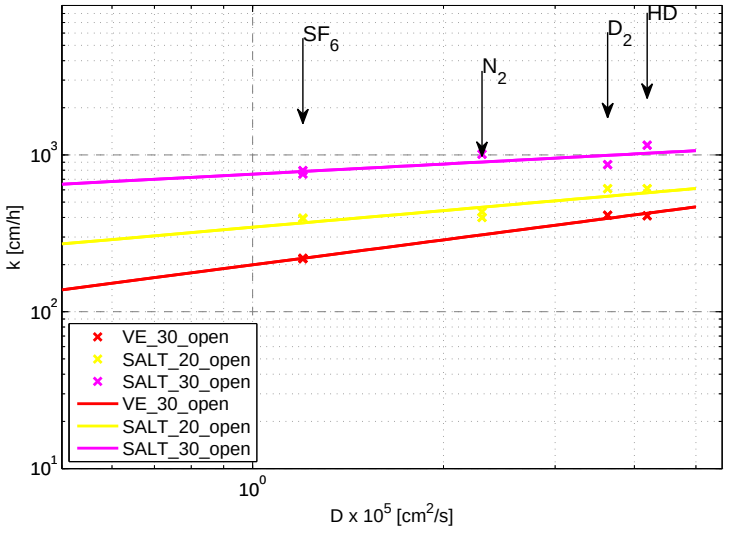

Figure .43.: D dependency of k_{bub} for all SALT conditions.

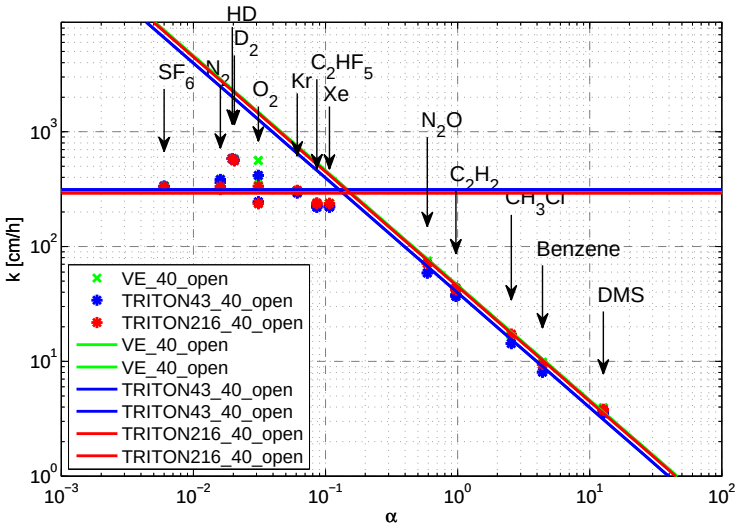

Figure .44.: Asymptotes of k_{bub} for all TRITON conditions.

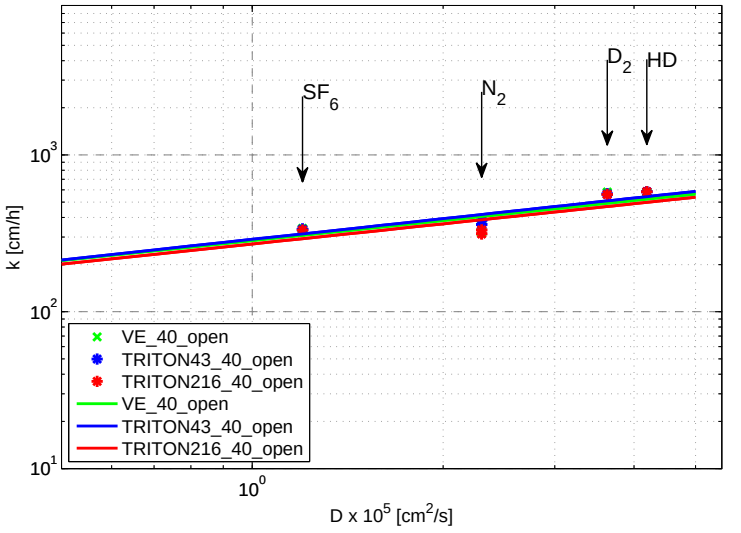

Figure .45.: D dependency of k_{bub} for all TRITON conditions.

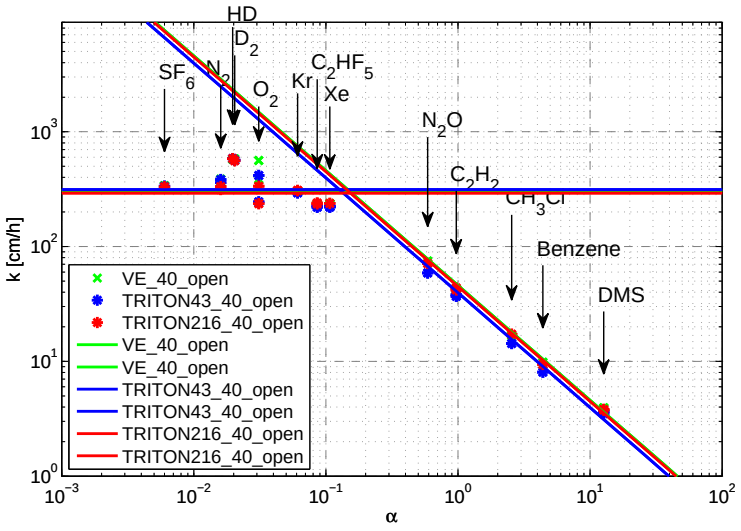

Figure .46.: Asymptotes of k_{bub} for the GLYCEROL condition.

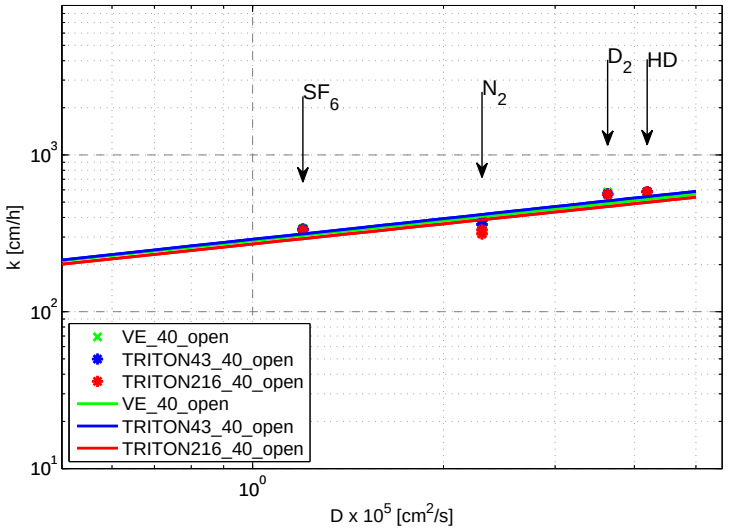

Figure .47.: D dependency of k_{bub} for the GLYCEROL condition.

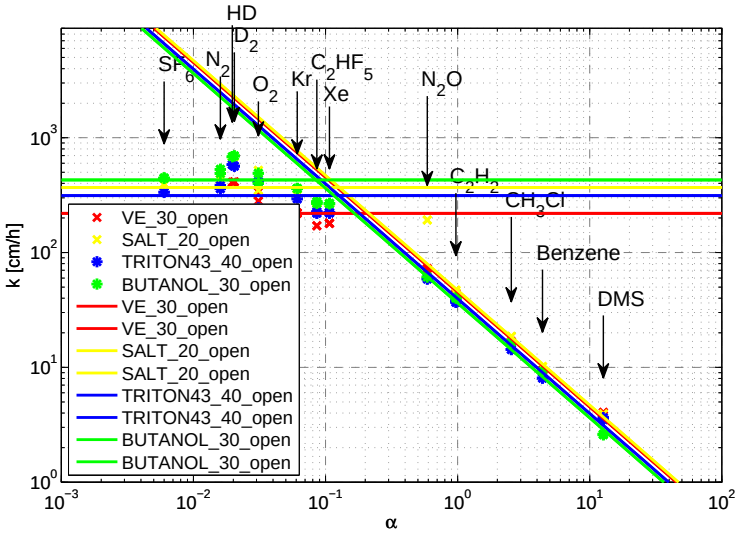

Figure .48.: Asymptotes of k_{bub} for a selection of conditions.

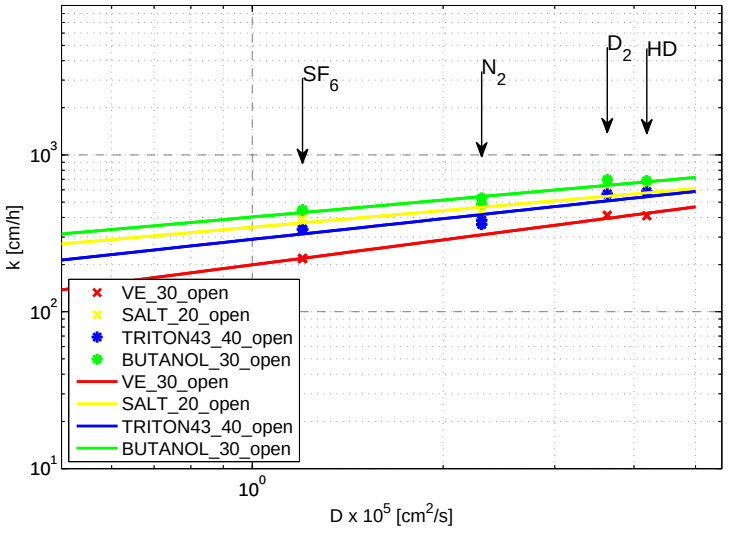

Figure .49.: D dependency of k_{bub} for a selection of conditions.

C.3. Comparison of Invasion and Evasion

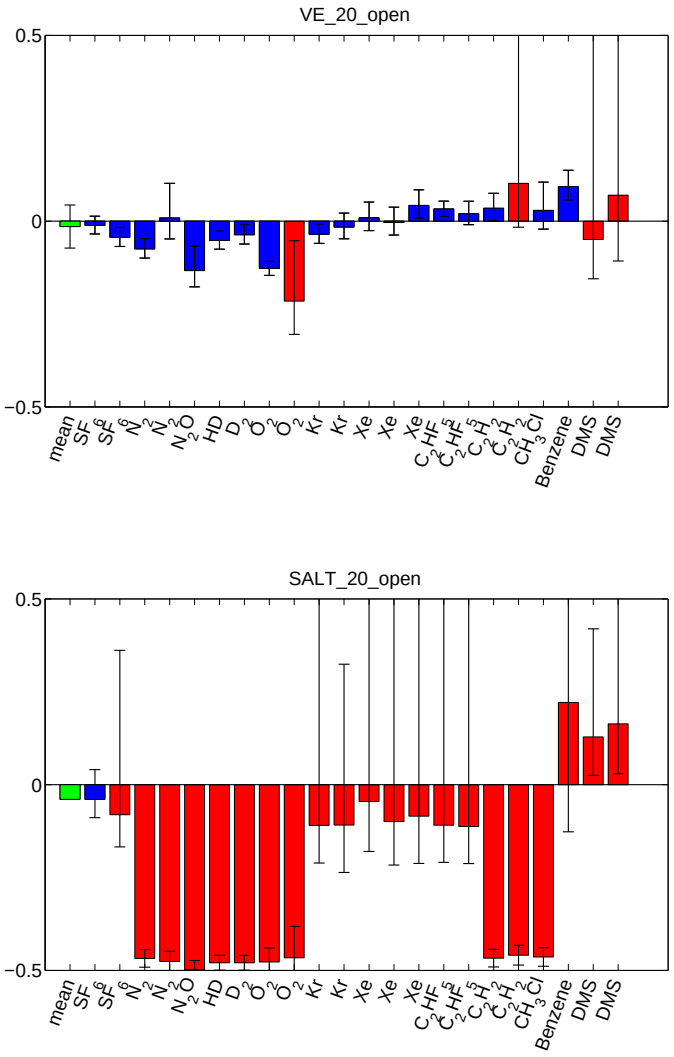

Figure .50.: Relative enhancement of invasion over evasion measurements. Blue bars denote measurements used for mean calculation. Red bars are excluded due to a errors larger than 15% or a deviation larger than 15%, which are attributed to experimental problems of the invasion measurement. *top*: VE_20 *bottom*: SALT_20

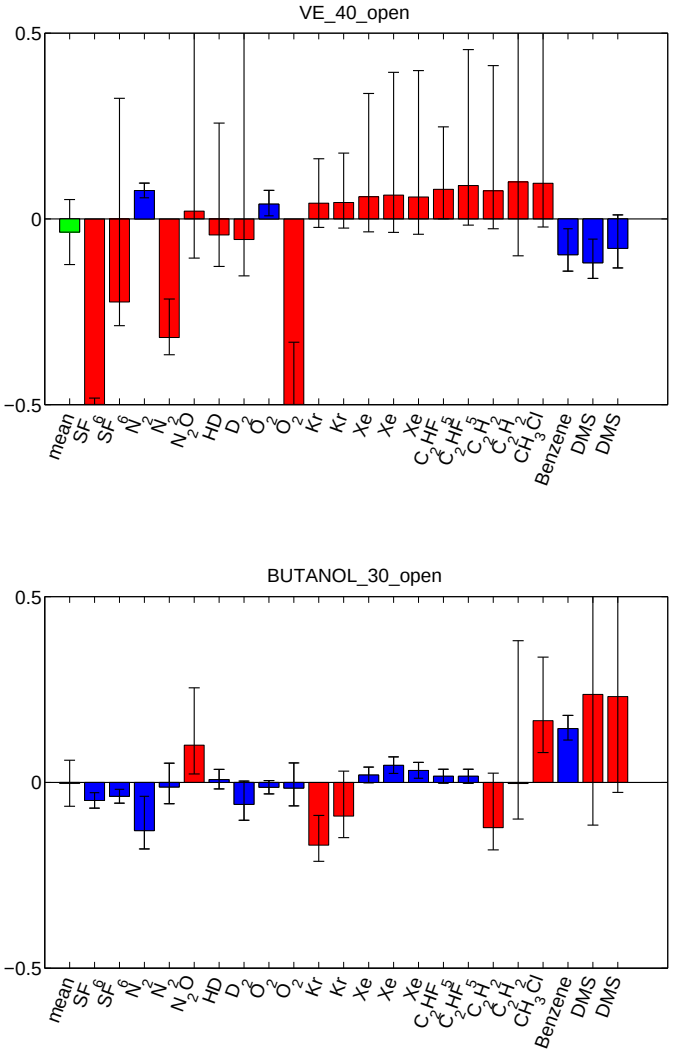

Figure .51.: Relative enhancement of invasion over evasion measurements. Blue bars denote measurements used for mean calculation. Red bars are excluded due to a errors larger than 15% or a deviation larger than 15%, which are attributed to experimental problems of the invasion measurement. *top*: VE_40 *bottom*: GLYCEROL_20

Danksagung

Ich möchte allen danken, die zum Gelingen dieser Arbeit, ob fachbezogen oder auf andere Weise unterstützend, beigetragen haben. Prof. Bernd Jähne möchte ich für die Möglichkeit und die Unterstützung bei der Durchführung dieser Arbeit danken. Auch die zahlreichen Gelegenheiten für fachübergreifende Projekte, die einen neuen Blick auf das ein oder andere Problem aufzeigten, waren sehr lehr- und hilfreich. Die Gelegenheit für die Besuche mehrerer internationaler Konferenzen bzw. Auslandsaufenthalten, um sich mit anderen Wissenschaftlern über das eigene Gebiet auszutauschen und Kontakte zu knüpfen, weiß ich sehr zu schätzen. In diesem Zusammenhang möchte ich auch Prof. Satoru Komori und seiner Arbeitsgruppe von der Universität Kyoto für die Möglichkeit von Messungen in Kyoto und für Ihre Gastfreundschaft danken. Herrn Prof. Werner Aeschbach-Hertig möchte ich für die kurzfristige Übernahme des Zweitgutachtens danken, im Besonderen im Angesicht des hohen Arbeitsaufkommens. Herrn Prof. Matthias Bartelmann danke ich für die Bereitschaft, Teil meines Prüfungskomitees zu sein. Sowie Herrn
Prof. Dirk Dubbers, der den angestrebten Prüfungstermin durch sein kurzfristiges einspringen als Prüfer ermöglicht hat. Der gesamten Arbeitsgruppe möchte ich für die bereitwillige und hilfreiche Korrektur dieser Arbeit danken. Auch für die allgemein gute Atmosphähre in der Gruppe bin ich dankbar, da sie die Arbeit wesentlich erleichtert hat. Im Besonderen möchte ich Dasha Trofimova und Christine Kräuter danken, da sie vor allem in der Endphase wesentlich zu meinem Durchhalten beigetragen haben und einen großteil der Korrekturen übernommen haben. Daniel Kiefhaber danke ich für seine wertvollen Anregungen und Hilfe bezüglich der Korrektur der Arbeit, sowie für den zahlreichen und anregenden Austausch über Wellen, Elektronik, Optik, Programmierung und vieles andere. Roland Rochholz danke ich dafür, mir diese Arbeit durch seine tatkräftige Unterstützung bei der Beendigung der Diplomarbeit, erst ermöglicht zu haben und auch beim Beginn der Dissertation stets zu Hilfe bereit war. Felix Friedl bin ich für die häufigen und klärenden Diskussionen über Optik, Prismen, Scheimpflug und Bildverarbeitung dankbar. Nils Krah möchte ich für neue Denkanstösse und Erklärungen bei einer Vielzahl von Aspekten des Gasaustausch danken. Kerstin Krall danke ich für die Hilfe bei praktischen Problemen mit dem Gasaustausch jeglicher Art, sei es der Nachweis von Gasen oder der Aufbau von Experimenten. Günther Balschbach will ich für seine Hilfsbereitschaft bei Problemen aller Art, während meiner gesamten Zeit am IUP, danken. Max Bopp danke ich für die tatkräftige Unterstützung bei handwerklichen Problemen bei dem Aufbau von dem Experiement.

Meiner Familie und meinen Freunden möchte ich für das große Verständnis für meine Abwesenheit in der Endphase meiner Arbeit und die bedingungslose Unterstützung in dieser Zeit danken.